Journal of Fluids Engineering

Published Quarterly by The American Society of Mechanical Engineers

VOLUME 111 • NUMBER 2 • JUNE 1989

Contents (continued)

GEORGE FRIEDRICH WISLICENUS

Dr. George Friedrich Wislicenus died in Santa Rosa, California, on Saturday, April 2, 1988, at the age of eighty-four. Dr. Wislicenus was Mr. Turbomachinery to several generations of practitioners in fluids engineering and remained active during his retirement as a consultant and author in the field. His most recent publication was the "Preliminary Design of Turbopumps and Related Machinery" which was published by NASA as Reference Publication 1170 in October 1986.

Dr. Wislicenus was well-known for his contributions to the field of fluids engineering, most specifically in the areas of turbomachinery, cavitation, compressors, and pumping machinery. He was an early pioneer in the transonic compressor field, and made notable contributions to the unified theory of turbomachinery. His book, *Fluid Mechanics of Turbomachinery*, first published in 1949, and then supplemented and reprinted in 1965 by Dover, is considered to be one of the most authoritative in the design of turbomachinery, and remains a leading source of information for workers in that field of engineering. In addition to many contributions to technical journals, Dr. Wislicenus authored a section on "Centrifugal Pumps" in *Marks' Mechanical Engineers Handbook*.

In July 1969, Dr. Wislicenus retired from The Pennsylvania State University, University Park, Pennsylvania, where he served as Head of the Department of Aerospace Engineering, and Director of the Garfield Thomas Water Tunnel of that University's Applied Research Laboratory. As director of the largest known water tunnel in the world, he directed research on the propulsion of submerged bodies and brought many principles of air-breathing propulsion to the field of underwater propulsion; in so doing, he developed design methods which greatly extended the cavitation-free operating limits of underwater propulsors. In 1979 he received the Applied Research Laboratory's Distinguished Performance Award.

Before going to Penn State in 1954, Dr. Wislicenus was Chairman of the Mechanical Engineering Department at Johns Hopkins University in Baltimore Maryland, a position he held for six years. During this same period, he participated in an aircraft nuclear propulsion project at the Oak Ridge National Laboratories. From 1945 to 1948, he was Assistant Chief Engineer of Design and Research in the Aircraft Engine Division of the Packard Motor Company at Toledo, Ohio, where he signed as inventor for the first American fan engine. As hydraulic engineer and research engineer with the Worthington Pump and Machinery Company in Harrison, N.J., from 1935 to 1945, Dr. Wislicenus directed the design and development of a variety of pumps, and pioneered the application of supersonic relative velocities in axial flow compressors. During his career he served as consultant to the Worthington Corporation, the Aeronautical Division of Curtis-Wright Corporation, Oak Ridge National Laboratories, General Electric Company, Rocketdyne Division of North American Aviation, Inc., Goulds Pump Company and the U.S. Navy. For many years he worked closely with the NASA Lewis Research Center on their research in the fluid mechanics of turbomachinery. Dr. Wislicenus was granted fourteen patents by the United States in areas involving design of compressors, pumps, propellers, and propulsion systems.

Dr. Wislicenus served as a member of the NASA Research and Technology Advisory Subcommittee on Air Breathing Propulsion, and as a member of the NACA Subcommittee on Compressors and Turbines. He was a member of the National Research Council's Panel on Hydrodynamics of Submerged Bodies, and in 1958 was Chairman of the Bureau of Naval Ordnance Systems Command Hydroballistics Advisory Committee.

A Fellow of The American Society of Mechanical Engineers, he served that organization as Chairman of its Hydraulic Division in 1957, as chairman of its Cavitation Committee in 1960–1961, and as a member of the Executive Committee for its Professional Group on Underwater Technology. He received the first ASME Fluids Engineering Division Award in 1968 in Philadelphia where the spring conference of the Fluids Engineering Division was dedicated to him. In 1980 he received the ASME Centennial Medallion for distinguished service. He was a Fellow of the American Institute of Aeronautics and Astronautics, and in 1960 was an initial and founding member of that society's Technical Committee on Underwater Propulsion. Dr. Wislicenus was a member of the American Society of Engineering Education, the International Association for Hydraulic Research, the American Society for the Advancement of Science, Sigma Xi, and Pi Tau Sigma.

Dr. Wislicenus was born in Strasbourg, Alsace, on August 27, 1903. After receiving his degree from the State School of Mechanical Engineering in Wurzburg, Germany, he came to the United States in December 1926, and then completed his master of science and doctor of philosophy degrees at the California Institute of Technology under the guidance of Dr. Theodore von Karman. On May 13, 1931, he married Lisel Weischedel, who died on November 2, 1987. Dr. Wislicenus is survived by his three grandchildren, Christie, Sandie, and Mark, and by one great-grandchild, Ashley Wislicenus. His only child, Wolfram Dreyer Wislicenus, died in an accident in 1976. Members of the immediate family may be contacted at 5911 La Cuesta Drive, Santa Rosa, California 95409 (Telephone: 707-538-1348).

Throughout his career, Dr. Wislicenus was an inspirational leader and a strong advocate of advanced training and graduate study in fluids engineering. Consequently a fund is being established at Penn State which will eventually be used to assist students in graduate study. Contributions may be made to the George F. Wislicenus Memorial Fund, One Old Main, The Pennsylvania State University, University Park, PA 16802.

Studies of Flow Patterns in a Diffuser Designed to Generate Longitudinal Vortices

L. N. Goenka

R. L. Panton

D. G. Bogard

Department of Mechanical Engineering,
The University of Texas,
Austin, Texas 78712

This paper describes flow visualization studies on a three-dimensional diffuser that generates two longitudinal vortices. The premise is that the three-dimensional flow patterns of this diffuser may have attributes that are superior to the two-dimensional flows of conventional diffusers. The diffuser geometry consists of a wide-angle, plane-wall diffuser with a pyramid-shaped insert attached to its expansion wall. The upsweep on the insert upper surface increases the pressure of the incoming flow, which rolls over into the expansion region in the presence of a transverse pressure gradient to form two symmetric, longitudinal vortices. At low Reynolds numbers (below 6000 based on the diffuser inlet height), the flow exhibited three flow patterns with subtle distinctions. The flowfield contained longitudinal vortices that modified and reduced in extent the separated regions that were present along the diffuser expansion wall. At high Reynolds numbers (above 6000), the separated regions along the diffuser expansion wall were replaced by a turbulent vortex. The lack of closed separated regions in the flow implies the absence of low-frequency effects that are characteristic of such regions. In addition, the flowfield exhibited little or no hysteresis with respect to changes in Reynolds number. These flowfield features are desirable in certain applications, such as exhaust diffusers for turbomachinery.

1 Introduction

The devices employed to control fluid flows are usually two-dimensional: either plane or axisymmetric. This is probably the direct result of the simplicity that two-dimensional objects have in construction, experimentation, and analysis. These are great advantages, and many two-dimensional flows are undoubtedly optimum for their intended purpose. However, it is not without merit to ask: Are there essentially three-dimensional flow patterns that might be useful and perhaps have attributes that are superior to the common two-dimensional flows? It was this line of thought that lead us to consider the project reported herein.

Diffusers have received much attention and research. They are a frequent element in many fluid devices. Furthermore, they are prone to hysteresis, separation, and poor performance in certain situations. For these reasons plane-wall diffusers were chosen as a specific case where the approach outlined above might be applied. The project was to take a plane-wall diffuser and by various inserts generate a large-scale three-dimensional flow. The objectives were to document the characteristics of this flow throughout a range of Reynolds number and to determine how various important characteristics of the flow responded to changes in the geometric parameters of the insert. The information from these tests is a basis from which one may judge the ap-

propriateness of using this specific type of three-dimensional flow, or an adaption thereof, for a particular application. A preliminary report of this work was presented in a conference article by Panton, Goenka, and Bogard, 1986. The information in this paper supercedes the previous report and gives a complete account of the flow visualization problem.

The diffuser geometry is shown in Fig. 1. For simplicity, the top and side walls are not included in this figure. The basic part is a plane-wall diffuser which has an expansion angle of 20 degrees so that the flow would normally separate with a large recirculation region. A pyramid-shaped insert is attached to the diffuser expansion wall. The idea is that the two side walls of the pyramid act like delta wings at an angle of attack. From experience with delta wings one expects vortices to form as the flow rolls over the edge into the expansion region. These longitudinal vortices will give the flow different characteristics
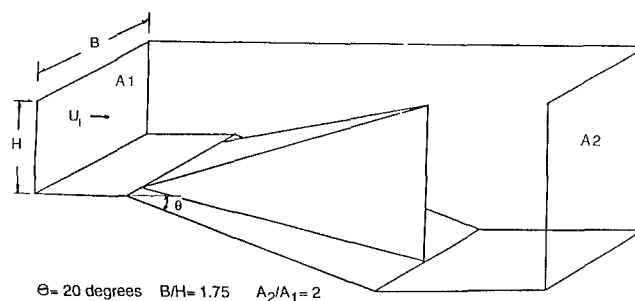
$\Theta = 20$ degrees   B/H= 1.75 $A_2/A_1 = 2$

Fig. 1 Test diffuser geometry
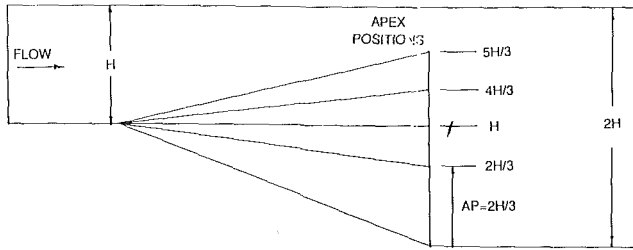
Fig. 2 Side view of diffuser showing the four different apex positions for the pyramid inserts
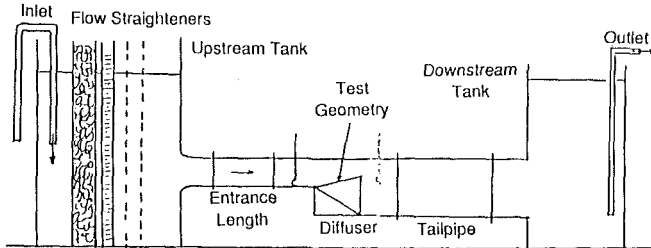
Fig. 3 Schematic of water channel facility

Fig. 4 Schematic of air channel facility

Fig. 5 Incompressible plane-wall diffuser flow-regime map (Fox and Kline, 1962) showing the location of present diffuser

than the separated flow that is customary for just the plane-wall diffuser.

The basic premise that a ledge at a sweep angle to the flow would tend to form a streamwise vortex, as it does in the case of a delta wing, was investigated with a variety of geometric configurations in the diffuser. Many of these were not promising while others were too complex with several geometric parameters. From these preliminary tests the full-length pyramid was selected as a typical generic configuration. This paper is limited to reporting on this configuration as the data from other configurations is not extensive enough to warrant inclusion. This is not to imply that the present configuration is thought to be optimal.

The pyramid has a variety of geometric parameters that can be changed to modify the flow. More or less arbitrarily it was decided to keep the apex located directly above the corner that marks the diffuser exit. The upstream spanwise base was held constant (100 mm) and a gap of 12 percent of the span (16 mm) was left on either side. This was done so that the side corners of the pyramid would be free of influences from the side walls. Four different apex locations were tested (Fig. 2). As measured from a line projected from the bottom of the upstream wall, these were 2H/3, H/3, 0, and −H/3. Alternatively, one could locate the apexes using the length of the downstream edge, AP. That is, AP=5H/3, 4H/3, H, and 2H/3. The edge AP rises from the lower wall in the exit plane of the diffuser. The latter notation for locating the apexes is used herein.

2 Experimental Apparatus and Procedures

A water channel facility, shown in Fig. 3, was built for the flow visualization studies. Flow was introduced from a 686-mm-high, 610-mm-square upstream tank into a 914-mm-long (L/H-12), 76-mm × 133-mm entrance duct to the test diffuser. The diffuser had a 2:1 expansion and a 20-degree wall angle. Subsequently, the flow passed through a rectangular tailpipe 152-mm × 133-mm and 1016-mm long before discharging into a 550-mm-high, 305-mm-square downstream tank. Two centrifugal pumps returned the flow to the upstream tank.

Sodium fluorescein dye was used as the marker to visualize the flowfield. The surfaces of the pyramid were painted black so as to provide maximum contrast between the dye and the surroundings. The dye was introduced either by dye injector probes, or through small holes drilled on the pyramid walls. At any given time holes on only one surface were used. This procedure enabled one to follow the flow originating from a particular part of the flowfield. Two 100-watt ultraviolet lightbulbs were used as light sources to excite the dye and illuminate the flowfield. Slit lighting was employed whenever necessary to examine cross-sections of the flowfield, especially in regions containing separated flow.
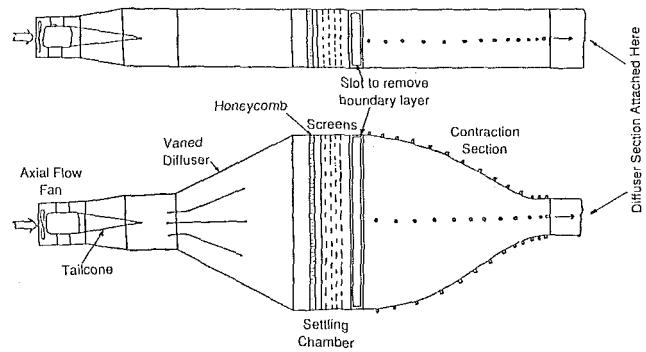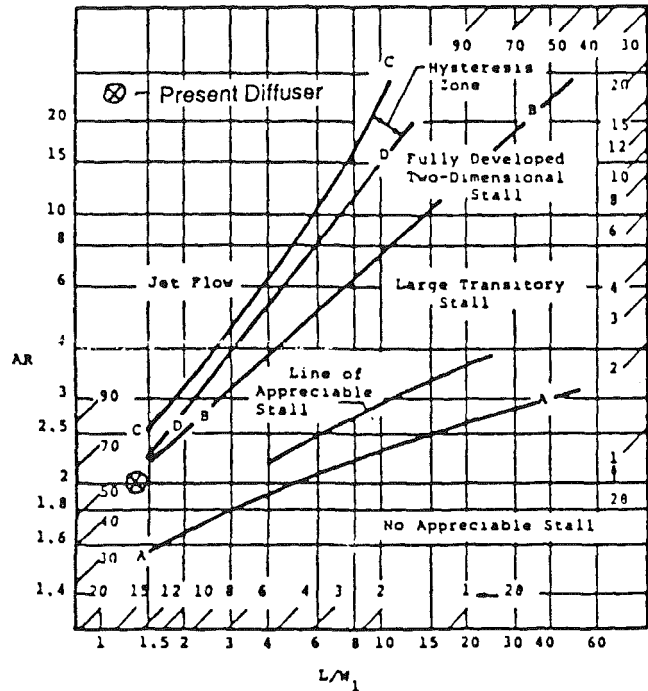
In addition to the water channel tests, some flow visualization studies using tufts were conducted in an air channel facility. Higher Reynolds numbers, more typical of industrial practice, were attained in this facility than in the water channel. A schematic of the air channel facility is shown in Fig. 4. A 5-hp Hartzell axial-flow fan was used to provide the airflow. The flow leaving the blower passed through a vaned diffuser into a 1219-mm by 445-mm cross-section settling chamber containing a honeycomb and screens. Flow from the settling chamber entered a 4.8 contraction and passed through a 254-mm by 445-mm entrance duct before entering the diffuser. The tuft studies in the air channel revealed the flow pattern at the higher Reynolds numbers that are characteristic of industrial situations.

Table 1 Nominal Reynolds number for transition to neighboring mode

Pyramid Geometry	Mode	Increasing	Decreasing
AP = H	A		
		2850	2150
	B		
		6000	5200
	C		
AP = 4H/3	1		
		1900	1400
	2		
		3150	3050
	3		
		6000	5350
	4		
AP = 5H/3	1		
		1400	500
	2		
		2850	2800
	3		
		11,300	7050
	4		

Fig. 6 Transition Reynolds numbers for different modes

3 Results and Discussion

The major emphasis of this paper is on what the flow patterns in the diffuser were like and how they changed with Reynolds number and pyramid height. As a basis for comparison, the flow in the plane-wall diffuser was studied. The location of the equivalent diffuser is shown on the flow-regime map in Fig. 5 (Fox and Kline, 1962). Although it is almost too short to be on the map, one sees that it lies near the edge of the fully developed two-dimensional stall (or bistable stall) regime. This flow-regime map is based on turbulent inlet boundary layers and exit flow into a plenum. In contrast, the present study was conducted with a tailpipe attached to the diffuser exit. The presence of the tailpipe should not change the major features of the flow pattern within the diffuser. Additional pressure recovery usually occurs in the tailpipe due to an improvement in the uniformity of the exit-velocity profile.

Flow visualization studies showed that the flow in the plane-wall diffuser was always separated. At low Reynolds numbers (below 900), separation began in the downstream third of the expansion wall and extended all the way through the tailpipe and into the receiving tank. As the Reynolds number increased, the flow reattached in the tailpipe, and the reattachment point moved upstream. The separation point also moved upstream with Reynolds number. A significant change occurred when the inlet boundary layers became turbulent at a Reynolds number of 6000 (based on the inlet height of the entrance duct). Turbulence was determined by observing dye injected along the bottom wall of the entrance duct from an upstream dye injector. For Reynolds numbers greater than 6000, the separation began immediately at the leading edge and reattachment occurred about 1.7 exit diameters into the tailpipe. For this "half-diffuser," and unlike the symmetric diffusers normally tested, the separation was reasonably steady. Thus, at high Reynolds numbers, the basic diffuser flow was completely separated.

The discussion of the flow patterns with the pyramid inserts is organized according to geometry, and for each geometry the flow patterns are presented as a function of Reynolds number. A summary of the modes and the transition Reynolds numbers is given in Table 1, and is graphically depicted in Fig. 6.

The pyramid with AP = 2H/3 had an apex which was a distance H/3 below the level of the upstream wall. This configuration never produced a vortex. The flow separated from the leading edge for all Reynolds numbers and the pyramid was completely submerged in the separated region. Since the fluid in the separated region moved very slowly the insert
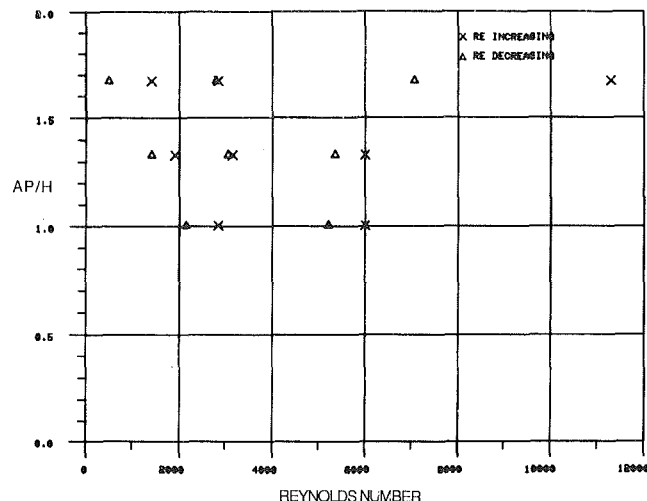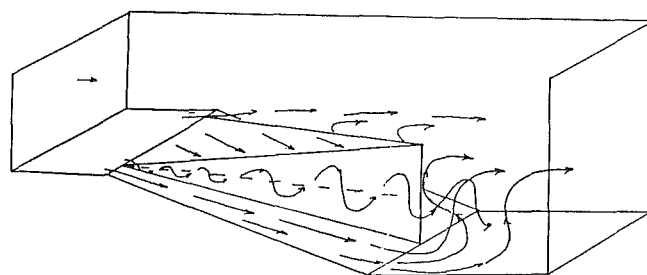
Fig. 7 Flow characteristics of AP = H in the mode C pattern

caused no appreciable effect on the size or extent of the region.

The second configuration tested, AP = H, had a top surface that was level with the upstream entrance section wall, as shown in Fig. 7. This geometry exhibited three different patterns as the Reynolds number was increased. In the first mode, A, which was present up to a Reynolds number of 2700, two weak, symmetric, streamwise vortices with their axes lying adjacent to the top edges of the pyramid side surfaces were present. These had little or no effect on the separation that was present on the diffuser expansion wall. The second mode, B, started at a Reynolds number of 2800. The flowfield in this mode was asymmetric and bi-stable. A vortex lying slightly above the diffuser expansion wall was present on one side of the pyramid, while the other side was completely separated. All the flow on the top surface of the insert was drawn into the side containing the vortex. The third mode, C, occurred at Reynolds number above 6000, and was still present up to a Reynolds number of 30,000, which was the maximum Reynolds number attained in the water channel. (Recall that 6000 marks the transition of the inlet boundary layers to a turbulent state.) A schematic representation of Mode C is shown in Fig. 7. The flowfield was still asymmetric and bi-stable. Mode C was characterized by a vortex so strong that it eliminated any separation along the diffuser expansion wall. However, the flow on the other side was still completely separated. Figure 8 is a photograph showing the vortex in this mode, and Fig. 9 is a photograph showing the flow along the top surface of the insert.

These first two configurations were relatively ineffective in eliminating the separated flow region. As a general rule they revealed that any three-dimensional object submerged in a normally separated region has relatively little effect on the overall flow pattern.
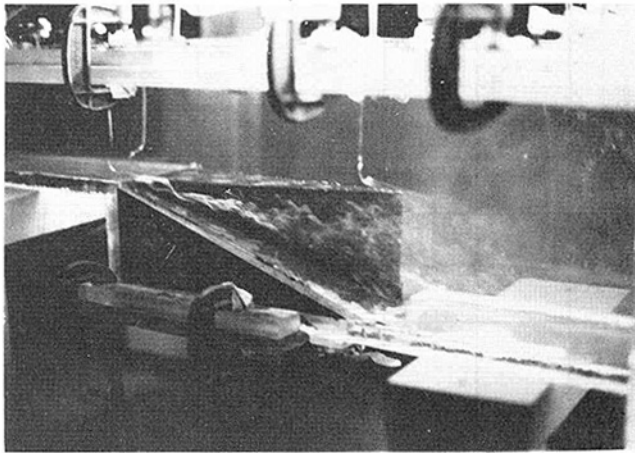
Fig. 8   AP = H; mode C; Re = 8650. Note the streamwise vortex is only on this side.
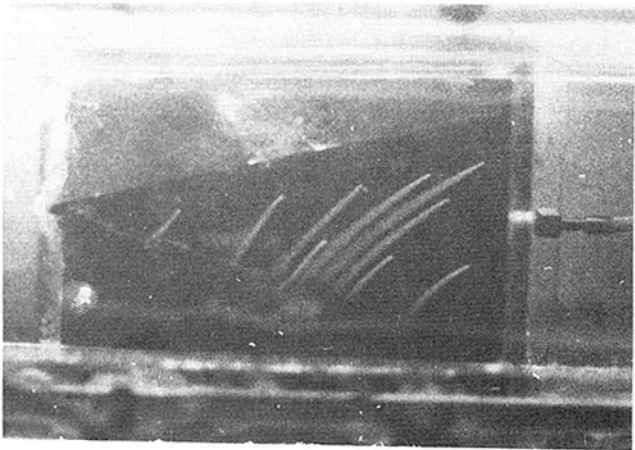
Fig. 9   AP = H; mode C. Plan view of flow along inset top surface; Re = 7000.
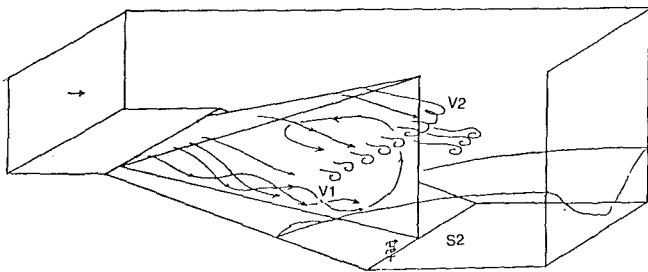
Fig. 10   Flow characteristics of mode 1

Fig. 11   AP = 5H/3; mode 1; Re = 950

Fig. 12   AP = 5H/3. Flow in transition from mode 1 to mode 2; Re = 1950.

In the final two configurations, AP = 4H/3 and 5H/3, the apex was above the level of the inlet wall producing an upsweep of the pyramid surface that faces the flow. The flow for these configurations exhibited four modes as a function of the Reynolds number. Before discussing each mode in detail an overview of the general trends and features is in order. The corresponding modes for the low and high upsweep, i.e., AP = 4H/3 and 5H/3, had the same basic features but occurred at different values of the Reynolds number. In all modes the vortex intensities (i.e., angular velocities in the vortex) were in general higher for the high upsweep configuration. At low Reynolds numbers, the vortex core lay adjacent to the diffuser expansion wall. This flow pattern was called Mode 1. As the Reynolds number was increased, the vortex moved away from the expansion wall so that its axis was horizontal. This pattern with a horizontal vortex axis was

termed Mode 2. In this mode, the vortex was laminar and experienced breakdown and transition to turbulence near the diffuser exit. Vortex breakdown is marked by a rapid deceleration of the axial flow and the formation of a stagnation point on the vortex axis (Leibovich, 1978). A deformation and/or expansion of the vortex core then occurs. The flow following this is marked by a large increase in the turbulence intensity. Underneath the vortex there was a closed separation bubble. At higher Reynolds numbers, the vortex breakdown moved upstream and the diffuse turbulent flow following breakdown encroached into the separated regions present along the diffuser expansion wall until these were entirely entrained and eliminated. This flow is termed Mode 4. Mode 3 is a transitional mode between 2 and 4 in which the flow pattern is asymmetric and bistable in nature.

Mode 1 was present up to a Reynolds number of 1900 for the case AP = 5H/3, and 1400 for the case AP = 4H/3. A schematic representation of this mode is shown in Fig. 10, and Fig. 11 gives the corresponding photograph. The flowfield contained a streamwise vortex, V1, with an axis adjacent to the diffuser expansion wall. The vortex was very weak at low Reynolds numbers, but become stronger as the Reynolds number was increased. As the vortex entrained more fluid it became diffuse and decreased in strength. This was not quite like the classic vortex breakdown. A region of separation, S2, existed under the vortex in the downstream portion of the expansion wall. Apparently the presence of the vortex along the expansion wall inhibited separation in its vicinity, and, within the diffuser itself, the separation was present only in a small region along the diffuser side walls. A region of reversed flow was also present along the side walls of the pyramid. The flow
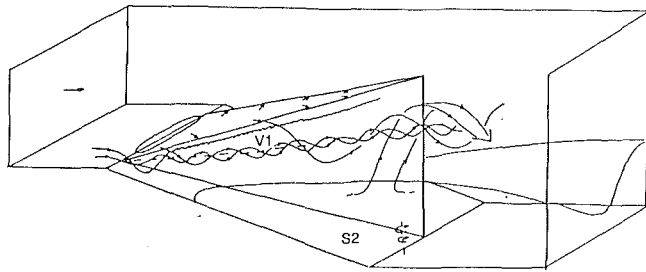
Fig. 13   Flow characteristics of mode 2

Fig. 16   AP = 5H/3; mode 2. Slit-lighted cross-sectional view of vortex V1 and separated region S2; Re = 2150.

Fig. 14   AP = 5H/3; mode 2; Re = 2100.

Fig. 17   Flow characteristics of mode 3

Fig. 15   AP = 4H/3; mode 2; Re = 2300.

in this region seemed to originate from the vortex V1 following its dispersion. Vortices such as V2 periodically formed in the shear layer leaving the top surface of the pyramid. This is the common Kelvin-Helmholtz instability observed in shear layers.

The transition from Mode 1 to Mode 2 occurred abruptly over a small range of Reynolds number, and the location of the vortex breakdown when Mode 2 first appeared was at the pyramid's trailing edge. Figure 12 is a photograph that shows the flow in transition from Mode 1 to Mode 2. The structure of the vortex during transition appears to be slightly different as compared to its structure before and after transition.

Mode 2 was present for Reynolds numbers below 2850 for the AP = 5H/3 case and below 3150 for the AP = 4H/3 case. A

schematic representation of this mode is shown in Fig. 13. Figure 14 is a photograph that shows the flow in the AP = 5H/3 case, while Fig. 15 is a photograph of the flow in the AP = 4H/3 case. In this mode, the axis of the vortex V1 lifted up so that it was almost horizontal. The vortex intensity increased with the Reynolds number, and the position of the vortex breakdown moved upstream. A region of separation, S2, existed along the diffuser expansion wall and extended to about one diameter downstream. Initially, the cross-section of this separated region did not extend all the way from the channel side wall to the insert. However, it broadened in extent as one moved downstream and met with the walls of the insert. Figure 16 is a photograph that shows cross sections of the region S2 with simultaneous dye injection from an upstream injector. The curved shear layer is clearly evident in these photographs. The presence of the vortex caused transverse shear forces to be generated on the separated flow. The flow in S2 behaved to some extent like a cavity-driven flow. As the flowrate was increased, progressively larger and larger portions of the region S2 began peeling off and wrapped up around the vortex V1. The flow in S2 was unsteady, as was the flow along the insert side wall where S2 began peeling off. As the Reynolds number was increased, the swirling flow following breakdown (which had moved upstream) began encroaching into S2 until it was entirely eliminated.

Mode 3 occurred for Reynolds numbers less than 6000 for the case AP = 5H/3 and below 11,300 for the case AP = 4H/3. A schematic representation of the flow is shown in Fig. 17. Interestingly enough, the flow in this mode was asymmetric and bi-stable. One side contained a longitudinal vortex which was strong enough to eliminate the separated regions along the diffuser expansion wall. The other side contained a weaker vortex whose axis lay adjacent to the diffuser expansion wall. The flow from this vortex wrapped around vortices having a vertical axis that were present along the expansion wall and
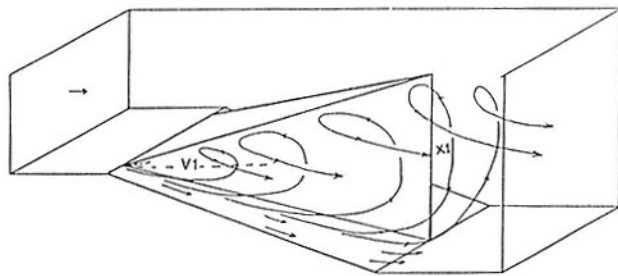
Fig. 18 Flow characteristics of mode 4
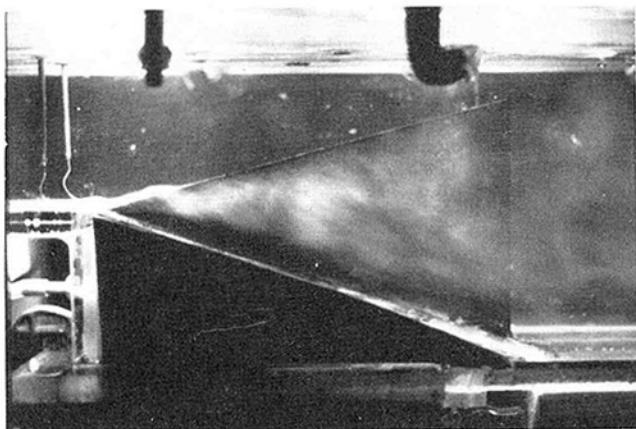
Fig. 19 $AP = 5H/3$; mode 4; Re = 6450.

Fig. 20 $AP = 4H/3$; mode 4. Flow visualization using tufts in the air channel; Re = 2.75×10^5.

then flowed downstream. A large disturbance would cause the flow pattern to switch sides.

The fourth and final mode was present for Reynolds greater than 6000 for the $AP = 5H/3$ case and above 11,300 for the $AP = 4H/3$ case. As the inlet boundary layers were now turbulent one could anticipate that this mode would persist in the air channel. A schematic representation of this mode is shown in Fig. 18. Figure 19 is a photograph of the flowfield. In this mode, closed separation bubbles along the diffuser expansion wall were eliminated. The vortex V1, which was now very intense, suffered a breakdown near the diffuser inlet, and the diffuse flow following breakdown swirled out downstream, giving rise to an open separated region.

The flow in the region behind the insert trailing edge (marked X1 in Fig. 18) was unsteady, and the unsteadiness appeared to have a definite periodicity. This unsteadiness was observed by injecting dye through a probe located in this region. The dye leaving the probe experienced a vertical oscillation. The flow in the tailpipe was hard to visualize due to the turbulence, and did not appear to have the same periodic unsteadiness that was characteristic of region X1. There also appeared to be a swirling motion carried downstream in the tailpipe. The flow in this mode seemed stable to any abrupt changes in the Reynolds number. Flow visualization studies using tufts in the air channel indicated that the flow pattern seemed to be unchanged at Reynolds numbers equal to 2.75×10^5. Figures 20 (a) and (b) are photographs showing the tuft flow visualization. Figure 20 (a) indicates that the flow was attached along the diffuser expansion wall, and that the flow along the side surface of the insert had an upward motion. Figure 20 (b) shows that the flow along the top surface experienced a lateral motion. This lateral motion, coupled with the upward flow along the insert side surface, implied the presence of the vortex in the flow.

Figures 21 (a), (b), and (c) show the flow along the top sur-

face of the insert in modes 1, 2 and 4. These figures show that the lateral motion of the flow along the top surface increased with the Reynolds number. This implies that the swirl angle of the flow in the vortex increased with the Reynolds number.
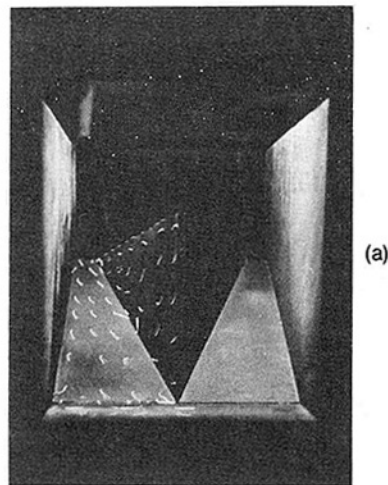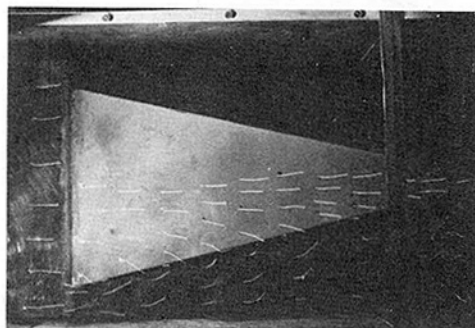
The introduction of three-dimensional effects in the flow produced some desirable flowfield characteristics. The lack of closed separated regions in the flow at practical Reynolds numbers implies the absence of low-frequency effects that are characteristic of such regions. In addition, the flow field exhibits little or no hysteresis with respect to changes in Reynolds number. These features make this diffuser design desirable in applications to turbomachinery.

4 Summary and Conclusions

Many of the devices used to manipulate and control fluid flows result in flowfields that are predominantly two-dimensional. In some instances, however, three-dimensional flows may have characteristics that are better than two-dimensional or axisymmetric flowfields. With the idea in mind, the flow in a wide-angle, plane-wall diffuser with a pyramid insert attached to its expansion wall was investigated. The angle of the plane-wall diffuser was chosen such that the flow would normally separate with a large recirculation region. Variation in pyramid height lead to two categories of behavior. One category resulted when the pyramid apex height was below the diffuser entrance, and the other when the apex was above the entrance.

When the pyramid apex was lower than the diffuser entrance, the separated region was undisturbed and the overall flow pattern was unchanged. The flow was insensitive to changes in the Reynolds number. This leads to the conclusion that to be effective in producing a three-dimensional flow, an insert should protrude from any existing separated regions. In

Fig. 21 $AP = 5H/3$. **Flow along the insert top surface at different Reynolds numbers.**
(a) Re = 950. (b) Re = 2800. (c) Re = 8650.

go around the blocking insert. This generates a secondary flow and angular momentum in the cross-flow plane. The subsequent ledge intensifies this motion and the flow forms a streamwise vortex.

At low Reynolds numbers (below 6000), the flow exhibited three patterns with subtle distinctions. The flow contained longitudinal vortices that were predominantly laminar and experienced a breakdown downstream of the diffuser exit. These vortices modified and reduced in extent the separated regions that were present along the diffuser expansion wall.

At high Reynolds numbers (above 6000), the flow exhibited a single pattern where a turbulent vortex replaced the closed separated region. Vortex bursting and turbulence began immediately so that frictional losses were modest.

The flow over the pyramid has a geometric analogy to the flow past a delta wing. The upsweep of the top face has the same effect on the vortex intensity and final breakdown position as the sweepback angle does for a delta wing. Vortex intensities are higher and breakdown occurs further upstream for smaller sweepback angles. The inlet width would have an effect that is analogous to the angle of attack for the delta wing. For a given sweepback angle, lower angles of attack result in lower vortex intensities and vortex breakdown positions which are further downstream. Thus, although this effect was not tested, it is expected that vortex intensities would be lower for smaller values of the initial width of the top surface of the pyramid.

The flowfield exhibited several desirable features. The absence of any closed separated regions implied that the flow was free of low-frequency effects that are characteristic of such regions. In addition, the modes exhibited little hysteresis with respect to changes in Reynolds number. These flowfield features may be valuable in certain diffuser applications.

Trends revealed in this study may be useful in constructing other types of insert geometries. For example, placing a pyramid on the opposite, the flat upper wall, might be more effective than the present configuration. A smaller height pyramid may have the same blocking effect and may turn the flow down to avoid separation from the expansion, while generating smaller vortices.

this case where separation is at the leading edge, the insert should protrude into the oncoming stream.

The case where the pyramid apex height was at the same level as the diffuser entrance represents a marginal situation with bi-stable flow. One side of the pyramid was separated while the other side contained a longitudinal vortex.

The second category is when the pyramid apex is higher than the diffuser entrance. In this case, the flow must turn to

References

Fox, R. W., and Kline, S. J., "Flow Regime Data and Design Methods for Subsonic Diffusers," ASME *Journal of Basic Engineering*, Vol. 84, 1962.

Leibovich, S., "The Structure of Vortex Breakdown," *Annual Review of Fluid Mechanics*, Vol. 10, 1978.

Panton, R. L., Goenka, L. N., and Bogard, D. G., "Flow Patterns in a Three-Dimensional Diffuser Designed to Generate Longitudinal Vortices," Fourth International Conference of Flow Visualization, 1986, Paris, France.

E. A. Baskharone
Assistant Professor.
Mem. ASME

S. J. Hensel
Graduate Research Assistant.

Department of Mechanical Engineering,
Texas A&M University,
College Station, Texas 77843

A New Model for Leakage Prediction in Shrouded-Impeller Turobpumps

The swirling secondary flow in the shroud-to-housing passage of a turbopump stage is analyzed. The flow model is based on the weighted-residual finite-element method to solve the axisymmetric flow field in this passage. A unique feature of the present analysis is the inclusion of two primary flow segments in the definition of the solution domain. This allows full interaction between the primary and secondary flow streams and alleviates what would otherwise be an iterative procedure to calculate the leakage flow rate. Full ellipticity of the flow field throughout the entire domain is maintained for accurate modeling of separation and recirculation zones. Applicability of the computational model to generally shaped secondary flow passages is illustrated through a sample pump that is similar to the boost-impeller stage in the oxidizer turbopump of the U.S. Space Shuttle Main Engine. The secondary flow field in this case is investigated over a range of Reynolds number.

Introduction

A primary source of stage losses in turbomachines is the secondary flow in the rotor tip clearnace region. As much as one third to one half of the rotor losses have reportedly been attributed to tip leakage in turbines and compressors of the unshrouded impeller type [1,2]. The leakage in this case is composed of two distinct mechanisms; the direct through-flow motion, as driven by the leading-to-trailing edge static pressure difference across the blade tip section, and the indirect flow migration over the tip as a result of the local pressure differential between the pressure and suction sides. Shrouded rotors, on the other hand, suffer only the former of these leakage mechanisms [3]. Research in these two areas has been focused on axial-flow turbomachinery [4, 5, and 6].

Tip leakage in radial turbomachines, on the other hand, remains less investigated and comparatively less understood. Among the few experimental studies in this category is that by Mashimo [7] for a centrifugal compressor of the unshrouded-impeller type. This was a mixed experimental/analytical effort aimed at quantifying the tip clearance losses in terms of such parameters as the clearance size, Reynolds number, and impeller blade aerodynamic loading. However, due to the various geometry and flow simplifications involved in his model, Mashimo's correlation was understandably a rough approximation of the losses incurred. Another model in this category was devised by Kirk [8], where the secondary flow passage of a shrouded compressor impeller was replaced by a radial chamber leading to the labyrinth seal. Apart from the obvious geometry idealization in this case, the secondary flow computations involved a simplified free-vortex behavior in the

clearance gap and a pressure field that is totally based on an inviscid flow pattern.

Analysis

Definition of the Solution Domain. An obvious choice of the solution domain is the secondary flow passage as isolated from that of the primary flow (e.g., darkened region in Fig. 1). This has traditionally been the case whether the flow consideration is that through the full-scale leakage gap [8] or an
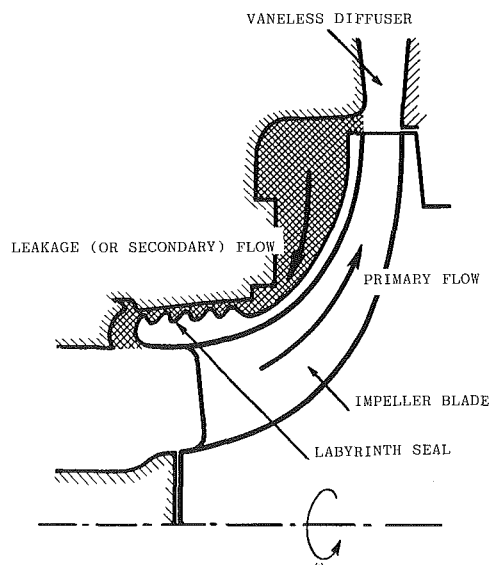
Fig. 1 Primary and secondary flow within a centrifugal pump stage
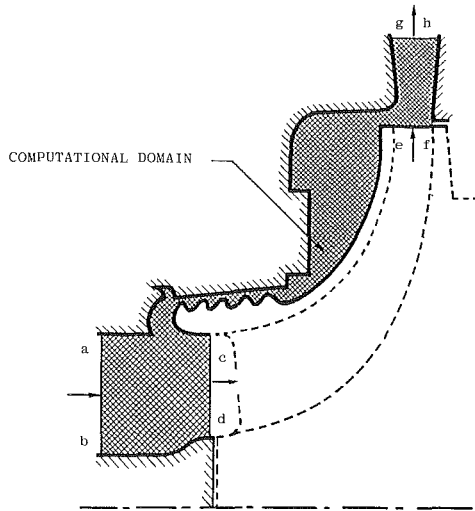
Fig. 2   Definition of the computational domain in the present analysis

annular seal [9]. The secondary flow rate in this case is assumed known, estimated via one-dimensional flow calculations, or obtained iteratively as the flow conditions at both ends of the leakage passageway are matched to the primary flow conditions at these two locations in an average sense.

The computational domain in the present analysis allows the mutual iteraction of the secondary/primary flow passages resulting in a unique value of the secondary flow rate. This value is part of the numerical solution and not externally imposed. This is made possible by including two primary flow segments upstream and downstream from the impeller in the manner indicated in Fig. 2. Contouring the domain in this manner clearly results in a region with multiple flow-permeable stations for which the prescribed boundary conditions are carefully selected in such a way to avoid over-specification of the problem.

Governing Equations.   It is assumed that the secondary flow is steady, incompressible, adiabatic and axisymmetric. Furthermore, a sufficiently low Reynolds number justifying a laminar flow behavior is also adopted for simplicity. Under these assumptions, the conservation of mass and momentum can be expressed in the following linearized form:

$$\frac{\partial V_z}{\partial z} + \frac{\partial V_r}{\partial r} + \frac{V_r}{r} = 0 \tag{1}$$

$$\frac{1}{Re} \nabla^2 V_z = \frac{\partial p}{\partial z} + \hat{V}_z \frac{\partial V_z}{\partial z} + \hat{V}_r \frac{\partial V_z}{\partial r} \tag{2}$$

$$\frac{1}{Re} \nabla^2 V_r = \frac{\partial p}{\partial r} + \hat{V}_z \frac{\partial V_r}{\partial z} + \hat{V}_r \frac{\partial V_r}{\partial r}$$
$$- \hat{V}_\theta \frac{V_\theta}{r} + \frac{1}{Re}\left(\frac{V_r}{r^2}\right) \tag{3}$$

$$\frac{1}{Re} \nabla^2 V_\theta = \hat{V}_z \frac{\partial V_\theta}{\partial z} + \hat{V}_r \frac{\partial V_\theta}{\partial r} + \hat{V}_r\left(\frac{V_\theta}{r}\right) + \frac{1}{Re}\left(\frac{V_\theta}{r^2}\right) \tag{4}$$

Where:

V_z, V_r, and V_θ are the z, r, and θ components of the absolute velocity,

p is the static pressure,

Re   is the Reynolds number based on the impeller tip radius and tip speed; and

$\hat{V}_z$, $\hat{V}_r$, and $\hat{V}_\theta$ are the velocity components obtained from a previous iteration or an initial guess.

The flow variables in equations (1) through (4) are non dimensional, and can be related back to the physical variables as follows:

$$V_z = \frac{V_z^*}{U_t}$$

$$V_r = \frac{V_r^*}{U_t}$$

$$V_\theta = \frac{V_\theta^*}{U_t}$$

$$p = \frac{(p^* - p_{in})}{\rho U_t^2}$$

with U_t referring to the impeller tip speed and the asterisk to physical flow properties. The spatial coordinates are also non-dimensionalized using the impeller tip radius as a reference length.

Boundary Conditions.   With the flow ellipticity retained throughout the computational domain, appropriate boundary conditions are needed over the entire boundary. These are best categorized, in reference to Fig. 2, by the boundary segment type as follows:

(i) *Flow Inlet Station.*   This is the boundary segment $a-b$ in Fig. 2, which is located far enough upstream from the inducer. Fully developed flow is assumed at this location, giving rise to the following boundary condition:

$$\frac{\partial V_z}{\partial z} = \frac{\partial V_r}{\partial z} = \frac{\partial V_\theta}{\partial z} = 0$$

Nomenclature

A	=	area (m²)	p_i^*	=	inlet static pressure (N/m²)	
b	=	diffuser endwall spacing (m)	Re	=	Reynolds number	
F	=	thrust force exerted on the shroud by the secondary flow (N)	r	=	radial coordinate (m)	
			U_t	=	impeller tip speed (m/s)	
L	=	length (m)	V	=	nondimensional flow velocity	
$\dot{m}$	=	secondary mass flow rate	z	=	axial coordinate (m)	
M_i	=	linear shape function	ξ, ζ	=	coordiantes in the local frame of reference	
N_i	=	quadratic shape function	ρ	=	flow density (kg/m³)	
n	=	local normal unit vector	θ	=	tangential coordinate (rad)	
p	=	nondimensional static pressure	ω	=	impeller rotational speed (rad/s)	

Subscripts

in = flow inlet station
ref. = reference operating conditions corresponding to Re = 3500
t = impeller tip

Superscripts

(e) = a typical finite element
(n) = an iterative step
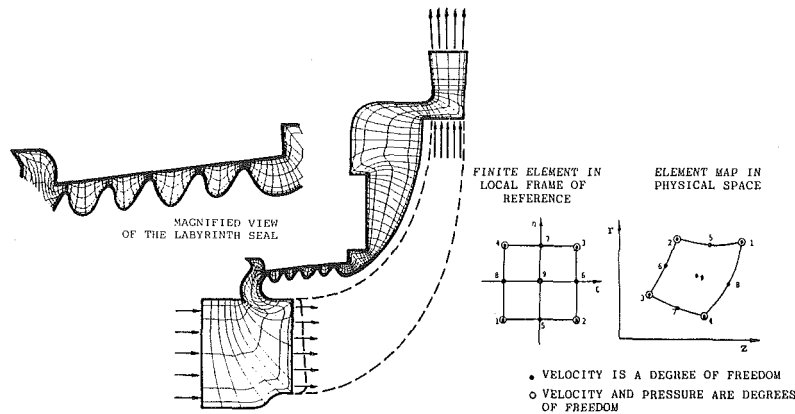
Fig. 3 Finite-element discretization model

In addition, the nondimensional static pressure is set equal to zero at one node on the same station.

(*ii*) *Impeller Inlet and Exit Stations.* These are the boundary segments $c-d$ and $e-f$ in Fig. 2. Fixed profiles of the nondimensional velocity components at these stations, corresponding to the stage operating conditions are imposed. Note that the operating conditions here involve the primary impeller passage, and do not include the secondary mass flow rate. The latter is viewed in the current analysis as an internal parameter that is implied by such factors as the static pressure differential across the impeller, the geometry of the secondary passage and the way it is naturally connected to the primary flow passage.

(*iii*) *Flow Exit Station.* The flow behavior at this station (designated $g-h$ in Fig. 2) is viewed as predominately confined to satisfying the mass and angular momentum conservation equations in a global sense. These constraints can be expressed as follows:

$$\frac{\partial V_r}{\partial r} = -\frac{1}{br}\left(b + r\frac{db}{dr}\right)V_r \tag{5}$$

$$\frac{\partial V_\theta}{\partial r} = -\frac{V_\theta}{r} \tag{6}$$

where b is the vaneless diffuser endwall spacing. Expressions (5) and (6) define linear Neumann-type boundary conditions and are, therefore, introduced noniteratively in the numerical solution. The error in this approximation of exit flow behavior is clearly confined to the viscous layer next to the endwalls at the flow exit station. The inaccuracy in the secondary-passage flow field under such approximation is tolerable, provided that the exit station is sufficiently far from this passage. Furthermore, it is assumed that the meridional flow trajectories coincide with the streamwise grid lines as the exit station is approached, giving rise to the condition: $V_z = (1/K)\ V_r$, where K refers to the local slope of the grid line. This approximation is reasonably valid as long as the flow near the exit station remains attached to the endwalls. Finally, the nondimensional pressure is fixed at one node on this station in accordance with the stage operating conditions.

(*iv*) *Solid Boundary Segments.* These include both the housing, seal, hub and shroud surfaces in contact with the flow in the solution domain. Here, the no-slip boundary conditions are imposed in the following general form:

$$V_z = 0$$
$$V_r = 0$$

$$V_\theta = \omega r/U_t \qquad \text{for a rotating-boundary segment.}$$
$$= 0 \qquad \text{for a stationary-boundary type.}$$

where ω refers to the impeller rotational speed.

Finite-Element Formulation. The solution domain in Fig. 2 is replaced by an assembly of non-overlapping subdomains termed elements as shown in Fig. 3. Throughout each element, the field variables are then interpolated in terms of the unknown nodal values. Substitution of these interpolating functions in the flow-governing equations yields a set of residual functions. Following Galerkin's weighted residual approach [10], these residuals are made orthogonal to the basis, or shape, functions in the interpolation expressions throughout the entire element.

Experience with the finite-element solution of Navier-Stokes equations over the past two decades has led to specific conclusions concerning the pressure field simulation in a finite-element model. According to Hood et al. [11], the so-called "error consistency" criterion necessitates a pressure interpolation function, which is one degree less than those of the velocity components. The slow convergence and/or wiggles in the computed pressure in inertia-dominated flows have also been investigated and remedies by several authors recommended. These include the use of interior nodes in interpolating the velocity components [12] and use of the upwinding technique [13]. It was, however, concluded by Gresho et al. [14] that a wiggle-free pressure field can, in most cases, be obtained by simply refining the finite-element discretization pattern in regions with severe pressure gradients.

It was decided, in view of the preceding guidelines, to proceed with the nine-node curve-sided Lagrangian element in Fig. 3 as the discretization unit. The decision to favor this high-order element was based on the numerical accuracy study by Huyakorn et al. [12]. It was also decided to utilize a mixed isoparametric/superparametric element [10] for the velocity and pressure fields, respectively. The latter choice was based on a preliminary assessment of the solution accuracy by the authors for different element types.

Throughout a typical element (e) in Fig. 3, let the velocity, pressure and spatial coordinates be interpolated as follows:

$$V_z^{(e)} = \sum_{i=1}^{9} N_i(\zeta,\eta)\,V_{z,i} \tag{7}$$

$$V_r^{(e)} = \sum_{i=1}^{9} N_i(\zeta,\eta)\,V_{r,i} \tag{8}$$

$$V_\theta^{(e)} = \sum_{i=1}^{9} N_i(\zeta,\eta) V_{\theta,i} \qquad (9)$$

$$p^{(e)} = \sum_{i=1}^{4} M_i(\zeta,\eta) p_i \qquad (10)$$

$$z^{(e)} = \sum_{i=1}^{9} N_i(\zeta,\eta) z_i \qquad (11)$$

$$r^{(e)} = \sum_{i=1}^{9} N_i(\zeta,\eta) r_i \qquad (12)$$

where:

N_i and M_i are, respectively, quadratic and linear functions of ζ and η, often referred to as the element "shape" functions.

ζ and η are the spatial coordinates in the local frame of reference, where the "parent" straight-sided element (Fig. 3) is defined.

Substitution of expressions (7) through (12) in equations (1) through (4) yields a residual (or error) function for each equation. When the residual functions are made orthogonal to the element shape functions, the following set of equations is obtained.

$$\left[\iint_{A^{(e)}} M_i \frac{\partial N_j}{\partial z} \, rdA \right] V_{z,j}$$

$$+ \left[\iint_{A^{(e)}} \left(M_i \frac{\partial N_j}{\partial r} + \frac{1}{r} M_i N_j \right) rdA \right] V_{r,j} = 0 \qquad (13)$$

$$\left[\iint_{A^{(e)}} \left\{ \frac{1}{Re} \left(\frac{\partial N_i}{\partial z} \frac{\partial N_j}{\partial z} + \frac{\partial N_i}{\partial r} \frac{\partial N_j}{\partial r} \right) \right. \right.$$

$$\left. \left. + \hat{V}_z N_i \frac{\partial N_j}{\partial z} + \hat{V}_r N_i \frac{\partial N_j}{\partial r} \right\} rdA \right] V_{z,j} +$$

$$\left[\iint_{A^{(e)}} N_i \frac{\partial M_k}{\partial z} \, rdA \right] p_k = \frac{1}{Re} \oint_{L^{(e)}} rN_i \frac{\partial V_z}{\partial n} \, dL \qquad (14)$$

$$\left[\iint_{A^{(e)}} \left\{ \frac{1}{Re} \left(\frac{\partial N_i}{\partial z} \frac{\partial N_j}{\partial z} + \frac{\partial N_i}{\partial r} \frac{\partial N_j}{\partial r} + \frac{1}{r^2} N_i N_j \right) \right. \right.$$

$$\left. \left. + \hat{V}_z N_i \frac{\partial N_j}{\partial z} + \hat{V}_r N_i \frac{\partial N_j}{\partial r} \right\} rdA \right] V_{r,j} -$$

$$\left[\iint_{A^{(e)}} \frac{\hat{V}_\theta}{r} N_i N_j rdA \right] V_{\theta,j} + \left[\iint_{A^{(e)}} N_i \frac{\partial M_k}{\partial z} \, rdA \right] p_k$$

$$= \frac{1}{Re} \oint_{L^{(e)}} rN_i \frac{\partial V_r}{\partial n} \, dL \qquad (15)$$

$$\left[\iint_{A^{(e)}} \left\{ \frac{1}{Re} \left(\frac{\partial N_i}{\partial z} \frac{\partial N_j}{\partial z} + \frac{\partial N_i}{\partial r} \frac{\partial N_j}{\partial r} \right. \right. \right.$$

$$\left. + \frac{1}{r^2} N_i N_j \right) + \hat{V}_z N_i \frac{\partial N_j}{\partial z} + \hat{V}_r N_i \frac{\partial N_j}{\partial r} +$$

$$\left. \left. \frac{\hat{V}_r}{r} N_i N_j \right\} rdA \right] V_{\theta,j} = \frac{1}{Re} \oint_{L^{(e)}} rN_i \frac{\partial N_\theta}{\partial n} \, dL \qquad (16)$$

where:

n denotes the outward unit vector normal to the element boundary.

$i = 1,2,3, \ldots 9$

$j = 1,2,3, \ldots 9$

$k = 1,2,3,4$

$dA = |J| d\zeta d\eta$

with J being the Jacobian of local-to-meridional coordinate transformation.

The finite element equations (13) through (16) are then assembled among all elements sharing the same nodal variable. The result is a system of algebraic equations in the nodal degrees of freedom at each iterative step for which the functions $\hat{V}_z$, $\hat{V}_r$, and $\hat{V}_\theta$ are known.

Method of Numerical Solution

In an effort to reduce the core size and CPU-time requirements, the θ-momentum equation (4) is uncoupled and solved separately. The process, now consisting of two phases per iteration, is repeatedly executed toward convergence. The numerical solution was considered practically convergent at an iterative step (n), whenever the following criteria were simultaneously met:

$$\sum_{i=1}^{N} |(V_{z,i}^{(n)} - V_{z,i}^{(n-1)})/V_{z,i}^{(n)}|^2 \le \epsilon_1$$

$$\sum_{i=1}^{N} |(V_{r,i}^{(n)} - V_{r,i}^{(n-1)})/V_{r,i}^{(n)}|^2 \le \epsilon_1$$

$$\sum_{i=1}^{M} |(p_i^{(n)} - p_i^{(n-1)})/p_i^{(n)}|^2 \le \epsilon_2$$

where N is the total number of the corner, midside and interior nodes, and M is the number of corner nodes in the finite element discretization model. The convergence parameters ϵ_1 and ϵ_2 were arbitrarily set to 0.03 and 0.02, respectively. There was no convergence criterion set on the tangential velocity component, V_θ, since this component is essentially dependent on V_z and V_r as a result of decoupling the θ-momentum equation in the manner discussed earlier.

In progressing from one iteration to the next, an underrelaxation factor λ was used to ensure monotonic convergence. In the current analysis, values of λ ranging from 0.4 to 0.7 were introduced depending on the nonlinearity of the flow governing equations or, equivalently, the value of Reynolds number. Except for the fast monotonic convergence in the cases where the Reynolds number was below 100, it was generally observed that the error rises during the first few iterations, and then declines montonically.

Details of the algebraic equation solver are similar to those of the frontal method proposed by Hood [15]. This method is based on a partial-pivoting Gauss elimination technique, whereby only a submatrix of the coefficient matrix is stored in core during execution.

Results and Discussion

A representative pump stage was selected as a test case for the current leakage flow model. This is a centrifugal stage that is geometrically similar to the oxidizer boost-impeller pump stage of the U.S. Space Shuttle Main Engine. The impeller of this pump stage has a tip radius of 9.0 cm, and the design point is defined as follows:

Volumetric rate of primary flow $= 0.4685$ m^3/s

Impeller speed $= 29,194$ rpm

Stage total head $= 2,577$ m

Figure 3 shows the finite-element discretization model created for the computational domain in this case by a special preprocessor that was developed for this purpose. A range of low Reynolds number between 0 and 3500 was then considered. This corresponds to a band of impeller speeds that are substantially lower than those within the boost-impeller stage normal power settings. The intention here was to illustrate the
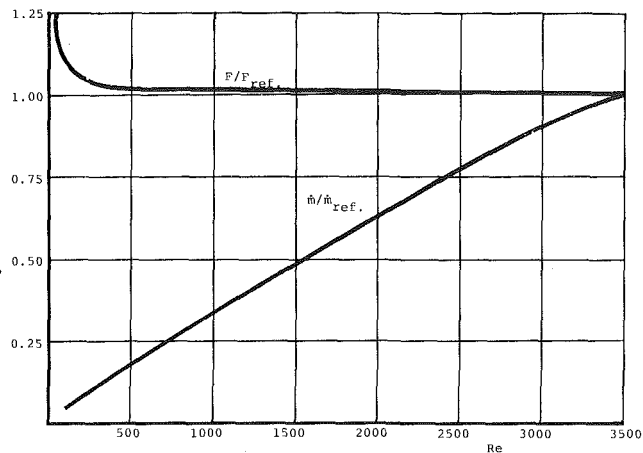
Fig. 4 Variation of the nondimensional shroud thrust force and leakage flow rate with Reynolds number

applicability of the new flow model to a complex secondary flow passage with reasonably limited core and CPU time consumption. It can be argued, however, that the use of high-order iterative methods, such as Newton's technique, may have lowered the consumption of computer resources and, consequently, made high Reynolds number laminar-flow solutions possible. Nevertheless, the simplicity of the current successive linearization procedure, coupled with the fact that an expectedly modest elevation in the Reynolds number as a result of employing such methods would not significantly alter the conclusions drawn in this study, both weakened the motivation behind such a shift in the numerical process.

Figure 4 is a plot of the nondimensional leakage flow rate and the thrust force exerted on the shroud, as functions of the Reynolds number. The leakage flow rate in this figure was obtained by integrating the mass flux over a surface of revolution that is generated by the cross-flow grid line located midway between the secondary passage inlet and exit stations. The shroud force, on the other hand was obtained by integrating
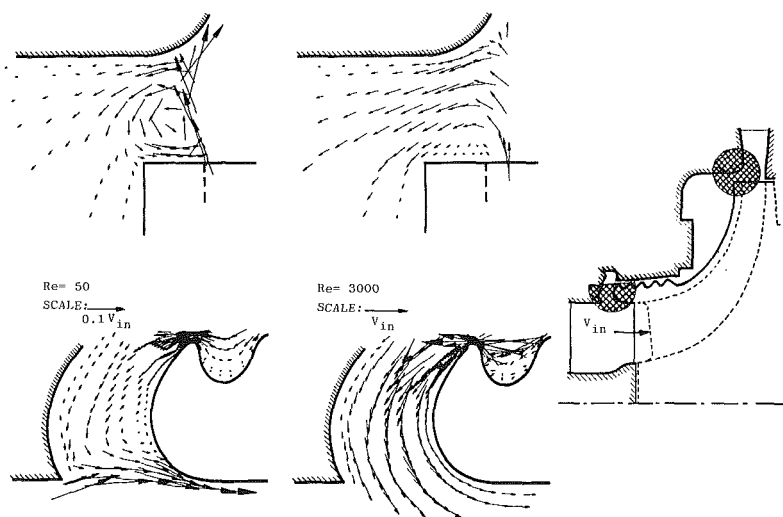
Fig. 5 Vector plots of the meridional velocity in the secondary passage inlet and exit segments
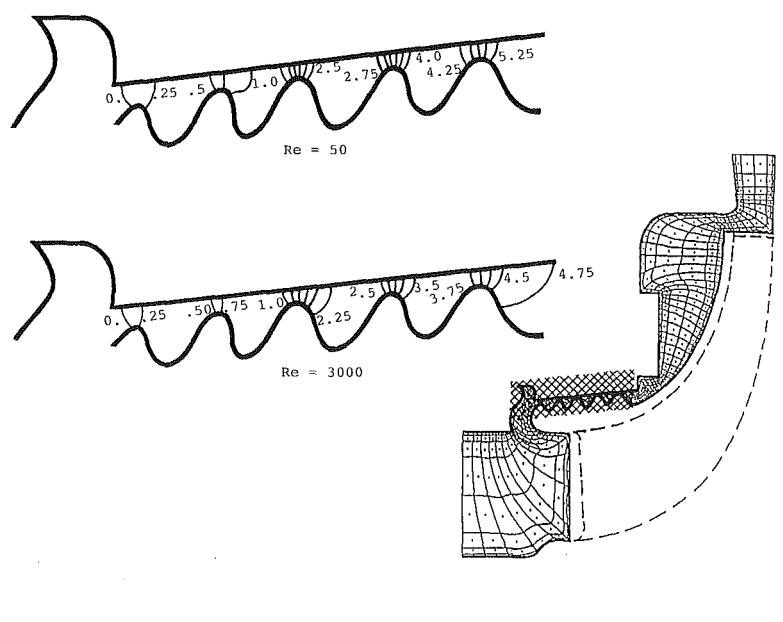
Fig. 6 Contour plot of the nondimensional static pressure across the labyrinth seal
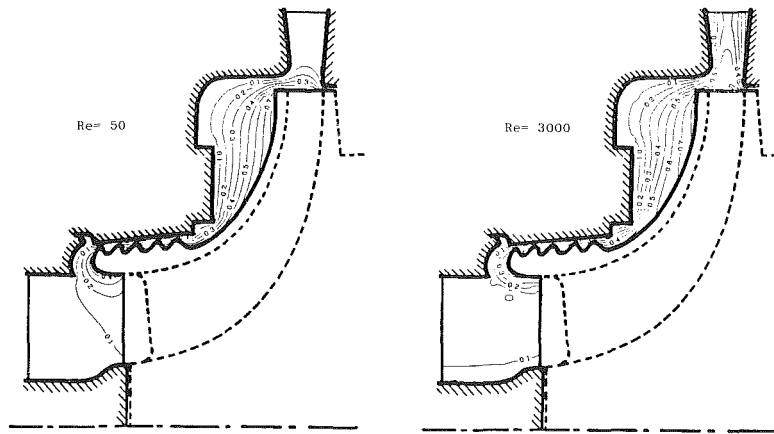
Fig. 7 Contour plots of the nondimensional tangential velocity component

the axial component of the pressure force over the inner surface of the secondary passage, including the shroud and labyrinth seal. In both cases, the reference values were those corresponding to a Reynolds number of 3500. Figure 4 shows a weak dependence of the shroud force on the Reynolds number as the latter exceeds a value of approximately 500. The figure also shows that leakage through the secondary flow passage is a strong function of the Reynolds number. This is, for the major part, due to the blocakge effect at the entrance of this passage that is caused by the existance of a local region of flow recirculation at low Reynolds numbers. The recirculation region is shown in Fig. 5 for a low Reynolds number of 50.

Details of the flow behavior at two different Reynolds numbers of 50 and 3000 are shown in Figs. 5 through 7 for comparison. These are vector plots of the flow meridional velocity component, and contour plots of the static pressure and tangential velocity component. Examination of the through-flow field in Fig. 5 reveals two distinct regions of flow recirculation near the secondary passage inlet and exit stations for Re = 50. The figure also shows flow recirculation zones within the labyrinth seal cavities at both Reynolds numbers. It is worth noting that a radial outflow would normally exist near the shroud in the large shroud-to-housing cavity under sufficiently high impeller speeds due to the significant magnitude of the local centrifugal force, as compared to the static pressure differential across the secondary passage. However, the substantially reduced impeller speeds, associated with the low Reynolds numbers under consideration in the current study, prohibits such flow behavior. As for the static pressure and swirl velocity contours in Figs. 6 and 7, no significant change in the secondary passage contours between the two Reynolds numbers can be distinctly observed. Nevertheless, the swirl velocity contours in Fig. 7 discredits the claim that the flow pattern in the secondary passage upstream from the seal is that of a free-vortex type (e.g., Kirk [8]).

Conclusion

A new model for predicting the secondary flow field in the shroud-to-housing passage of a turbopump stage was developed. Application of this flow model to complex secondary flow passages in the Space Shuttle Main Engine was illustrated for a stage of the oxidizer turbopump under a range of low Reynolds numbers. In addition to the obvious potential of the current flow model as a design tool, the shroud force components produced by this model are currently being used

by the authors to investigate the rotordynamics characteristics of the same pump stage. These characteristics are crucial to the turbopump life computations from a mechanical standpoint.

Acknowledgment

References

1 Bolyle, R. J., Haas, J. E., and Katsanis, T., "Comparison Between Measured Turbine Stage Performance and the Predicted Performance Using Quasi-3D Flow and Boundary Layer Analyses," NASA TM-83640, Presented at the Twentieth Joint Propulsion Conference (AIAA, SAE, ASME), Cincinnati, Ohio, June 1984.

2 Lakshminarayana, B., Zhang, J., and Murthy, K. N. S., "An Experimental Study on the Effects of Tip Clearance on Flow Field and Losses in an Axial Flow Compressor Rotor," AIAA Paper No. 87-7045, 1987.

3 Patel, K. V., "Research on High Work Axial Gas Generator Turbine," SAE Paper No. 800618, 1980.

4 Rains, D. A., "Tip Clearance Flow in Axial Flow Compressors and Pumps," California Institute of Technology, Mechanical Engineering Laboratory, Report No. 5, 1954.

5 Wadia, A. R., and Booth, T. C., "Rotor-Tip Leakage: Part II-Design Optimization Through Viscous Analysis and Experiment," ASME *Journal of Engineering for Power*, Vol. 104, 1982, pp. 162-169.

6 Hah, C., "A Numerical Modeling of Endwall and Tip-Clearance Flow of an Isolated Compressor Rotor," ASME *Journal of Engineering for Gas Turbines and Power*, Vol. 108, Jan. 1986, pp. 15-21.

7 Mashimo, T., Watanable, I., and Ariga, I., "Effects of Fluid Leakage on Performance of a Centrifugal Compressor," ASME *Journal of Engineering for Power*, Vol. 101, July 1979.

8 Kirk, R. G., "Evaluation of Aerodynamic Stability Mechanism for Centrifugal Compressor," ASME Paper No. 85-DET-147, Sept. 1985.

9 Nelson, C. C., "Rotordynamic Coefficients for Compressible Flow in Tapered Annular Seals," ASME JOURNAL OF TRIBOLOGY, Vol. 107, July 1985, pp. 318-325.

10 Zienkiewicz, O. C., *The Finite Element Method in Engineering Science*, McGraw-Hill, London, 1971.

11 Hood, P., and Taylor, C., "Navier-Stokes Equations Using Mixed Interpolation," *Proceedings of the International Symposium on Finite-Element Methods in Flow Problems*, University of Wales, Swansea, United Kingdom, Jan. 1974.

12 Huyakorn, P. S., Taylor, C., Lee, R. L., Gresho, P. M., "A Comparison of Various Mixed-Interpolation Finite Elements in the Velocity-Pressure Formulation of the Navier-Stokes Equations," *Computers and Fluids*, Vol. 6, 1978, pp. 25-35.

13 Hughes, T. J., Liu, W. K., and Brooks, A., "Finite-Element Analysis of Incompressible Viscous Flow by the Penalty Function Formulation," *Journal of Computational Physics*, Vol. 30, No. 1, Jan. 1979, pp. 1-60.

14 Gresho, P. M., and Lee, R. L., "Don't Suppress the Wiggles—They're Telling You Something!," Finite-Element Methods for Convection Dominated Flows, ASME Publication AMD-Vol. 34, 1979.

15 Hood, P., "Frontal Solution Program for Unsymmetric Matrices," *Int. J. Num. Meth. Eng.*, Vol. 10, No. 2, 1976, pp. 379-399.

Flow About a Circular Cylinder in and Near a Turbulent Plane Mixing Layer

M. Kiya
Professor.

H. Tamura
Instructor.

Department of Mechanical Engineering,
Hokkaido University,
Sapporo, 060 Japan

This paper deals with an experimental study of the fluid forces, surface pressure, and vortex-shedding frequency of a circular cylinder placed in and near a turbulent plane mixing layer with zero velocity ratio. These characteristics are given as functions of the cylinder diameter d divided by the local mixing-layer width δ and the nondimensional transverse coordinate of the center of the cylinder in a Reynolds number range 5500–46000. For the cylinder $d/\delta = 2.2$–2.3 the r.m.s. lift attained a maximum 40 percent higher than that in the uniform flow when a part of the cylinder surface was near an intermittently turbulent edge on the high-velocity side of the mixing layer; the time-mean resultant force attained a sharp maximum as high as 80 percent of that in the uniform flow when the axis of the cylinder was located at the center of the mixing layer. The former maximum was interpreted in terms of a vortex-body interaction while the latter maximum was found to be associated with a large delay of the boundary-layer separation on the low-velocity side of the cylinder.

1 Introduction

This paper describes the time-mean and fluctuating forces and the vortex-shedding frequency of a circular cylinder placed in and near a turbulent plane mixing layer. In practice flow configurations similar to this appear when a cylindrical body is exposed to the separated shear layer from another cylindrical body of much larger cross section.

The time-mean force and the vortex-shedding frequency of a circular cylinder immersed in the mixing layer were studied by Kiya, Tamura, and Arie [1]. The present paper extends this previous work by covering a wider range of the governing parameters and by obtaining the fluctuation components of the force and the surface-pressure on the cylinder. A square cylinder in the mixing layer is studied by Taniguchi, Miyakoshi, and Dohda [2] [3].

We describe the governing parameters in Section 2, experimental apparatus and method in Section 3 and the results in Section 4. Conclusions are given in Section 5. One of the main findings in the present study is that the r.m.s. lift attained a 40 percent larger maximum than that in the uniform flow when a circular cylinder was near the high-velocity edge of the mixing layer; this was interpreted in terms of the enhancement of vortices shed from the cylinder by a vortex-body interaction.

2 Governing Parameters

The flow configuration is illustrated in Fig. 1. We consider a turbulent plane mixing layer originating from the mixing of a fluid of velocity U_∞ (from now on referred to as uniform flow) with the same fluid at rest. The velocity U_∞ is assumed to be much smaller than that of sound. The origin of the Cartesian coordinate XYZ is located at the middle of the straight trailing edge (normal to the uniform flow) of a thin splitter plate; the streamwise X axis is taken parallel to the surface of the plate, the transverse Y axis in the direction of decreasing velocity, and the Z axis parallel to the trailing edge. The origin of the xy coordinate is taken at the center of the cylinder; the x- and y-axes are parallel to the X- and Y-axes. The time-mean and fluctuating components of velocity in the X direction and pressure are denoted by u, u' and p, p', respectively. In the self-preserving region u/U_∞, $(\overline{u'^2})^{1/2}/U_\infty$, etc., have similar profiles at different X positions when they are plotted against the nondimensional transverse coordinate η defined by $\eta = (Y - Y_{1/2})/(X - X_0)$ where $Y_{1/2}$ is the Y coordinate at which u is equal to $U_\infty/2$ and X_0 denotes the virtual origin of the self-preserving mixing layer. We introduce a measure of width of the mixing layer δ by $\delta = Y_{3/4} - Y_{1/4}$, where $Y_{3/4}$ and $Y_{1/4}$ refer to the values of Y at which u is equal to $(3/4)U_\infty$ and $U_\infty/4$. The width δ is given by $\delta = \alpha(X - X_0)$, α being a constant.
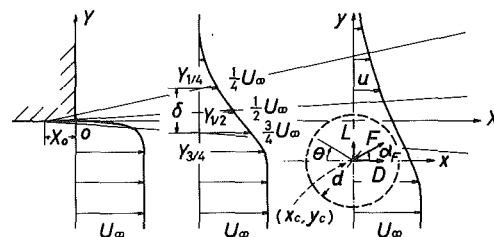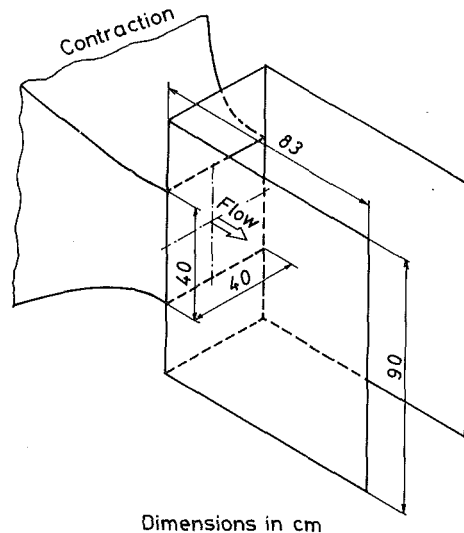

Fig. 1 Flow configuration

Fig. 2 Arrangement of end plates

Fig. 3 Time-mean force coefficient C_F, its angle of action α_F, and angle of stagnation point $-\theta_{st}$ plotted against η_c. Top curve is distribution of u in mixing layer. (Uncertainty in $C_F = \pm 0.02$, in $\alpha_F = \pm 1°$, in $\theta_{st} = \pm 2°$, in $\eta_c = \pm 0.01$ and in $d/\delta = \pm 0.01$).

Let the center of a circular cylinder with diameter d be located at a position (X_c, Y_c), which can also be described in terms of η_c $(= (Y_c - Y_{1/2})/(X_c - X_0))$. We have two length scales, i.e., the width δ and the unit Reynolds number ν/U_∞, ν being the kinematic viscosity. Accordingly, the flow around a circular cylinder in the mixing layer is governed by three independent parameters η_c, d/δ and the Reynolds number $U_\infty d/\nu$ $(= \mathrm{Re})$.

3 Experimental Apparatus and Methods

The mixing layer employed in the present study was a boundary of a free jet issuing into the ambient atmosphere from a 40 cm $\times$ 40 cm square nozzle with a contraction ratio 9:1. Rectangular end plates (83 cm $\times$ 90 cm) were installed as shown in Fig. 2. The distance between the end plates was 40 cm.

Five circular cylinders with diameters of 0.91–6.0 cm were tested. Three smaller cylinders of 0.91–3.17 cm diameter were machined brass tubes, being used to measure the vortex-shedding frequency. A brass cylinder with 4.37 cm diameter was fitted with two pressure taps (of 0.8 mm diameter) connected to semi-conductor strain-gaged pressure transducers (TOYODA PD 104K) which were mounted inside the cylinder, with a small cavity between the pressure tap and the diaphragm of the transducer. The spanwise distance between the pressure taps was 6.0 mm ($= 0.14d$). The pressure transducers measured pressure fluctuations at two points on the surface, their r.m.s. values and the cross correlations. The gain factor of the pressure transducers was found to be 1 ± 0.06 for frequencies less than 500 Hz with negligibly small phase shift.

The largest cylinder of 6.0 cm diameter, which was a machined acrylicresin tube, was used for direct measurement of the fluctuating force. Two strain-gaged load cells were installed inside the cylinder to detect the force acting on an active part whose spanwise length was equal to the diameter. This active length is expected to yield the sectional force with an error less than several percent (Surry [4]). The natural frequency of the active part was 175 Hz, which was about four times larger than the highest central frequency of the fluctuating force. Finally, the maximum radial displacement of the active part was estimated to be less than $0.001d$ throughout the present experiment.

The circular cylinders spanned the distance between the end plates, thus having aspect ratios of 6.7–44.0. They were traversed through a few pairs of slits being parallel to the Y
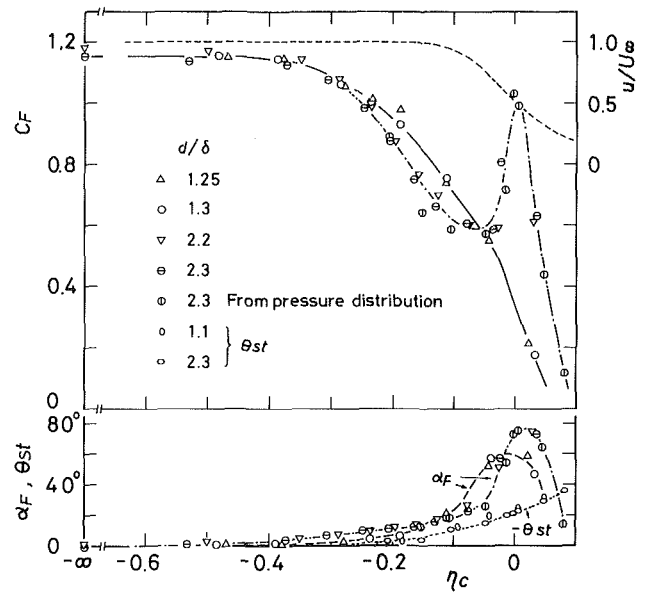
direction. The distance between the center of the cylinders and the trailing edges of the end plates was greater than 7.5 diameters of the largest cylinder.

The force on the active part was measured by a dynamic strain meter (KYOWA DPM-110) and velocities u and u' by a constant-temperature hot-wire anemometer (KANOMAX 21-1000). Signals from these instruments were analyzed by a digital signal processor (ONOSOKKI CF-500) to obtain the time-mean and r.m.s. values, the power spectra and the cross correlations. The time-mean velocity u in the mixing layer was also measured by a total head tube of 1.2 mm diameter.

The main flow was uniform within $\pm 0.01 U_\infty$ in the YZ plane 10-45 cm downstream of the nozzle. The turbulence intensity $(\overline{u'^2})^{1/2}/U_\infty$ in the main flow was 0.5–0.9 percent at main-flow velocities $U_\infty = 7$–13.8 m/s, which were employed in the present experiment. The velocity u in the mixing layer measured in the YZ plane 45 cm downstream of the nozzle was found to be uniform within $\pm 0.025 U_\infty$ in the range of $u/U_\infty > 0.4$, which corresponds to $\eta \lesssim 0.04$. Reynolds number Re ranged from 5500 to 46000 and the ratio d/δ from 0.20 to 2.3.

4 Results and Discussion

4.1 Mixing Layer. Profiles of the velocities u and $(\overline{u'^2})^{1/2}$ were consistent with a classical measurement (Wygnanski and Fiedler [5]). The profiles are given in a previous paper [1]. The linear increase of δ with $X - X_0$ was realized in the range $X - X_0 \gtrsim 14$ cm and represented by $\delta = 0.13 (X - X_0)$.

4.2 Time-Mean Force. The magnitude F of the time-mean force acting on the cylinder and its angle α_F measured from the positive x axis (see Fig. 1) are plotted against η_c in Fig. 3, where F is represented by the force coefficient C_F $(= 2F/\rho U_\infty^2 d)$. For the purpose of comparison u/U_∞ in the undisturbed mixing layer is also included.

Surprisingly enough a sharp maximum of C_F, say C_{Fmax}, appears at $\eta_c = 0$ for the cylinders of $d/\delta = 2.2$ and 2.3; C_{Fmax} is as high as 80 percent of the value of C_F in the uniform flow. It may be noted that for $d/\delta = 2.3$ the cylinder occupies a range of 0.3 in η. Since α_F corresponding to C_{Fmax} is about 80 deg., the force acts mostly as a side force (from now on referred to as lift) in the direction of positive Y.
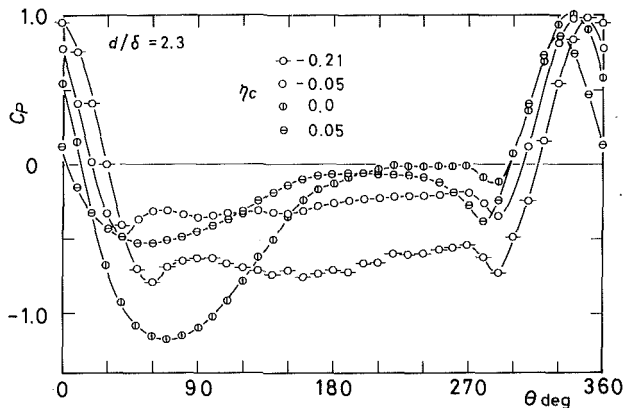
Fig. 4 Time-mean surface-pressure distribution. (Uncertainty in $C_p = \pm 0.02$, in $\theta = \pm 0.25°$, in $d/\delta = \pm 0.01$ and $\eta_c = \pm 0.01$).

Fig. 6 Time-mean lift and drag coefficients C_L and C_D plotted against η_c. (Uncertainty in $C_L = \pm 0.02$, in $C_D = \pm 0.02$, in $\eta_c = \pm 0.01$ and in $d/\delta = \pm 0.01$).

Fig. 5 Distribution of time-mean longitudinal velocity u near circular cylinder along radial lines $\theta = \pm 90$ deg. (Uncertainty in $y/d = \pm 0.02$, in $u/U_\infty = \pm 0.01$, in $d/\delta = \pm 0.01$, in $\eta_c = \pm 0.01$).

(a)

(b)
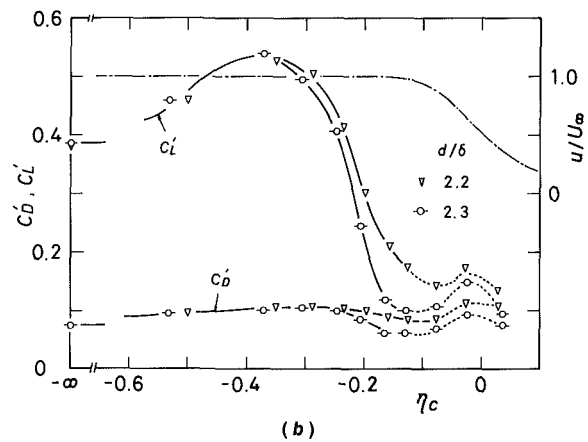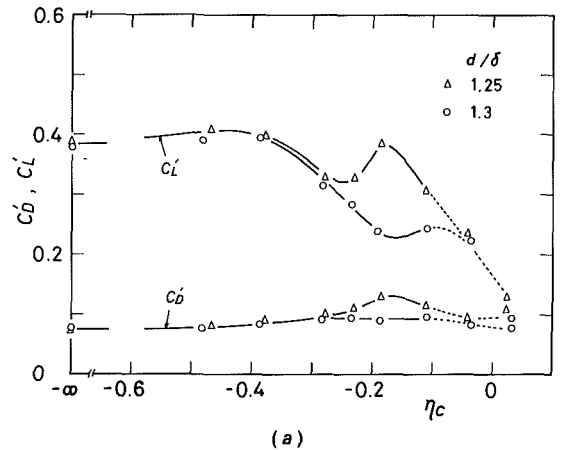
Fig. 7 R.m.s. lift and drag coefficients $C_L{}'$ and $C_D{}'$ plotted against η_c for (a) $d/\delta = 1.25, 1.3$ and (b) 2.2, 2.3. Chain-dotted line shows distribution of u in mixing Layer. (Uncertainty in $C_L{}' = \pm 0.01$, in $C_D{}' = \pm 0.01$, in $\eta_c = \pm 0.01$ and in $d/\delta = \pm 0.01$).

The surface-pressure distributions shown in Fig. 4 give a clue as to why $C_{F\max}$ appears. Here the pressure is represented by the pressure coefficient C_p ($= 2(p - p_0)/\rho U_\infty^2$, p_0: pressure in the uniform flow, ρ: density of the fluid). The pressure distribution for $\eta_c = 0.0$ is exceptional in that it has a high suction peak on the low-velocity side at $\theta \doteq 70$ deg, θ being the angle measured from the negative x axis (see Fig. 1); this suction peak is the main contribution to $C_{F\max}$. This pressure distribution suggests that the separation of flow from the surface on the low-velocity side occurred far downstream of the stagnation point, i.e., at $\theta \doteq 150$ deg, because of high level of turbulence in the boundary layer.

Such a large delay of the separation was accompanied by a wall-jet-like flow of the high dynamic pressure along the low-velocity side of the cylinder. The formation of the flow is demonstrated by the distribution of u along the y axis (i.e., the radial lines $\theta = \pm 90$ deg), which is shown in Fig. 5. For $\eta_c = 0.0$ the velocity on the low-velocity side is seen to have a maximum value amounting to 1.35 U_∞, which is equal to the value obtained in the main flow; the maximum occurs much closer to the surface than that for other values of η_c.

The force F is divided into the lift component L and the drag component D. The lift is taken as positive if it is in the direction of the positive Y axis. Figure 6 gives the lift coefficient C_L ($= 2L/\rho U_\infty^2 d$) and the drag coefficient C_D ($= 2D/\rho U_\infty^2 d$) plotted against η_c.

4.3 Fluctuating Force. Figure 7 shows η_c and d/δ dependence of the r.m.s. lift coefficient $C_L{}' (= 2(\overline{L'^2})^{1/2}/\rho U_\infty^2 d)$ and the r.m.s. drag coefficient $C_D{}' (= 2(\overline{D'^2})^{1/2}/\rho U_\infty^2 d)$, where L' and D' are fluctuating components of the lift and the drag. In Fig. 7 it is worth noting that for $d/\delta = 2.2$
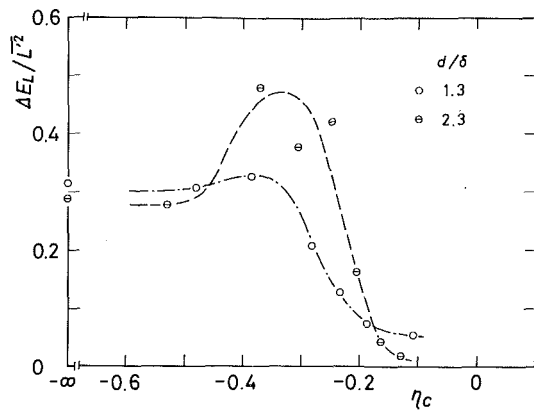
Fig. 8 Energy of fluctuating lift ΔE_L contained in frequency range $f_v \pm \Delta f/2$ ($\Delta f = 0.25$ Hz $\doteq f_v/120$) divided by overall energy $\overline{L'^2}$. (Uncertainty in $\Delta E_L/\overline{L'^2} = \pm 0.02$, in $\eta_c = \pm 0.01$ and in $d/\delta = \pm 0.01$).

Fig. 9 Strouhal number St plotted against η_c. Chain-dotted line is given by equation (1); broken line shows distribution of u in mixing layer. (Uncertainty in St $= \pm 0.002$, in $\eta_c = \pm 0.01$, in $d/\delta = \pm 0.01$ and in Re $= \pm 100$).

and 2.3 C_L' attains a maximum (say, $C_{L'\mathrm{max}}$) at $\eta_c = -0.35$, which is about 40 percent larger than C_L' obtained in the main flow, say $C_{L'\infty}$. Most of the increase $C_{L'\mathrm{max}} - C_{L'\infty}$ is caused by an increase in the energy of L' contained in a narrow frequency range centered around the vortex-shedding frequency f_v. This is demonstrated in Fig. 8, which shows the energy ΔE_L contained in a range $f_v \pm (\Delta f/2)$, where $\Delta f = 0.25$ Hz $= f_v/120$, divided by the overall energy $\overline{L'^2}$. This ratio takes a maximum at $\eta_c = -0.35$, which is about 80 percent larger than the value in the main flow.

A problem which we pose is why $C_{L'\mathrm{max}}$ is greater than $C_{L'\infty}$. For the above values of η_c and d/δ the cylinder is immersed in the main flow near the time-mean edge of the mixing layer ($\eta \doteq -0.15$), the top of the cylinder (see Fig. 1) being located at $\eta = -0.2$ outside the edge. At this position $\eta = -0.2$ the top of the cylinder is exposed to an intermittently turbulent region of the mixing layer. We believe that large spanwise vortices in the mixing layer (Brown and Roshko [6]) passing near the top of the cylinder enhanced the strength of the vortices shed periodically from the cylinder. If this is the case, (i) the frequency f_m at which the mixing-layer vortices pass the position X_c should be equal to f_v, the vortex shedding frequency and (ii) the strength or circulation of the mixing-layer vortices should be of the same order as that of the shed vortices.

We consider the first point. Power spectrum of the fluctuating velocity component in the Y direction, v', measured at $\eta = 0$ (Wygnanski and Fielder [5]) has a definite peak at a frequency f given by $f(X - X_0)/U\delta = 0.80$. Since v' at $\eta = 0$ well reflects the passing of the mixing-layer vortices, this frequency can be taken equal to f_m. Employing the present relation $\delta = 0.13$ $(X - X_0)$ we have $f_m\delta/U_\infty \doteq 0.1$. On the other hand, at Reynolds numbers of the present experiment, the vortex-shedding frequency is given by $f_v d/U_\infty \doteq 0.20$. This relation combined with the above one yields $f_m/f_v \doteq 2.0$ $(d/\delta)^{-1}$. Accordingly we have $f_m/f_v \doteq 0.9$ for $d/\delta = 2.2$ and 2.3.

Next we discuss the second point. The convection velocity U_c of the mixing-layer vortices and the distance l between two consecutive ones are related to f_m by $f_m l = U_c$. Since $U_c = 0.43 U_\infty$ and $f_m\delta/U_\infty = 0.10$ (Wygnanski and Fielder [5]), we have $l = 4.3\delta$. The circulation of these vortices Γ_m is approximately equal to $U_\infty l$ and thus given by $\Gamma_m = 4.3 U_\infty \delta$. On the other hand, the circulation of vortices shed from the cylinder Γ_v is given by $f_v\Gamma_v = (1/2)U_s^2\epsilon$, where U_s is the velocity at the edge of the boundary layer at separation and $1 - \epsilon$ denotes the fraction of circulation cancelled in the vortex-formation region. We have $U_s = 1.35 U_\infty$ from Fig. 5 and $f_v d/U_\infty \doteq 0.20$ for the cylinder in the main flow. Although there is a large scatter in measured values of ϵ, we take a typical value $\epsilon = 0.40$ (Berger and Wille [7]). These values of
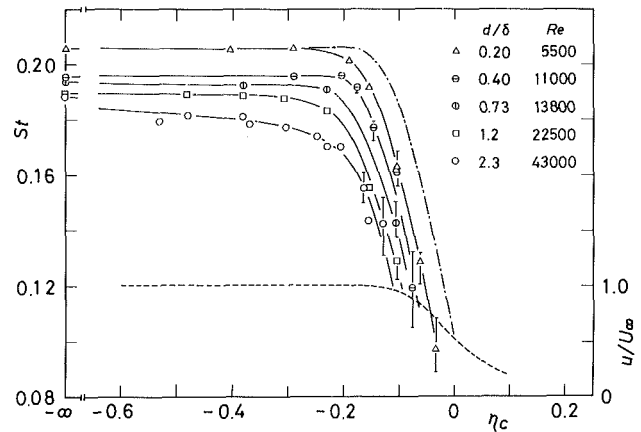
the parameters yield $\Gamma_v \doteq 1.8 U_\infty d$. Finally we have $\Gamma_m/\Gamma_v = 2.4(d/\delta)^{-1}$, which gives $\Gamma_m/\Gamma_v \doteq 1.0$ for $d/\delta = 2.2$ and 2.3. The above considerations on (i) and (ii) might suggest that the maximum $C_{L'\mathrm{rms}}$ as high as 1.4 $C_{L\infty}'$ will appear only when the ratio d/δ is near 2.0.

4.4 Strouhal Number. Figure 9 shows the η_c and d/δ dependence of Strouhal number St $= f_v d/U_\infty$. In this figure we notice that, for each value of d/δ, St decreases with increasing η_c; this is generally due to a decrease in the velocity of local flow approaching to the cylinder. We also notice that St measured in the uniform flow decreases with increasing d/δ; this is caused by an associated increase in Reynolds number Re, being consistent with previous data (McCroskey [8]).

All of the first decrease cannot be attributed to the decrease in the approaching velocity. To discuss this point, we introduce a velocity u_c which would be measured at the center of the cylinder (X_c, Y_c) if the cylinder were absent. If the decrease in St is assumed to be caused only by the decrease in u_c, a Strouhal number St$_c = f_c d/u_c$ would be constant and equal to St measured in the main flow, say St$_\infty$. Thus, neglecting a small Reynolds-number effect, St of the cylinder in the mixing layer would be represented by

$$\mathrm{St} = \mathrm{St}_\infty (u_c/U_\infty), \tag{1}$$

which is shown in Fig. 9 by a chain-dotted line for $d/\delta = 0.2$ and Re $= 5500$. This is by about 0.02 higher than measured St. The difference is conjectured to be produced by a combined effect of (i) the velocity gradient $|\partial u/\partial Y|$ in the mixing layer, (ii) its development downstream, i.e., $d\delta/dX > 0$ and (iii) its finite width.

The periodic vortex shedding from the cylinder disappeared when η_c was greater than about -0.1. As is shown in Fig. 10, an exact position of the disappearance is dependent on d/δ. We believe that for cylinders with $d/\delta \gtrsim 1$ the vortex shedding was suppressed owning to a large value of $|\partial u/\partial Y| (d/U_\infty)$ of the approaching flow. On the other hand, for cylinders with $d/\delta < < 1$ where $|\partial u/\partial Y| (d/U_\infty)$ is relatively small, the high turbulence in the mixing layer destroyed the periodic vortex shedding.

4.5 Fluctuating Surface Pressures. Fluctuating surface pressures were obtained for the cylinder with $d/\delta = 1.9$; this cylinder attained the maximum $C_{L'\mathrm{max}}$ equal to 1.25 $C_{L'\infty}$ at $\eta_c = -0.25$. For a few η_c's near this value, Fig. 11(a) shows circumferential distributions of the r.m.s. surface-
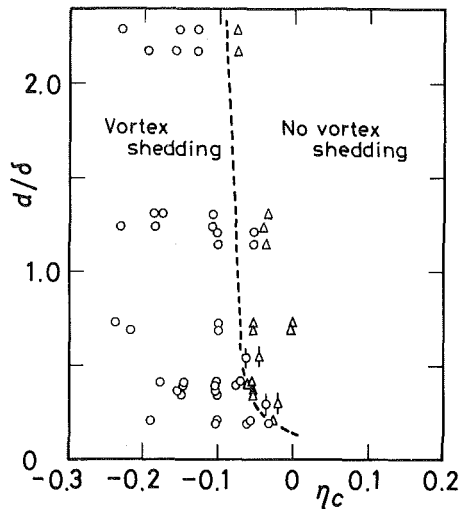
Fig. 10 Position of diappearance of periodic vortex shedding in parameter space (η_c, d/δ). Re = 5500 – 44000; o, ϕ , vortex shedding; $\triangle$, $\underset{\triangle}{\triangle}$, no vortex shedding; flagged data are from Kiya et al. [1]. (Uncertainty in η_c = ± 0.01 and in d/δ = ± 0.01.

pressure coefficient $c_p' = 2(\overline{p'^2})^{1/2}/\rho U_\infty^2$. We believe that c_p' in the separated region (80 deg $\leq \theta \leq$ 280 deg) is generally larger for η_c = − 0.26 and − 0.22 than for the uniform flow. This is further evidence of the fact that the shed vortices are enhanced at these η_c's. On the other hand, the value of c_p' becomes much lower when the center of the cylinder is immersed in the mixing layer as shown in Fig. 11(b).

The enhancement of the shed vortices is also accompanied by the enhancement of periodicity of the vortex shedding. This is indicated in Fig. 12 by the autocorrelation of the fluctuating lift; that is, decay of its amplitude with increasing time lag τ is slower for η_c = − 0.27 and − 0.22 than in the main flow.

5 Conclusion

Measurements of forces, surface-pressure, and vortex-shedding frequency of a circular cylinder of diameter d placed in and near a turbulent plane mixing layer are described. Governing parameters are Reynolds number Re based on U_∞ and d, the ratio d/δ (δ being the mixing-layer width) and the nondimensional transverse coordinates of the center of the cylinder η_c; Re and d/δ ranged from 5500 to 46000 and from 0.2 to 2.3, respectively. Main results of this study can be summarized as follows.

(1) The dependence on η_c and d/δ of the forces, the surface pressures and the vortex-shedding frequency was demonstrated within the range of the parameters investigated.

(2) The r.m.s. lift for d/δ = 2.2 and 2.3 attained a maximum 40 percent larger than that in the uniform flow when the cylinder was located in the uniform flow in such a manner that a part of its surface was exposed to an intermittently turbulent edge of the otherwise undisturbed mixing layer. This was caused by the enhancement of vortices shed periodically from the cylinder; the enhancement was interpreted in terms of large spanwise vortices of the mixing layer passing near the cylinder with a frequency equal to the vortex-shedding frequency f_v.

(3) The time-mean resultant force for d/δ = 2.2 − 2.3 attained a sharp maximum as high as 80 percent of that in the main flow when the center of the cylinder was located at the center of the mixing layer; this maximum force was directed from the high-velocity side to the low-velocity side of the mixing layer.

(4) The periodic vortex shedding from the cylinder disappeared when η_c was larger than a critical value of about − 0.1. This critical value increases slightly with decreasing d/δ.

(a)

(b)
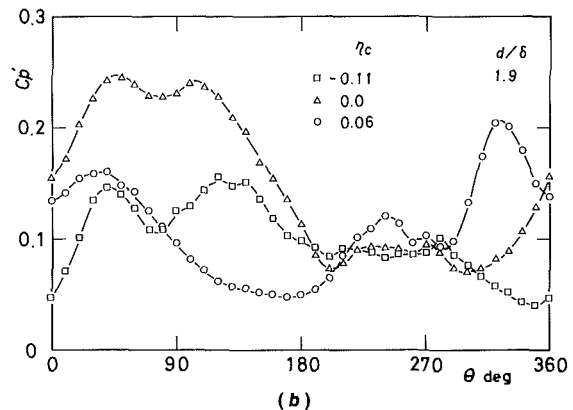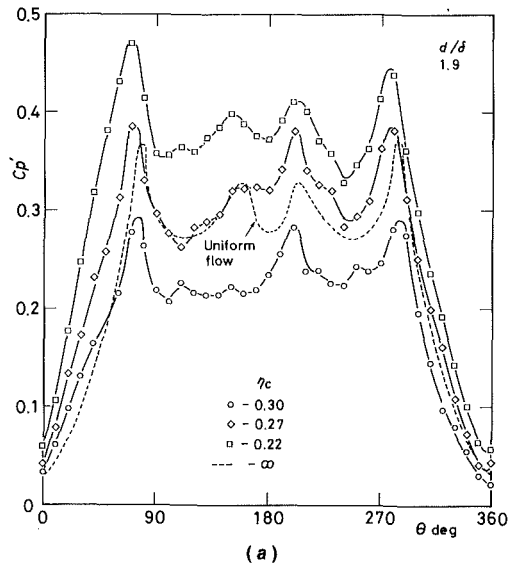
Fig. 11 Distribution of r.m.s. surface-pressure coefficient c_p for d/δ = 1.9; (a) η_c = − ∞ (uniform flow), − 0.30, − 0.27, − 0.22 and (b) − 0.11, 0.0, 0.06. (Uncertainty in c_p' = ± 0.015, in θ = ± 0.25°, in η_c = ± 0.01 and in d/δ = ± 0.01).
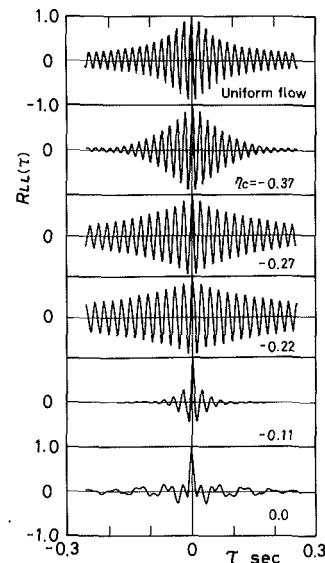
Fig. 12 Auto-correlation coefficient of fluctuating lift for d/δ = 1.9

their assistance in the construction of the experimental apparatus. The present study was supported by the Grant-in-Aid for Scientific Research from the Ministry of Education, Science and Culture of Japan.

References

1 Kiya, M., Tamura, H., and Arie, M., "Forces Acting on Circular Cylinder Placed in a Turbulent Plane Mixing Layer," *Journal of Industrial Aerodynamics*, Vol. 5, No. 1-2, 1979, pp. 13–33.

2 Taniguchi, S., Miyakoshi, K., and Dohda, S., "Characteristics of Fluid Forces Acting on a Square Cylinder in a Free Turbulent Mixing Layer," *Transactions of the JSME*, Vol. 51, No. 467, 1985, pp. 2265–2270 (in Japanese).

3 Taniguchi, S., Miyakoshi, K., and Dohda, S., "Characteristics of Fluid Forces Acting on a Square Cylinder in a Free Turbulent Mixing Layer; 2nd Report, Characteristics of Fluctuating Pressure and Approaching Flow," *Transactions of the JSME*, Vol. 52, No. 473, 1986, pp. 285–289 (in Japanese).

4 Surry, D., "Some Effects of Intense Turbulence on the Aerodynamics of a Circular Cylinder at Subcritical Reynolds Number," *Journal of Fluid Mechanics*, Vol. 52, Part 3, 1972, pp. 543–563.

5 Wygnanski, I., and Fiedler, H. E., "Two-Dimensional Mixing Region," *Journal of Fluid Mechanics*, Vol. 41, Part 2, 1970, pp. 327–361.

6 Brown, G. L., and Roshko, A., "On Density Effects and Large Structure in Turbulent Mixing Layers," *Journal of Fluid Mechanics*, Vol. 65, Part 4, 1974, pp. 775–816.

7 Berger, E., and Wille, R., "Periodic Flow Phenomena," *Annual Review of Fluid Mechanics*, Vol. 4, 1972, pp. 313–340.

8 McCroskey, W. J., "Some Current Research in Unsteady Fluid Dynamics—The 1976 Freeman Scholar Lecture," ASME JOURNAL OF FLUIDS ENGINEERING, Vol. 99, No. 1, 1977, pp. 8–39.

B. R. Ramaprian

Professor,
Department of Mechanical and
Materials Engineering,
Washington State University,
Pullman, WA
Mem. ASME

H. Haniu

Associate Professor,
Department of Mechanical Engineering,
Kitami Institute of Technology,
Hakkaido, Japan

Measurements in Two-Dimensional Plumes in Crossflow

The mean-flow and turbulent properties of two-dimensional buoyant jets discharged vertically upward into a crossflowing ambient have been measured in a hydraulic flume, using laser velocimetry and microresistance thermometry. The trajectory of the resulting inclined plume is found to be nearly straight, beyond a short distance from the source. The flow is essentially characterized by the presence of buoyancy forces along (s-direction) and perpendicular (n-direction) to the trajectory. While the s-component buoyancy tends to destabilize the flow and hence raise the overall level of turbulence in the flow, the n-component buoyancy tends to augment turbulence on the upper part of the flow and inhibit turbulence on the lower part. The experimental data are used to examine these effects quantitatively.

Introduction

Consider a vertical heated jet of width (or diameter) D, issuing at a velocity U_j and a temperature excess ΔT_j (or density defect $-\Delta\rho$) relative to the ambient. Let the crossflow velocity of the ambient be U_a. The overall behavior of this buoyant jet (which will be inclined to the vertical, because of the crossflow) at a moderately large distance (of the order of $100D$) from the source can be shown to depend principally on two parameters, the exit Richardson number R_j defined by

$$R_j = \frac{(\Delta\rho/\rho_a)gD}{U_j^2} \qquad (1)$$

and the velocity ratio $K = U_j/U_a$ (Wright [1]). Ambient turbulence is assumed to have no effect at these distances. It may, however, be important at very large distances. In the region within $100D$, the overall jet behavior can depend, to varying extents, on the initial mass, momentum and buoyancy fluxes at exit. Wright derived, from dimensional analysis, different asymptotic relations for plume rise and dilution, for various subregions of this range, for the case of a circular buoyant jet discharged into crossflow. Many others [2–6] proposed "plume-rise laws" for circular buoyant jets in crossflow. More recent approaches involve the solution of the governing partial differential equations using appropriate turbulence model(s) [7–10]. Progress in this direction has, however, been slowed by the lack of experimental data. While there have been a number of experiments reported on round jets in crossflow, these have mostly been restricted to mean temperature or concentration measurements. Turbulence data in plane jets in crossflow with or without buoyancy effects were not available, prior to the present work.

The two most important features of buoyant jets in crossflow of relevance to turbulence modeling are the presence of streamline curvature and buoyancy. A series of experiments were designed by the authors to obtain detailed information on the structure of turbulence in the presence of these two

features. The studies on the effect of curvature in nonbuoyant jets in crossflow are reported separately in [11]. The present paper is concerned with the study of the effects of buoyancy in jets in crossflow.

A very detailed study of axial buoyancy effects in a plane vertical plume was performed by Ramaprian and Chandrasekhara [12, 13] in essentially the same experimental apparatus as the one in which the present study was conducted. Significant increases were observed by them in the levels of all the turbulence properties of the vertical plume relative to a nonbuoyant jet. The results of that study will frequently be used in this paper for comparison with the present results.

There is a fair amount of information available on turbulence in stratified shear flows (e.g., [14], [15]). Webster [15] conducted experiments on stably stratified shear flow and investigated the dependence of the various turbulent quantities upon the gradient Richardson number defined as

$$R_{gw} = \frac{g\partial\bar{T}/\partial x}{\bar{T}(\partial\bar{U}/\partial x)^2} \qquad (2)$$

It was found that the turbulent and length scale decrease as the gradient Richardson number increases. These results were predicted well by Launder [7] using a two-equation model of turbulence.

One of the interesting aspects of nonvertical buoyant flows is that a significant component of buoyancy acts in a direction normal to the axis of the flow and that this component tends to inhibit turbulent motions on the lower side of the inclined jet and augment them on the upper side. This effect is superimposed on the overall destabilizing effect of the axial component of buoyancy. The primary objective of the present study was to study the effect of the normal component of buoyancy on the structure of turbulence in a two-dimensional plume in crossflow. Fortunately, a highly buoyant jet in crossflow becomes a plume (i.e. buoyancy dominated) and has nearly a straight trajectory, beyond a short distance from the source (as will be shown later in this paper). It was thus possible to study buoyancy effects on an inclined plume in the absence of any significant streamline curvature. The results

presented in this report compliment those on the effects of stream-line curvature in nonbuoyant jets in crossflow reported in [11] and the effects of (axial) destabilizing buoyancy in vertical plumes reported in [13].

Experimental Details

The experiments were carried out in the same hydraulic flume as the one in which nonbuoyant jets in crossflow were studied [11, 16]. Briefly, the apparatus consisted of a hydraulic flume 7 m long $\times$ 0.45 m wide $\times$ 0.75 m deep, in which a very small velocity (of the order of 1 cm/s) was maintained to simulate the cross flow. A hot water jet introduced vertically upwards through a rectangular slot of 5 mm width $\times$ 250 mm span located near the bottom of the flume served as the buoyant jet. The flow was confined between two false side walls made of Plexiglas and spaced 250 mm apart, to improve the two-dimensionality of the flow. The cross flow caused the trajectory of the buoyant jet to be inclined to the vertical. A schematic view of the two-dimensional buoyant jet in crossflow is shown in Fig. 1 to explain the nomenclature. Measurements were made in the range $14 \leq s/D \leq 55$. The measurement stations and the traverse directions were selected after obtaining preliminary information on the plume trajectory from dye photographs. Instantaneous velocity as well as instantaneous temperature excess above the ambient were measured using two-component laser Doppler anemometry (LDA) and microresistance ("cold-film") thermometry respectively. The LDA consisted of a 15-mw Helium-Neon laser, 3-beam, frequency-shifted optics and a pair of frequency trackers, manufactured by TSI. Polarization was used to separate the two components of velocity. The cold-film thermometer consisted of a DISA hot-film probe driven by a constant-current bridge, whose out-of-balance voltage is proportional to the instantaneous temperature in the flow. The LDA had a spatial resolution of 0.1 mm in the n-direction and
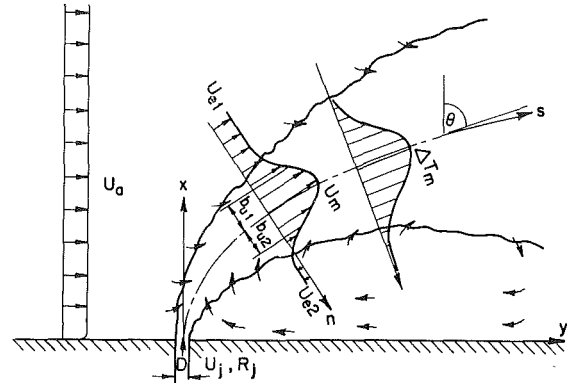
Fig. 1 Schematic of the two-dimensional jet in crossflow

1.1 mm in the spanwise direction. The hot-film sensor was located within about 1 mm downstream of the LDA focal volume. This arrangement had been found satisfactory in the earlier experiments. The jet velocity and temperature excess at the exit were monitored and maintained constant at the desired values. The details of instrumentation and data acquisition/processing, and the special techniques used to obtain reliable measurements are described in related publications [11, 13, 17]. It was also established from these earlier studies, that the experimental arrangement produced acceptably two-dimensional flow (to within ± 2 percent in mean velocity), that there were no significant free-surface effects and that the flow was fully turbulent beyond $s/D \approx 30$.

Most of the measurements were made with $U_j = 10$ cm/s, $K = 9$ and $\Delta T_j = 20°$C (jet number 100920 M^*). The properties

*The first two digits in this designation denote the nominal exit velocity in cm/s, the second and third digits denote the nominal velocity ratio K, and the last two digits denote the nominal exit temperature excess in °C. This scheme of test designation is retained for consistency with that used for nonbuoyant jets in crossflow [11].

_____ Nomenclature _____

b = half width

C_E = entrainment coefficient defined by equation (28)

C_D = drag coefficient defined by equation (21)

D = jet width at exit

E = spectral density of $\overline{u^2}$, $\overline{v^2}$ or $\overline{w^2}$

g = acceleration due to gravity

H = kinematic heat flux (mean + turbulent)

H_U = plume rise (height of the maximum velocity point from the exit plane)

h = turbulent heat flux in the s-direction

K = velocity ratio, U_j/U_a

l_b = buoyancy length scale defined by equation (7)

M = kinematic momentum flux

n = direction normal to the trajectory (see Fig. 1)

Q = kinematic mass flux

R = axial Richardson number defined by equation (13)

R_g = gradient Richardson number defined by equation (29)

R_{gw} = gradient Richardson number used by Webster (equation (2))

$\hat{R}_g$ = global gradient Richardson number (equations (32) and (33))

s = direction along the trajectory (see Fig. 1)

s^* = $s - s_o$

T = temperature

t = turbulent temperature fluctuation

U = s-component of velocity

u = turbulent fluctuation in U

V = n-component of velocity

v = turbulent fluctuation in V

W = wave number $2\pi f/\bar{U}$ where f is the frequency

x = vertical coordinate (see Fig. 1)

y = horizontal (downwind) coordinate

α = coefficient of thermal expansion

β = kinematic buoyancy flux

ϵ_m = eddy viscosity $-uv/(\partial \bar{U}/\partial n)$

ρ = density

σ = coefficient

θ = inclination of trajectory to the vertical

Subscripts

a = ambient

e = edge of jet

j = jet exit

m = maximum value

o = virtual origin

t = pertaining to temperature

u = pertaining to velocity component in the s-direction

v = pertaining to velocity component in the n-direction

x, y = components in x and y directions

1 = upper part of plume

2 = lower part of plume

Other Symbols

overbar = time average

prime = rms value

∞ = value at the last measurement station

Δ = excess over reference or ambient
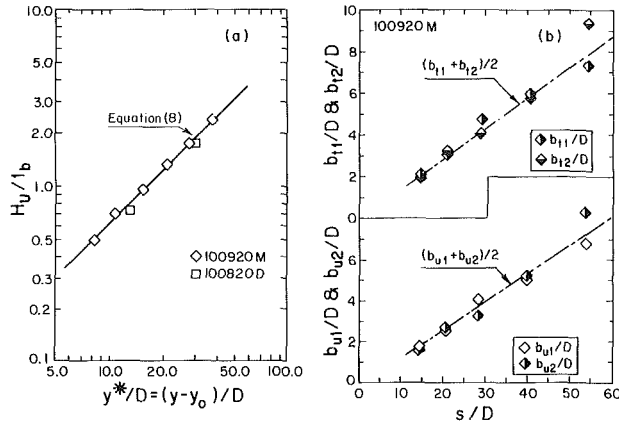
Fig. 2 Data on plume trajectory and spreading. (a) plume rise (b) veloci-
ty and temperature half-widths b_u and b_t. Uncertainties: y^*/D: ± 2;
H_U/l_b: ± 5 percent; s/D: ± 0.070; b/D: ± 0.1.

measured in this experiment included mean velocities,
Reynolds stresses and diffusion fluxes of turbulent kinetic
energy. More detailed measurements such as spectra and mix-
ing intermittency were measured (at a limited number of
points in the flow) in a separate experiment in which the flow
conditions were: $U_j = 10$ cm/s, $K = 8$ and $\Delta_j = 20°C$ (jet
number 100820 D). The exit Richardson number for these two
flows $R_j \approx -0.038$. The inclination of the jet trajectory in
both these experiments was about 30 degrees to the vertical. At
smaller ratios of the jet exit velocity to crossflow velocity (but
the same buoyancy strength), the trajectory would be more in-
clined to the vertical. It was found that in such cases, the
stratification in the flume (resulting from the presence of the
hot jet sandwiched between the cold fluid at top and bottom)
introduced instability which caused the two-dimensionality of
the flow to break down quickly. Hence values in the range of
8–10 were chosen for K in the present buoyant jet studies. The
detailed experimental results have been stored on magnetic
tape. They are also available from [16]. The following are the
uncertainty estimates of the experimental quantities directly
measured: $\bar{U}$:2.5 mm/s, $\Delta \bar{T}$: 0.2°C, u', v', w': 5 percent, $\overline{uv}$,
$\overline{ut}$, $\overline{vt}$: 10 percent. The uncertainties of the results shown in the
figures were estimated by performing an error propagation
analysis and are indicated in each figure.

Results

Trajectory and Spreading. In the case of highly buoyant
jets, sufficiently far from the jet exit, buoyancy is the major
driving force and the initial mass and momentum fluxes have
little influence on the flow properties. Hence, the rise of this
momentum-dominated "plume" can be described by the func-
tional relationship

$$f(H_U, y, U_a, \beta_j) = 0 \tag{3}$$

where the buoyancy flux β_j is defined as

$$\beta_j \equiv -g \frac{\Delta \rho}{\rho a} U_j D = -U_j^3 R_j \tag{4}$$

The kinematic definition for β_j in equation (4) is convenient
for flows in which $|\Delta \rho / \rho a| \ll 1$ (Boussinesq approximation).
Dimensional analysis yields

$$H_U \propto \frac{\beta_j y}{U_a^3} \tag{5}$$

or

$$\frac{H_U}{l_b} \propto \frac{y}{D} \tag{6}$$

where l_b is a buoyancy length scale defined by

$$l_b \equiv \frac{\beta_j D}{U_a^3} = -K^3 R_j D \tag{7}$$

Hence, a two-dimensional plume in crossflow can be expected
to rise linearly with downstream distance at "large" distances
from the source. The experimental data shown in Fig. 2(a)
shows the rise data for the two buoyant jets studied. It is seen
that the data for the two flows nearly collapse on to a single
line, over the range of s/D studied. The small deviation be-
tween the two data sets is mostly due to uncertainty in the
velocity ratio K (note that $l_b \propto K^3$). The best fit to the line
shown in Fig. 2(a) is given by

$$\frac{H_U}{l_b} = 0.061 \left(\frac{y - y_0}{D} \right)^{1.01} \tag{8}$$

where y_0 is the location of the virtual origin. This is in
reasonable agreement with the linear trend indicated by equa-
tion (6). Figure 2(a) thus indicates that both the flows studied
can be regarded as plumes over the measurement range.

The spreading rate of a symmetrical jet or plume is usually
presented in terms of the increase in the "half-width" b_u,
which is distance from the jet axis to the point where
$(U_m - \bar{U}) = 1/2(U_m + U_e)$. In the present case, since the
velocity distribution in the plume is asymmetric, the half-
width b_u is defined as the average of the half-widths b_{u1} and
b_{u2} for the upper and lower parts of the plume (see Fig. 1).
The variations of b_{u1} and b_{u2} are shown in Fig. 2(b). Also
shown is the best fitting straight line for b_u. The slope of this
line is about 0.14, which is higher than the value of 0.11 for
vertical plumes as measured in the same apparatus by
Ramaprian and Chandrasekhara [13].

Temperature half-width (b_t) data obtained from mean
temperature distributions are presented in Fig. 2(c). The
spreading rate of b_t from the best fitting straight line is also
about 0.14 and is slightly higher than the value of about 0.13
obtained in the same apparatus for vertical plumes. The in-
creases in the spreading rates relative to the vertical plume can
be attributed to the effect of the component of the buoyancy
force acting along the n-direction. Other influences such as
those of finite axial edge velocity U_e and its gradient ($\partial U_e/\partial s$),
that are imporatnt in a curved nonbuoyant jet in crossflow
[11] are not significant in this case. This is because the edge
velocities U_{e1} and U_{e2} are both very small.

Heat and Buoyancy Fluxes. The fluxes of mass, momen-
tum, heat and buoyancy through any plane normal to the axis
of a buoyant jet can be obtained from the definitions

$$Q(s) = \int_{ne1(s)}^{ne2(s)} \bar{U} dn \tag{9}$$

$$M(s) = \int_{ne1}^{ne2} \bar{U}^2 dn \tag{10}$$

$$H(s) = \int_{ne1}^{ne2} (\bar{U}\Delta \bar{T} + \overline{ut}) dn \tag{11}$$

and

$$\beta(s) = -\int_{ne1}^{ne2} \left[\frac{\Delta \rho}{\rho a} g\bar{U} + \frac{\overline{gu\Delta \rho'}}{\rho a} \right] dn$$

$$= -\int_{ne1}^{ne2} g \left[\frac{\Delta \rho}{\rho a} \bar{U} - \alpha \overline{ut} \right] dn \tag{12}$$

Again, kinematic definitions have been used above since den-
sity variations $\Delta \rho$ and ρ' are small. Note that, in general, the
definitions require the limits of integration to be defined. In
the present case, however, since the edge velocities (U_{e1}, U_{e2}),
as well as the edge excess temperatures (ΔT_{e1}, ΔT_{e2}), are very
small (relative to their respective maximum values in the jet),
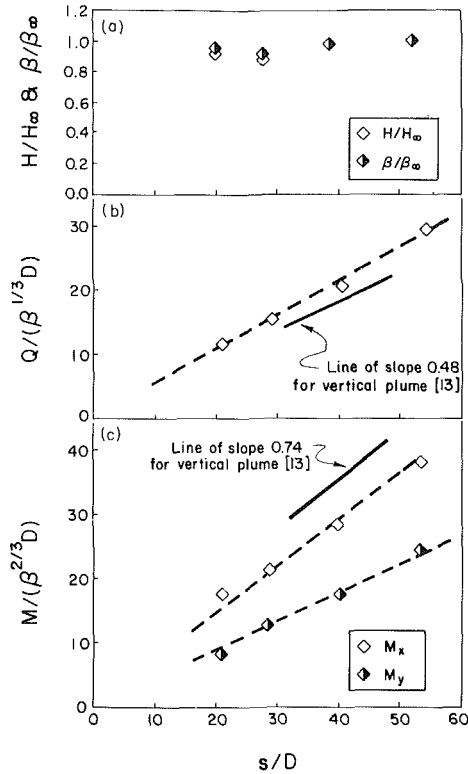the choice of the limits n_{e1} and n_{e2} is not very critical.

Fig. 3 Variation of heat, mass and momentum fluxes along the plume. Uncertainties: s/D: ±0.070; H: ±0.03; β: ±0.03; Q: ±0.6; M: ±1.2.

From the above definitions of the fluxes, one can define, for any axial location, a local Richardson number in the axial direction, as in [13],

$$R(s) = -\left(\frac{Q}{M}\right)^3 \beta \cos \theta \qquad (13)$$

Note that $\beta \cos \theta$ is the flux of buoyancy in the s-direction and can serve as the basis of comparison with a vertical, upward rising buoyant jet. Note also that the negative sign in equation (13) is used to associate positive (destabilizing) buoyancy with negative Richardson number. While this is opposite to the vention used in [13], it is consistent with the definition used for the n-component buoyancy. At the jet exit, $\theta = 0$ and equation (13) reduces to

$$R_j \equiv -\left(\frac{Q_j}{M_j}\right)^3 \beta_j \qquad (14)$$

which is identical to the jet exit Richardson number defined in equation (1), if the velocity and temperature at exit are assumed to have top-hat distributions.

The thermal expansion coefficient α for water increases with temperature in a nonlinear manner. However, within the range of present interest $(s/D>20)$, the maximum excess temperature is sufficiently small that α can be treated as constant. Then, from equations (11) and (12), one obtains, for the vector flux β,

$$\beta(s) = \alpha g H(s) \qquad (15)$$

It can easily be shown from the energy equation for a two-dimensional heated jet, that if the edge temperature excess $\Delta T_{e1} \approx \Delta T_{e2} \approx 0$, and if the velocity/temperature fluctuations go to zero beyond the edges n_{e1} and n_{e2}, the heat flux $H(s)$ must be conserved along the jet. Hence, from equation (15), the buoyancy flux β must also be conserved in the region where α is constant. Figure 3 (a) shows the results for heat flux and the buoyancy flux along the s-direction, obtained from equation (11) and (12) using the measured velocity and temperature distributions in the buoyant jet 100920M. In this

figure, each flux is normalized with the corresponding flux at the last measurement station, namely $x/D = 53.33$ (referred to by the subscript ∞). It is seen that both the fluxes are conserved reasonably well within the limits of experimental accuracy. This confirms that the flow is acceptably two-dimensional, at least in the neighborhood of the plane of measurement.

Mass and Momentum Fluxes. Since the trajectory of the buoyant jet is straight for $s/D>20$, and the s-component velocity at the edge is very small, it is reasonable to look for an asymptotic analysis based on the assumption of self-preservation. Velocity distributions (to be discussed later) were indeed found to be self-preserving. In the asymptotic buoyant jet (plume) in crossflow, one can write, for the kinematic mass flux Q,

$$Q = f[\beta, U_a, (s - s_0)] \qquad (16)$$

where s_0 is the location of the virtual origin. Dimensional analysis yields

$$\frac{Q}{\beta^{1/3} s^*} = f(\beta^{1/3}/U_a) = \sigma_Q \qquad (17)$$

where σ_Q is constant for a *given* flow and $s^* = (s - s_0)$. The parameter σ_Q, however, depends on $(\beta^{1/3}/U_a)$ which is a measure of the relative strength of crossflow effects to buoyancy effects. Figure 3 (b) shows experimental data of mass flux, plotted $(Q/\beta^{1/3})$ versus s/D. It is seen that Q varies linearly with s as implied by the plume-equation (17). The results are compared with the results from [13] for a vertical plume $(U_a = 0)$. It is seen that slope σ_Q is slightly larger with crossflow. Since (dQ/ds) represents the entrainment rate, it can be concluded that the plume in crossflow entrains more fluid from the ambient than the vertical plume with the same buoyancy flux.

Consider now the momentum flux. For a plume in crossflow, one can write for the horizontal and vertical components of the momentum flux, the functional relations:

$$M \cos \theta = M_x = f_1(\beta, s^*) \qquad (18)$$
$$M \sin \theta = M_y = f_2(U_a, s^*) \qquad (19)$$

Dimensional analysis yields

$$\frac{M_x}{\beta^{2/3} s^*} = \sigma_{Mx} \qquad (20)$$

and

$$\frac{M_y}{U_a^2 s^*} = C_D \qquad (21)$$

Hence, it follows

$$\frac{M_x}{M_y} = \cot \theta = (\beta^{1/3}/U_a)^2 \frac{\sigma_{Mx}}{C_D}$$
$$= \text{constant} \qquad (22)$$

for a given flow. This again shows that the trajectory of the plume in crossflow is a straight line the slope of which depends on the parameter $\beta^{1/3}/U_a$. Figure 3(c) shows the variation of M_x and M_y in the buoyant jet 100920M along with the vertical plume data of [13]. It is seen that the data indicate the validity of the linear relations (20) and (21). The data also indicate that the slope σ_{Mx} has a value of 0.7, which is nearly the same as for a vertical plume. The M_y-data suggest a value of about 3.8 for C_D, which can be regarded as a drag coefficient.

Maximum Velocity and Excess Temperature. The maximum velocity U_m in the plume in crossflow, can be estimated as a function of s, if a self-preserving velocity distribution is assumed across the plume. Thus, the momentum flux M in the s-direction, given by
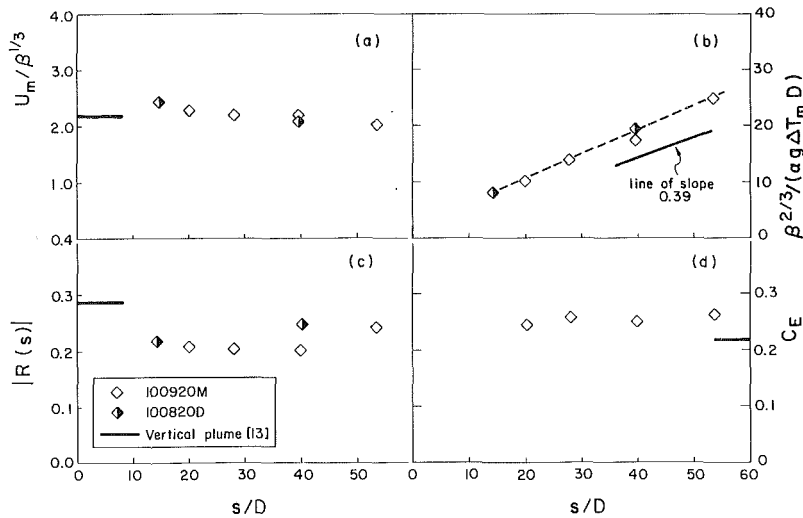
Fig. 4 Variation of centerline velocity, centerline excess temperature, Richardson number and entrainment coefficient, along the plume. Uncertainties: s/D: ± 0.070; U_m: ± 0.1; T_m: ± 1.2; $|R|$: ± 0.04; C_E: ± 0.017.

$$M = \frac{M_x}{\cos\theta} = \int_{n_{e1}}^{n_{e2}} \overline{U^2}\, dn \qquad (23)$$

can be expressed as

$$M = U_m^2 b_u \int_{n_{e1}/b_{u1}}^{n_{e2}/b_{u2}} \left(\frac{\bar{U}^2}{U_m^2} + \frac{\overline{u^2}}{U_m^2}\right) d\left(\frac{n}{b_u}\right)$$

$$= U_m^2 b_u I_2 \qquad (24)$$

where I_2 is a constant associated with the self-preserving profile integral. Hence,

$$U_m = \left[\frac{M}{b_u I_2}\right]^{1/2} = \left[\frac{\sigma_{Mx} s^*}{b_u I_2 \cos\theta}\right]^{1/2} \beta^{1/3}$$

or

$$U_m = \sigma_u \beta^{1/3} \qquad (25)$$

The coefficient σ_u depends, in principle, on the value of the parameter $\beta^{1/3}/U_a$ but can be expected to be a constant for a given value of $\beta^{1/3}/U_a$, if b_u increases linearly with s^*. Figure 4(a) shows the experimental data for U_m for the two buoyant jets studied. The maximum velocity is seen to remain nearly constant, the slight decrease in σ_u along s essentially being due to the increasing spreading rate (db_u/ds) with s (see Fig. 2(b)). The value of σ_u for the inclined plumes is not too different from the value of 2.16 for vertical plumes. This is probably because the increase in (db_u/ds) and the decrease in $\cos\theta$ relative to a vertical plume $(\theta = 0)$ tend to cancel each other in the flows studied.

The maximum excess temperature ΔT_m in a plume in crossflow, can be estimated from the heat flux H, with the assumption of self-preservation. One can, for example, write

$$H = \Delta T_m U_m b_u C I_2 \qquad (26)$$

where C is a scaling factor of the order of unity. Substituting $\beta = \alpha g\, H$ and $U_m = \sigma_u \beta^{1/3}$, one gets the linear relation

$$\frac{\beta^{2/3}}{\alpha g \Delta T_m} = \sigma_t \frac{s^*}{D} \qquad (27)$$

where $\sigma_t = \sigma_u C I_2 b_u/s^*$. Figure 4(b) showing the experimental data for the two buoyant jets indicates this linear variation. The coefficient σ_t, which is the slope of the decay line in this figure has a value of about 0.45, compared to the vertical-plume value of 0.39. This means that the inclined plumes decay slightly faster than the vertical plume. The specific value

of σ_t can, once again, be expected to be a function of the parameter $\beta^{1/3}/U_a$.

Axial Richardson Number. Using equations (17), (18), and (19), one can derive an expression for the axial Richardson number $R(s)$ defined in equation (13), for a plume in crossflow. Such an expression shows that R attains a constant value in an inclined plume and that this constant, like the other plume properties, depends on the parameter $\beta^{1/3}/U_a$ (or equivalently the angle of inclination of the plume trajectory, θ). Figure 4(c) shows the axial variation of the magnitude of R, estimated from equation (13) using the measured velocity and temperature distributions in the two buoyant-jet experiments. The scatter in the data is due to the presence of the cubic power in the expression for R. However, the data indicate that $|R|$ remains approximately constant along the flow. It is also seen that this value is lower than the value of 0.28 corresponding to the vertical plume. The result is thus consistent with the plume theory. In fact the results in Figs. 4(a), 4(b), 4(c) confirm that the two flows studied can be regarded as asymptotic plumes, over the measurement region. All the plume properties depend only on the value of the parameter $\beta^{1/3}/U_a$. If the buoyancy flux is conserved at all distances from the exit, this parameter becomes identical to $(K|R_j|^{1/3})$. However, since buoyancy flux may vary in the near field (because of the variation in α), the two parameters are usually different in practice. Nevertheless, one can use the latter parameter for approximately characterizing the inclined plume, since it is a known quantity in practical applications.

From the mass-flux data shown in Fig. 3(a), one can estimate the entrainment rate dQ/ds for the plume in crossflow. A coefficient of entrainment C_E can be defined in the usual way as

$$C_E = \frac{1}{U_m} \frac{dQ}{ds} \qquad (28)$$

Experimental results for C_E are shown in Fig. 4(d). It is seen that there is a significant increase (about 20 percent) in the entrainment rate relative to a vertical plume. The increase is primarily due to the action of the n-component buoyancy force and, to a much smaller extent, due to the presence of the (very small) edge velocity components U_{e1} and U_{e2}. This increased entrainment is responsible for the larger spreading rate and faster decay of the maximum excess temperature in the inclined plume.
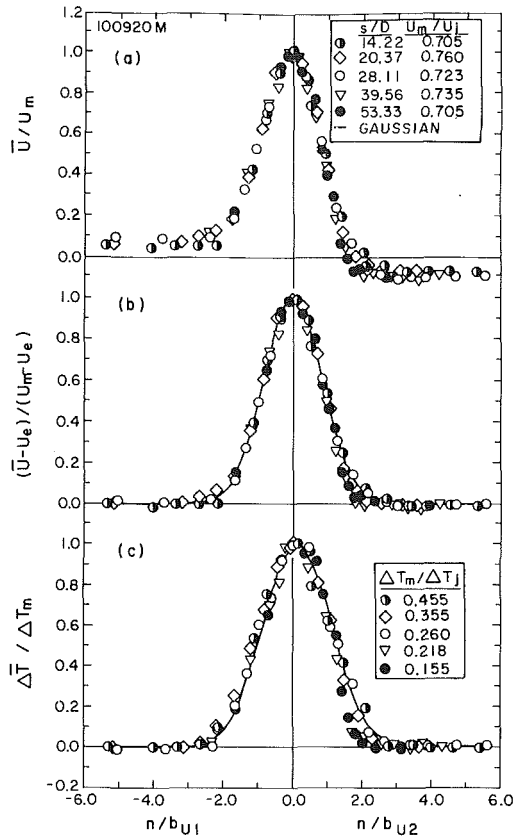
Fig. 5 Distributions of velocity and temperature across the plume. Uncertainties: n/b_u: ± 0.06; velocity: ± 0.015; temperature: ± 0.014.

Fig. 6 Variations of the global Richardson numbers along the plume. Uncertainties: s/D: ± 0.070; $\hat{R}_g$: ± 0.01.

Mean Velocity and Temperature Distributions. The s-component mean velocity profiles in the plume shown in Fig. 5(a) are seen to be nearly self-similar, but asymmetrical about the axis of the plume. One can observe small positive velocities at the outer edge and slight negative velocities at the inner edge of the plume. These are due to the crossflow and consequent inclination of the trajectory of the plume. The asymmetry disappears if the velocity profiles are plotted in defect coordinates as shown in Fig. 5(b). It is seen that the self-similar distributions are also nearly Gaussian, in spite of the presence of significant n-component buoyancy force. The distributions of excess mean temperature $\Delta \bar{T}$ normalized with respect to the maximum excess temperature ΔT_m are presented in Fig. 5(c). It is seen that the location of the maximum excess temperature is shifted slightly towards the inner portion of the plume. Also, the temperature profiles are seen to be nearly self-preserving and Gaussian (with the peak at $n/b_u \approx 0.07$), though not to the same extent as the velocity distributions.

Turbulence Properties. The effect of positive, axial buoyancy force on the turbulence structure in a plane vertical plume was studied in detail in [13]. Since the trajectory of the plume in crossflow is a straight line inclined at an angle to the vertical, there is an n-component of buoyancy force acting on the flow, in addition to the s-component. One would therefore expect to see additional effects on the turbulence structure brought about by the n-component buoyancy force. Because of the absence of any significant streamline curvature effects, it is possible to isolate the effects of this n-component buoyancy. From the distributions of the temperature excess presented earlier, it is seen that if a fluid particle momentarily attains a higher temperature (say, due to temperature fluctuations) it tends to travel upwards. In the lower part of the plume, this motion would bring the fluid particle to a warmer region,
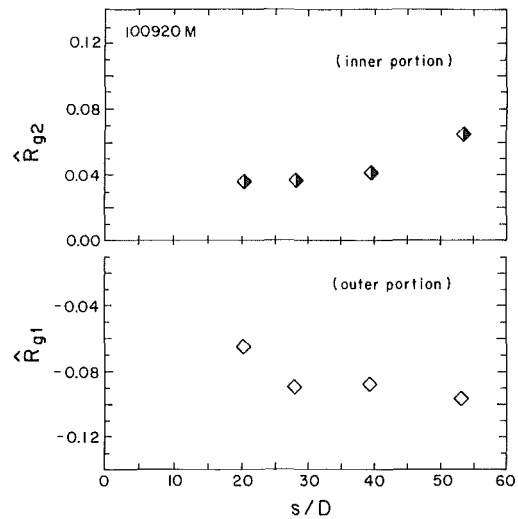
resulting in a n-component buoyancy force that would oppose the initial motion. This stabilizing effect inhibits turbulence. In the upper part of the plume, the n-component buoyancy has the opposite effect of augmenting turbulence. The effect of the n-component buoyancy force is characterized by a "gradient Richardson number" R_g defined as

$$R_g = -\frac{g \sin \theta (\partial \Delta \bar{T}/\partial n)}{\Delta \bar{T}(\partial \bar{U}/\partial n)^2} \qquad (29)$$

The gradient Richardson number is usually used as the parameter for characterizing buoyancy-driven shear flows. This is a locally defined quantity being evaluated at a particular point in flow field. It is, however, desirable to use, instead, a global buoyancy parameter for each portion of the plume. Such a parameter can be obtained from equation (29) itself, for a self-preserving flow, in terms of the scaling quantities ΔT_m, U_m, b_{u1}, and b_{u2} as

$$\hat{R}_{g1} = +\frac{\Delta \rho_m}{\rho_a}\frac{g b_{u1}}{U_m^2} \sin \theta \qquad (30)$$

and

$$\hat{R}_{g2} = -\frac{g \Delta \rho_m}{\rho_a}\frac{g b_{u2}}{U_m^2} \sin \theta \qquad (31)$$

for the upper and lower portions of the plume, respectively. The expressions for $\hat{R}_{g1}$ and $\hat{R}_{g2}$ can, in fact, be reduced to the familiar form

$$\hat{R}_{g1} = -\frac{Q_1^3}{M_1^3} \beta_1 \sin \theta \qquad (32)$$

$$\hat{R}_{g2} = +\frac{Q_2^3}{M_2^3} \beta_2 \sin \theta \qquad (33)$$

in terms of the fluxes through the upper and lower portions. Values of global gradient Richardson number along the flow 100920M are presented in Fig. 6. It is seen that $\hat{R}_g$ is, on the average, approximately -0.10 in the upper portion and about 0.05 in the lower portion.

The turbulence properties of the upper and lower portions of the plume are presented separately, in Figs. 7 and 8, using $(U_m - U_{e1})$ and $(U_m - U_{e2})$ respectively as the normalizing velocity scales. Note, however, that the edge velocities U_{e1} and U_{e2} are small. Since there is no mean excess temperature at the edges, ΔT_m is chosen as the temperature scale for normalization.
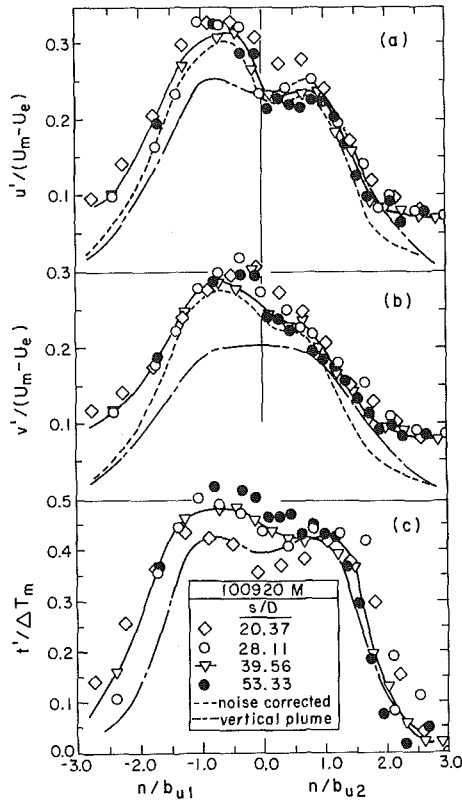
Fig. 7 Distributions of rms turbulence intensities across the plume.
Uncertainties: n/b_u: ±0.070; u': ±0.02; v': ±0.02; t': ±0.02.

Fig. 8 Distributions of the local Reynolds shear stress $-\overline{uv}$ and the turbulent heat fluxes $\overline{ut}$ and $\overline{vt}$. Uncertainties: n/b_u: ±0.070; $\overline{uv}$: ±0.3; $\overline{vt}$: ±0.3; $\overline{ut}$: ±0.3.

Figure 7 shows the distributions of the rms turbulence intensities u', v', and t'. The solid line drawn through a typical set of data at $s/D = 39.56$ indicates the data trend in each case. These data, after an approximate correction for noise, (see [13] for details), are shown by the dashed line in Figs. 7(a,b). It is seen that noise correction is not crucial to the interpretation of the experimental results. Results for the asymptotic vertical plume, from [13], are also shown in the figures for comparison. It is clear that the outer portion exhibits higher values of u' and the inner portion exhibits lower values than a vertical plume. Since there is almost no streamline curvature or significant edge velocity, this difference is essentially due to the n-component buoyancy. It also is seen from the figure that the region of turbulent flow is significantly wider in the outer portion and slightly narrower in the inner portion compared with the vertical plume. A reference to Fig. 5(b) shows that the s-component mean velocity in the plume, however, does not show significant difference between the outer and inner portions. The v'-distributions (Fig. 7(b)- in the outer portion also indicate an increase relative to the vertical plume. For example, the peak value of v' is about 30 percent higher than that in a vertical plume. The intensities of v' in the inner portion, however, do not show significant variation from the plane vertical plume. Also, as in the case of the s-component turbulence intensity, the turbulent region is wider in the outer portion and narrower in the inner portion. The t'-distributions shown in Fig. 7(c) generally exhibit the same trend as those of u' and v'.

The distribution of turbulent shear stress is shown and compared with vertical-plume results in Fig. 8(a). Note that since there is no correlation between the noise on the two channels of data, the shear stress results are not contaminated by noise to any significant extent. It is seen that the magnitude of the peak shear stress is increased by nearly 50 percent in the outer portion and decreased by nearly 35 percent in the inner portion, compared with the vertical plume. The increase in the
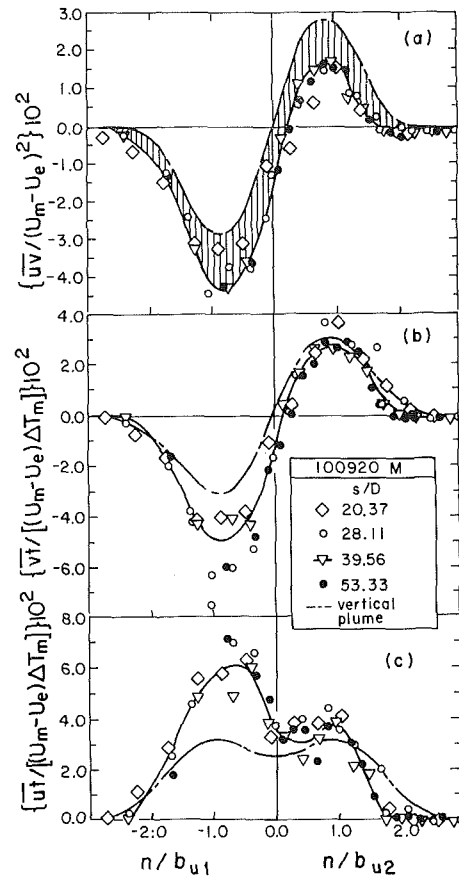
width of the turbulent region in the outer portion and its reduction in the inner portion are also clearly seen in this figure. It is also seen that the shear-stress goes to zero at a location shifted slightly inwards (downward) from the center. Lastly the location of maximum shear stress corresponds to $n/b_{u1} \approx -0.8$ for the outer portion and $n/b_{u2} \approx 1.0$ for the inner portion. Distribution of $\overline{ut}$ and $\overline{vt}$ (which are proportional to the s- and n-component turbulent heat fluxes) shown in Figs. 8(b) and (c) also indicate clearly the effects of the n-component buoyancy. The destabilizing effect in the outer portion is very large compared with the stabilizing effect in the inner portion.

The $\overline{ut}$-distributions in the two parts were separately integrated to obtain the corresponding turbulent heat fluxes h_1, h_2 and hence, the total turbulent heat flux h. Also, the corresponding total heat fluxes (mean plus turbulent) H_1, H_2, and H were evaluated. The results are shown in Fig. 9(a) and (b). It is seen that nearly equal amounts of total heat flux are transported through each portion of the plume. However, the turbulent heat flux forms a much larger percentage of the total flux in the outer portion than in the inner portion. The overall turbulent heat flux h is about 8 percent of the total flux through the jet. This is about twice the value observed in nonbuoyant jets [11] but is yet not large enough to invalidate boundary layer approximations.

Eddy viscosity and eddy thermal diffusivity calcualted from the above measurements showed that these quantities vary drastically across the inclined plume. These large variations are mostly caused by the shift in the zero shear-stress and zero heat-flux points from the axis towards the inner portion. Thus, constant eddy viscosity models are not strictly appropriate for these flows. Nevertheless, the general effect of n-
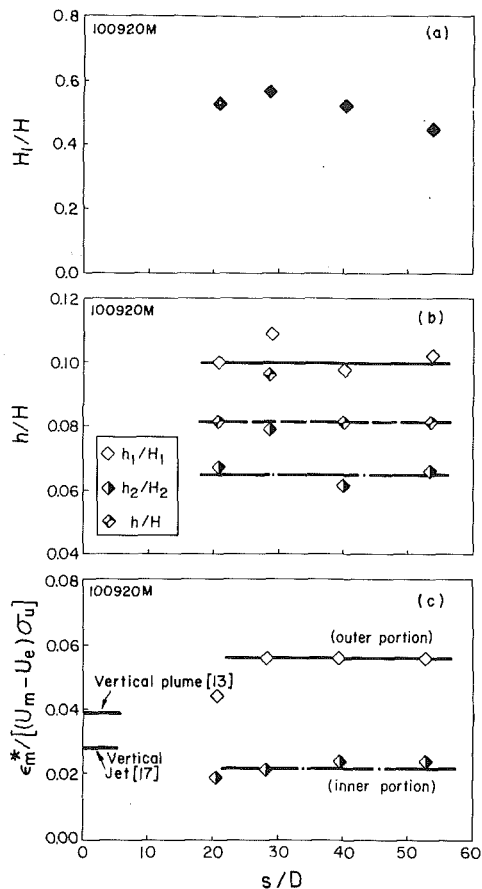
Fig. 9 Turbulent heat transport and eddy viscosity in the inclined plume. Uncertainties: s/D: ±0.070; H_1/H: ±0.028; h/H: ±0.005; ϵ_m^*: ±0.003.

Fig. 10 Spectra of $\overline{u^2}$, $\overline{v^2}$, and $\overline{t^2}$ in the inclined plume. Note that b_{u1} and b_{u2} are used for normalization for outer and inner sides respectively. Uncertainties: ordinate: ±2 percent; abscissa: ±10 percent.

component buoyancy on turbulent coefficients can be understood from Fig. 9(c), which shows the variation of eddy viscosity at the maximum shear-stress point along the jet. It is seen that the increase of the eddy viscosity in the outer portion and its decrease in the inner portion are both very large and are as much as 40 percent of the eddy viscosity in a vertical plume. The large decrease in the inner portion is in agreement with the results of Webster [15] for small positive (stable) values of gradient Richardson number. The large increase in the outer portion indicates that the eddy viscosity is also very sensitive to small negative (unstable) values of gradient Richardson number.

Turbulence Spectra. Typical spectra of $\overline{u^2}$, $\overline{v^2}$, and $\overline{t^2}$ for the flow 100820D are presented in Fig. 10(a), (b), (c) using as length scale, the value of b_u appropriate for each side, namely b_{u1} or b_{u2}. The spectra of s-component velocity and those of temperature fluctuations do not show drastic differences between the outer and inner portions, especially in the energy containing range. However, in the low wave number range, where the size of the eddy is larger than the velocity half width ($Wb_u < 1$), the inner portion of the jet exhibits larger contributions in the $\overline{u^2}$- and $\overline{t^2}$-spectra than the outer portion. One can see from the $\overline{t^2}$-spectra that the characteristic size of these large eddies is approximately 1.6 times the velocity half width b_u, corresponding to $Wb_u \approx 0.6$. The differential effect of buoyancy on the inner and outer portions of the jet are, however, most clearly seen from the $\overline{v^2}$-spectra. It is seen that the n-component buoyancy force reduces drastically, in the inner portion, the v-fluctuations in the low-wave number range, but increases them significantly in the energy containing wave number range (1–10), relative to the outer part. If the average
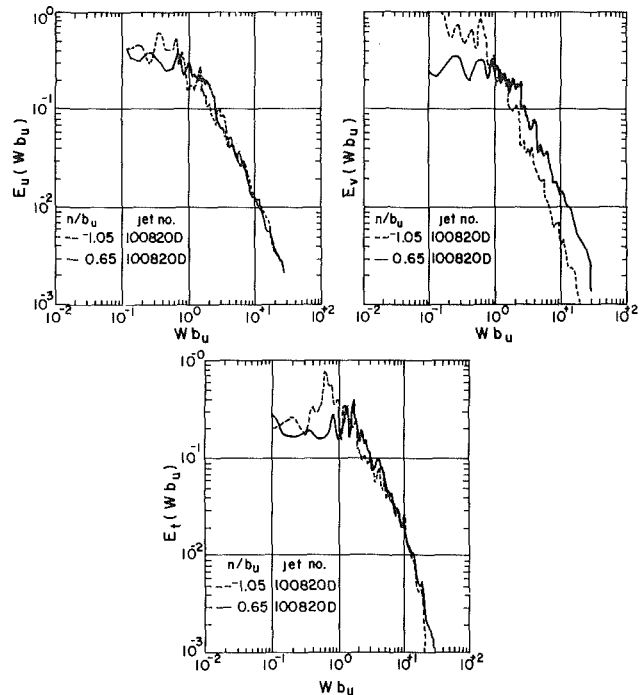
of the spectra for the outer and inner portion of the buoyant jet is considered, the effects of n-component buoyancy are nearly eliminated and the effects of s-component buoyancy are highlighted. Such a study shows that there is increased large-eddy ($Wb_u < 1$) activity due to the s-component buoyancy force. This agrees qualitatively with the results obtained in [13] for a vertical plume.

Conclusions

The present studies on two-dimensional buoyant jets in mild crossflow lead to the following conclusions.

1. Highly buoyant jets attain the plume state within a relatively short distance from the exit ($s/D < 20$ in the present experiments). In this buoyancy-dominated state, the plume trajectory is a straight line. The inclination of the trajectory depends on the parameter $\beta_j^{1/3}/U_a$, or equivalently, $(K|R_j|^{1/3})$. The spreading and entrainment rates of the plume in crossflow are higher than those of a vertical plume. The flow, however, exhibits near-selfsimilar distributions of mean and turbulent properties.

2. The maximum velocity, maximum temperature excess and axial Richardson number in plumes in crossflow behave very similar to their counterparts in vertical plumes except that σ_u, σ_t, and R have different values in the two cases. These values depend on the parameter $\beta^{1/3}/U_a$, or approximately on the parameter $(K|R_j|^{1/3})$.

3. The n-component buoyancy force causes the turbulent stresses and fluxes to increase in the upper part and decrease in the lower part of the inclined plume, relative to a vertical plume. The differential effect of the n-component buoyancy force on the two parts is also very clearly noticeable in the $\overline{v^2}$-spectra.

The experimental data have been documented in detail and are expected to be useful in the development and verification of complex turbulence models.

Acknowledgment

References

1 Wright, S. J., "Buoyant Jets in Density-Stratified Crossflow," *J. Hydr. Div.*, ASCE, Vol. 110, 1984, pp. 643–656.

2 Abramovich, G. N., *The Theory of Turbulent Jets*, M.I.T. Press, 1963.

3 Briggs, G. A., "Plume Rise," U.S. Atomic Energy Commission, Division of Technical Information, Oak Ridge, Tenn., 1969.

4 Slawson, P. R., and Csanady, G. T., "On the Mean Path of Buoyant, Bent-Over Chimney Plumes," *J. Fluid Mech.*, Vol. 28, 1967, p. 311.

5 Chu, V. H., and Goldberg, M. B., "Buoyant Forced Plumes in Crossflow," *J. Hydr. Div., ASCE*, Vol. 100, HY9, 1974, pp. 1203–1213. Div.

6 Escudier, M. P., "Aerodynamics of a Burning Turbulent Gas Jet in a Crossflow," *Combustion Science and Technology*, Vol. 28, 1967, pp. 293–301.

7 Launder, B. E., "On the Effects of a Gravitational Field on the Turbulent Transport of Heat and Momentum," *J. Fluid Mech.*, Vol. 67, 1975, pp. 569–581.

8 Patankar, S. V., Pratap, S. V., and Spalding, D. B., "Prediction of Turbulent Flow in Curved Pipes," *J. Fluid Mech.*, Vol. 67, 1975, p. 583.

9 Hwang, S. S., and Pletcher, R. H., "Prediction of Turbulent Jets and Plumes in Flowing Ambient," Technical Report, HTL-15, ERI-ISU-AMES-7903, Engineering Research Institute, Iowa State University, Ames, Iowa, 1978.

10 McGuirk, J. J., and Rodi, W., "A Depth-Averaged Mathematical Model of the Near Field of Side Discharge into Open-Channel Flow," *J. Fluid Mech.*, Vol. 86, 1978, pp. 761–781.

11 Haniu, H., and Ramaprian, B. R., "Studies on Two-Dimensional Curved Nonbuoyant Jets in Crossflow," ASME JOURNAL OF FLUIDS ENGINEERING, Vol. 111, Mar. 1989, pp. 78–86.

12 Ramaprian, B. R., and Chandrasekhara, M. S., "Study of Vertical Plane Turbulent Jets and Plumes," IIHR Report No. 257, University of Iowa, Iowa City, 1983.

13 Ramaprian, B. R., and Chandrasekhara, M. S., "Measurements in Vertical Plane Turbulent Plumes," ASME JOURNAL OF FLUIDS ENGINEERING, Vol. 111, Mar. 1989, pp. 69–77.

14 Ellison, T. H., "Turbulent Transport of Heat and Momentum from an Infinite Rough Plane," *J. Fluid Mech.*, Vol. 2, 1957, p. 456.

15 Webster, C. A. G., "An Experimental Study of Turbulence in a Density-Stratified Shear Flow," *J. Fluid Mech.*, Vol. 19, 1964, pp. 221–245.

16 Ramaprian, B. R., and Haniu, H., "Turbulence Measurements in Plane Jets and Plumes in Crossflow," IIHR Report No. 266, University of Iowa, 1983.

17 Ramaprian, B. R., and Chandrasekhara, M. S., "LDA Measurements in Plane Turbulent Jets," ASME JOURNAL OF FLUIDS ENGINEERING, Vol. 107, 1985, pp 264–271.

Y. Lecointe

J. Piquet

CFD Group,
Laboratoire d'Hydrodynamique Navale,
UA 1217, ENSM, 1 44072 Nantes Cedex,
France

Flow Structure in the Wake of an Oscillating Cylinder

The numerical solution of the unsteady two-dimensional Navier-Stokes equations is used to investigate the vortex-shedding characteristics behind a circular cylinder immersed in a uniform stream and performing superimposed in-line or transversed oscillations of a given reduced amplitude.

1 Introduction

The unsteady bluff body flow has received a great deal of attention especially for the prediction of the loads on engineering structures such as ocean pipelines or risers, offshore-platform supports, bridge piers or smoke stacks. Although numerical computations based on the unsteady Navier-Stokes equations are restricted to laminar flows at low Reynolds number, they offer a valuable tool to understand the structure of the above mentioned flows at a level of detail and with a volume of simultaneous information not attainable with experimental techniques.

In the following, attention is focussed on the mechanisms of unsteady separation and vortex shedding past an oscillating circular cylinder. The circular cylinder is immersed in a uniform flow for several values of the Reynolds number. Oscillations can be either in line or transverse at a frequency close to the Strouhal frequency or close to a harmonic of it. The effects of the Reynolds number $Re = U_\infty D/\nu$, of the reduced frequency $F = f_c D/U_\infty$ and of the reduced amplitude a/D of the oscillations on the laminar periodic or quasiperiodic wake evolution are studied.

Our purpose is to investigate several types of modifications of the near-wake structure that occur when the reduced frequency F is close to the free vortex shedding frequency S_0 (corresponding to a fixed cylinder), both for in-line and transverse rectilinear motions. The numerical solution of the unsteady two-dimensional Navier-Stokes equations which is used rests on the vorticity streamfunction formulation and thus differs from the two previous similar studies [1], [2] which use the pressure-velocity formulation. Detailed features of the numerical method and systematic validations have been outlined in [3], [4]; therefore section 2 only briefly summarizes the equations, the numerics and its validation. The study of the unsteady wake behind a circular cylinder is then considered, both for transverse (section 3) and in line (section 4) superimposed motions.

2 The Equations and the Numerics

The body B is a circular shaped cylinder, the axis $\mathbf{k}$ of which is orthogonal to the plane of the flow induced by a (uniform) oncoming stream $U_\infty \mathbf{i}$. B has a motion characterized by its translation velocity $\mathbf{u_B}$ in an absolute frame so that the veloci-

ty $\mathbf{V}$ with respect to the body is connected to the absolute velocity $\mathbf{V_a}$ by (1)

$$\mathbf{V_a} = \mathbf{U_B} + \mathbf{V}. \tag{1}$$

Streamlines defined by $\mathbf{dr} \times \mathbf{V_a} = 0$ are therefore not invariant with respect to a change of frame so that streamline patterns in different frames differ from each other. The body contour being a relative streamline, the relative frame is the most convenient to discuss flow separation (although the definition of separation in the steady state $\zeta = 0$; $d\zeta/ds < 0$ does not hold since the flow is still time dependent in the relative frame). Therefore, understanding of events constituting the shedding phenomenon and determining the evolution of forces and moments will be easier in this relative frame. A direct consequence of (1) is that vorticity fields are identical $\mathbf{curl}\ \mathbf{V_a} = \mathbf{curl}\ \mathbf{V}$ so that equivorticity patterns are invariant. After a conformal mapping, the Navier-Stokes equations can be written in the computational plane $Z = \lambda + i\eta$:

$$g\zeta_t - \psi_\eta \zeta_\lambda + \psi_\lambda \zeta_\eta = (2/\text{Re})\nabla^2 \zeta; \quad \nabla^2 \psi + g\zeta = 0 \tag{2}$$

ψ is the relative streamfunction such that $\mathbf{V} = \mathbf{curl}\ (\psi \mathbf{k})$, $\mathbf{curl}\ \mathbf{V} = \zeta \mathbf{k}$; $g(Z) = (dz/dZ)^2$ $(z = x + iy)$ is the square of the Jacobian of the transformation; for a circular cylinder $g = \exp(2\lambda)$. Physical components of the velocity (u-radial, v-circumferential) result from $u = -g^{-1/2}\psi_\eta$; $v = g^{-1/2}\psi_\lambda$. In the computational Z-domain, the wall boundary is specified by the line $\lambda = 0$ and the mesh is of O-type. The factor $2/\text{Re}$ comes from the fact that lengths are nondimensionalized with the radius of the cylinder in the computational domain while Re is defined with the diameter.

Several numerical schemes have been tested. The spatial discretization of the vorticity equation is of compact type: an upwind conservative scheme with second order corrections (UCh^2) or a centered conservative scheme (CCh^2) can be used with an ADI Peaceman Rachford time discretization [5]. The Poisson equation is solved by an optimized ADI method, the convergence of which rests on the predetermination of optimized parameters [6]. The spatial discretization is of the so-called "Operator Compact Implicit" type [3], [7] so that fourth order accuracy on ψ is obtained.

Detailed features of the schemes and systematic comparisons have been outlined in [3] where test problems include the impulsively started circular cylinder problem (Re = 200, 550) (symmetric flow) and the problem of vortex shedding behind a circular cylinder with or without superimposed oscillations at Re = 200. Fourth order accurate schemes were

proved to lead to the best results especially for long time resolutions as indicated by the value of the Strouhal number S_0; but only second order schemes were able to provide numerical solutions at high Re. This was evidenced for the symmetric flow past an impulsively started circular cylinder both at Re = 3000 and Re = 9500 [8]. For the free vortex shedding problem (unsymmetric flow) it was found that second order conservative schemes needed a higher grid resolution that fourth order schemes [4] but the inherent robustness of their conservative form allowed their systematic use in this work. Also, because tests for upwinding are either avoided (CCh^2) or simpler (UCh^2) than with fourth order accurate

order 1 percent). The amplitudes a_n indicate the relative amount of each term of the decomposition with respect to the fundamental contribution $n=0$ from which the Strouhal frequency is found.

3 Transverse Superimposed Vibration

3.1 Unsteady Laminar Wake of a Circular Cylinder. The subject of unsteady bluff body flow has received a great deal of attention as reported in several review paper [10], [11]. The case Re = 200 has been mainly considered in the following as it

Table 1

Re	S_0	C_x	C_y	C_M	grid $r x \theta$	Δt	r_∞	test
140	0.18	1.28 ± 0.02	± 0.356	± 0.017	151×151	.01	80	(a)
200	0.2	1.27 ± 0.04	± 0.55	± 0.024	151×101	.025	60	(b)
"	0.2	1.26 ± 0.038	± 0.52	± 0.024	151×101	.01	80	(c)
"	0.2	1.32 ± 0.064	± 0.74	± 0.026	151×101	.025	100	(d)
"	0.195	1.29 ± 0.04	± 0.60	± 0.0245	301×361	.005	110	(e)
500	0.226	1.35 ± 0.14	± 1.012	± 0.043	151×151	.01	80	(f)
855	0.236	1.44 ± 0.23	± 1.30	± 0.053	151×151	.01	100	(g)
1000	0.240	1.5 ± 0.25	± 1.38	± 0.058	151×151	.01	80	(h)
2000	0.266	1.62 ± 0.277	± 1.58	± 0.072	301×361	.005	110	(i)

schemes, the speed-up ratio on vector processing machines with respect to scalar ones can be made higher.

The outputs of the numerical computation are analyzed by means of an harmonic analysis in which functions of time are identified with the following form:

$$f(t) = A \sum_{n=0}^{N} a_n \cos[2\pi f_n (t' - t'_a) + \phi_n]$$

$$= A \sum_{n=0}^{N} a_n \cos[\pi S_n (t - t_a) + \phi_n], \quad n = 0, \ldots, N \quad (3)$$

where $t' = tU_\infty/R$; $S_n = f_n \cdot D/U_\infty$; $D = 2R$; $a_0 = 1$; $N < 3$ usually; f_n are the frequencies of the numerical signal while the phase angles are determined within an arbitrary constant so that only phase shifts are significant. The identification of the signal is performed for $t_a \leq t \leq t_b$ following the procedure [9]. Therefore frequencies less than $F_k = 2/(t_b - t_a)$ cannot be validated while frequencies which differ by less than $2F_k$ cannot be distinguished. Nevertheless, the identification of the frequencies occurring is very accurate (usually the error is of

corresponds to the highest Reynolds number for which the wake of the cylinder remains laminar. In the case of a classical free vortex shedding (no superimposed motion) the lift coefficient C_y and the moment coefficient C_M oscillate at the
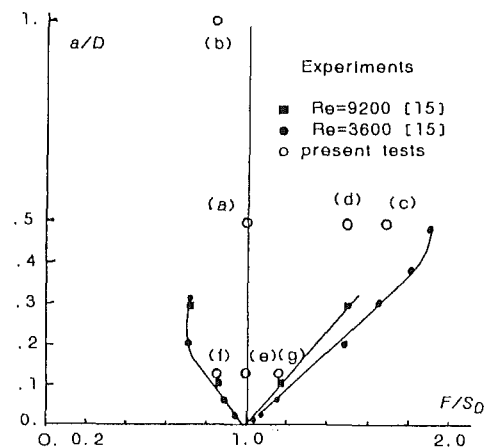
Fig. 1   Primary locking-on zone

———— Nomenclature ————

a = amplitude of the superimposed motion

a = subscript = refer to an absolute frame

C_x = drag coefficient = $2\mathbf{F} \cdot \mathbf{i}/\rho DU_\infty^2$

C_y = lift coefficient = $2\mathbf{F} \cdot \mathbf{j}/\rho DU_\infty^2$

C_M = moment coefficient = $2\mathbf{M} \cdot \mathbf{k}/\rho D^2 U_\infty^2$

D = diameter of the cylinder

F = reduced frequency of the motion ($= f_c D/U_\infty$)

f_c = frequency of the motion

f_0 = recovering frequency

$\mathbf{i},\mathbf{j}$ = unit vectors in the plane of the cylinder

$\mathbf{k}$ = $\mathbf{i} \mathbf{x} \mathbf{j}$

Re = Reynolds number = $U_\infty D/\nu$

r_∞ = number of diameters of the far field boundary

S_0 = Strouhal number

t = adimensionalized time (with $D/2U_\infty$)

T_e = ($= F^{-1}$) adimensional period of the motion

t_a, t_b = bounds for the time frequency analysis

t_p = time when the motion is set in

u, v = radial and circumferential relative velocity components

$U_\infty \mathbf{i}$ = free stream velocity

y_{min} = maximum negative transverse displacement of the cylinder

Δt = adimensional time step

ψ = relative streamfunction

ζ = vorticity

ζ_{wr} = wall vorticity on the rear axis of the cylinder

Table 2

a/D	F	C_x	C_y	C_M	Δt	r_∞	case
		Re $=200$, grid 151×151 (except (a): 151×101)					
.5	.2	$1.82 \pm .55$	± 2.9	$\pm .1$	.025	100	(a) LU
1.	.17	$1.95 \pm .75$	± 1.55	$\pm .11$	.0125	80	(b) L
.5	.34	$1.86 \pm .44$	± 4.9	$\pm .17$	.01	80	(c)
		Re $=500$: grid 151×151					
.5	.34	$1.84 \pm .5$	± 4.1	$\pm .14$	.01	80	(d) L
		Re $=855$: grid 151×101					
.13	.24	$1.62 \pm .36$	± 1.35	$\pm .06$	.01	100	(e) LU
.13	.205	lock-on boundaries			.01	100	(f)
.13	.282				.01	100	(g)
.13	.12	$1.48 \pm .27$	± 1.24	$\pm .06$	.01	100	(h)
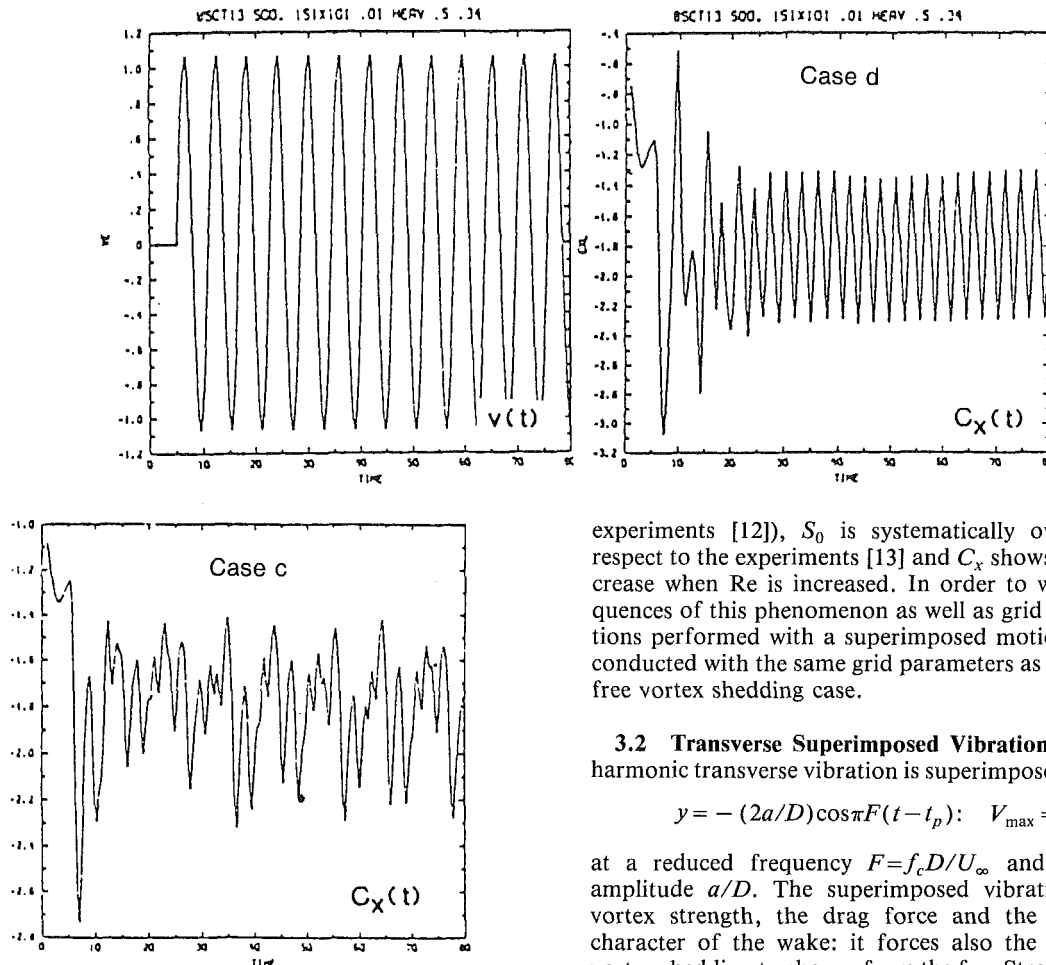
Fig. 2 Reordering phenomenon comparison of $C_x(t)$ between two values of Re tests (c), (d)

Strouhal frequency S_0 while the drag coefficient C_x oscillates at $2S_0$. Table 1 gives the value of S_0 together with the levels of C_x, C_y, C_M for several values of Re and for several grids:

Comparisons with other retained parameters in tests (b) to (e) show that r_∞ is too low in (b) and that Δt is too high in (d). A correct picture of the improvement resulting from increased grid resolution is provided comparing (c) and (e). It indicates that the convergence on S_0 is rather from above if the values of S_0 are systematically computed from C_x, the frequency coherence of the wake being improved with the grid resolution.

Taken as a whole, tests (a) to (i) indicate that the discrepancy between computations and experiments increases with Re and with the three-dimensionality of the flow. While computed results are correct for Re $= 200$ ($\bar{C}_x = 1.29$ according to

experiments [12]), S_0 is systematically overpredicted with respect to the experiments [13] and C_x shows an unrealistic increase when Re is increased. In order to weaken the consequences of this phenomenon as well as grid effects, computations performed with a superimposed motion will be usually conducted with the same grid parameters as those used for the free vortex shedding case.

3.2 Transverse Superimposed Vibration. The following harmonic transverse vibration is superimposed for $t \geq t_p$:

$$y = -(2a/D)\cos \pi F(t-t_p): \quad V_{\max} = 2\pi aF/D \qquad (4)$$

at a reduced frequency $F = f_c D/U_\infty$ and with a reduced amplitude a/D. The superimposed vibration increases the vortex strength, the drag force and the two dimensional character of the wake: it forces also the frequency of the vortex shedding to change from the free Strouhal frequency S_0 to the cylinder heaving frequency F. This lock-on effect [12], [13] is apparent from C_y and C_M which oscillates at F while C_x oscillates at $2F$. In the plane (F/S_0, a/D), the synchronization zone has usually a triangular shape peaking at $F/S_0 = 1$, $a/D = 0$ and broadening when a/D increases: Fig. 1 indicates that the boundaries of this zone depends slightly on Re [13] and gathers the set of performed tests the parameters of which are given in Table 2.

Tests (a) and (b) are fully locked-on (L) with odd harmonics on $C_y \cdot C_M$ and ζ_{wr}—the wall vorticity on the rear axis of the cylinder—and a 4F harmonic on C_x. Both are aerodynamically stable [16] but, for (a) which is not fully established (U), the drag amplification is underestimated by a factor of 2 (as in [1], [2]) with respect to experiments [17] at Re $= 144$. Reasons for this discrepancy are under investigation.

The influence of Re is studied in tests (c) and (d) at $F = 1.7S_0$. The drag coefficient (Fig. 2) oscillates classically at
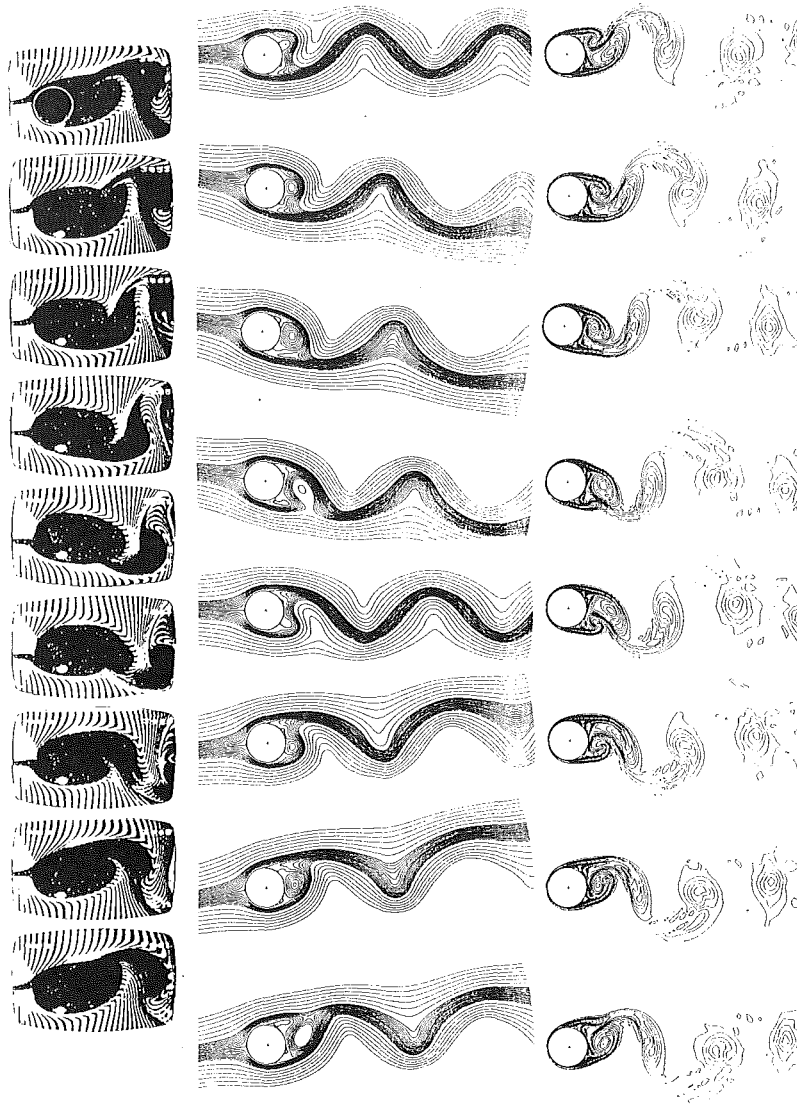
Fig. 3 Sequence of relative streamlines and isovorticity plots. Transverse motion.

$2F$ with a 28.6 percent harmonic at $4F$ in (d). Because $(F/S_0)_{min}$ value is farther from 1 at Re = 200 than at Re = 500, the drag evolution (Fig. 2) is more complex in (c): the fundamental oscillation is at $2F$ but a 95 percent harmonic is present at a resonant frequency $S_R = S_0$ which corresponds to a frequency recovery allowed by the large scale vortex formation in the wake. Such a large scale motion is well evidenced from streamline plots presented in [18] which indicate no coalescence, at least in the near wake. Other significant contributions involve the interaction of harmonics of F and S_R as well as another component at $f = .091 \cong S_R/2$ [16].

Test (e) is at $F = S_0$ and is not fully established (U). Lock-on is found (L) and the motion leads the lift (which peaks about 1.35 in agreement with experiments [19]) by 32 deg. (In agreement with [20]) and the moment lags the motion by 27.5 deg. A characteristic shortening of the vortex length of shedding is evidenced from iso $-\psi$ and iso $-\zeta$ lines (Fig. 3) which can be compared with hydrogen bubble visualizations [19].

Tests (f) and (g), respectively, refer to the lower and upper primary lock-on boundaries: $F/S_0 = .85$ and $F/S_0 = 1.17$. An harmonic analysis—with a Nyquist frequency of .04—shows that a beating mechanism controls the shedding in test (f): the leading frequency is at $f_0 = .23$ which controls C_y, C_M and ζ_{wr} while C_x oscillates at $2f_0$ with a significant harmonic at $F + f_0$

(57 percent) and an important (nonvalid with respect to F_K) "slow" component at .02 which confirms that forces are not yet fully established (Fig. 4). ζ_{wr} shows also several harmonics, particularly at $3f_0$ and at .16 (21 percent). Far field results [16] are omitted here because the grid appears systematically too coarse in the downstream wake so that important dispersion errors occur more than two diameters away from the cylinder.

The frequency analysis of test (g) is performed on the window [17.6, 140]. It indicates that the motion is controlled by F and by a recovering frequency $f_0 = .049 \cong F/6$: C_x oscillates at f_0 with harmonics at $2F - 2f_0$ (72.2 percent), $2F - f_0$ (63.2 percent), $2F - 3f_0$ (25.6 percent), $2F$(24.6 percent), $f_1 = .105$ (10.2 percent) and lower amplitude harmonics at $F - 4f_0$, $3f_0$, $2F - 5f_0$ and $2F - 4f_0$. C_y, C_M and ζ_{wr} are controlled by $F - f_0$ with significant harmonics on C_y at F (72.5 percent) and at $F - 2f_0$ (10.7 percent): on C_M at F (55.3 percent) and on ζ_{wr} at $F - 2f_0$ (42.5 percent), $3F - 2f_0$, (37.6 percent), F (28.9 percent), $3F - f_0$ (19.2 percent), $3F - 5f_0$ (15.4 percent), 0.587 (14.1 percent), $3F - 4f_0$ (13.4 percent). Force evolutions (Fig. 5) are very similar to those of Fig. 4 and the effect of the f_0 frequency is here again evidenced.

Test (h) is characteristic of subharmonic synchronization where the shedding frequency being at S_0, four vortices per cycle are shed.
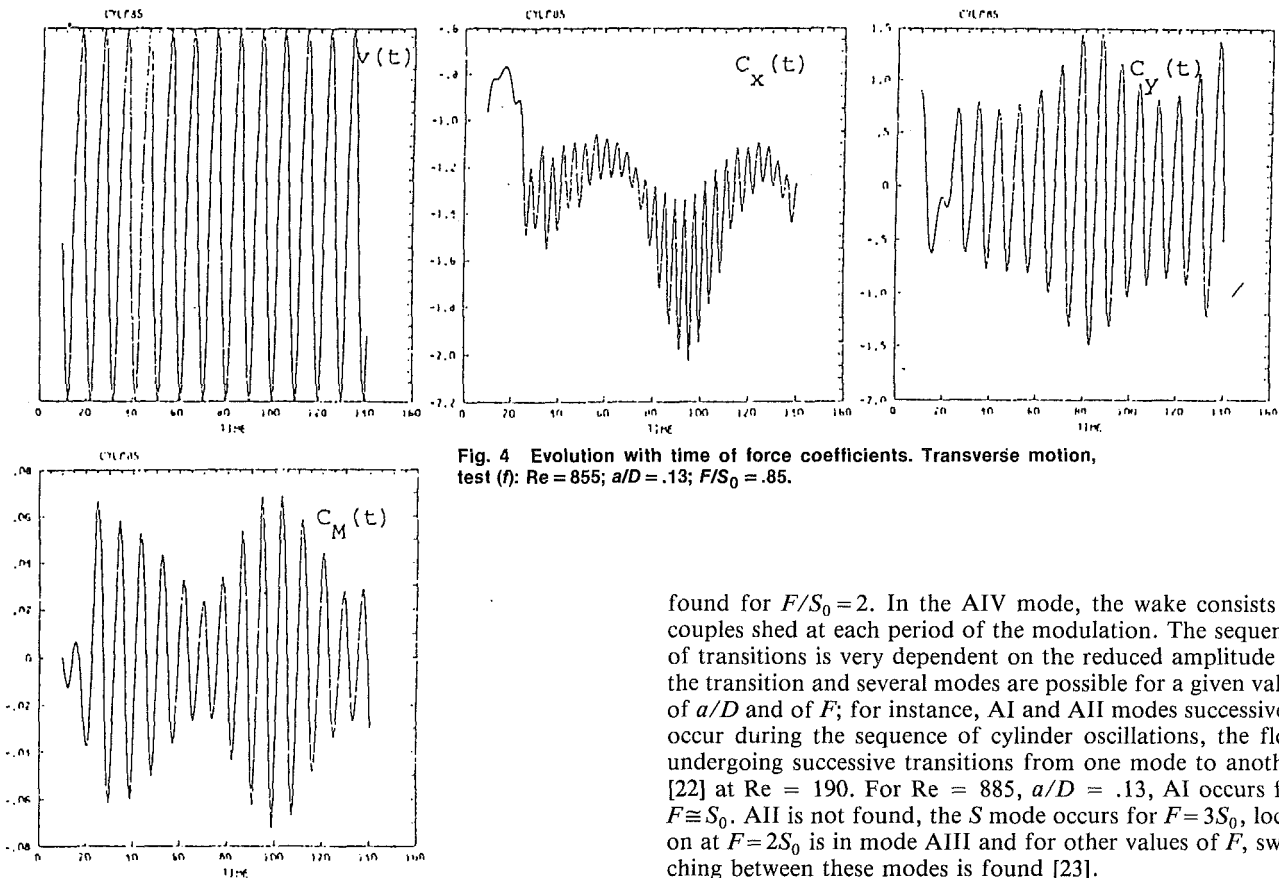
Fig. 4 Evolution with time of force coefficients. Transverse motion, test (f): Re = 855; a/D = .13; F/S₀ = .85.

$$Re = 855; \quad a/D = .13; \quad F/S_0 = .85$$

4 In-Line Motion

The in-line motion, which is set in at $t = t_p$, is defined by

$$x = -(2a/D)\cos \pi F(t-t_p); \quad U_{max} = 2\pi Fa/D \qquad (5)$$

In this case, experiments indicate also the existence of a lock-on regime: several types of instability are known depending on the values of the reduced frequency and, eventually, of the reduced amplitude [21]. (*i*) *the symmetric mode S* for which a pair of vortices is shed in phase from both sides of the cylinder during one oscillation cycle. This was confirmed by numerical experiments [4] at Re = 200 for moderate or high reduced amplitude (e.g., > .5), the stability of the symmetric mode increasing with the reduced amplitude. (ii) *the antisymmetric mode AI* for which two vortices are shed from alternate sides of the cylinder during one cycle of the cylinder's motion—as in the case of a transverse motion—and is often found for $F < 2S_0$. (iii) *the antisymmetric mode AII* is similar to AI but the period of the vortex pattern is $2T_e$ as shedding of two successively antisymmetric vortices requires two cycles T_e of cylinder motion. This mode is rather found for $F \cong S_0$ in [22] and the lock-on frequency in then $F/2$; it is also found for $F > 2S_0$ in [1], [4] but for low Re and low reduced amplitudes. *Modes AIII and AIV* involve the formation of counterrotating pairs and occur only at the boundary between symmetric and antisymmetric modes. When the vibration amplitude is too high to allow an alternate pattern, "vortex fission" becomes possible with the decrease to zero of the transverse spacing of the street in mode AII [22]. In the AIII mode, a single counterclockwise vortex is shed during one cycle while two clockwise vortices are shed during alternate cycles; this happens as a consequence of the transition between the so-called AIV mode found for F/S_0 around 1 and the symmetric mode

found for $F/S_0 = 2$. In the AIV mode, the wake consists in couples shed at each period of the modulation. The sequence of transitions is very dependent on the reduced amplitude of the transition and several modes are possible for a given value of a/D and of F; for instance, AI and AII modes successively occur during the sequence of cylinder oscillations, the flow undergoing successive transitions from one mode to another [22] at Re = 190. For Re = 885, a/D = .13, AI occurs for $F \cong S_0$. AII is not found, the S mode occurs for $F = 3S_0$, lock-on at $F = 2S_0$ is in mode AIII and for other values of F, switching between these modes is found [23].

In order to investigate the effect of reduced frequency close to a subharmonic of $2S_0$, new tests have been performed with a 151×101 mesh $\Delta t = .0125$; $r_\infty = 80$ at $F = .16$; $a/D = .25$; Re = 200. The results appear to lead in this case to an asymmetric shedding and the flow does not evolve back to a symmetric wake flow as can be seen from Fig. 6 which depicts the evolution with time of force coefficients. Lock-on is still found but, while C_x oscillates classically at F with an harmonic of 12 percent at $2F$; C_y, C_M, ζ_{wr} oscillate also at F (instead of $F/2$) with harmonics at $2F$ (26.5 percent for C_y 33.8 percent for C_M, 9.6 percent for ζ_{wr}) and $3F$ (5.9 percent for C_y, 6.3 percent for C_M). These results which confirm the time evolution of forces are enlightened by the consideration of streamline plots which are shown in Fig. 7 for $96.88 \leq t \leq 109.38$. The fact that the asymmetry has been initially triggered by a pitching motion of the cylinder [3] is not forgotten: the bubble to be shed is always generated on the same rearside of the cylinder but if the pitching destabilizing motion was reversed, the bubble would be shed from the other rearside.

For $F > 2S_0$ only one vortice per cycle is shed leading to the antisymmetric mode AII downstream of the cylinder but only if the reduced amplitude a/D is low enough (e.g., $0.1 - 0.3$) [1], [4]. More striking is the fact that for moderate reduced amplitudes ($a/D = .5$, Re = 200), a symmetric shedding similar to that found for $F < 2S_0$ is obtained [4]. Moreover this symmetric pattern is stable in the sense that if the computation is started frm an asymmetric pattern, the solution evolves backs to a symmetric wake flow.

Table 3 gathers the set of tests performed for Re = 855; $a/D = .13$; $\Delta t = .01$; $r_\infty = 110$ [23].

We focus only on the main results of the analysis, further details on the force evolutions and on the harmonic analysis of the wake being given in [16]. For case (*a*)-harmonic excitation at .48-, lock-on occurs in the AIII mode: C_x oscillates at F while C_y, C_M and ζ_{wr}, oscillates at $F/2$. Figure 8 compares the computed relative streamline and isovorticity plots with
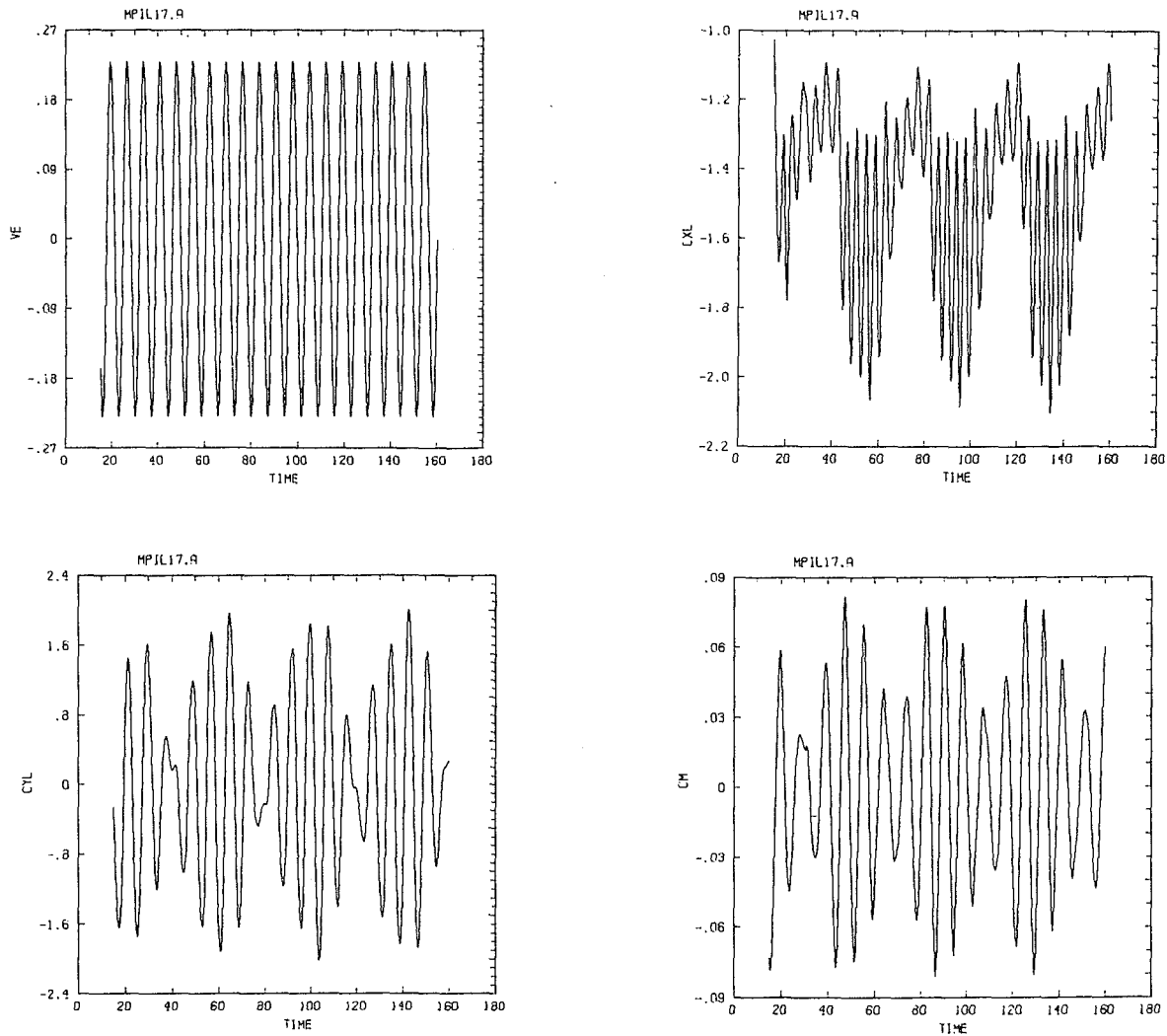
Fig. 5 Evolution with time of force coefficients. Transverse motion,
test (g): Re = 855; a/D = .13; F/S₀ = 1.17.

hydrogen bubble visualizations [23] for $75.63 \le t \le 82.63$. The sequence starts once a vortex has been shed on the upper side of the cylinder at its maximum negative upstream position. As the cylinder moves downstream, a second vortex is formed as the cylinder passes through its maximum positive downstream position and changes direction ($76 \le t \le 77$). This shedding of two vortices from the upper side is followed by the formation of a single vortex on the lower side ($t \cong 78$). The completion of this single vortex formation and its downstream convection follows for $79 \le t \le 85$, $t - 81.13$ corresponding to the maximum upstream position of the cylinder. The frequency analysis of forces in the case (b) indicates that, while C_x oscillates at F, a frequency recovery at $f_0 = 2F/5 = .096$ is well evidenced, force plots exhibiting a somewhat erratic behavior [16]. In case (c), lock-on is found on C_x which lags the motion by 30 deg. Starting from a nonsymmetric situation, the flow evolves towards symmetric shedding in agreement with experiments (Fig. 9). The outputs of case (d) are frequency analyzed with the window $64.5 \le t \le 187.3$, C_x oscillates at F and lags the motion by 102 deg. A frequency recovery is found at $f_0 = .278$ as C_y and ζ_{wr} oscillate at $F - f_0$ and C_M at f_0. C_y presents several harmonics at f_0 (93 percent), $2F - f_0$ (45.5 percent), $3f_0 - F$ (38.8 percent), $3(F - f_0)$ (31.4 percent), $f_1 = .165$ (22 percent). For C_M, $F - F_0$ (99.4 percent), $3(F - f_0)$ (32 percent) and f_1 (18 percent) are found. Mode competition is

Table 3 In line cases

F/S_0	C_x	C_y	C_M	case
2	long time behavior			(a)
1	$1.15 \pm .75$	± 1.6	$\pm .065$	(b)
3	$1. \pm 4.$	low amplitudes		(c)
2.2	short term synchroniz.			(d)

demonstrated from the evolution with time of lift, moment coefficients, velocity components and vorticity in the near wake (Fig. 10) where low levels of oscillations indicate the predominance of the S mode, 19 oscillations between predominant AII modes being evidenced, in agreement with [23].

5 Conclusion

Synchronization, which is characterized by the fact that the vortex formation is locked to the cylinder motion takes two basic forms. One which is subharmonic synchronization has been well evidenced for in-line motions: the initially formed vortex is always from the same side of the body. The other is fundamental synchronization, it involves successive vortex
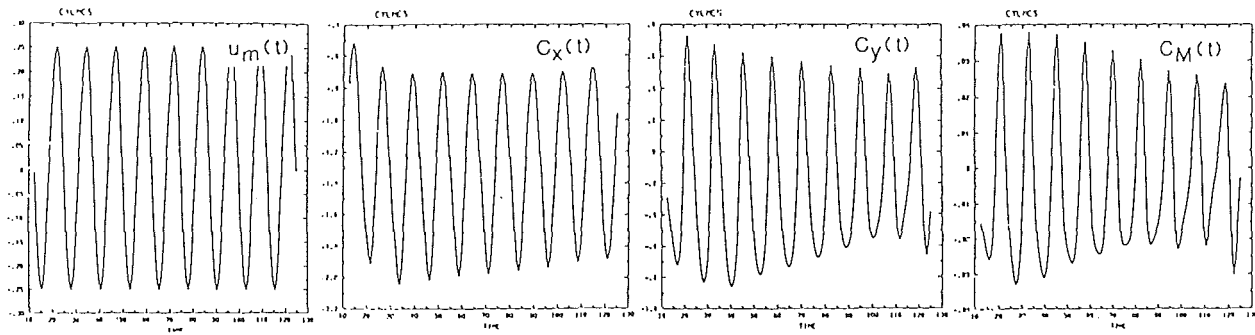
Fig. 6 Evolution with time of force coefficients. In-line motion Case
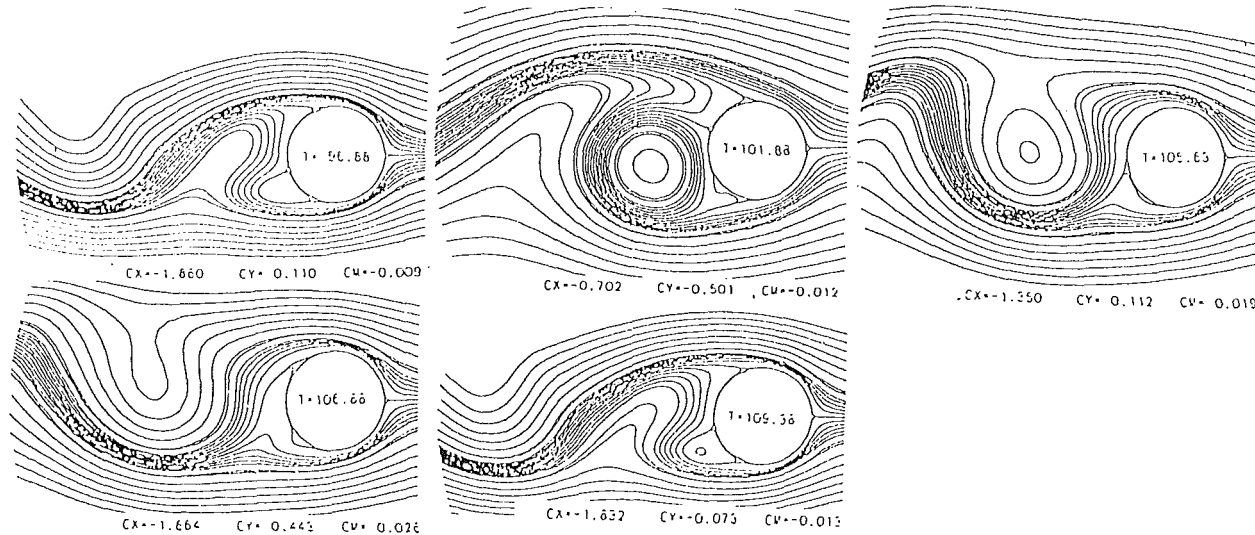**Re = 200; a/D = .25; F/S₀ = .8.**

Fig. 7 Sequence of relative streamline plots. In-line motion; Re = 200.

shedding from either side of the cylinder. For transverse oscillations, excitations at frequencies well separated from the free vortex shedding frequency produce a recovering frequency S_R which can be identified as one of the dominant frequencies apparent from the harmonic analysis. S_R is significantly different from the free vortex shedding frequency S_0. Therefore a numerical confirmation of results [19] has been obtained. Particularly remarkable is the occurrence, for in-line oscillations, of several modes for the vortex shedding which have been found experimentally [23] as well as numerically. For nonharmonic excitations, mode competition has been clearly demonstrated. To give an idea of the involved cpu's, the computational effort on Cray2 (CFT77 1.2 compiler) is $6.76 \; 10^{-6}$ s per point and time step (computed from case (e) : section 3.1).

Acknowledgments

References

1 Hurlbut, S. E., Spaulding, M. L., and White, F. M., "Numerical Solution for Laminar Two-dimensional Flow About a Cylinder Oscillating in a Uniform Stream," ASME JOURNAL OF FLUIDS ENGINEERING, Vol. 104, 1982, pp. 214–222.

2 Chilukuri, R., "Incompressible Laminar Flow Past a Transversely Vibrating Cylinder," ASME JOURNAL OF FLUIDS ENGINEERING, Vol. 109, 1987, pp. 166–171.

3 Lecointe, Y., and Piquet, J., "On the Use of Several Compact Methods for the Study of Unsteady Incompressible Viscous Flow around Circular Cylinders," Comp. and Fluids, Vol. 12, No. 4, 1984, pp. 255–280.

4 Lecointe, Y., and Piquet, J., "Compact Finite-Difference Methods for Solving Incompressible Navier-Stokes Equations around Oscillating Bodies," Von Karman Lecture Series 1985-04, Computational Fluid Dynamics: 210 pages.

5 Daube, O., and Ta Phuoc, L., "Etude numérique d'écoulements instationnaires de fluides visqueux incompressibles autour de corps profilés par une méthode combinée d'ordre $O(h^2)$ et $O(h^4)$," Journ. Méca., Vol. 17, 1978, pp. 651–678.

6 Wachpress, E., Iterative Solution of Elliptic Systems and Applications to the Neutron Diffusion Equations of Reactor Physics, ed., Prentice Hall, Englewood Cliffs, 1966.

7 Berger, A. E., Solomon, J. M., Clement, M., Leventhal, S. H., and Weinberg, B. C., "On Generalized OCI schemes for Boundary Layer Problems," Maths. of Comp., Vol. 35, pp. 695–731.

8 Lecointe, Y., and Piquet, J., "Numerical Solution of Unsteady Incompressible Viscous Flow Around Bodies," Proc. Third Symp. Num. Phys. Aspects Aerod. Flows., ed. Cebeci, T., Long Beach Univ., Jan. 1985, pp. 5–15/29.

9 Sulmont, P., and Rajaona, R. D., "A Method of Spectral Analysis Applied to Periodic and Pseudoperiodic Signals," Journ. Comp. Phys., Vol. 61, No. 1, 1985, pp. 186–193.

10 King, R., "A Review of Vortex Shedding Research and its Applications," Ocean Engineering, Vol. 4, 1977, pp. 141–172.

11 Sarpkaya, T., "Vortex Induced Oscillations. A Selective Review," ASME Journal of Applied Mechanics, Vol. 46, 1979, pp. 241–258.

12 Wille, R., "Karman Vortex Streets," Adv. Applied Mech., Vol. 6, ed. Academic Press, New York, 1960, p. 273.

13 Kovasznay, L. S. G., "Hot-Wire Investigation of the Wake Behind Cylinders at Low Reynolds Numbers," Proc. Roy. Soc. London, Series A, Vol. 198, 1949, pp. 174–190.
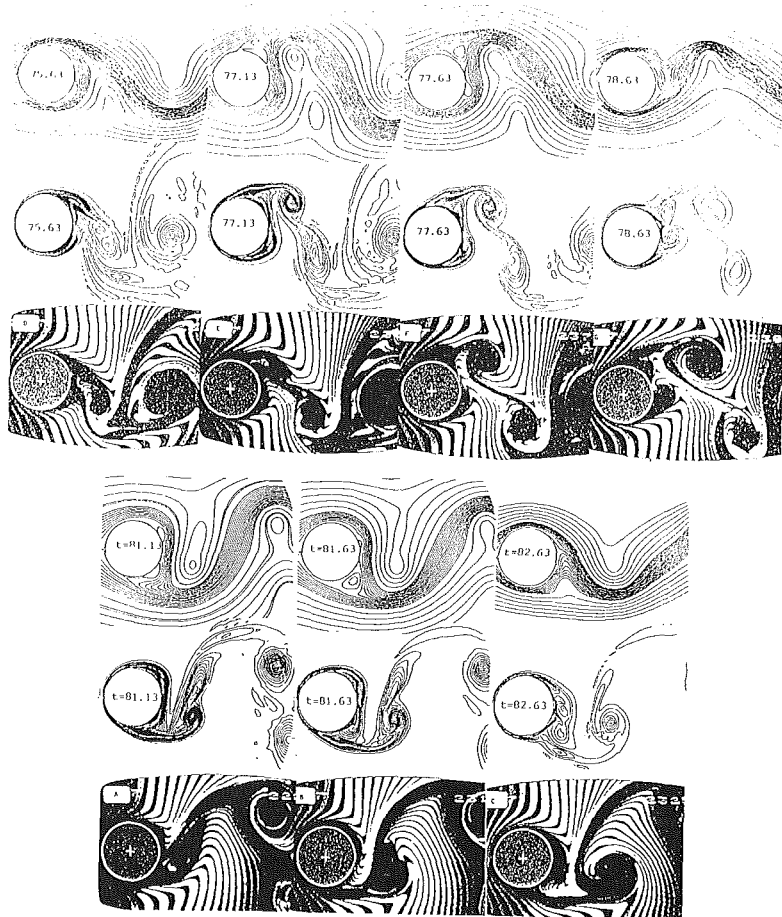
Fig. 8 Comparison of relative streamlines and isovorticity lines with hydrogen bubble visualizations [23]. In-line motion. Case $Re = 855$; $a/D = .13$; $F/S_0 = 2$.
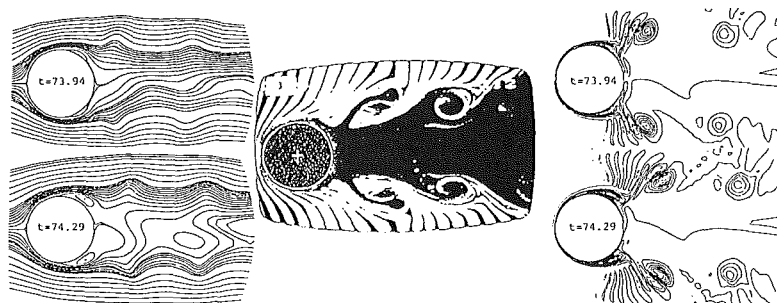
Fig. 9 Comparison of relative streamlines and isovorticity lines with hydrogen bubble visualizations [23]. In-line motion. Case $Re = 855$; $a/D = .13$; $F/S_0 = 3$.

14 Bishop, R. E. D., and Hassan, A. Y., "The Lift and the Drag Forces on a Circular Cylinder in a Flowing Field," *Proc. Roy. Soc. London*, Series A, Vol. 277, 1964, pp. 51–75.

15 Stansby, P. K., "The Locking-on of Vortex Shedding Due to the Cross-stream Vibration of Circular Cylinders in Uniform and Shear Flows," *J. Fluid Mech.*, Vol. 74, Part 4, 1976, pp. 641–665.

16 Lecointe, Y., Piquet, J., and Peantec, J. Y., "Flow Structure in the Wake of an Oscillating Cylinder," *Forum on Unsteady Separation*, ASME-FED Vol. 52, 1987, pp. 147–157, ed., Ghia, K. N. (Book No. H00384).

17 Griffin, O. M., "Vibrations and Flow-Induced Forces Caused by Vortex Shedding," *Proc. Symp. on Flow-Induced Vibrations*, Vol. 1, ASME Winter Annual Meeting, New Orleans, Dec. 1984.

18 Lecointe, Y., and Piquet, J., "Unsteady Viscous Flow Round Moving Circular Cylinders and Airfoils II," *Proc. Int. Symp. on Refined Flow Modelling and Turbulence Measurements*, Univ. Iowa, Sept. 1985, pp. F14-1/10.

19 Ongoren, A., and Rockwell, D., "Flow Structure from an Oscillating Cylinder. Part I: Mechanisms of Phase Shift in the Near Wake," *Journal of Fluid Mechanics*, Vol. 191, June 1988, pp. 197–224.

20 Staubli, T., "Calculation of the Vibration of an Elastically Mounted Cylinder Using Experimental Data from Forced Oscillation," ASME JOURNAL OF FLUIDS ENGINEERING, Vol. 105, June 1983, pp. 225–229.

21 Lecointe, Y., and Piquet, J., "Periodic and Multiple Periodic Behavior of Locked-in Vortex Shedding," *Proc. 16th Symp. on Naval Hydrodynamics*, ed., Webster, W. C., Univ. of California, Berkeley, 1986, pp. 470–489.

22 Griffin, O. M., and Ramberg, S. E., "Vortex Shedding from a Cylinder Vibrating in Line with an Incident Uniform Flow," *J. Fluid Mech.*, Vol. 75, Part 2, 1976, pp. 257–271.

23 Ongoren, A., and Rockwell, D., "Flow Structure from an Oscillating Cylinder. Part II: Mode Competition in the Near-Wake," Vol. 197, June 1988, pp. 225–246.
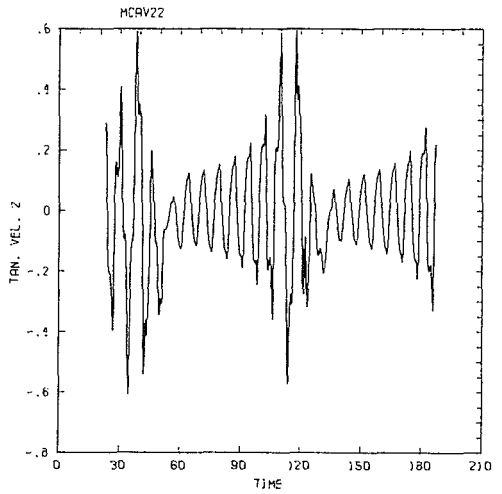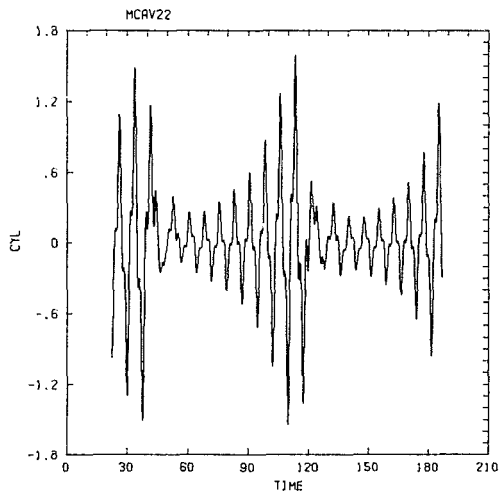
Fig. 10 Evolution with time of force coefficients, vorticity and velocity components in the wake, on the rear axis of the cylinder. In-line motion. Case Re = 855; _a/D_ = .13; _F/S_$_0$ = 2.2 (subscripts 1 and 2 refer to 1 and 2 diameters away from the cylinder).
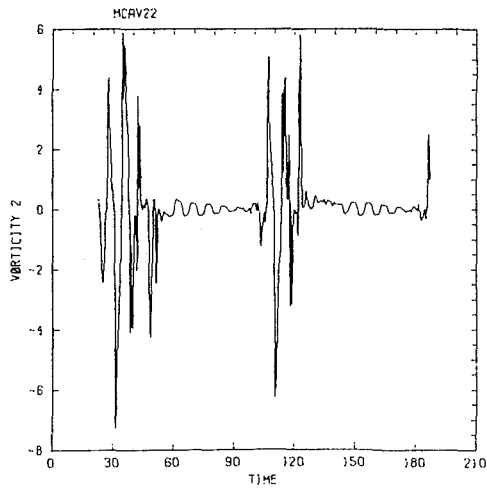
Fig. 10 (cont.)

E. Logan

Professor,
Mechanical and Aerospace
Engineering Department,
Arizona State University,
Tempe, Ariz. 85287

P. Phataraphruk

Engineer,
Structure and Dynamics Group,
Allied Signal Aerospace Company,
Fluid Systems Division,
Tempe, Ariz.

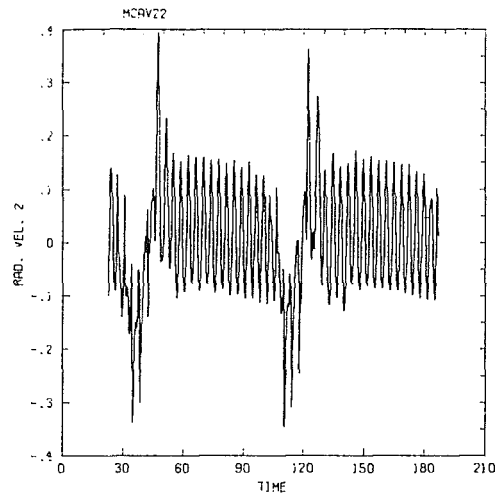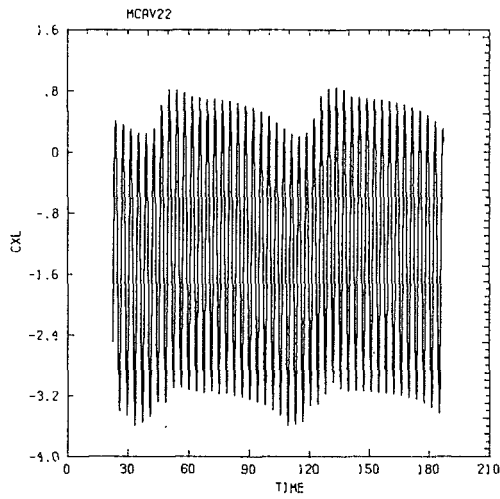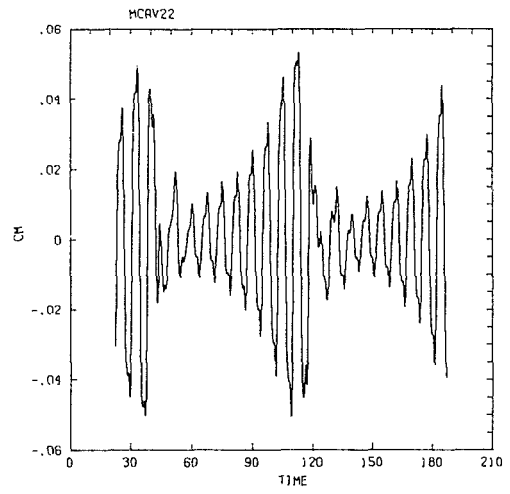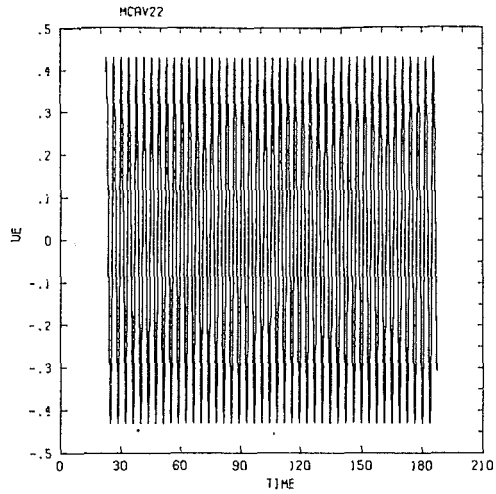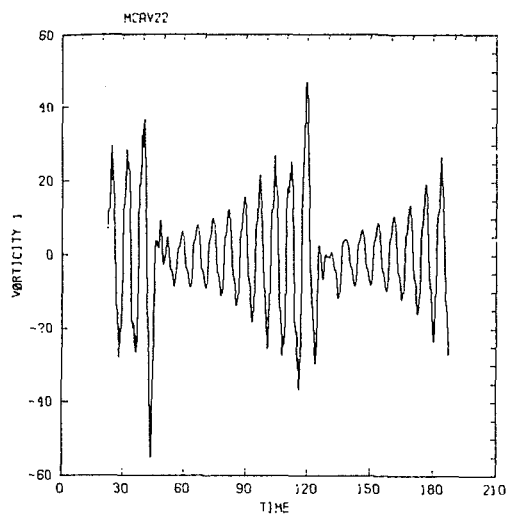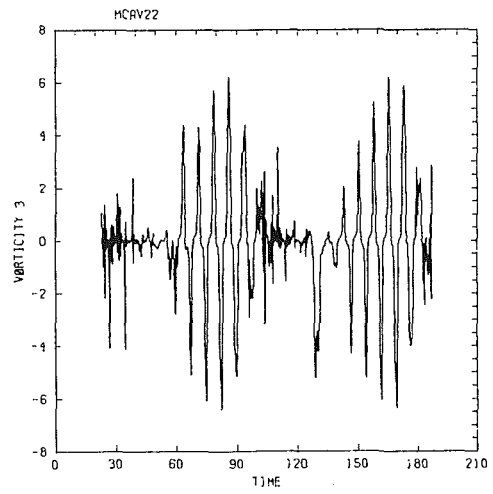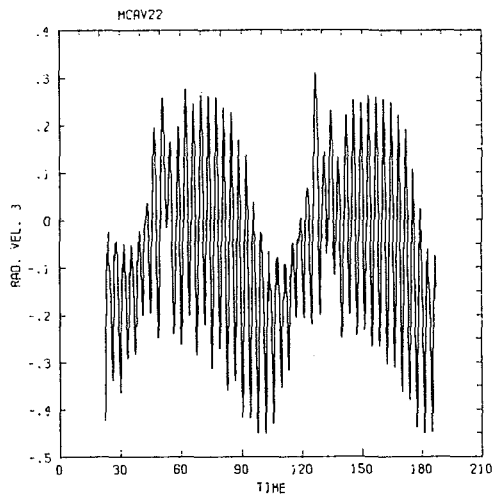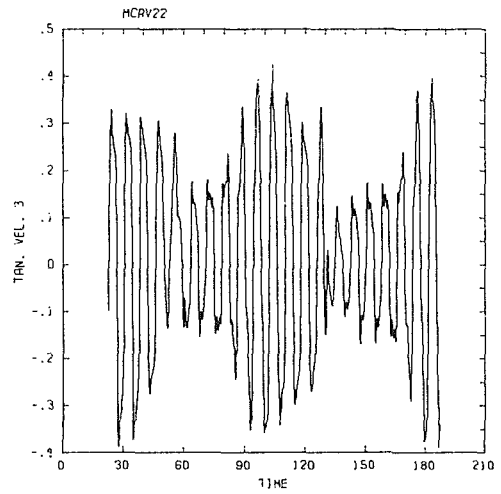# Mean Flow Downstream of Two-Dimensional Roughness Elements

The response of a fully developed pipe flow to wall mounted roughness elements of rectangular cross section was investigated experimentally using a probe with a single hot-wire. Four heights of rectangular, ring-type elements were installed rigidly in a 63.5-mm diameter, smooth-walled, circular pipe in which air was flowing at a Reynolds number of 50,000. After passing over the roughness element, the flow recovery occurred in three stages. The three flow regions are delineated, and the velocity profiles for each are correlated.

Introduction

Tani [1] classified disturbances to boundary layers as step-wise and pulsewise perturbations. The stepwise perturbation may be the result of a change in surface roughness, whereas the pulsewise type may originate from the presence of a single roughness element on the flow boundary. Following any perturbation the flow will achieve a new equilibrium state at some distance downstream of the disturbance. Measurements of flow properties made in these relaxing boundary layers can be useful in the testing of turbulence models used in computational fluid mechanics, if initial and boundary conditions are clearly specified. They are also useful in establishing the sequence of events involved in the readjustment and in establishing the affected domain and the magnitudes of the perturbations present.

In the present study a fully developed pipe flow was used ahead of a single roughness element of rectangular cross section. The disturbed flow relaxes to its initial fully developed state after flowing a sufficient downstream distance past the element. Flow over a two-dimensional obstacle of this type is of interest in meteorology, wind engineering, environmental science, heat transfer and piping system design. The ring-shaped protuberance may represent a weld, a gasket or a rib for the augmentation of heat transfer. Study of flow over a single rib is important for the analysis of measurements of flow over a surface roughened with repeated ribs. The repeated-rib configuration was used by Savage and Myers [2] and by Siuru and Logan [3], who concluded that the roughness element located at a smooth-rough wall boundary is of major importance in the transformation from smooth to rough-wall flow. This conclusion motivated the present work, which was carried out in the same pipe flow apparatus used by Siuru and Logan [3]. Preliminary reports of the single-element work have been presented by the authors [4, 5]. Some turbulence measurements are included in these reports.

Experimental Work

The flow facility, traversing device and instrumentation are shown schematically in Fig. 1. Room air was drawn into a centrifugal fan and discharged into a plenum which supplied a steady flow of air to a brass tube of length sufficient to produce a fully developed flow at its exit. A flanged coupling was used to join the brass pipe to a plastic tube 63.5 mm in diameter which served as the test section and contained a single aluminum roughness element of rectangular cross section. This element, which has the form of a ring, was fitted tightly against the wall of the plastic tube and was sealed with an O-ring. The tube length downstream of the element was increased incrementally by successive addition of spool pieces having lengths of 152.4 mm or 304.8 mm. The first flanged tube section, or spool piece, is shown schematically in Fig. 2. The flow field downstream of nine different roughness elements, designated as configurations A through I was studied, and the dimensions of each are given in Table 1.

The primary instrument used in the investigation of the wakes from the roughness elements was a constant temperature hot-wire anemometer. The probes were inserted into the flow through the open end of the pipe and were

Fig. 1 Flow facility

Fig. 2 Test section

Copyright © 1989 by ASME

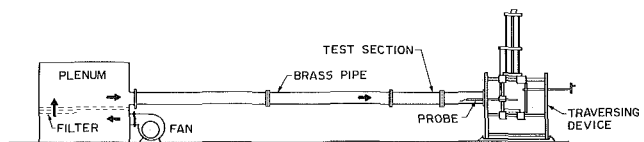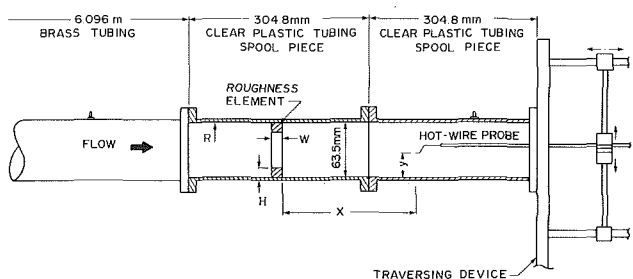**Table 1 Roughness and wake-characterization**

Conf.	H/R	W/H	x_s/H	n	C_1	x_I/H	x_I/R	n'	C_2
A	.1	1.05	6.8	.49	.875	145	14.5	.496	.405
B	.1	2.1	*	.51	.915	109	10.9	.4947	.335
C	.15	.7	8.5	.399	1.103	91	13.65	.507	.337
D	.15	1.4	7.2	.43	1.178	56	8.4	.47	.304
E	.2	.52	10.0	.395	.966	64	12.8	.38	.408
F	.2	1.05	*	.4	1.18	37	7.4	.459	.326
G	.2	2.1	6.8	.49	.829	39	7.8	.486	.293
H	.3	.35	*	.43	.869	23	6.9	.433	.319
I	.3	1.75	*	.39	1.08	18	5.4	.382	.389

*Data are insufficient to accurately determine these values.
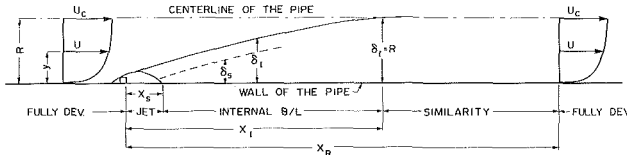
Fig. 3 Flow regions in the wake of a single roughness element

located axially and radially by a traversing mechanism. The DISA 55D01 type anemometer was used with a DISA 55D10 linearizer, a 55D30 DC voltmeter and a 55D35 RMS voltmeter. The DISA 55F14 and 55P11 normal wire probes and the 55F12 and 55P12 slanting wire probes were used. Axial and radial mean velocity components and turbulence stresses were measured with these probes. Only the mean velocities are reported in the present paper.

Frequent calibrations of the hot wires were made near the open end of the test section, and the linearizer was adjusted accordingly. Initially a comparison of fully developed mean velocity profiles for smooth-pipe flow taken with the hot wire and with a Pitot tube was made. These profiles were also compared with that obtained by Laufer [6]. The radial distributions of Reynolds normal and shear stresses for fully developed smooth-pipe flow were also measured and compared with those of Laufer. Good agreement was obtained in all cases.

Measurements of mean velocity components were made by traversing between the wall and the centerline of the pipe with normal and slant-wire probes at several distances, x, downstream of the plane of the rear face of the roughness element. The Reynolds number, based on average velocity and pipe diameter, was $50,000 \pm 400$ for all runs. Static pressure taps, 24 inches apart, were used to determine the pressure gra-

dient upstream of the roughness element. For the Reynolds number used the skin friction coefficient inferred from these pressure measurements was 0.0035.

Uncertainty for the dimensionless mean velocity U/U_c is estimated as $\pm.75$ percent in the core region and as ± 8 percent in the vicinity of the separation region behind the element. The uncertainty in the friction velocity u_τ/U_c was ± 4 percent when determined from Clauser charts downstream of the elements and ± 2 percent when determined from pressure drop measurements upstream of the elements.

Results

The regions of affected flow are delineated in Fig. 3. A region of separated flow occupies a region of length X_s behind the element. This region is designated as the jet region. An internal boundary layer region, designated as the IBL region, forms behind the jet region and extends a distance x_I behind the element. The IBL region terminates when the thickness of the IBL equals the pipe radius. A similarity region exists between the IBL region and the region of fully developed flow. The length of the three regions combined, the recovery length, is denoted by x_R.

Figure 4 is a plot of estimated separation-zone or reattachment length x_s as a function of element width-to-height ratio W/H. The distance x_s is estimated by extrapolating plots of C_f as a function of x/H to locate the intercept on the x/H axis. Values of C_f are determined from Clauser charts using the mean velocity data. Reattachment lengths determined by Good and Joubert [7] for a thin fence, by Mueller and Robertson [8] for an element with a rounded forward face and by Oka and Kostic [9] for a roughness element of square cross section are shown in Fig. 4 for comparison with the present data. An uncertainty of $\pm 1H$ is estimated for the present

---

Nomenclature

C_1 = factor in equation for growth of IBL
C_2 = factor in equation for growth of sublayer
C_3 = factor in equation for k
C_d = drag coefficient of roughness element
C_f = skin friction coefficient
G = Clauser mean velocity parameter
H = height of roughness element
h^+ = $(C_f/2)^{1/2} (U_{av}H/\nu)$
IBL = internal boundary layer
k = factor appearing in Prandtl Velocity-Defect Equation
m = κ times slope of velocity profile for $y < \delta_i'$
m' = κ times slope of velocity profile segment for $\delta_i' < y < \delta_i$

n = exponent in equation for growth of IBL
n' = exponent in equation for growth of sublayer
R = inside radius of pipe
U = axial component of mean velocity
U_{av} = average mean velocity in pipe
U_c = mean velocity at centerline of pipe
U_r = reference velocity used in velocity correlation
u_τ = friction velocity
x = axial coordinate measured from rear of element
x_I = distance x required for IBL thickness to equal pipe radius

x_R = distance x required for recovery of fully developed flow
x_s = reattachment length behind element
W = width of roughness element in axial direction
y = wall distance
$y_{1/2}$ = wall distance at which $U=.5 U_r$
δ_i = internal boundary layer thickness
δ_i' = sublayer thickness
κ = Von Karman constant
ν = kinematic viscosity
σ = constant in jet region equal to 14.5

Fig. 4 Length of separation region behind a single roughness element
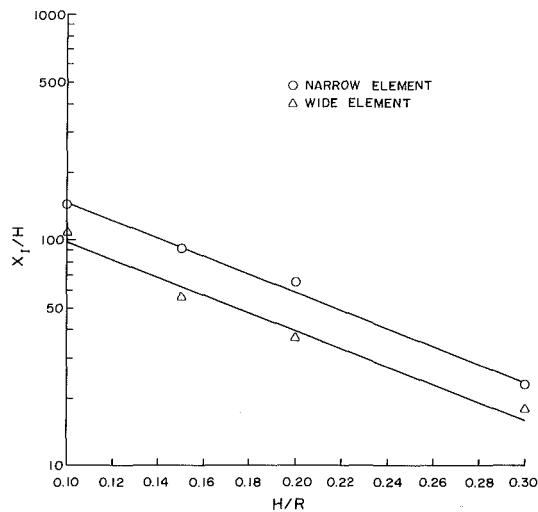
Fig. 5 Length of jet and IBL regions

Fig. 6 Velocity profiles in jet region for configuration A

Fig. 7 Velocity profiles in the jet region

values. Figure 4 shows that wider roughness elements have reduced reattachment lengths, and that a limiting value of about 6.8 roughness element heights is reached for W/H greater than about 1.4. This observation agrees qualitatively with that of Bergeles and Athanassiadis [10]. The effect could result from the presence of the low-pressure, separation region near the leading edge of the crest of the element. Arie et al. [11] have shown that the wider the element, the lower the surface pressure and the longer the transverse pressure force is sustained. The fluid particles follow paths of greater curvature, which results in shorter reattachment lengths behind the element, as long as the flow does not also reattach on the crest of the element itself. Rettachment lengths measured on the top of forward-facing steps by Robertson and Taulbee [12] indicate the extent of this low-pressure zone; these lengths divided by step height may be used as approximations of critical values of W/H for the rectangular elements, i.e., values of W/H greater than these result in no further reduction in x_s. The data of Robertson and Taulbee indicate that the critical W/H is around 1.3 for H/R of 0.1 and 1.6 for H/R of 0.3. This range of critical values of W/H agrees with that reported by Castro and Dianat [13].

The length x_I of the jet and IBL regions may be obtained from Table 1 and is shown as a function of element height in Fig. 5. The upper bound of these data is approximated by the linear equation,

$$x_I/H = \exp(5.92 - 9.206\ H/R) \qquad (1)$$

and the lower bound may be represented by

$$x_I/H = \exp(5.487 - 9\ H/R) \qquad (2)$$

Using these formulas allows the prediction of the axial extent of the IBL region to within about 10 percent.

The recovery length x_R is more difficult to define, since the flow parameters tend to approach their equilibrium values after many oscillations about these final values. Schofield and Logan [14] have used the Clauser mean velocity parameter G to indicate the attainment of final equilibrium. An alternate approach is to relate the recovery length to the time scale of the large eddies produced by the obstacle and to use the formulations of Tennekes and Lumley [15] and Reynolds [16] to obtain an expression for x_R. The data of Sami and Liu [17] were utilized to estimate the starting value of Taylor microscale. The empirical correlation of Nigim and Cockrell [18] was used to estimate drag coefficients of the obstacle within the logarithmic part of the boundary layer. Values of x_R obtained by this method were found to exceed the length of the test section used in the present experiment by a factor of two or more.

Figure 6 shows velocity profiles in the jet region for Configuration A. A region of high shear stress is created immediately behind and above the element. The core flow is also modified by the acceleration above the element. The velocity gradient decreases with downstream distance, but the width of the high shear layer is increased.

Representative profiles in the jet region are shown in Fig. 7. The profiles are generally correlated by a conventional mixing-layer correlation and may be represented well by the relation,
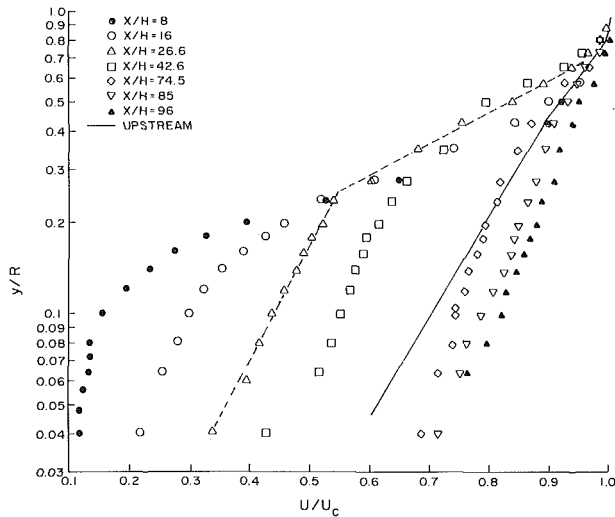
Fig. 8 Development of velocity profiles in the IBL region for configuration C
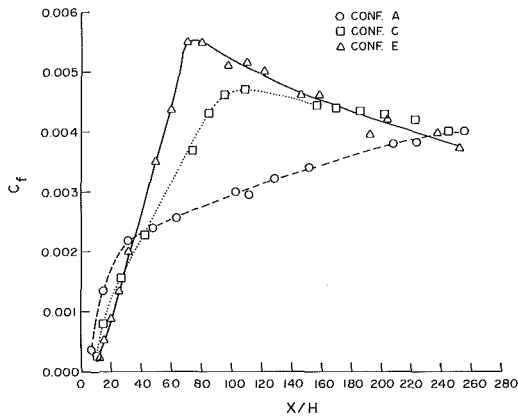
Fig. 9 Skin friction coefficients in IBL and similarity regions

Fig. 10 Correlation of slope of mean velocity profiles
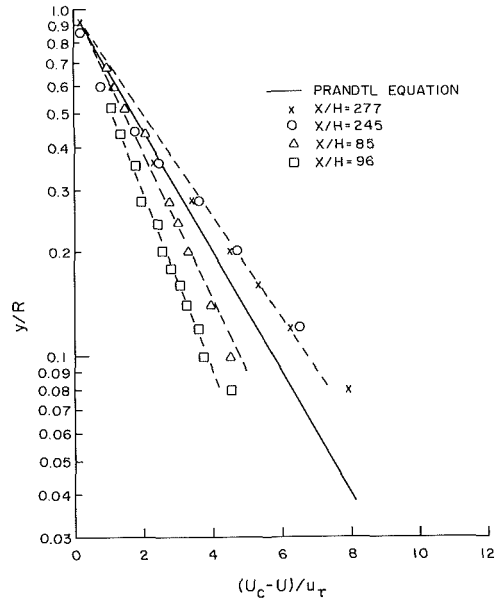
Fig. 11 Velocity profiles in the similarity region for configuration C

$$U/U_r = 0.5 + .3 \ \mathrm{erf}[\sigma(y - y_{1/2})/x] \qquad (3)$$

Velocity profiles in the IBL region are of the form shown in Fig. 8 for Configuration C, and these profiles are representative of the other configurations as well. The distorted profile may be divided into three sections: the lower section which has a slope m/κ associated with the local wall stress; an intermediate section containing a large slope m^l/κ associated with the high velocity gradient of the shear layer just behind the crest of the element; and the upper portion of the profile, which very closely approximates the undisturbed profile. As x/H increases the slope of the middle region decreases, and this region moves towards the centerline. The distance from the upper end of the middle region, or the location of the "upper knee," to the wall is defined as the IBL thickness δ_i. The distance from the lower end of the middle region to the wall, the location of the "lower knee," is defined as the sublayer thickness δ_i'. Both thicknesses grow roughly as the 1/2 power of x, and their growth can be described by the following equations:

$$\delta_i/H = C_1 \ (x/H)^n \qquad (4)$$

$$\delta_i'/H = C_2 \ (x/H)^{n'} \qquad (5)$$

where C_1, C_2, n and n' are given for each configuration in Table 1.

The axial distance x_I to the end of the IBL region is found by setting δ_i equal to the pipe radius R in (4). For $x > x_I$ the "knees" disappear, and the three distinct slopes of the veloci-

ty profiles in the IBL region do not persist into the similarity region.

The slope m/κ of the velocity profile in the developing sublayer in the IBL region is that given by the Law of the Wall, where

$$m = (C_f/2)^{1/2} \qquad (6)$$

Values of C_f, which were calculated from Clauser Charts, are shown in Fig. 9.

The slope m'/κ of the intermediate region is related to the velocity gradient in this region through

$$d(U/U_c)/d(y/H) = m'H/\kappa y \qquad (7)$$

and can be calculated by the following empirical equation:

$$m' = (C_d/2)^{1/2}(x/H')^{-.547} \qquad (8)$$

(see Fig. 10) where C_d is calculated from the correlation of Nigim and Cockrell,

$$C_d/C_f = 150 \ \log h^+ - 190 \qquad (9)$$

and

$$H' = H[21.668(C_d/2)^{1/2} - 7.3673] \qquad (10)$$

Equation (8) correlates data for Configuration A to $x/H = 145$, for Configuration C to $x/H = 85$ and for Configuration E to $x/H = 32$. Equation (8) can be utilized to estimate m' in the IBL region providing $H/R < .15$.

Typical velocity profiles in the similarity region are plotted in Fig. 11 for configuration C. These profiles are similar to

those for configurations A and E as well. At $x = x_R$ the velocity data are expected to agree with the Prandtl equation,

$$(U_c - U)/u_\tau = (1/k) \ln (y/R) \tag{11}$$

which has been shown by Schlichting [19] to predict fully developed velocity profiles in smooth and rough pipes if k is set equal to .4, the von Karman constant. The data in the similarity region, $x_I < x < x_R$, are correlated approximately by (11), provided that k is varied to suit the slopes of the straight lines through the data as plotted in Fig. 11. The curves show the extreme values of the slopes $1/k$ encountered in the similarity region. At the final measuring station the value of k approaches .4. The graph of (11) with $k = .4$ is shown as a solid line in the figure.

The derivation of (11) utilizes the concept of mixing length 1, which is equated to ky. The mixing length may be taken as a measure of eddy size, which increases with increasing wall distance. The effect of the roughness element is to generate large eddies of a diameter comparable with the element height H. The distribution of mixing length and its average value is modified by the vortices created in the shear layer of the jet region. The perturbation of mixing length 1 is proportional to the perturbation of k and is also proportional to the height of the element. Troutt, Scheelke, and Norman [20] have shown the presence of these vortices in the mixing region behind a backward facing step and have concluded that vortex pairing, i.e., vortex enlargement, is greatly inhibited downstream of the reattachment point. The perturbation 1 decays as $x \to x_R$ and is proportional to $(1 - x/x_R)$. Combining the above assumptions, it may be postulated that

$$k = .4 + 100\, C_3 (H/R)(1 - x/x_R) \tag{12}$$

C_3 in (12) has a value of about 5.6 at $x = x_I$ but appears to decrease in an unknown manner as $x \to x_R$.

Conclusions

The following conclusions can be drawn for wake flows in pipes behind single, wall-mounted roughness elements of heights, $.1 < H/R < .3$ at a Reynolds number of 50,000:

1. The length of the separation zone behind the element depends on W/H and decreases to a limiting value of 6.8 for $W/H > 1.4$

2. The length of x_I of the jet and IBL regions is an exponentially decreasing function of H/R. Increasing W/H at a given H/R reduces this length significantly.

3. The recovery length x_R is greater than x_I and much longer than the test sections used.

4. Velocity profiles in the jet region are approximately correlated by a conventional mixing layer correlation (3).

5. The three layers of the IBL region have velocity distributions represented approximately by straight lines, when plotted semilogarithmically. The thicknesses of the layers may be determined from equations (4) and (5). Slopes m/κ and m'/κ, which occur in the sublayer and middle layer, may be estimated from equations (6) and (8), respectively, provided $H/R < .15$.

6. Velocity profiles in the similarity region can be represented approximately by the Prandtl equation (11), provided that k is allowed to vary between a starting value, given by (12), and a final value of 0.4.

References

1 Tani, I., "Review of Some Experimental Results on the Response of a Turbulent Boundary Layer to Sudden Perturbations," *Proceedings of 1968 AFOSR-IFP-Stanford Conference on Computation of Turbulent Boundary Layers*, Vol. I, Stanford University, 1969, pp. 483-494.

2 Savage, D. W., and Myers, J. E., "The Effect of Artificial Roughness on Heat and Momentum Transfer," *A.I.Ch.E.J.*, Vol. 9, 1963, pp. 113-135.

3 Siuru, W. D., and Logan, E., "Response of a Turbulent Pipe Flow to a Change in Roughness," ASME JOURNAL OF FLUIDS ENGINEERING, Vol. 99, 1977, pp. 548-555.

4 Phataraphruk, P., and Logan, E., "Response of a Turbulent Pipe Flow to a Single Roughness Element," *Proceedings of the Ninth Southeastern Conference on Theoretical and Applied Mechanics*, 1978, pp. 139-149.

5 Phataraphruk, P., and Logan, E., "Turbulent Pipe Flow Past a Rectangular Roughness Element," *Turbulent Boundary Layers*, H. E. Weber, Ed., New York, ASME, 1979, pp. 187-196.

6 Laufer, J., "The Structure of Turbulence in Fully Developed Pipe Flow," NACA Rept. 1174, 1954, 18 p.

7 Good, M. C., and Joubert, P. N., "The Form Drag of Two-Dimensional Bluff Plates Immersed in Turbulent Boundary Layers," *J. Fluid Mechanics*, Vol. 31, 1968, pp. 547-582.

8 Mueller, T. J., and Robertson, J. M., "A Study of the Mean Motion and Turbulence Downstream of a Roughness Element," *Modern Developments in Theoretical and Applied Mechanics*, Vol. 1, Plenum Press, 1963, pp. 326-340.

9 Oka, S., and Kostic, Z., "Flow Field Past a Single Roughness Element in Channel of Rectangular Cross Section," N. Afgan et al., *Heat and Mass Transfer in Boundary Layers*, Vol. I, Pergamon Press, 1972, pp. 425-435.

10 Bergeles, G., and Athanassiadis, N., "The Flow Past a Surface-Mounted Obstacle," JOURNAL OF FLUIDS ENGINEERING, Vol. 105, 1983, pp. 461-463.

11 Arie, M., Kiya, M., Tamura, H., Kosugi, M., and Takaoka, K., "Flow Over Rectangular Cylinders Immersed in a Turbulent Boundary Layer," *Bulletin of the JSME*, Vol. 18, No. 125, 1975, pp. 1269-1276.

12 Robertson, J. M., and Taulbee, D. B., "Turbulent Boundary Layer and Separation Ahead of a Step," H. J. Weiss et al., *Developments in Mechanics*, Vol. 5, 1969, pp. 171-200.

13 Castro, I. P., and Dianat, M., "Surface Flow Patterns on Rectangular Bodies in Thick Boundary Layers," Fifth Colloquium on Industrial Aerodynamics, Aachen, Germany, June 1982.

14 Schofield, W. H., and Logan, E., "Viscous Flow Around Wall Mounted Obstacles," Aero Propulsion Report 172, Aeronautical Research Laboratories, Melbourne, Australia, 1986.

15 Tennekes, H., and Lumley, J. L., *A First Course in Turbulence*, MIT Press, 1972, p. 72.

16 Reynolds, A. J., *Turbulent Flows in Engineering*, Wiley, 1974, p. 80.

17 Sami, S., and Liu, W. H., "Confined Shear Layer Approaching A Stagnation Point," *Developments in Mechanics*, Vol. 8, 1975, pp. 497-516.

18 Nigim, H. H., and Cockrell, D. J., "Effects Caused by Small Discrete Two-dimensional Roughness Elements Immersed in Turbulent Boundary Layers," *J. Fluid Mechanics*, Vol. 153, 1985, pp. 17-30.

19 Schlichting, H., *Boundary Layer Theory*, McGraw-Hill, New York, 1960.

20 Troutt, T. R., Scheelke, B., and Norman, T. R., "Organized Structures in a Reattaching Separated Flow Field," *J. Fluid Mech.*, Vol. 143, 1984, pp. 413-427.

Experimental Study of the Aerodynamic Interaction Between an Enclosed-Wheel Racing-Car and Its Rear Wing

J. Katz
Professor.

R. Largman
Graduate Student.

Department of Aerospace Engineering
and Engineering Mechanics,
SDSU,
San Diego, Calif. 92182

A quarter-scale model of an enclosed wheel racing car was tested using the elevated ground plane wind tunnel technique. To increase the aerodynamic down force, two longitudinal underbody channels were built into the vehicle's lower surface, and a rear wing was added. The effect of these underbody channels, and of wing angle of attack and position, on the vehicle's drag and down force was experimentally investigated. Results of the experiments indicate that the flow under the car is affected by the presence of the wheels, and the vehicle without a rear wing generates only a negligible downforce. However, the addition of a rear wing enhanced the flow under the vehicle body, resulting in an increased aerodynamic downforce.

Introduction

The performance of high speed ground vehicles and race cars is strongly influenced by their aerodynamic characteristics. Reduced aerodynamic drag, for example, can considerably improve high speed efficiency, whereas vehicle acceleration and turning rate can be improved by increased aerodynamic downforce which will increase tire adhesion. This additional downforce can be created by adding lifting surfaces [1-4] onto the vehicle's body or by using the ground effect of the body. The development of vehicle shape, and the corresponding aerodynamic information can be obtained by using analytical/computational or experimental techniques. Because of the limited length/width ratio and the curved and complex geometry, the flow field about road vehicles includes regions of flow separation, which imposes severe difficulties on current computational methods [5]. On the other hand, experimental wind-tunnel investigation of road vehicle aerodynamics is complicated by the presence of the wind-tunnel ground boundary layer (which is absent in the case of actual road conditions) [6-8]. Road testing is a possible alternative [9], but only one vehicle can be instrumented at a time and model shape changes are more elaborate and expensive, and depend on atmospheric and road conditions. The advantage of a controlled environment has made wind-tunnels a frequently used automotive aerodynamic development tool. Consequently, a variety of techniques have been used to obtain a closer simulation of actual road conditions, to overcome complication due to the relative motion between the vehicle and the ground, wheel rotation, and the change in separation lines location (Reynolds

number effect) in smaller scale testing [6-8]. Linearized computational techniques [10-12] have been used too, in a complementary manner with wind-tunnel testing, and were successful in estimating the aerodynamic down force created by the vehicle's lifting surfaces [12].

In this study the elevated ground plane method was used for an extensive wind tunnel investigation of a generic IMSA (International Motor Sport Association) Prototype race car model (in quarter scale). The main objective of the study was the broad documentation of aerodynamic data (such as vehicle, ground plane, tunnel wall, and ceiling pressures, along with measurements of the vehicle's lift and drag), so that theoretical tools [12] could be calibrated and their effective boundaries defined. Also, the effect of the underbody channels and of the wing location and orientation on vehicle aerodynamics was investigated.

Experimental Apparatus

The description and dimensions of the quarter-scale race-car model, as mounted in the wind-tunnel, are shown in Fig. 1. The wind tunnel is a closed return type with an inlet contraction ratio of 7:1, utilizing three anti-turbulence screens (turbulence levels are less than 1 percent). Test section speeds can vary between 18–80 m/s (40–180 miles/hr), and for the data reported here the range of 36–49 m/s (or about 80–110 miles/hr) was used, which is considered to be adequate for the testing of such vehicle sizes and types [13–15]. For each configuration, the forces were measured at this speed range with increments of 10 miles/hr and the aerodynamic coefficients were obtained by averaging these values. An individual lift or drag coefficient could be measured with an accuracy of less than 1 percent, but because of the above averaging process,
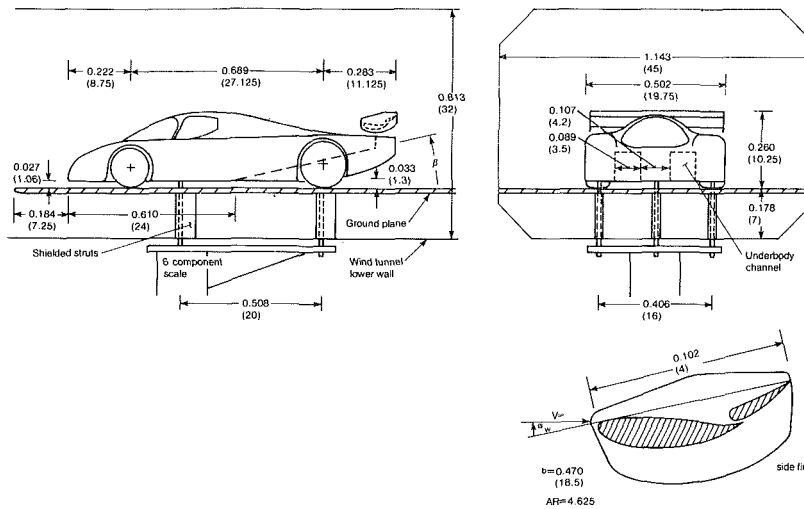
Fig. 1 Geometrical details of the wind-tunnel and of the quarter-scale model, dimensions in m (in.)

the uncertainty of the reported aerodynamic coefficients was about 3 percent.

The model was mounted on three vertical struts which were aerodynamically shielded in the tunnel section, under the ground plane (as shown in Fig. 1). Two underbody rectangular cross-section channels, with variable angles were fabricated to enhance the vehicle's downforce. The channels angle could vary between $0 < \beta < 14$ deg, but was tested only at $\beta = 0$, 9, or 14 deg. This simplified channel geometry resulted in sharp edges, which fixed the location of the underbody flow separation lines. Also the body was made smooth (by closing the cooling ducts) and flow visualizations indicated that the flow stayed attached on the upper surface. Consequently, the upper-surface separation lines were fixed at the vehicle's rear section, while the lower flow-separation pattern was controlled by the sharp-edged channels and the wheels, so that Reynolds no. effects were kept minimum. The rear wing had an aspect ratio (AR) of 4.625 and the geometry of its two-element airfoil is shown in the insert to Fig. 1. Static pressure ports on the race-car model were located along its centerline and in the middle of the left channel. Similarly, the ground plane pressure ports were located along the centerline and under the vehicle's left channel (Fig. 1). Additional static pressure data, at the test section right wall and on its ceiling, was recorded to provide sufficient input for some wind-tunnel blockage correction methods [16] (since model to wind tunnel cross-section area ratio was about 11.6%). Because of the attached flow over the upper surface of the model, wind tunnel corrections (using a panel code [12]) resulted in blockage corrections in the range of 10 percent. This correction is smaller than expected by simpler blockage correction methods [6, 17] that are more useful for conditions with massive flow separation behind the vehicle and can indicate corrections of up to 14 percent.

Prior to placing the model in the test section, a velocity survey over the ground plane was conducted. Boundary layer and velocity-distribution data along the centerline of the
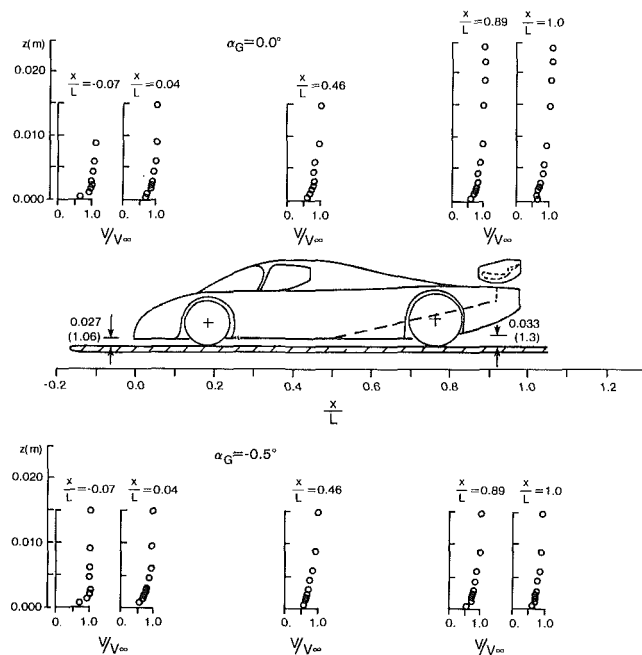
Fig. 2 Boundary layer velocity distributions along the centerline of the ground plane (at $V_\infty = 100$ mph or 160 km/hr, uncertainty in $V/V_\infty = \pm 0.03$, in $z = \pm 0.001$ m)

groundplane are shown in Fig. 2. The displacement thickness was less than 5 mm toward the end of the plane (where the Reynolds no., based on model length, was $\mathrm{Re}_L \approx 3.3 \times 10^6$). Additional data at the plane quarter span were similar to the data measured at the centerline and, therefore, are not being presented here. Creating a negative ground-plane incidence of

---

Nomenclature

A = reference area (0.10451592 m^2, or 162 in^2)
AR = aspect ratio (area/b^2)
b = wing span
c = wing chord
C_D = drag coefficient (drag/ $0.5\rho V_\infty^2 A$)

C_L = lift coefficient (lift/ $0.5\rho V_\infty^2 A$)
C_p = pressure coefficient ($p - p_\infty$/ $0.5\rho V_\infty^2$)
H = vertical clearance
L = vehicle length
p = pressure

Re_L = Reynolds no., based on L
V_0 = reference velocity (100 mph)
V_∞ = free-stream velocity
x, y, z = body coordinates
α_G = ground plane angle of attack
α_W = wing angle of attack
β = underbody channel angle
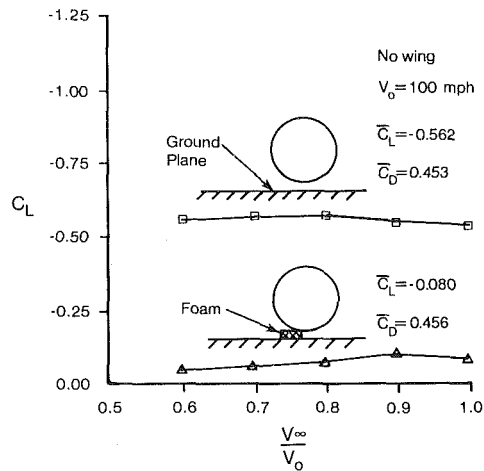
Fig. 3 Effect of gap under the wheels on model lift coefficient, $Re_L \approx$ 3.3 × 10^6 (uncertainty in C_L = ±0.015, in V_∞/V_0 = ±0.03)
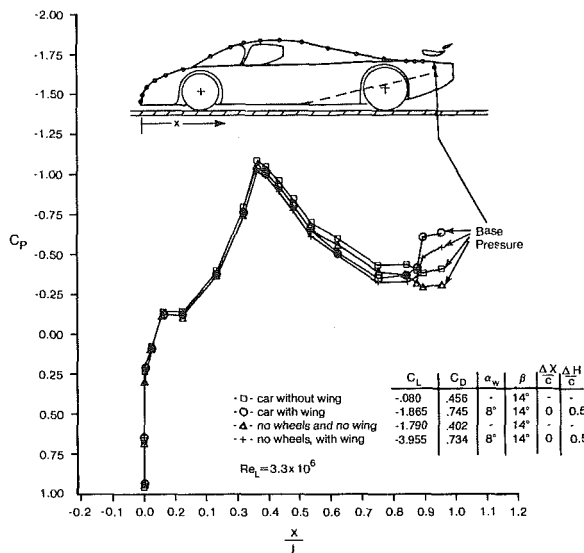
Fig. 4 Pressure distribution along vehicle's upper centerline, y/L = 0 (uncertainty in C_p = ±0.05, in x/L = ±0.005)

Fig. 5 Pressure distribution along vehicle's lower centerline, y/L = 0 (uncertainty in C_p = ±0.05, in x/L = ±0.005)

Fig. 6 Pressure distribution along the centerline of the vehicle's underbody channel, y/L = 0.082 (uncertainty in C_p = ±0.05, in x/L = ±0.005)

$\alpha_G = -0.5$ deg resulted in a slight reduction in the boundary layer thickness as shown in the lower side of Fig. 2. Because of the limited influence of ground plane incidence, $\alpha_G = 0$ was used throughout the experiment. To correct for the effect of the boundary layer displacement, so that the flow beneath the vehicle will better simulate actual road conditions, the model was raised by 7 mm. To account for the small negative incidence of the actual race car the rear edge was raised by an additional 3 mm (as shown in Figs. 1 and 2).

Because of this vertical correction in placing the model over the ground plane (due to boundary layer displacement thickness) and because any contact between the model (mounted on the scales) and the ground plane needs to be avoided, a small gap was left between the ground plane and the wheels. The effect of such a small gap under the wheels on the force data, is reported in [18] and is demonstrated in Fig. 3, where an average lift coefficient of $C_L = -.562$ was measured for the model without the rear wing. By cementing a small strip of flexible foam, ahead and under the wheels, and without applying pressure to the model wheels, the airflow in the gap was eliminated (and the lift was reduced to $C_L = -.080$). The drag force data are almost unaffected by the above change, which indicate that this large lift change is created by the local flow in the wheel and ground-plane gap.

Results

The sleek bodywork of enclosed-wheel race-cars makes it possible to utilize the vehicle shape to increase the aerodynamic downforce by accelerating the flow beneath the vehicle [14, 15, 19] ("ground effect"). Unfortunately, the automobile wheels interact unfavorably with the underbody flow and most of the "natural" ground effect is lost. To regain some of the lost ground effect, on some race cars [20, 21] and in the case of the model tested here, underbody channels are added to increase airflow beneath the vehicle. The pressure distribution data presented in Figs. 4 to 9 demonstrate this vehicle/ground interaction and its sensitivity to the presence of the vehicle's wheels and rear wing.
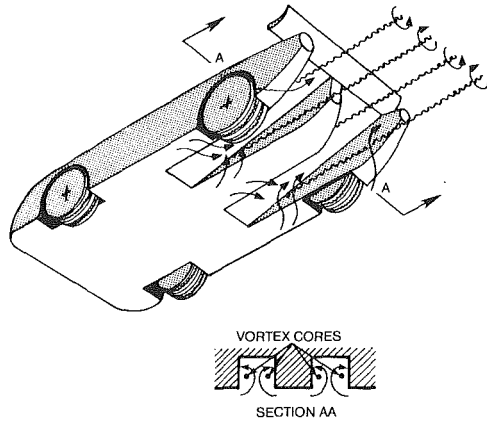
Fig. 7 Schematic description of the flow field under the vehicle (based on flow visualisation with tufts)

	C_L	C_D	α_w	β	$\frac{\Delta X}{c}$	$\frac{\Delta H}{c}$
□ car without wing	-.080	.456	-	14°	-	-
O car with wing	-1.865	.745	8°	14°	0	0.5
△ no wheels and no wing	-1.790	.402	-	14°	-	-
+ no wheels, with wing	-3.955	.734	8°	14°	0	0.5

$Re_L = 3.3 \times 10^6$
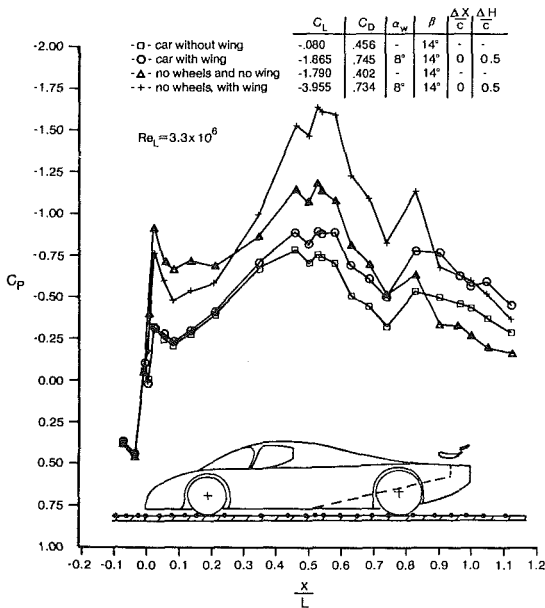
Fig. 8 Pressure distribution along ground plane centerline, $y/L = 0$ (uncertainty in $C_p = \pm 0.05$, in $x/L = \pm 0.005$)

	C_L	C_D	α_w	β	$\frac{\Delta X}{c}$	$\frac{\Delta H}{c}$
□ car without wing	-.080	.456	-	14°	-	-
O car with wing	-1.865	.745	8°	14°	0	0.5
△ no wheels and no wing	-1.790	.402	-	14°	-	-
+ no wheels, with wing	-3.955	.734	8°	14°	0	0.5

$Re_L = 3.3 \times 10^6$

Fig. 9 Pressure distribution on the ground plane, under the centerline of the vehicle's underbody channel, $y/L = 0.082$ (uncertainty in $C_p = \pm 0.05$, in $x/L = \pm 0.005$)

The measured pressure coefficients on the upper centerline of the vehicle are shown in Fig. 4 for the vehicle with and without wing or wheels. Location of the pressure ports are shown by the dots in the figure, and x is measured from the vehicle's leading edge. The location of the stagnation point at the lower front of the car and most of the other upper surface pressures are not affected much by the above model changes. The addition of the wing increased the magnitude of $-C_p$ at the last two points by about 0.2 (last point is the vehicle's base pressure and the one before is located at about 0.4-wing-chords ahead of the wing leading edge). Removing the vehicle's wheels (and smoothly enclosing the wheel wells) resulted in a reduction of flow separation (that was behind the wheels), and the magnitude of $-C_p$ is slightly reduced.

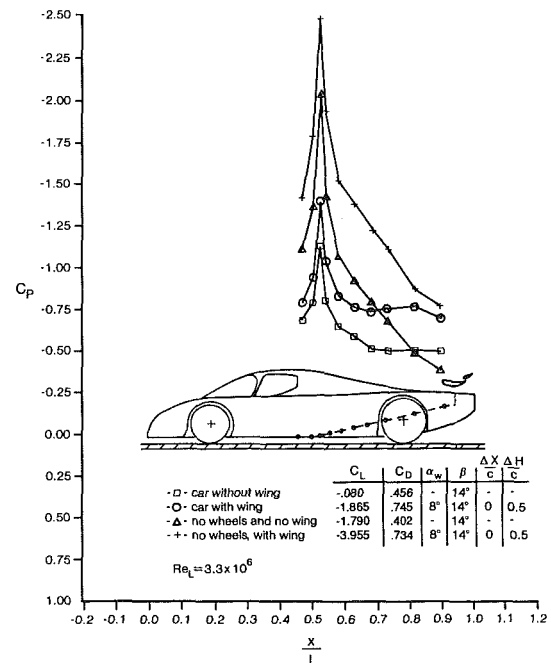Pressure coefficients on the lower centerline of the car and for the same configurations, as in Fig. 4, are presented in Figs. 5 and 6. The addition of wheels to the vehicle's body clearly reduces the downforce (less $-C_p$), while the addition of the rear wing increases the downforce along most of the vehicle's length. The centerline of the car was planar from front to rear (see Fig. 7) and the large suction peaks in Fig. 5 are near the inlets to the underbody channels (located at $x/L = 0.51$). The
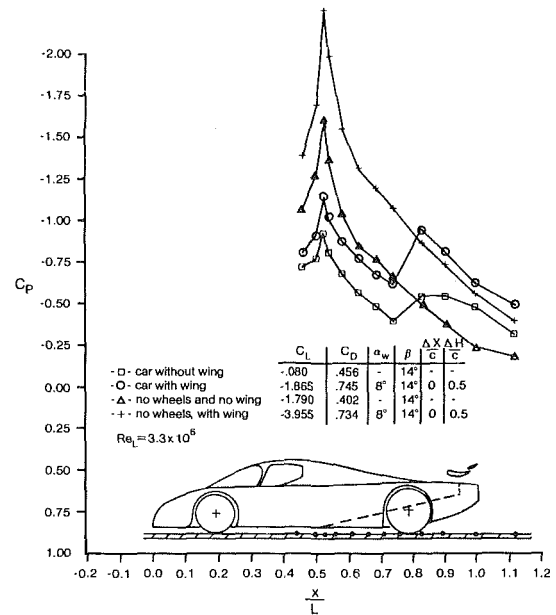
pressure distributions along the centerline of these channels are presented in Fig. 6 where the suction peaks at the channel entrance are much larger.

Schematic results of flow visualization with tufts (Fig. 7) indicate that inside each channel two concentrated vortices exist. This separated flow pattern resembles the leading edge vortices found over sharp edged delta wings at high angles of attack [22]. The presence of the wheels created a strong lateral flow (from outside to inside) and when flowing into the channels the crossflow pattern, shown in section AA of Fig. 7 is obtained. Having sharper channel edges at the outer edge will increase the vortex strength, which will result in larger suction forces and more downforce.

Pressure coefficients at the centerline of the groundplane and under the channel for the previous four model configurations are presented in Figs. 8 and 9, respectively. The influence of the suction peak at the lower front of the vehicle and under the channel entrance (as in Fig. 5) is visible. The pressure signature of these figures (8 and 9) resembles the data of Figs. 5 and 6, but the pressure peaks are slightly reduced.

The interaction between the rear wing and the car body is demonstrated by the lift and drag coefficient plots versus wing angle of attack α_W in Figs. 10 and 11 (coefficients are based on car reference area, which is 2.19 times larger than wing area). First, the isolated wing was tested in the wind tunnel (lower curve) and then the experiment was done with the wing positioned on the race car (as shown in Fig. 1). Because of the wing induced negative pressures under the vehicle, the lift and the drag curve slopes of the complete vehicle are larger throughout the whole region. The negative lift coefficients shown here are larger than reported in [13], and smaller than the data of [15]. In principle, the larger down force values were obtained with moving ground plane apparatus, which tend to overestimate the front axle lift [13]. For the actual race car, larger coefficients can be obtained by improved vehicle shapes (e.g., wider inlets to the channels, front winglets, more efficient rear wing etc.)

The effect of a change in wing angle of attack on the pressures in the channel (and on the downforce) is shown in Fig. 12. From the pressure distribution in the underbody channel and on the groundplane beneath this channel, the increase in the vehicle down force (created mainly at the rear section) is
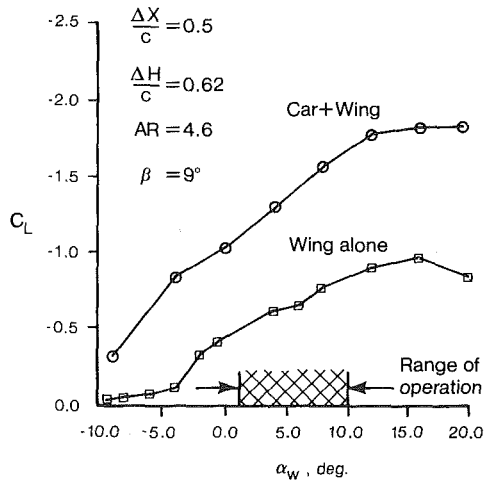
Fig. 10 Aerodynamic downforce versus wing angle of attack (based on vehicle's reference area, uncertainty in $C_L = \pm 0.03$, in $\alpha = \pm 0.2$ deg)
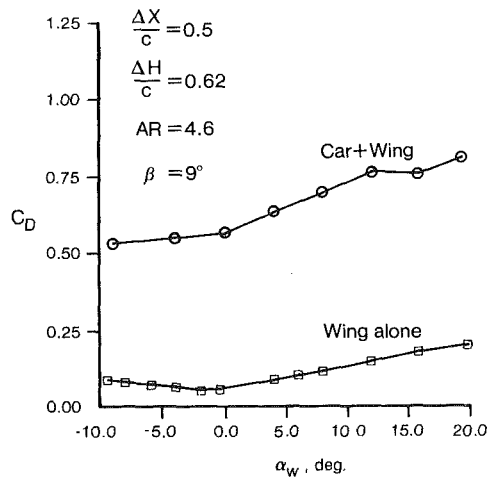
Fig. 11 Aerodynamic drag versus wing angle of attack (based on vehicle's reference area, uncertainty in $C_D = \pm 0.015$, in $\alpha = \pm 0.2$ deg)
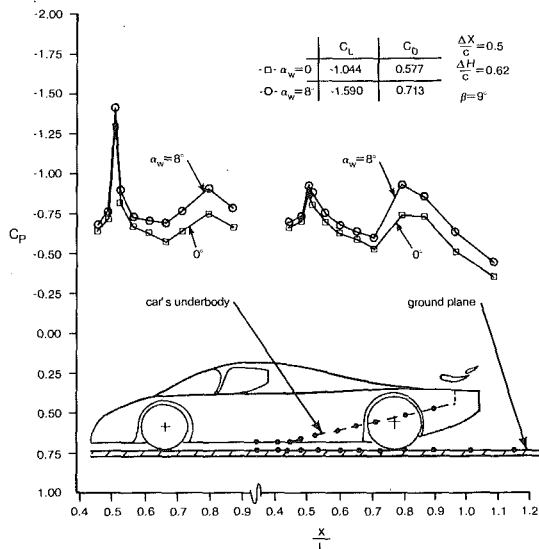
Fig. 12 Effect of wing angle of attack on the pressure distribution along the centerline of channel (both on vehicle's surface and on ground plane at $y/L = 0.082$, uncertainty in $C_p = \pm 0.05$, in $x/L = \pm 0.005$)
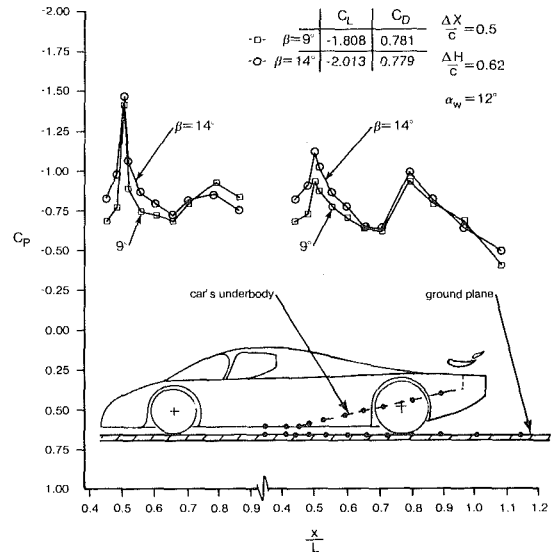
Fig. 13 Effect of underbody channel angle on the pressure distribution along the centerline of channel (both on vehicle's surface and on ground plane at $y/L = 0.082$, uncertainty in $C_p = \pm 0.05$, in $x/L = \pm 0.005$)
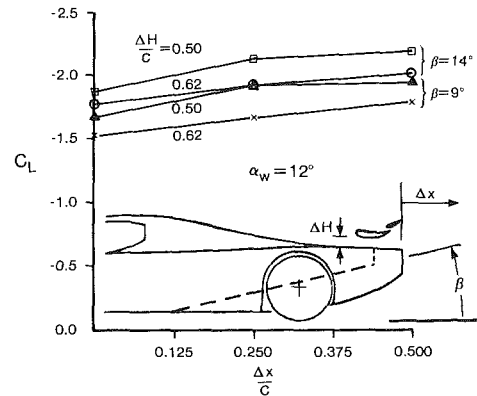
Fig. 14 Effect of rear wing position on vehicle's aerodynamic downforce (uncertainty in $C_L = \pm 0.03$, in $\Delta x/c = \pm 0.01$)

visible. On the other hand, an increase in the underbody channel angle will result in a similar increase in the body downforce (Fig. 13), but now the suction force change is generated near the inlet of the channel.

In view of the considerable interference between the rear wing and the downforce created by the vehicle's body (Figs. 4–12), the effect of varying the wing location was examined in Fig. 14. The motion of the wing was limited by race car regulations to a maximum vehicle height of $\Delta H/c = 0.62$ (and a minimum of $\Delta H/c = 0.50$ dictated by the side fin lower edge), and a maximum backward position that corresponds to $\Delta x/c = 0$ (so the Δx range in the figure is not allowed by IMSA race car regulations). Consequently, the wing height was varied between the above two positions only, and Fig. 14 shows that a lower wing position will have more downforce because of the wing/body interaction. This result is in disagreement with the data presented in [1] and [15], which show a loss in the negative lift, when the wing was lowered toward the vehicle's body.

Varying the horizontal position of the wing results in a moderate optimum in the downforce, as shown in Fig. 14. This optimum is obtained when the wing leading edge is in the vicinity of the channel trailing edge, resembling the interaction between the airfoils of a multi-element wing. Increasing the

channel angle β will increase the body's downforce because of the lower pressure coefficients shown in Fig. 13. Also, the cross-sectional area of the separated flow region behind the car will be reduced and in many cases a reduction in the base drag is observed (see drag data in the table inserted in Fig. 13).

Concluding Remarks

The aerodynamic downforce of enclosed wheel race car configurations, as the one tested here, is strongly affected by the interaction between the rear wing and the flow beneath the vehicle. Placing the rear wing's leading edge near the trailing edge of the underbody channels will increase vehicle's overall downforce. This aerodynamic interference resembles the interaction between the components of a multi-element wing.

Flow visualization indicated that the vehicle wheels deflect the underbody flow, causing strong lateral velocity components. When this inward flow turns sharply upward at the channel sides, two concentrated vortices are being created in each of the underbody channels. The suction force induced by these vortices enhances the downforce, which can be increased by sharper channel side edges (that will increase vortex strength).

The elevated ground-plane wind-tunnel technique is a simple method for reducing the effect of the wind-tunnel floor-boundary-layer (when compared with methods such as moving ground, blowing, suction, etc.). In this case of an enclosed-wheel race-car, this technique was able to capture the primary features of the flow field beneath the vehicle—thus allowing a much less expensive configuration development process. This was observed when model changes tested by the above method had a similar effect on racetrack performance.

References

1 Scibor-Rylski, A., "Experimental Investigation of the Negative Aerodynamic Lift Wings Used on Racing Cars," *Advances in Road Vehicle Aerodynamics*, BHRA Fluid Engineering, 1973, pp. 147–154.

2 Dominy, J. A., and Dominy, R. G., "Aerodynamic Influences on the Performance of the Grand Prix Racing Car," *Proceedings of the Institution of Mechanical Engineers*, Vol. 198 D, 1984, pp. 1–7.

3 Katz, J., "Investigation of Negative Lifting Surfaces Attached to an Open-Wheel Racing Car Configuration," SAE Paper No. 85-0283, Feb. 1985.

4 Wright, P. G., "The Influence of Aerodynamics on the Design of Formula One Racing Cars," *Int. Journal of Vehicle Design*, Vol. 3, No. 4, 1982, pp. 383–397.

5 Miranda, L. R., "Application of Computational Aerodynamics to Airplane Design," *J. Aircraft*, Vol. 21, No. 6, 1984, pp. 355–370.

6 Gross, D. S., and Sekcienski, W. S., "Some Problems Concerning Wind Tunnel Testing of Automotive Vehicles," SAE Paper 660385, June 1966.

7 Beauvais, F. N., Tignor, S. C., and Turner, T. R., "Problems of Ground Simulation in Automotive Aerodynamics," SAE Paper 680121, Jan. 1968.

8 Hucho, W. H., Janssen, L. J., and Schwarz, G., "The Wind Tunnel's Ground Plane Boundary Layer—Its Interference with the Flow Underneath Cars," SAE Paper 750066, Feb. 1975.

9 Fanger-Vexler, S., Katz, J., and Foux, A., "Full-Scale, On-Road Study of the Effect of Automobile Shape on its Aerodynamic Characteristics, and Comparison with Small-Scale Wind Tunnel Results," SAE Paper 850287, Feb. 1985.

10 Summa, J. M., and Maskew, B., "Predicting Automobile Aerodynamic Characteristics Using an Iterative Viscous/Potential Flow Technique," SAE Paper 830303, Feb. 1983.

11 Katz, J., "Calculation of the Aerodynamic Forces on Automotive Lifting Surfaces," JOURNAL OF FLUIDS ENGINEERING, Vol. 107, No. 4, 1985, pp. 438–443.

12 Katz, J., "Aerodynamic Model for Wing-Generated Down Force on Open-Wheel Racing-Car Configurations," SAE Paper 860218, Feb. 1986.

13 Carr, G. W., "A Comparison of the Ground-Plane-Suction and Moving-Belt Ground-Representation Techniques," SAE Paper 880249, Feb. 1988.

14 Bonis, B., and Quagliotti, F. B., "A Study of the Validity of Fixed-Ground Testing for Formula 1 Racing Cars," SAE Paper 860092, Feb. 1986.

15 Beccio, S., Lombardi, C., Garrone, A., and Berta, C., "Endurance Group C1 Lancia Racing Car-Definition of Rear Wing Aerodynamic Contour," SAE Paper 870727, Jan. 1987.

16 Hackett, J. E., Sampath, S., and Phillips, C. G., "Determination of Wind Tunnel Constraint Effects by a Unified Wall Pressure Signature Method," NASA CR-166, 186, June 1981.

17 Carr, G. W., and Stapleford, W. R., "Blockage Effects in Automotive Wind-Tunnel Testing," SAE Paper No. 860093, Feb. 1986.

18 Hucho, W. H., *Aerodynamics of Road Vehicles*, Butterworth & Co. Ltd., 1987, pp. 419–422.

19 Poncini, G. F., and Di Giusto, N., "Experimental Methods for Wind Tunnel Testing of Racing Cars with Ground Effect," *Int. J. of Vehicle Design*, Technological Advances in Vehicle Design Series SP3, Impact of Aerodynamics on Vehicle Design, 1983, pp. 480–492.

20 George, A. R., and Donis, J. E., "Flow Patterns, Pressures, and Forces on the Underside of Idealized Ground Effect Vehicles," Aerodynamics of Transportation-II, Fluids Engineering Division, ASME, FED-Vol. 7, 1983, pp. 69–79.

21 Metz, D., and Maddock, J., "Optimal Ride Height and Pitch Control for Championship Race Cars," *Automatica*, Vol. 22, No. 5, 1986, pp. 509–520.

22 Verghaagen, N. G., and Kruisbrick, A. C. H., "Entrainment Effect of a Leading-Edge Vortex," *AIAA J.*, Vol. 25, No. 8, 1987, pp. 1025–1032.

The Law of the Wall for Swirling Flow in Annular Ducts

R. J. Kind

F. M. Yowakim

S. A. Sjolander

Department of Mechanical and Aerospace
Engineering,
Carleton University,
Ottawa, Canada

Expressions for the logarithmic portion of the law of the wall are derived for the axial and tangential velocity components of swirling flow in annular ducts. These expressions involve new shear-velocity scales and curvature terms. They are shown to agree well with experiment over a substantial portion of the flow near both walls of an annulus. The resultant velocity data also agree with the law of the wall. The success of the proposed logarithmic expressions implies that the mixing-length model used in deriving them correctly describes flow-velocity behavior. This model indicates that the velocity gradient at any height y in the near-wall region is determined by the wall shear stress, not by the local shear stress. This suggests that the influence of wall shear stress is dominant and that it determines the near-wall wall flow even in flows with curvature and pressure gradient. A physical explanation is suggested for this.

Introduction

Wall-bounded swirling flows occur in a variety of applications, including turbomachinery, cyclones, combustion equipment, and cooling passages of electrical machines. A knowledge of the flow behavior near walls is important for predictive purposes, particularly as regards skin friction and heat transfer. Swirling flows in annuli are three-dimensional with substantial wall curvature, both convex and concave. The literature contains little information on behavior of near-wall mixing length or length scale or on validity of the usual law of the wall for these flows. The present paper addresses these questions.

A generalized form of the law of the wall has been deduced by extending the mixing-length relation proposed by Galbraith et al. (1977) to swirling flows. The generalized law can be applied separately to the axial and tangential velocity components, or to the resultant velocity. The key innovation is identification of the appropriate shear-velocity scale for each component direction. It is shown that the generalized form of the law of the wall agrees well with measurements of several swirl flows in an annulus. The experiments are described elsewhere by Yowakim and Kind (1988) but the data are presented here in law-of-the-wall format. The success of the extended mixing-length model has interesting implications regarding turbulence structure in the near-wall region; these are pointed out and discussed.

Background

Curvature has large effects on behavior of turbulent flows. Bradshaw (1973) points out in his review that the effects are often an order of magnitude larger than would be expected on the basis of dimensional arguments. It was apparent at the

1980-1981 AFOSR–HTTM-Stanford Conference on Complex Turbulent Flows (Kline et al., 1982) that prediction of turbulent flows over curved walls is particularly difficult. Scott and Rask (1973) and others have measured swirling flows in annuli. Their results showed that swirling flows behave in a manner consistent with that found in numerous investigations of two-dimensional flows in curved channels: wall shear stress and intensity of turbulent fluctuations are substantially increased near the concave wall and decreased near the convex wall. This is what one would expect in a view of the Rayleigh stability criterion. Some earlier work, such as that of Meroney and Bradshaw (1975), suggested that the law of the wall would apply only in modified form. However it has since been established that the usual flat-plate form of the law of the wall persists near both convex and concave walls, for both mild ($\delta/r_w \sim 0.01$) curvature (Ramaprian and Shivaprasad, 1978; Hunt and Joubert, 1979; and others) and strong ($\delta/r_w \sim 0.1$) curvature (So and Mellor, 1973; Ellis and Joubert, 1974; and others). For weak curvature the law of the wall appears to extend over about the same range as for plane flows. Ellis and Joubert found that strong curvature substantially reduced the value of (yU^*/ν) up to which the law of the wall applies in their fully developed curved-channel flow. So and Mellor, on the other hand, state that the velocity profiles in their convex-wall boundary layer deviate from the logarithmic law at about the same point as for their flat-plate profile. Taylor-Gortler vortices are usually present near the concave wall and may sometimes limit the range of the law of the wall.

The persistence of the usual law of the wall in curved channel flows indicates that curvature does not have a direct effect on the turbulence structure near the walls. It does however, have a strong indirect effect through its influence on the wall shear stress levels. Also, strong curvature appears to reduce the range over which the law applies.

Scott and Rask (1973) used Preston tubes and Clauser plots to determine wall shear stresses in their swirl flows. They thus

assumed existence of the flat-plate form of the law of the wall. Other than this, they did not consider the near-wall flow in detail.

Van den Berg (1975) has examined and modified the law of the wall for three-dimensional boundary layers with significant skew due to cross-stream pressure gradients. His results include formulae for prediction of skew angle in the wall-law region; these agree well with experimental data. The present work focuses on effects of swirl and is not directly concerned with skew. Although three-dimensional, swirl flows in annuli are not necessarily highly skewed near the walls because cross-stream pressure gradients tend to be small. Only modest skew was present in the experiments of Yowakim and Kind (1988); the maximum variation of flow angle across the annulus was four degrees. Because their measurements are the only ones of swirl flows in annuli to include Reynolds stresses and reliable wall shear stresses, the present paper relies heavily on their data for support. Its results can therefore only be applied with confidence to swirling flows with skew less than about five degrees.

Derivation of the Generalized Law of the Wall

The fully turbulent, or logarithmic, portion of the law of the wall is considered first for each of the two velocity components, axial and tangential, of an axisymmetric swirling flow.

It is well known that the logarithmic law can be derived for two dimensional flows by substituting the mixing length relation

$$l = ky \qquad (1)$$

into the definition of mixing length

$$\frac{\tau}{\rho} = l^2 \left(\frac{dU}{dy} \right)^2 \qquad (2)$$

and integrating. The symbol k is the von Karman constant and y is the distance from the wall. This derivation requires the assumption that the shear stress, τ, remains constant and equal to the wall value, τ_w, near the wall. Galbraith et al. (1977) point out that the logarithmic law is quite "robust" and persists in many cases where τ is definitely not constant near the wall. Notable examples are fully developed pipe flow and boundary layers in pressure gradients: in both cases $d\tau/dy$ must be nonzero to maintain equilibrium with pressure-gradient forces. Cases were identified where the logarithmic law persisted even though τ differed from τ_w by a factor of four. Galbraith et al. recommend that equation (1) be replaced by the modified mixing length model

$$l = ky\sqrt{\tau/\tau_w} \qquad (3)$$

Their recommendation is based on the fact that substitution of equation (3) into equation (2) leads to the logarithmic law without the need to assume constancy of τ. Equation (3) is thus in accord with the experimental fact that the logarithmic law is quite persistent even when τ is known to vary, "a fact of life that we ignore at our cost" according to the Ad-Hoc Committee of Computers at the 1980-1981 Conference on Complex Turbulent Flows (Kline et al., 1982). Rodi and Scheuerer (1986) recently derived improvements to the $k - \epsilon$ turbulence model on the basis of the persistence of the logarithmic law in adverse pressure gradients.

The approach of the preceding paragraph is adopted for both component directions in annular swirl flows. It should be noted that both the axial and the tangential shear stress, τ_{rx} and $\tau_{r\theta}$, must vary quite rapidly in the radial direction in such flows because they must change sign from the inner to the outer wall of the annulus. Following Lilley and Chigier (1971), the two components of mixing length, l_{rx} and $l_{r\theta}$, are defined, for the fully-turbulent region, by

$$\frac{\tau_{rx}}{\rho} = l_{rx}^2 \left(\frac{\partial U}{\partial r} \right) \left[\left(\frac{\partial U}{\partial r} \right)^2 + \left(r \frac{\partial}{\partial r} \left(\frac{W}{r} \right) \right)^2 \right]^{1/2} \qquad (4)$$

$$\frac{\tau_{r\theta}}{\rho} = l_{r\theta}^2 \left(r \frac{\partial}{\partial r} \left(\frac{W}{r} \right) \right) \left[\left(\frac{\partial U}{\partial r} \right)^2 + \left(r \frac{\partial}{\partial r} \left(\frac{W}{r} \right) \right)^2 \right]^{1/2} \qquad (5)$$

These relations are analogous to equation (2). U and W are the mean axial and tangential velocity components. The mixing length components are modelled by analogy with equation (3), that is:

$$l_{lx} = ky\sqrt{\tau_{rx}/\tau_{x,w}} \text{ and } l_{r\theta} = ky\sqrt{\tau_{r\theta}/\tau_{\theta,w}} \qquad (6)$$

where the subscript w denotes values at the wall. The experimental data reported by Yowakim and Kind (1988) support these relations. Substitution of equation (6) into equations (4) and (5) gives expressions for the wall shear stress components $\tau_{x,w}$ and $\tau_{\theta,w}$. These can be combined to obtain an expression for the resultant wall shear stress, τ_w. Substitution of this expression into those for $\tau_{x,w}$ and $\tau_{\theta,w}$ gives the following simpler expressions

$$\frac{\tau_{x,w}}{\rho} = ky\sqrt{\frac{\tau_w}{\rho}} \frac{\partial U}{\partial r} \qquad (7)$$

$$\frac{\tau_{\theta,w}}{\rho} = ky\sqrt{\frac{\tau_w}{\rho}} r \frac{\partial}{\partial r} \left(\frac{W}{r} \right) \qquad (8)$$

The following velocity scales are now defined:

$$U^* = \sqrt{\tau_{x,w}/\rho} \quad w^* = \sqrt{\tau_{\theta,w}/\rho} \quad Q^* = \sqrt{\tau_w/\rho} \qquad (9)$$

$$U^{**} = U^{*2}/Q^* \quad W^{**} = W^{*2}/Q^* \qquad (10)$$

_____ Nomenclature _____

B = constant in logarithmic laws
D_h = hydraulic diameter, $2(r_o - r_i)$
k = von Karman constant
l = mixing length
Q = resultant mean flow velocity
Q^* = a shear velocity scale; see equation (9)
r = radial coordinate; radius of curvature
r_{eff} = effective radius of curvature of streamlines at walls

U = axial component of mean flow velocity
$\bar{U}$ = mean axial velocity in annular duct
U^*, U^{**} = shear velocity scales; see equations (9) and (10)
W = tangential component of mean flow velocity
W^*, W^{**} = shear velocity scales; see equations (9) and (10)
x = axial distance from inlet guide vanes

y = distance from wall
δ = shear layer thickness
ν = kinematic viscosity
ρ = density
τ = shear stress

Subscripts

i = inner wall
o = outer wall
w = wall values
x = axial component
θ = tangential component

Substitution of equations (9) and (10) into (7) and (8) and integration, recognizing that $dy = \pm dr$, yields the logarithmic laws:

$$\frac{U}{U^{**}} = \frac{1}{k} \ln\left(\frac{yU^{**}}{\nu}\right) + B \qquad (11)$$

$$\frac{W}{W^{**}} = \left(1 \pm \frac{y}{r_w}\right)\left[\frac{1}{k} \ln\left(\frac{yW^{**}}{\nu(1 \pm y/r_w)}\right) + B\right] \qquad (12)$$

The minus signs in equation (12) apply for the outer wall. Equation (11), and also equation (12) when the wall radius, r_w, becomes large, clearly has the same form as the usual logarithmic law of the wall for two-dimensional flows. This suggests that B should have its usual value of about 5.5, a choice which gives very good agreement with the experimental data. The velocity scales, U^{**} and W^{**}, in equations (11) and (12), respectively, are different from the scales U^* and W^* that one might intuitively select. Therein lies the main novelty of these relations. If the derivation were to be applied for the direction of τ_w, the velocity scale would be (Q^{*2}/Q^*) and the usual logarithmic law would be obtained, albeit with curvature terms similar to those in equation (12) since the effective radius of curvature is not infinite for the τ_w direction.

In the viscous sub-layer and buffer layer the mixing length relations of equation (6) continue to be used, but they are multiplied by the van Driest (1956) damping factor, DF:

$$DF = 1 - \exp(-yQ^*/26\nu) \qquad (13)$$

This implies the assumption that the law of the wall assumes its usual form in the viscous sub-layer, namely

$$Q/Q^* = yQ^*/\nu \qquad (14)$$

Q is the resultant velocity.

Application to Experimental Results

Only the experiments reported by Yowakim (1985) and Yowakim and Kind (1988) provide sufficiently detailed information on wall shear stresses and velocity distributions to permit comparison with the relations derived in the preceding section. Four air flows, having nominal swirl angles of 0, 15, 30, and 45 degrees, were measured. The annular duct had inner and outer radii, r_i and r_o, of 0.127 and 0.203m, respectively. Reynolds number based on mean axial velocity and hydraulic diameter, $D_h = 2(r_o - r_i)$, was 3.1×10^5. Swirl was imparted by a row of adjustable inlet guide vanes at entry to the annulus ($x = 0$). The flow left the annulus via a set of outlet guide vanes which removed the swirl. The two sets of vanes were 1.8m apart, equivalent to 12.3 hydraulic diameters. There were no struts or other obstructions over this distance.

At the first measurement station ($x/D_h = 1.65$) the dynamic pressure at mid-radius was uniform within 3 percent. The flow was not fully developed, so that the velocity profiles changed gradually with x. The mean axial velocity, $\bar{U}$, must however remain constant since the flow was incompressible; the data satisfied this requirement within ± 0.7 percent. Even though the flow is not fully developed the static pressure must decrease with x, as in the entry region of a pipe. Details on the experiments are given by Yowakim and Kind (1988).

Values of wall shear stress are of course required if velocity data are to be compared with the law of the wall. The comparison process is usually somewhat "circular" because indirect methods such as Preston-tube measurements or Clauser plots are used to determine wall shear stresses. These two methods were used in the present work. However there are independent corroborating data in the form of the radial distribution of Reynolds shear stresses measured in the flow by means of hot wire anemomentry. Extrapolation of these data to the walls gives wall shear stresses in very good agree-
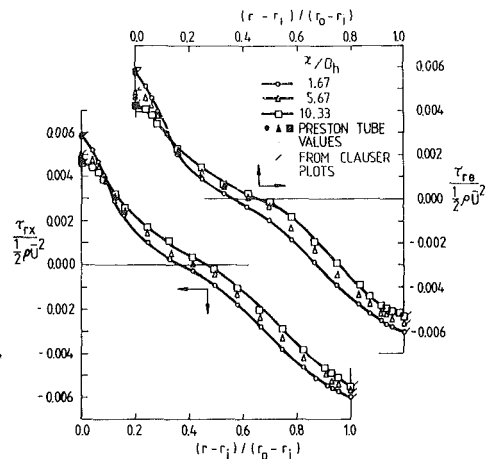
Fig. 1 Radial distributions of axial and tangential shear stress in 45-degree swirl flow. Wall values are from Clauser plots. Preston-tube measurements are also shown for the inner wall.

ment with those obtained by Clauser plots and Preston-tube measurements. A typical example of this can be seen in Fig. 1. The estimated uncertainty of the wall shear stress values is $\pm 0.0001\,\rho\bar{U}^2$; for the Reynolds shear stresses $\rho\overline{uv}$ and $\rho\overline{uw}$ it is ± 15 and ± 20 percent, respectively. The data satisfy axial and angular momentum conservation within 1.7 percent of initial momentum or angular momentum. A more complete discussion of consistency checks and uncertainty appears in Yowakim and Kind (1988). The data are believed to be of high quality.

The Clauser plotting technique is as follows. Curves of equation (11) are plotted in the form U versus (y/ν) for a number of values of the velocity scale U^{**}. Similarly, equation (12) is plotted as W versus (y/ν) with W^{**} as the parameter; separate charts of equation (12) are required for the inner and outer walls. The U and W velocity data are plotted on the appropriate chart. U^{**} and W^{**} can be read from the charts just as from a Clauser chart for a two-dimensional smooth-wall flow. Q^*, U^* and W^* are then easily calculated using equations (9) and (10); note that

$$Q^{*2} = (U^{**2} + W^{**2}).$$

The axial velocity data for flows having nominal swirl angles of 15, 30, and 45 degrees are compared with equation (11) in Fig. 2. The data for both the inner and outer walls are seen to agree with the equation for (yU^{**}/ν) up to about 1000. This corresponds to $(y/(r_o - r_i)) \approx 0.15$ so that the law of the wall for the axial velocity prevails over about 30 percent of the annulus height. K and B in equations (11) and (12) have been assigned the values 0.4 and 5.5, respectively; these are within the usual ranges for these constants. The tangential velocity data are compared with equation (12) in Fig. 3. Note that when the curvature term (y/r_w) is not small equation (12) produces distinct curves for different values of $(W^{**}r_w/\nu)$, reflecting the increasing relative importance of the curvature terms as W^{**} decreases or wall radius, r_w, decreases. Near both walls the data agree well with equation (12) up to $(y/r_w) \sim 0.04$ for the 15 and 30 degree swirl flows and up to $y/r_w \sim 0.1$ for the 45 degree flow. Agreement between equations (11) and (12) and the corresponding data prevails over about the same regions of the flows, except near the inner wall for the 15 and 30 degree swirl flows where equation (12) agrees with the data over only half as thick a region as equation (11). Equation (12) appears to over-estimate the effects of curvature at the lower values of $(W^{**}r_w/\nu)$ near the inner wall. If the data had been reduced using U^* or W^* as the velocity scale, instead of U^{**} or W^{**}, there would have been no agreement with the logarithmic law. This is illustrated in Fig. 4.

Fig. 2 Semi-logarithmic plots of axial velocity profiles at inner and outer annulus walls for 15, 30, and 45 degree swirl flows. $U^{**} \approx 1.4$ m/s for all profiles.

Fig. 3 Semi-logarithmic plots of tangential velocity profiles at inner and outer annulus walls for 15, 30, and 45 degree swirl flows. $W_i^{**} \approx .0.4$, 0.8, 1.2 m/s; $W_0^{**} \approx 0.4$, 0.9, 1.4 m/s; $(W^{**}r_w/\nu)_i \approx 0.3$, 0.6,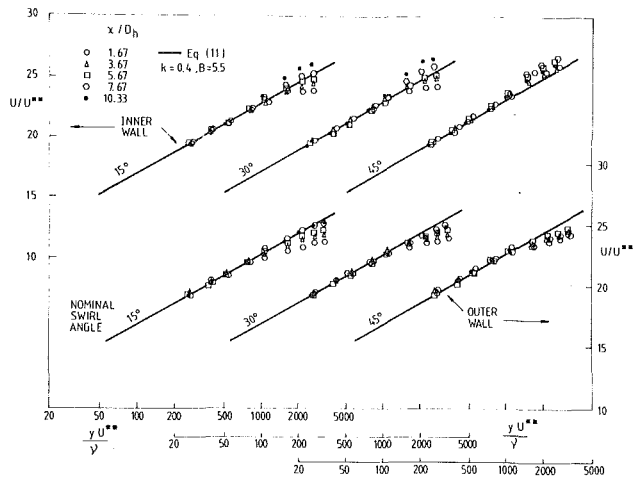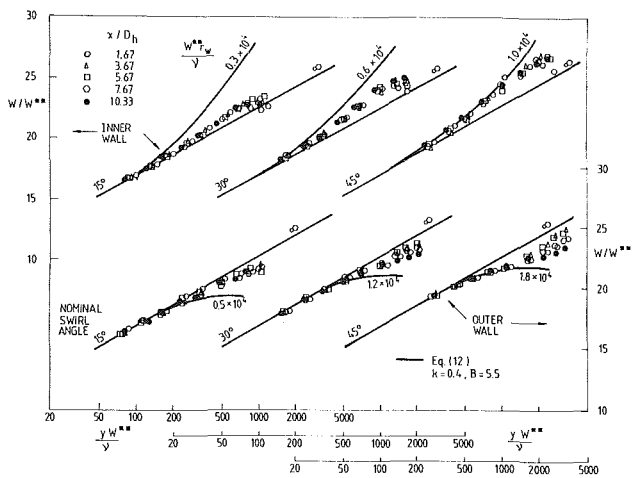 1.0×10^4; $(W^{**}r_w/\nu)_0 \approx 0.5$, 1.2, 1.8×10^4; for 15, 30, and 45 degree swirl flows, respectively.

The captions of Figs. (2) and (3) include nominal values of the parameters U^{**}, W^{**} and $W^{**}r_w/\nu$. Detailed information on wall shear stresses is available in Yowakim and Kind (1988) or Yowakim (1985).

Figure 5 shows the resultant velocity data for the 45 degree swirl flow in law-of-the-wall coordinates. As expected, the data agree with the logarithmic law. The equation plotted in Fig. 5 is identical in form to equation (12); Q^* is used as the velocity scale and the effective wall-streamline radius of curvature (equal to $2r_w$ for this case) is used for r_w. For the 0, 15, and 30 degree swirl flows the agreement between resultant velocity data and the logarithmic law is essentially the same as that seen in Fig. 5. It should be noted that the resultant-velocity data are best fitted by the equation when the von Karman constant, k, has the value 0.418 rather than 0.4 as used in Figs. 2 and 3. The reasons for the change in the best value of k are not apparent. There is, however, some disagreement over the values of the logarithmic-law constants and values in the range 0.40 to 0.42 are commonly used. For Fig. 5, k and B are assigned the values used by Patel (1973) and Patel et al. (1985). All the figures could, of course, have been plotted with $k = 0.41$ but the agreement would not have been quite as good.

Townsend (1961) and Patel (1973) have considered the effects of stress gradients in the near-wall region. Their equation
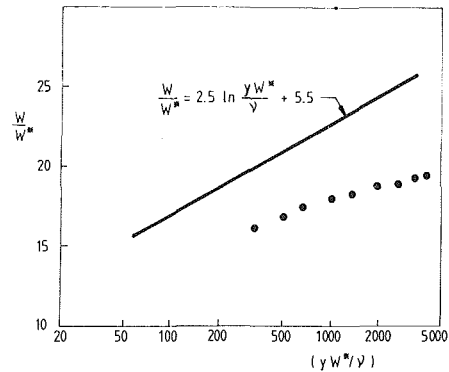
Fig. 4 Tanagential velocity data for 45 degree swirl flow, $x/D_h = 10.3$, outer wall, reduced using W^* as the velocity scale
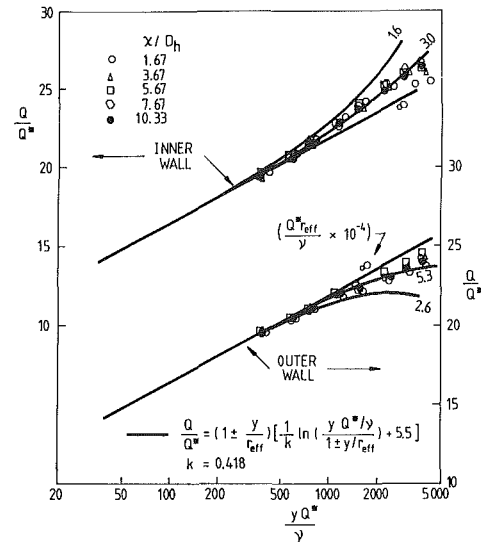
Fig. 5 Semi-logarithmic plot of the resultant velocity profiles at inner and outer annulus walls for the 45 degree swirl flow. $(Q^*r_{eff}/\nu)_i \approx 3 \times 10^4$; $(Q^*r_{eff}/\nu)_0 \approx 5.3 \times 10^4$.

for the velocity distribution in the fully turbulent near-wall region can be derived using the expression $l = ky$ for the mixing length. When applied, for example, to the present data for the 45 degree swirl flow at the inner wall of the annulus, their equation indicates that (Q/Q^*) at $(yQ^*/\nu) \approx 1000$ should be more than 2.5 units higher than the value given by the conventional logarithmic law. From Fig. 5 it is clear that this is at variance with the present data. This suggests that the actual behavior of the mixing length is better represented by equation (3).

Discussion

The work reported in this paper indicates that the law of the wall applies over substantial portions of the flow near both the inner and outer walls for swirling flow in annular ducts. This is true for the axial and tangential velocity components as well as for the resultant velocity, provided that the expressions presented herein are used for the axial and tangential components.

These findings can be incorporated into finite-difference computational methods simply by use of the mixing-length model represented by equations (4), (5), (6), and (13) for the near-wall region. The logarithmic relations (11) and (12) can also be used to provide good initial profiles in the near-wall region for starting predictive computations of swirling flows. Both of these points have been demonstrated by Reddy et al. (1987). Their computations produced velocity profiles which, in the near-wall regions, were in excellent agreement with the

experimental data presented in this paper and with expected behavior in the laminar sub-layer and buffer layer.

The persistence of the law of the wall in swirling flows in annular ducts is generally consistent with its persistence in two-dimensional flows, noted in sections 2 and 3 of this paper.

The present work supports the validity of the mixing-length relations, equations (4), (5) and (6). Equations (7) and (8) and a similar relation between the resultant wall shear stress and the resultant velocity gradient follow directly. The latter equations imply that velocity gradients in the near-wall region are determined by the *wall* shear stress, not by the local shear stress in the flow at height y. Recall (section 3) that the local shear stress varies rapidly with y in the flows under consideration here. Galbraith et al. (1977) make this point for two-dimensional flows; the present work indicates that it is also true for three-dimensional flows with substantial curvature, at least when skew is small.

The central importance of the wall shear stress is perhaps consistent with the discovery by Head and Bandyopadhyay (1979, 1981) that turbulent boundary layers are heavily populated by large-scale vortex loops. These appear to originate very close to the wall, possibly as the bursts and sweeps identified by Kline and his co-workers (Kim et al., 1971). The strength of the loops should therefore be determined by the vorticity at the wall, which is equal to $\tau_w/\rho\nu$. If, as seems likely, the vortex loops play an important or even dominant part in the momentum transport across the layer, then it is plausible that the near-wall velocity distribution depends only on the wall shear stress and fluid properties and that the direct effects of pressure gradient, curvature and shear stress variations are unimportant. That is what the aforementioned evidence suggests. Of course, pressure gradient and wall curvature have important indirect effects on the near-wall region through their influence on the wall shear stress. In the outer part of the layer, time scales are longer and the inclination of the vortex loops will reflect to some extent the upstream history of the layer. Therefore one would not expect the outer portion of the velocity profile to depend only on local conditions.

Conclusions

Expressions are presented for the logarithmic portion of the law of the wall for the axial and tangential velocity components of swirling flows in annular ducts. These expressions are similar in form to the usual law of the wall but make use of new shear-velocity scales.

The new expressions are shown to agree well with experimental data near both the inner, convex, wall and the outer, concave wall of an annular duct. Agreement prevails over a substantial portion of the flow. The data for resultant velocity also agree with the logarithmic law, which then has its usual form except that curvature terms are present.

The success of the logarithmic laws implies validity of the mixing-length model used in deriving them. This model indicates that the velocity gradient at any height y in the near-wall region is determined by the *wall* shear stress. That is, it is the wall shear stress, not variations of the local Reynolds shear stress, which determines the near-wall flow, even in flows with curvature and pressure gradient.

Acknowledgment

References

Bradshaw, P., 1973, "The Effects of Streamline Curvature on Turbulent Flow," *AGARDograph* no. 169.

Ellis, L. B., and Joubert, P. N., 1974, "Turbulent Shear Flow in a Curved Duct, *Journal of Fluid Mech.*, Vol. 62, pp. 65–84.

Galbraith, R. A. McD., Sjolander, S. A., and Head, M. R., 1977, "Mixing Length in the Wall Region of Turbulent Boundary Layers," *Aeronautical Quarterly*, Vol. XXVII, pp. 97–110.

Head, M. R., and Bandyopadhyay, P., 1979, "Flow Visualization of Turbulent Boundary Layer Structure," *AGARD Conference Proceedings* no. 271, Paper 25.

Head, M. R., and Bandyopadhyay, P., 1981, "New Aspects of Turbulent Boundary Layer Structure," *Journal of Fluid Mechanics*, Vol. 107, pp, 297–338.

Hunt, I. A., and Joubert, P. N., 1979, "Effects of Small Streamline Curvature on Turbulent Duct Flow," *Journal of Fluid Mechanics*, Vol. 91, pp. 633–659.

Kim, H. T., Kline, S. J., and Reynolds, W. C., 1971, "The Production of Turbulence Near a Smooth Wall in a Turbulent Boundary Layer," *Journal Fluid Mechanics*, Vol. 50, pp. 133–160.

Kline, S. J., Cantwell, B. J., and Lilley, G. M. (eds.), 1982, *Proceedings of the 1980-81 AFOSR-HTTM-Stanford Conference on Complex Turbulent Flows*, Vol. 2, Department of Mechanical Engineering, Stanford University, Stanford, Calif.

Lilley, D. G., and Chigier, N. A., 1971, "Nonisotropic Turbulent Stress Distribution in Swirling Flows From Mean Value Distributions," *International Journal Heat Mass Transfer 14*, Vol. 14, pp. 573–585.

Meroney, R. N., and Bradshaw, P., 1975, "Turbulent Boundary-Layer Growth Over a Longitudinally Curved Surface," *AIAA Journal*, Vol. 13, pp. 1448–1453.

Patel, V. C., 1973, "A Unified View of the Law of the Wall Using Mixing-Length Theory," *Aeronatuical Quarterly*, Vol. XXIV, pp. 55–70.

Patel, V. C., Rodi, W., and Scheuerer, G., 1985, "Turbulence Models for Near-Wall and Low Reynolds Number Flows: A Review," *AIAA Journal*, Vol. 23, pp. 1308–1319.

Ramaprian, B. R., and Shivaprasad, B. G., 1978, "The Structure of Turbulent Boundary Layers Along Mildly Curved Surfaces," *Journal of Fluid Mechanics*, Vol. 85, pp. 273–303.

Reddy, P. M., Kind, R. J., and Sjolander, S. A., 1987, "Computation of Turbulent Swirling Flow in an Annular Duct," *Proceedings of the 5th International Conference on Numerical Methods in Laminar and Turbulent Flow*, Montreal, Pineridge Press, Swansea, pp. 470–481.

Rodi, W., and Scheuerer, G., 1986, "Scrutinizing the k–ε Turbulence Model Under Adverse Pressure Gradient Conditions," ASME JOURNAL OF FLUIDS ENGINEERING, Vol. 108, pp. 174–179.

Scott, C. J., and Rask, D. R., 1973, "Turbulent Viscosities for Swirling Flow in a Stationary Annulus," ASME JOURNAL OF FLUIDS ENGINEERING, Vol. 95, pp. 557–566.

So, R. M. C., and Mellor, G. L., 1973, "Experiment on Convex Curvature Effects in Turbulent Boundary Layers," *Journal of Fluid Mechanics*, Vol. 60, pp. 43–62.

Townsend, A. A., 1961, "Equilibrium Layers and Wall Turbulence," *Journal of Fluid Mechanics*, Vol. 11, pp. 97–120.

Van den Berg, B., 1975, "A Three-Dimensional Law of the Wall for Turbulent Shear Flows," *Journal Fluid Mechanics*, Vol. 70, pp. 149–160.

Van Driest, E. R., 1956, "On Turbulent Flow Near a Wall," *Journal of the Aeronautical Sciences*, Vol. 23, pp. 1007–1011.

Yowakim, F. M., 1985, "Experimental Investigation of Turbulent Swirling Flow in an Annulus," Ph.D. dissertation, Carleton University, Ottawa, Canada.

Yowakim, F. M., and Kind, R. J., 1988, "Mean Flow and Turbulence Measurements of Annular Swirling Flows," ASME JOURNAL OF FLUIDS ENGINEERING, Vol. 110, pp. 257–263.

Measurements of the Flow and Turbulence Characteristics of Round Jets in Crossflow

S. A. Sherif*
Mem. ASME

R. H. Pletcher
Fellow ASME

Department of Mechanical Engineering,
Iowa State University,
Ames, Iowa

Measurements of the velocity and turbulence characteristics of a round turbulent jet in crossflow are reported. The experiments were conducted in a water channel, 8.53 m long, 0.61 m wide, and 1.067 m deep, of the recirculation type. Water was injected vertically upward from a circular pipe located near the channel bottom to simulate the turbulent jet. Normal and 45 deg-slanted fiber-film probes along with appropriate anemomenters and bridges were operated in the constant temperature mode to measure mean velocities, turbulence intensities, Reynolds stresses, structural parameters, correlation coefficients, and the turbulent kinetic energy. The measurements were carried out in the jet and its wake both in and outside the jet plane of symmetry. Details of the jet-wake cross section (including the vortex region) were revealed at a number of downstream locations using constant velocity and turbulence intensity contours.

Introduction

Jets discharging into flowing or quiescent ambients have been a subject for investigators for many years since they model heated and unheated discharges from power plants into neighboring water bodies, exhaust gases from combustion systems of aircraft or spacecraft, and gaseous jets from cooling towers or stacks.

Literature on jets and plumes discharging into cross-flowing streams may be classified as analytical, computational, or experimental. Most of the analytical work done so far on jets and plumes in crossflows has been directed toward finding closed-form expressions for the trajectory of the jet or plume. Other theoretical work focused on studying the mechanism by which the ambient fluid is entrained by the jet fluid. Still others tried to study the whole problem of interaction between a jet and a crossflow using purely theoretical analyses (e.g., using matched asymptotic expansions (Werner, 1969)). Computational work, using finite difference techniques, is somewhat limited (Patankar et al., 1977; Chien and Schetz, 1975; Hwang, 1978; Hwang and Pletcher, 1977, 1978 a, b; White, 1980; Baker et al., 1987; Roth, 1987; Claus, 1985; Sykes et al., 1986 and Harloff and Lytle, 1988). Experimental investigations have been mostly devoted to measuring the jet axis, jet spread, and the mean velocity field. Studies devoted to measuring the mean temperature field are not as numerous as those dealing with the velocity field (Ramsey, 1969; Ramsey and Goldstein, 1970; and Andreopoulos, 1984). Turbulence measurements are even fewer (Andreopoulos, 1982; Andreopoulos and Rodi, 1984; and Crabb et al., 1980). A small

number of experimental investigations were solely devoted to studying the jet-wake interference effects and related vorticity generation mechanisms (Margason, 1969a; 1969b; and McMahon, et al., 1971). Others studied the static pressure field associated with the jet in a cross flow (Volger, 1963; Bradbury and Wood, 1965; Wooler, et al., 1967; McMahon and Mosher, 1979; Rosen, et al., 1969; and Cubbison, et al., 1961). The latter type of measurement is particularly important in documenting the behavior of the jet in the V/STOL aircraft. A more complete survey of literature on jets in a cross flow can be found in Sherif (1985).

The jet in a crossflow is a typical example of a complex free turbulent shear flow. These flows are, generally, more difficult to model or predict than wall boundary-layer flows primarily because of the curvature of the shear layer and the complex turbulent flow pattern in the jet wake region (Chan and Kennedy, 1972; Keffer, 1969, Pratte and Baines, 1968; Bergles et al., 1975; Keffer and Baines, 1963; Platten and Keffer, 1968; and Rodi, 1982) (see Fig. 1). This experimental study was undertaken, in part, to provide additional data to guide the development, improvement, and evaluation of better prediction methods and turbulence models for these flows. In addition, the data should be helpful in terms of increasing understanding of the complex interaction mechanism between the turbulent jet and the cross stream.

The present paper reports on the velocity and turbulence fields of an isothermal jet in crossflow at velocity ratios of 2, 4, and 6. The mean velocity field is described first in terms of velocity magnitudes measured in the streamline direction. Detailed measurements of the streamwise and vertical components of velocity are presented next. The turbulence data are also given in terms of an overall turbulence intensity measured in the mean flow direction, followed by detailed data for the turbulence structure including the turbulent

Fig. 1 The round turbulent jet in a crossflow
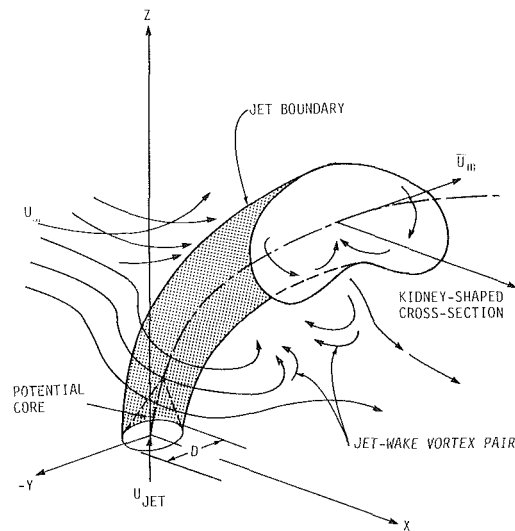

Fig. 2 Jet injection system

stresses, structural parameter, correlation coefficient, and the kinetic energy of turbulence. The measurements were carried out in the jet and its wake both in and outside the jet plane of symmetry.

Experimental Apparatus

The measurements were carried out in a semiclosed circuit water channel at Iowa State University. The channel is 8.53 m long and 0.61 m × 1.067 m in cross section. The water circulated from an inlet tank through a transition section (approximate area contraction was 5.25:1) to the channel and then to the pump suction in the turning tank. Water was returned through an overhead pipe to the inlet tank which is equipped with a honeycomb, a metal screen, and a 152.4 mm layer of Scott industrial foam for the purpose of providing a uniform stream velocity with a low level of turbulence. Probes were positioned in three directions by a motor driven traversing arrangement which could be controlled manually or by a computer.

The test platform was formed by an aluminum plate, 12.7 mm thick, 0.457 m wide, and 1.829 m long with a rounded (1:2 ellipse) leading edge and a trailing edge flap. The platform was located 152 mm above the channel floor. The plate length was chosen taking into account the range of jet trajectories for different jet inlet conditions and also considering space limitations. The plate width was chosen so as not to interfere with the turbulent boundary layers already developed on the chan-

nel sides. Two false sidewalls having a thickness of 8.73 mm, a height of 0.965 m and the same plate length of 1.829 m were installed on both sides of the plate to promote two-dimensionality for the flow and to serve as supporting members for the plate. Water was injected vertically upward from the plate through a circular pipe of 13.84 mm inside diameter located with its center 0.457 m downstream of the leading edge. The thickness of the boundary layers developing on the false walls was kept to a miminum by providing streamlined leading edges to the false walls. The flap provided at the plate trailing edge was adjusted so as to minimize the elliptic effects in the flow field and ensure that the flow approaches the plate at a zero angle of incidence. A sketch of the jet injection assembly is shown in Fig. 2.

Measurement Systems

Thermal anemometry methods were used extensively throughout the present study. Normal and 45 deg-fiber-film probes were used with anemometers operated in the constant temperature mode. Two hot-film channels were used. One channel was comprised of a DISA 55M01 main unit, a DISA 55M10 standard bridge, and a DISA 55M25 linearizer along with a DISA 55M05 power pack. The other channel was comprised of a DISA 55D01 main unit and a DISA 55D10 linearizer. The two channels were used in conjunction with a DISA 55R11-90 deg-probe and a DISA 55R12 45 deg-slant probe. An overheat ratio of 1.08 was used throughout the study. This value was chosen since it offered a compromise between a relatively high frequency response and an adequate probe lifetime. Also, at this overheat ratio, the voltage drift, mostly attributable to dirt and bubble accumulation on the

Nomenclature

D = jet diameter at discharge

M = velocity ratio, U_j/U_∞

$\overline{q'^2}$ = twice kinetic energy of turbulence, $\overline{(u'^2 + v'^2 + w'^2)}$

$R_{u'w'}$ = correlation coefficient, $\overline{u'w'} / \sqrt{\overline{u'^2}} \sqrt{\overline{w'^2}}$

T_j = jet discharge temperature

T_∞ = free stream temperature

$U, \bar{U}$ = instantaneous and time-averaged streamwise velocity components

U_j = jet discharge velocity

$U_m, \bar{U}_m$ = instantaneous and time-

averaged resultant velocities

U_∞ = free stream velocity

u' = streamwise velocity fluctuation component

v' = transverse velocity fluctuation component

w' = vertical velocity fluctuation component

$\overline{u'w'}$ = Reynolds stress

$V, \bar{V}$ = instantaneous and time-averaged velocities in the transverse direction

$W, \bar{W}$ = instantaneous and time-

averaged velocities in the vertical direction

X = streamwise distance measured from center of jet discharge pipe

Y = transverse (spanwise) distance measured from center of jet discharge pipe

Z = vertical distance measured from jet-injection platform

ρ = density

sensor, was tolerable. Usually the probe broke before it was too dirty to use. Supporting equipment included a DISA 55D25 auxiliary unit, a DISA 55D35 RMS meter, a HP 3435A multimeter, and a dual-beam oscilloscope.

The sensor was calibrated by adjusting the anemometer and the linearizer and recording their output voltages versus known velocity values. The known velocities were provided by the discharge of water from a pipe, 3.66 m long, 25.4 mm in diameter, operating in turbulent flow. The water flowrate, and consequently the water average velocity, was computed by collecting a known amount of water in a known period of time. The maximum centerline velocity was computed by assuming a fully-developed turbulent velocity profile at the pipe exit plane. The calibration was considered complete after the acquisition of 20 calibration points. The calibration data were correlated using a King's law type of relationship. The linearizer data were correlated using a relationship of the form:

$$\bar{E}_L = S\bar{U} \tag{1}$$

where S is a constant to be determined from a least-square curve-fit and $\bar{E}_L$ is the linearizer output voltage. The linearizer calibration line usually passed through or was very close to the origin because of proper initial adjustments of the linearizer. If this was not the case, the whole calibration run was repeated.

During a calibration run, the turbulence intensity ranged from 3 to 4 percent. The correlation coefficients were usually better than 0.9980. A specially-designed interactive computer program enabled the acquisition of several hundred samples for every calibration point which ensured maximum repeatability.

Measurements of all turbulence quantities including Reynolds stresses reported here were obtained from the normal and 45 deg probes using probe rotation techniques. Further details on the measurement techniques are given in Sherif (1985).

The present experiments were controlled by a Hewlett-Packard (HP) 87XM microcomputer. Other major components in the data acquisition system were a HP 3495A scanner and a Fluke 8520A digital multimeter. The latter was used for converting analog input signals to digital signals which were, in turn, transmitted to the computer for further processing. For all the experiments performed in this work, the DC voltages were sampled at 20 Hz, while the AC voltages were sampled at 10 Hz. The scanner was supplied with a ten-channel relay actuator assembly which enabled the scanner to control external devices with relay actuator closures. A twenty-channel low thermal emf relay assembly enabled the scanner to multiplex the low-level DC voltages from thermocouples and the hot-film anemometers into the Fluke 8520A voltmeter.

Qualification Tests

A series of tests was carried out to qualify the water channel basic characteristics. At the early stages of the experimental program, before the installation of the foam and the metal screen, the velocity profile was checked and found to be nonuniform. The turbulence intensity was also evaluated and found to be high, especially in the upstream portion of the channel. The installation of the foam and the metal screen upstream and downstream of the honeycomb, respectively, helped reduce both the intensity and scale of turbulence. The maximum free stream turbulence intensity near the boundaries became less than 1 percent and in the channel core (where all measurements were conducted) less than 0.25 percent.

The boundary layer developing on the plate at the jet discharge location was found to be laminar based on the observation of tufts suspended in the flow. With no jet flow,
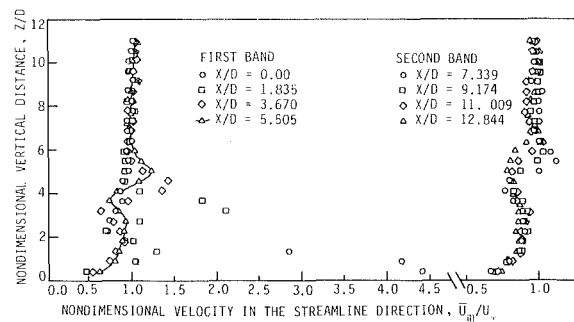
Fig. 3 Mean velocity profiles, $M = 4$, $Y/D = 0$, $Re = 17,632$, $T_j = 18°C$, $T_\infty = 18°C$, uncertainty = 3.18 percent
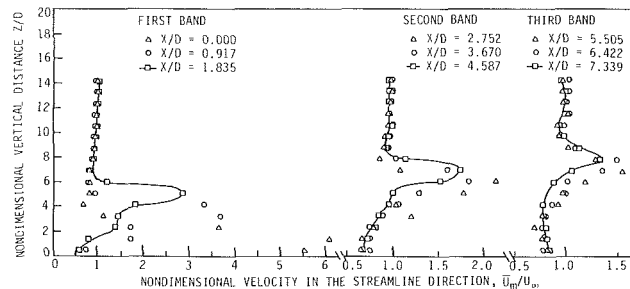
Fig. 4 Mean velocity profiles, $M = 6$, $Y/D = 0$, $Re = 25,934$, $T_j = 18°C$, $T_\infty = 18°C$, uncertainty = 3.18 percent

the boundary layer thickness, based on the 99 percent value, was observed to be 6.9 mm at the location of the center of the jet discharge pipe for the nominal freestream velocity used in all the present measurements, (0.35 m/s). At the velocity ratios considered in this study, the cross stream should have very little influence on the jet flow upstream of the discharge pipe (see, for example, Andreopoulos and Rodi, 1984).

Qualification of the measurement procedures for mean velocities was carried out in two independent ways. The centerline trajectory, for different velocity ratios, was traced by determining the locus of points of maximum velocity using a constant temperature anemometer and a normal hot-film probe. The results were compared to the trajectories obtained by previous investigators such as Keffer and Baines (1963), Kamotani and Greber (1971), Ramsey (1969), and Jordinson (1956) and very good agreement was obtained. The other check on the mean velocity measurement procedures was made by comparing the profiles of mean velocity (measured in the streamline direction) of an isothermal jet to those of Ramsey and Goldstein (1970) in the jet plane of symmetry at a velocity ratio of 2. Good agreement was also obtained in this case. The turbulence intensity (measured in the direction of the mean velocity of the same isothermal jet described above) was also compared to that of Ramsey and Goldstein (1970) at the same streamwise locations and good agreement was obtained.

Results

Mean Velocity in the Streamline Direction. The effect of the downstream distance on the shape of the mean velocity profiles is shown in Fig. 3 for a velocity ratio of 4, and in Fig. 4 for a velocity ratio of 6. The uncertainty associated with the measurement of the mean velocity magnitude is estimated to be 3.18 percent for an uncertainty in the calibration curve of 2.5 percent.

It is worth noticing here that in all the velocity profiles shown, there are two maxima, one in the jet wake which is

Fig. 5 Contour plots of mean velocity, $\bar{U}_m/U_\infty$, uncertainty = 3.18 percent

Fig. 7 Turbulence intensity contours, $\sqrt{\overline{u'^2}}/U_m$, uncertainty = 10 percent for 50 percent intensity

Fig. 6 Turbulence intensity profiles, $M = 4$, $Y/D = 0$, Re = 17,632, $T_j = 18°C$, $T_\infty = 18°C$, uncertainty = 10 percent for 50 percent intensity

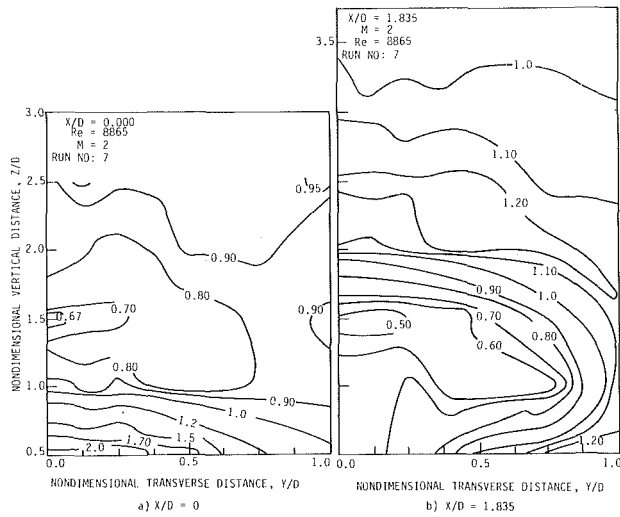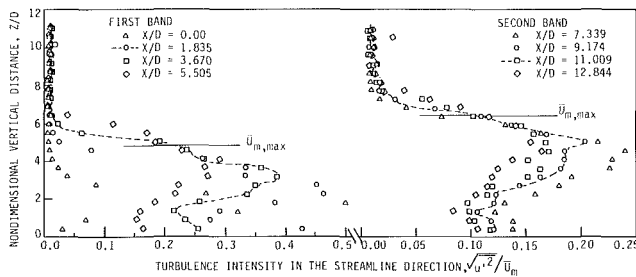usually a local maximum, while the other is in the jet field and is an absolute maximum. The latter maximum always corresponds to the jet centerline trajectory. These observations are true irrespective of the value of the velocity ratio. The location of both maxima, however, is a strong function of the velocity ratio and probably a weak function of the discharge Reynolds number and the shape of the discharge port.

The flow field in the jet cross-section is best described by examining constant velocity contours at a number of downstream stations. These are presented in Figs. 5(a) and 5(b) at a velocity ratio of 2 and X/D positions of 0 and 1.835, respectively. Figure 5(a) indicates that a fairly uniform region of high velocity exists just above the jet discharge. Farther downstream ($X/D = 1.835$), the jet cross section changes to a characteristic kidney shape and is, generally characterized by low velocity values. The free stream fluid can be seen to be slighty accelerated in the jet wake (as evidenced by the relatively high velocity region underneath the jet) and entrained into the jet.

Turbulence Intensity. The turbulence intensity was measured for the same jet runs reported in the last section. Figure 6, however, shows the effect of varying the streamwise distance on the turbulence intensity profiles in the jet plane of symmetry only for a velocity ratio of 4. This is given for 8 downstream positions up to an X/D of 12.844.

In the technique used to convert the voltage output readings of the nonlinearized constant temperature anemometer to turbulence intensity values, use was made of the fact that the fluctuating velocity components are small compared to the mean velocity. At a turbulence intensity of 25 percent, an uncertainty of 2.5 percent in the turbulence intensity reading is
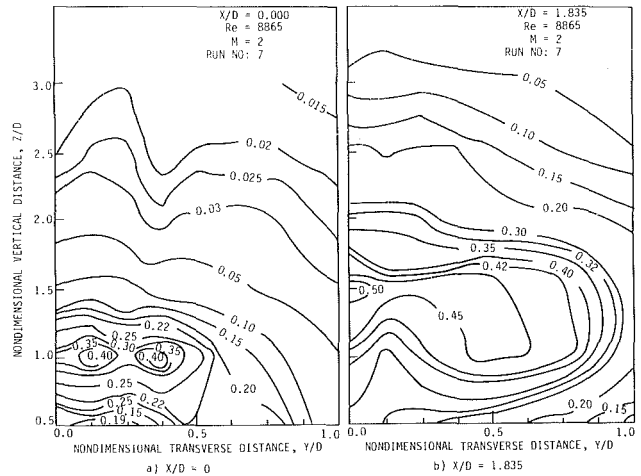
expected, while that uncertainty increases to 10 percent for a 50 percent intensity (see also Ramsey and Goldstein, 1970). It has to be kept in mind, however, that the aforementioned restriction does not apply to all other turbulent quantities since the linearized anemometer signal was employed instead.

Careful observation of the turbulence intensity profiles given in Fig. 6 shows that the intensity has an absolute maximum at the location of maximum velocity gradient and a local maximum near the plate surface in the wake region. Combining the velocity data (Fig. 3) with those of the turbulence intensity (Fig. 6) indicates that, in general, the turbulence intensity tends to be lower in regions of high velocity and vice versa.

The development of the turbulence structure of the jet cross-section is best illustrated using the contour plots of constant turbulence intensity at a number of downstream positions. These are presented in Fig. 7 at the same downstream positions and velocity ratio for which the constant velocity contours were presented.

At $X/D = 0$ (just above the jet discharge), the regions of high turbulence intensity are shown to occur at the interaction region between the jet and the cross-stream (where the velocity gradients are maximum) and not in the jet core (where the velocities are maximum). Farther downstream ($X/D = 1.835$), the kidney-shaped region identified in the constant velocity contours (Fig. 5) is shown here to be a region of very high turbulence.

At a given X/D, the maximum turbulence intensity was observed to decrease with increases in the velocity ratio, M. This trend can be detected by comparing the information available in Figs. 6 and 7 (b), but can be seen more clearly by examining the additional data reported on this study in Sherif (1985). This trend is consistent with the findings of previous investigators such as Ramsey and Goldstein (1969), Andreopoulos and Rodi (1984), and Crabb et al. (1980), as well as with a similar trend observed for the fluctuating temperature during the course of the present investigation (Sherif and Pletcher, 1986). This trend helps to explain why some turbulence modelers (Madni, 1975) found it necessary to include a velocity ratio parameter in the equation for the turbulent viscosity that decreases its value at larger velocity ratios.

Structure of the Velocity Field. A rotational hot-film probe technique was used to measure the streamwise and vertical components of velocity. The technique, however, is not capable of detecting flow reversals. Maximum values for the
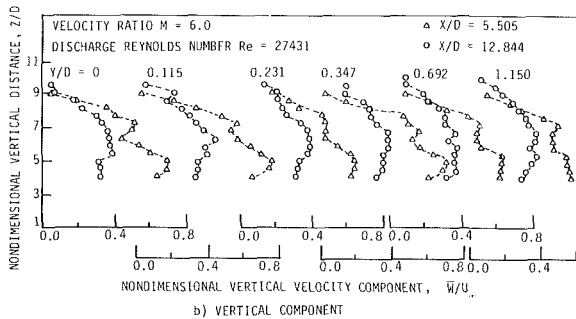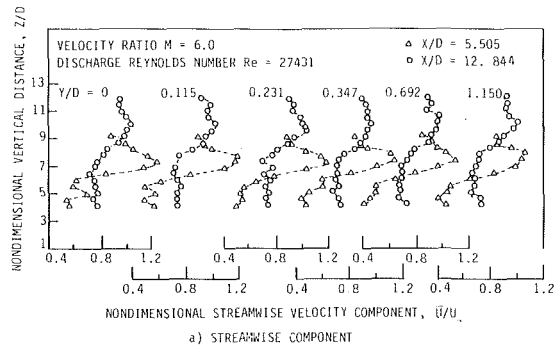
Fig. 8 Mean velocity profiles, $M = 6$, $Re = 27{,}431$, $T_j = 18°C$, $T_\infty = 18°C$, uncertainty: $\bar{U} = 6$ percent; $\bar{W} = 7.5$ percent
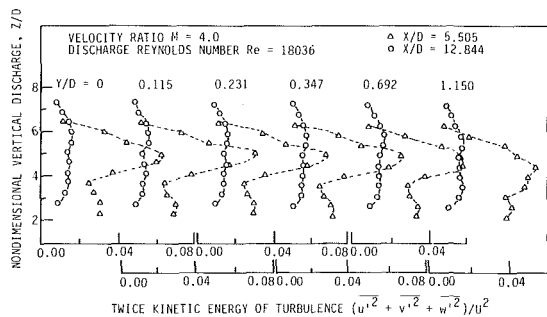
Fig. 9 Profiles of turbulent kinetic energy, uncertainty = 7 percent

Fig. 10 Reynolds stress profiles, uncertainty = 8 percent

uncertainties associated with the use of this technique are: $\bar{U}$, 6 percent and $\bar{W}$, 7.5 percent.

Figures 8(a) and 8(b) show the streamwise and vertical velocity components for an isothermal jet at a velocity ratio of 6. The data were taken at downstream locations of $X/D = 5.505$ and 12.844. The profiles were measured both in and outside the jet plane of symmetry with Y/D corresponding to 0, 0.115, 0.231, 0.347, 0.692, and 1.150.

Examination of the streamwise component indicated that it possesses characteristics similar to the resultant mean velocity given earlier in Figs. 3 and 4. It generally has an absolute maximum located in the jet field and a local maximum in the wake-like region. Also, the streamwise component decreases underneath the jet lower boundaries in the kidney-shaped region corresponding to the general flow deceleration in the same region observed in Figs. 3 and 4. The magnitude of the streamwise component eventually approaches that of the free stream far enough above the jet upper boundaries. Furthermore, the streamwise component becomes flatter and experiences less abrupt changes at a downstream position of $X/D = 12.844$ than at $X/D = 5.505$.

The vertical component, on the other hand, experiences a drastically different development than either the streamwise component, $\bar{U}$, or the resultant mean velocity $\bar{U}_m$. Examination of Fig. 8(b) indicates that the vertical component has an

absolute maximum right below the location at which the streamwise component reaches an absolute maximum. As Z/D increases, the vertical component decreases in a nonlinear fashion until it almost becomes zero far above the jet. Values of W as high as 0.7 U_∞ in the plane of symmetry and 0.75 U_∞ outside the plane of symmetry ($Y/D = 0.347$) have been observed.

Kinetic Energy of Turbulence. Profiles of the turbulent kinetic energy for an isothermal jet at a velocity ratio of 4 and a discharge Reynolds number of 18036 are presented in Fig. 9. The data are presented for downstream positions of $X/D = 5.505$ and 12.844, and transverse positions of $Y/D = 0$, 0.115, 0.231, 0.347, 0.692, and 1.150. Maximum uncertainty in the measured turbulent kinetic energy was estimated to be 7 percent.

At the smaller downstream position ($X/D = 5.505$), the profiles are nearly the same up to a transverse position of $Y/D = 0.692$. The turbulent kinetic energy has an absolute maximum and a local maximum similar to the mean velocity profiles. In the jet plane of symmetry, the location of the absolute maximum is the same as that of the resultant mean velocity. Outside the plane of symmetry, no matching velocity data are available. It is striking, however, to note that the location of absolute maximum outside the plane of symmetry up to a transverse position of $Y/D = 0.692$ corresponds very closely to that in it. Andreopoulos and Rodi (1984) observed the same behavior at a velocity ratio of 2. At lower velocity ratios ($M = 1$ and $M = 0.5$), they observed that the peak in the $\overline{q'^2}$ profile corresponds to the location where the velocity gradients are maximum. At the larger downstream position ($X/D = 12.844$), the magnitude of the turbulent kinetic energy is far less than that at $X/D = 5.505$. This is attributed to the fact that, farther downstream, the wake behavior is much weaker and the stresses are smaller which reduces the rate at which turbulent kinetic energy is generated. Furthermore, the turbulent kinetic energy produced upstream is convected downstream and diffused by the turbulent transport towards the plate. In the transverse direction, the turbulent kinetic energy attains the same level partly because of the above reasons.

The double-peak behavior in the $\overline{q'^2}$ profiles was first observed by Andreopoulos and Rodi (1984) at velocity ratios of 1 and 2. They reported that this behavior was more pronounced at a velocity ratio of 2 than at a velocity ratio of 1, and was hardly noticeable at a velocity ratio of 0.5. In the present study ($M = 4$), the double-peak behavior was much more pronounced than that reported by Andreopoulos and Rodi (1984). This obviously is in complete agreement with the trend first observed by Andreopoulos and Rodi.

Reynolds Stress, Structural Parameter, and Correlation Coefficient. Profiles of the Reynolds stress parameter,
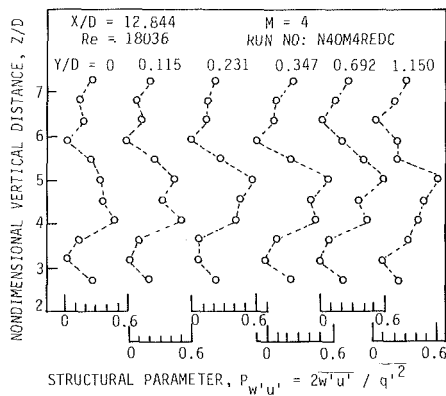
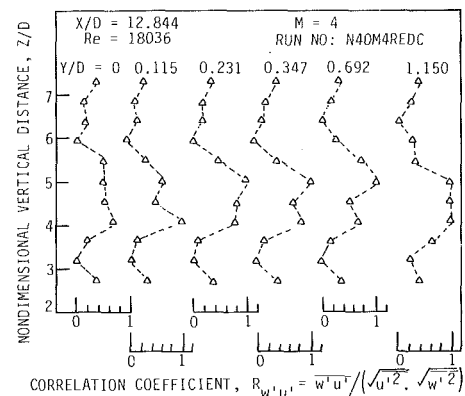Fig. 11 Profiles of the structural parameter, uncertainty = 14 percent

Fig. 12 Profiles of the correlation coefficient uncertainty = 17 percent

$\overline{u'w'}/U_\infty^2$, are presented in Fig. 10 for the same isothermal jet discussed above at a downstream position of $X/D = 12.844$ and the same spanwise locations for which the turbulent kinetic energy profiles were presented. The uncertainty associated with this measurement was estimated to be 8 percent.

Examination of Fig. 10 reveals that the shear stress increases with increasing transverse distance. Also, as the transverse distance is increased, the location at which the maximum shear stress occurs moves farther from the wall.

The development of the main shear stress relative to the turbulent kinetic energy can be described by examining the ratio $\overline{u'w'}/(1/2\ \overline{q'^2})$, which is referred to as the structural parameter. This is presented in Fig. 11 for the same jet at the same downstream and spanwise positions for which the shear stress was presented. The uncertainty of this parameter is estimated to be 14 percent. In the wake region, the shear stress is quite small compared to the turbulent kinetic energy up to a vertical distance from the wall of approximately $Z/D = 3.25$. Beyond this vertical position (at virtually all transverse locations), the shear stress increases relative to the turbulent kinetic energy and then decreases once more. The structural parameter usually peaks where the shear stress is maximum both in and outside the plane of symmetry. The maximum value of the structural parameter observed at this downstream location is about 0.59 at a transverse location of 1.150 D. In the plane of symmetry, the peak value is 0.48. These peaks are not in complete agreement with those reported by Andreopoulos and Rodi (1984) at lower velocity ratios. For example, at a velocity ratio of 0.5, they report a maximum value for the structural parameter of 0.49 in the jet plane of symmetry at $X/D = 0$. Farther downstream, at a downstream position close to that reported here ($X/D = 10$), a maximum value of 0.3 is given. Andreopoulos and Rodi (1984) argue that this is the value usually seen in undisturbed shear layers. This discrepancy may be attributed to differences in the flow character due to differences in the velocity ratios used. The relatively larger value attained by the structural parameter in the present study implies that the shear stress increases at a faster rate relative to the turbulent kinetic energy than at smaller velocity ratios.

The development of the Reynolds shear stress relative to the product of the streamwise and vertical componets of the turbulent velocity fluctuations can best be described in terms of the ratio $\overline{u'w'}/(\sqrt{\overline{w'^2}}\ \sqrt{\overline{u'^2}})$ known as the correlation coefficient, $R_{u'w'}$. This is presented in Fig. 12 for the same velocity ratio and positions for which the structural parameter was presented. The uncertainty associated with this parameter is estimated to be 17 percent. It is very striking to note that the profiles of the correlation coefficient are very much like those of the structural parameter, except, of course, for differences

between their respective magnitudes. The maximum value of the correlation coefficient increases from about 0.7 in the jet plane of symmetry to about 1.0 at a transverse position of $Y/D = 1.150$. The locations of the peaks in the correlation coefficient profiles remain virtually the same as those of the structural parameter where they mostly occur where the shear stress is maximum.

Conclusions

An experimental investigation of the flow and turbulence characteristics of isothermal turbulent jets in cross flow was carried out. The following is a summary of the major results and conclusions.

1. The resultant mean velocity profiles are characterized by two peaks. The larger peak consistently occurs in the jet core, while the smaller one corresponds to fluid entrained into the jet wake behind the near vertical portion of the jet. The streamwise component of the mean velocity, on the other hand, possesses characteristics similar to those of the resultant mean velocity in terms of the double-peak pattern. While the locations of the peaks remain virtually the same, the magnitudes are slightly smaller for the streamwise component than for the resultant velocity. The distribution of the vertical component of velocity, however, does not share similarities with either the resultant mean velocity or the streamwise component of velocity and has, generally, smaller values than either of them. The vertical component seemed to possess only one peak that consistently occurred in the wake-like region. The overall magnitude of the vertical component decreased with increasing vertical distance from the wall and eventually vanished far enough above the jet upper edge.

2. A double-peak pattern seems to develop for all turbulence quantities such as the turbulence intensity, turbulent velocity fluctuations, and the turbulent kinetic energy. This same trend was also observed for the temperature fluctuations during the course of the present investigation. One peak usually occurs in the wake, while a larger peak occurs above the jet centerline in a region of higher velocity (or temperature in the case of $\sqrt{t'^2}$) gradient. The only exception to the latter observation seems to be the turbulent kinetic energy at higher velocity ratios ($M > 1$). For smaller velocity ratios ($M \leq 1$), Andreopoulos and Rodi (1984) observed a trend for the turbulent kinetic energy similar to the one noted above for the other turbulent quantities.

Acknowledgments

Department of Mechanical Engineering at Iowa State University is also gratefully acknowledged.

References

Andreopoulos, J., 1982, "Measurements in a Pipe Flow Issuing Perpendicularly into a Cross Stream," ASME JOURNAL OF FLUIDS ENGINEERING, Vol. 104, pp. 493–499.

Andreopoulos, J., 1983, "Heat Transfer Measurements in a Heated Jet-Pipe Flow Issuing into a Cold Cross-Stream," *Physics of Fluids*, Vol. 26, pp. 3201-3210.

Andreopoulos, J., and Rodi, W., 1984, "Experimental Investigation of Jets in a Cross-Flow," *J. Fluid Mechanics*, Vol. 138, pp. 93–127.

Baker, A. J., Snyder, P. K., and Orzechowski, J. A., 1987, "Three Dimensional Nearfield Characterization of a VSTOL Jet in Turbulent Crossflow," AIAA Paper 87-0051.

Bergeles, G., Gosman, A. D., and Launder, B. E., 1976, "The Near-Field Character of a Jet Discharged Normal in a Main Stream" ASME *Journal of Heat Transfer*, Vol. 98, pp. 373-378.

Bradbury, L. J. S., and Wood, M. N., 1965, "The Static Pressure Distribution Around a Circular Jet Exhausting Normally from a Plane Wall into an Airstream," C. P. No. 822 British Aeronautical Research Council, London, England.

Chan, T., and Kennedy, J. F., 1972, "Turbulent Nonbuoyant or Buoyant Jets Discharged into Flowing or Quiescent Fluids," Report No. 140, Iowa Institute of Hydraulic Research, The University of Iowa, Iowa City, Iowa.

Chien, J. C., and Schetz, J. A., 1975, "Numerical Solution of the Three-Dimensional Navier-Stokes Equations with Applications to Channel Flows and a Buoyant Jet in a Cross-Flow," ASME *Journal of Applied Mechanics*, Vol. 42, pp. 575-579

Claus, R. W., 1985, "Numerical Calculation of Subsonic Jets in Crossflow with Reduced Numerical Diffusion," NASA TM 87003.

Crabb, D., Durao, D. F. G., and Whitelaw, J. H., 1980, "A Round Jet Normal to a Cross-Flow," ASME Paper 80-WA/FE-10.

Cubbison, R. W., Anderson, B. H., and Ward, J. J., 1961, "Surface Pressure Distribution with a Sonic Jet Normal to Adjacent Flat Surfaces at Mach 2.92 to 6.4," NASA TND-580, Lewis Research Center, Cleveland, Ohio.

Harloff, G. J., and Lytle, J. K., 1988, "Three-Dimensional Viscous Flow Computations of a Circular Jet in Subsonic and Supersonic Cross Flow," *Proceedings First National Fluid Dynamics Congress*, Part 2, AIAA, Washington, D.C., pp. 1159–1165.

Hwang, S. S., and Pletcher, R. H., 1977, "Prediction of Thermal Plumes from Power Plants," Annual Report ISU-ERI-Ames-77338, Affiliate Research Program in Electrical Power, Department of Mechanical Engineering, Iowa State University, Ames, Iowa.

Hwang, S. S., 1978, "Prediction of Turbulent Jets and Plumes in Flowing Ambients," Ph.D. dissertation, Iowa State University, Ames, Iowa.

Hwang, S. S., and Pletcher, R. H., 1978a, "Prediction of Turbulent Jets and Plumes in Flowing Ambients," Technical Report No. HTL-15, Department of Mechanical Engineering, Iowa State University, Ames, Iowa.

Hwang, S. S., and Pletcher, R. H., 1978b, "Prediction of Buoyant Turbulent Jets and Plumes in a Cross Flow," *Proceedings of the Sixth International Heat Transfer Conference*, Washington, D. C., Hemisphere Publishing Corp.

Jordinson, R., 1956, "Flow in a Jet Directed Normal to the Wind," British Aeronautical Research Council, R&M No. 3074.

Kamotani, Y., and Greber, I., 1971, "Experiments on a Turbulent Jet in a Cross Flow," Report FTAS/TR-71-62, Division of Fluid, Thermal, and Aerospace Sciences, Case Western Reserve University, Cleveland, Ohio.

Keffer, J. F., and Baines, W. D., 1963, "The Round Turbulent Jet in a Cross Wind," *J. Fluid Mechanics*, Vol. 15, No. 4, pp. 481-497.

Keffer, J. F., 1969, "The Physical Nature of the Subsonic Jet in a Cross-Stream," *Analysis of a Jet in a Subsonic Crosswind*, NASA SP-218, Washington, D.C., pp. 19–36.

Madni, I. K., 1975, "A Finite Difference Analysis of Turbulent, Axisymmetric, Buoyant Jets and Plumes," Ph.D. dissertation, Iowa State University, Ames, Iowa.

Margason, R. J., 1969, "Jet-Wake Characteristics and Their Induced Aerodynamic Effects on V/STOL Aircraft in Transition Flight," *Analysis of a Jet in a Subsonic Crosswind*, NASA SP-218, Washington, D.C. NASA, pp. 1–18.

Margason, R. J., 1969, "Analytic Description of Jet-Wake Cross Sections for a Jet Normal to a Subsonic Free Stream," *Analysis of a Jet in a Subsonic Crosswind*, NASA-SP-218, Washington, D.C., NASA, pp. 131–139.

McMahon, H. M., and Mosher, D. K., 1969, "Experimental Investigation of Pressures Induced on a Flat Plate by a Jet Issuing into a Subsonic Crosswind," *Analysis of a Jet in a Subsonic Crosswind*, NASA SP-218, Washington, D.C., NASA, pp. 49–62.

McMahon, H. M., Hester, D. D., and Palfery, J. G., 1971, "Vortex Shedding from a Turbulent Jet in a Cross-Wind," *J. Fluid Mechanics*, Vol. 48, pp. 73–80.

Patankar, S. V., Basu, D. K., and Alpay, S. A., 1977, "Prediction of the Three-Dimensional Velocity Field of a Deflected Turbulent Jet," ASME JOURNAL OF FLUIDS ENGINEERING, Vol. 99, pp. 758–762.

Platten, J. L., and Keffer, J. F., 1968, "Entrainment in Deflected Axisymmetric Jets at Various Angles to the Stream," UTME-TP-6808, University of Toronto, Department of Mechanical Engineering.

Pratte, B. D., and Baines, W. D., 1968, "Profiles of the Round Turbulent Jet in a Cross Flow, *J. Hydraulics Division, Proc. ASCE*, HY6, Vol. 93, pp. 53–64. Corrections, HY3, Vol. 94, 1968, pp. 815–816.

Ramsey, J. W., 1969, "The Interaction of a Heated Air Jet with a Deflecting Flow," Ph.D. dissertation, University of Minnesota, Minneapolis, MN.

Ramsey, J. W., and Goldstein, R. J., 1970, "Interaction of a Heated Jet with a Deflecting Stream," NASA CR-72613.

Rodi, W., 1982, *Turbulent Buoyant Jets and Plumes*, Pergamon Press, New York.

Rosen, R., Durando, N. A., and Cassel, L. A., 1969, "Inviscid Models for the Pressure Induced by a Jet Transverse to a Subsonic Stream," *Analysis of a Jet in a Subsonic Crosswind*, NASA SP-218, Washington, D.C., pp. 205–229.

Roth, K., 1987, "Numerical Simulation of a Subsonic Jet in a Crossflow," SAE 872343, International Powered Lift Conference and Exposition, Santa Clara, Calif.

Sherif, S. A., 1985, "Measurements of the Flow and Thermal Characteristics of Turbulent Jets in Cross Flow," Ph.D. dissertation, Iowa State University, Ames, Iowa.

Sherif, S. A., and Pletcher, R. H., 1986, "Measurements of the Thermal Characteristics of Heated Turbulent Jets in Cross Flow," ASME Paper 86-HT-34.

Sykes, R. I., Lewellen, W. S., and Parker, S. F., 1986, "On the Vorticity Dynamics of a Turbulent Jet in a Crossflow," *J. Fluid Mechanics*, Vol. 168, pp. 393–413.

Vogler, R. D., 1963, "Surface Pressure Distributions Induced on a Flat Plate by a Cold Air Jet Issuing Perpendicularly from the Plate and Normal to a Low-Speed Free-Stream Flow," NASA TN D-1629.

Werner, J. E., 1969, "The Use of Matched Asymptotic Expansions as an Approach to the Problem of the Jet in a Crossflow," *Analysis of a Jet in a Subsonic Crosswind*, NASA SP-218, Washington, D.C., NASA, pp. 239–247.

White, A. J., 1980, "The Prediction of the Flow and Heat Transfer in the Vicinity of a Jet in Crossflow," ASME Paper 80-WA/HT-26.

Wooler, P. T., Burghard, G. H., and Gallagher, J. T., 1967, "Pressure Distribution on a Rectangular Wing with a Jet Exhausting Normally into an Air Stream," AIAA *J. Aircraft*, Vol. 4, No. 6, pp. 537–543.

Fully Developed Flow in Curved Channels of Square Cross Sections Inclined

Tay-Yueh Duh

Yaw-Dong Shih

Department of Mechanical Engineering,
Tatung Institute of Technology,
Taipai, Taiwan

The fully developed viscous flow in curved channels of obliquely oriented square cross section with angle of inclination is analyzed for an incompressible fluid. A nonorthogonal helical coordinate system is introduced to study the flow field for various angles of inclination. To obtain a stationary numerical solution, a primitive-variable formulation of the pressure-velocity finite-difference scheme is formulated based on an ADI method. The results for the channel at zero angle are compared with data available in the literature. Detailed predictions of secondary-flow streamlines, axial velocities and friction factor ratios show that there are significant changes at inclination angles 0, 15, 30, 45, 60, and 75 deg. At a certain Dean number, it is found that no additional pair of vortices appears near the outer wall, except for angle of inclination 0 deg. If the Dean number is less than 125 the friction factor ratio has a minimum value at zero angle. If the Dean number is greater than 125, the minimum value of the friction factor ratio occurs at the angles of rotation 15 and 75 deg.

Introduction

Laminar flow in curved square channels is characterized by a secondary flow in the cross-sectional plane perpendicular to the axial-flow direction. The nature of this phenomenon depends upon the Dean number, which represents the ratio of the centrifugal force to the viscous force. Due to the effects of geometrical shape, the problem of flow in curved rectangular channels is more involved than in curved circular pipes. A review of flow in circular pipes can be found in a literature survey [1] by Berger et al. Assuming small curvature and employing a primitive variable formulation for a square channel, Joseph et al. [2] solved the governing equations numerically. Their solutions show the formation of two pairs of counter-rotating vortices, beyond a certain Dean number of about 152. In 1976, Cheng et al. [3] using a stream-function-vorticity formulation fully equivalent to the Navier-Stokes equations investigated the problem of flow in curved rectangular channels with a line iteration method. They found that the second vortex pair occurs at a Dean number greater than 150. Ghia [4] and Sokhey [5] solved the three-dimensional entrance flow in curved channels and obtained similar results (i.e., two pairs vortices) when the Dean number reaches 145. Secondary-flow measurements in curved square ducts were made by Hille et al. [6] with laser-Doppler anemometry (LDA). They observed that the second vortex pair appears in the range of Dean number from 150 to 300. Recently, Ghia et al. [7] using a multigrid technique showed that for curved square channel flow the second vortex pair occurs at De > 125.

By contrast to square channel flows, the second vortex pair is not likely to happen in curved circular duct flows as shown in References [8–10] and for elliptical duct flow in Reference [11] at high Dean number. But in a semicircular duct [12], with the plane surface as the outer wall, a two-pair-of-vortices pattern is observed in the plane of the cross-section. Summarizing the above mentioned results, two pairs of vortices are found readily for ducts with a flat outer wall at sufficiently high Dean numbers.

In industrial applications, the generation of vortices in curved channel flows may increase friction resistance. It would be an advantage to industry, if it would be possible to decrease the resistance of friction, which influences the efficiency of the operation. Here the problem of curved channel flow is solved for the angles of inclination, 0, 15, 30, 45, 60, and 75 deg, respectively. In addition, we like to know whether the effects of the angle of inclination influence the friction resistance.

Several authors utilized a concentric toroidal coordinate system to study the problem of flow in curved circular ducts [8, 9]. Wang [13] in 1981 first handled the problem of flow in a helical circular duct using a non-orthogonal helical coordinate system. The present authors also derive the governing equations for the flow in curved rectangular channels using a nonorthogonal helical coordinate system. In the formulation, the averaged axial non-dimensional velocity, is related to the Reynolds number Re in axial direction of the flow. In the calculations, authors let the axial pressure gradient and the curvature of the pipe centerline K to be prescribed, the solutions for the components of velocity profile of curved pipe flow are then determined. The significant parameters in this type of problem are the Reynolds number and curvature. The combination of these two parameters is the Dean
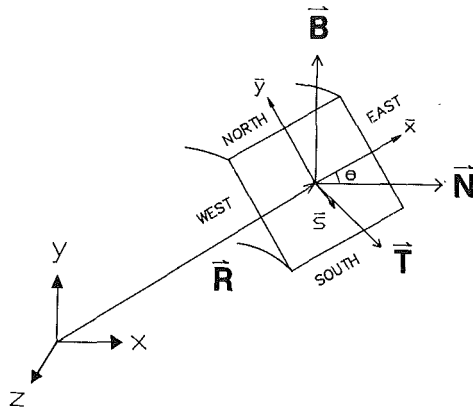
Fig. 1   Coordinate system

number($= \mathrm{Re}\sqrt{K}$) which is a measure of secondary flows in curved ducts with small curvature. The purpose of the present work is to study the effects of angle of inclination on the secondary flow pattern, the axial velocity distribution and the friction factor ratio. Our work applies to fully developed laminar flow in a curved duct of square cross section and it makes use of a nonorthogonal helical coordinate system.

Governing Equations

The development of the mathematical model for this flow problem starts with the nonorthogonal helical coordinate system [13]. A position vector $\mathbf{r}(\bar{x}, \bar{y}, \bar{s})$ as shown in Fig. 1 is given by

$$\mathbf{r} = \mathbf{R}(\bar{s}) + (\bar{y}\cos\theta + \bar{x}\sin\theta)\mathbf{B}(\bar{s})$$
$$+ (\bar{x}\cos\theta - \bar{y}\sin\theta)\mathbf{N}(\bar{s}) \tag{1}$$

where $\bar{s}$ is arc length, $\bar{x}, \bar{y}, \bar{s}$ is a new coordinate system, θ is the angle of inclination about the horizontal axis; orthogonal unit vectors, namely tangent $\mathbf{T}$, normal $\mathbf{N}$, and binormal $\mathbf{B}$, can be defined by

$$\mathbf{T} = \frac{d\mathbf{R}}{d\bar{s}}, \quad \mathbf{N} = -\frac{1}{K} \frac{d\mathbf{T}}{d\bar{s}}, \quad \mathbf{B} = \mathbf{T} \times \mathbf{N} \tag{2}$$

where $\bar{K}$ is the curvature. The Frenet formula [14] gives

$$\frac{d\mathbf{N}}{ds} = \bar{\tau}\mathbf{B} + K\mathbf{T}, \quad \frac{d\mathbf{B}}{ds} = -\bar{\tau}\mathbf{N} \tag{3}$$

where $\bar{\tau}$ is the torsion; the metric element is

$$(d\mathbf{r})^2 = \{ [1 + \bar{K}(\bar{x}\cos\theta - \bar{y}\sin\theta)]^2 + \bar{\tau}^2(\bar{x}^2 + \bar{y}^2)\} d\bar{s}^2$$
$$+ d\bar{x}^2 + d\bar{y}^2 + 2\bar{x}\bar{\tau}d\bar{y}d\bar{s} - 2\bar{y}\bar{\tau}d\bar{x}d\bar{s} \tag{4}$$

The Navier-Stokes equations and the continuity equation in tensorial form are

$$\frac{\partial V^i}{\partial t} + V^j \left(\frac{\partial V^i}{\partial X^j} + \Gamma^i_{\alpha j} V^\alpha \right)$$
$$= -\frac{g^{ij}}{\rho} \frac{\partial \bar{P}}{\partial X^j} + \nu g^{kj} V,^i_{jk} \tag{5}$$

$$\frac{\partial V^i}{\partial X^i} + \Gamma^i_{\alpha i} V^\alpha = 0 \tag{6}$$

Here Γ^i_{jk} is the Christoffel symbol, g^{ij} is metric tensor, and the covariant derivative is

$$V,^i_{jk} = \frac{\partial^2 V^i}{\partial X^k \partial X^j} + \Gamma^i_{j\alpha} \frac{\partial V^\alpha}{\partial X^k} + \Gamma^i_{\alpha k} \frac{\partial V^\alpha}{\partial X^j} - \Gamma^\alpha_{jk} \frac{\partial V^i}{\partial X^\alpha}$$
$$+ \left(\frac{\partial \Gamma^i_{j\alpha}}{\partial X^k} + \Gamma^i_{\beta k}\Gamma^\beta_{j\alpha} - \Gamma^\beta_{jk}\Gamma^i_{\beta\alpha} \right) V^\alpha \tag{7}$$

Let $X^1 = \bar{x}$, $X^2 = \bar{y}$, $X^3 = \bar{s}$ and $(\bar{U}, \bar{V}, \bar{W})$ be the physical velocity components in $(\bar{x}, \bar{y}, \bar{s})$ directions, respectively. Then $V^1 = \bar{U}$, $V^2 = \bar{V}$, $V^3 = \bar{W}/\sqrt{G}$ [13]

where
$$G = [1 + \bar{K}(\bar{x}\cos\theta - \bar{y}\sin\theta)]^2 + \bar{\tau}^2(\bar{x}^2 + \bar{y}^2) \tag{8}$$

Dimensionless variables are defined as follows:

Lengths are nondimensionalized by $(X, Y, Z) = (\bar{x}, \bar{y}, \bar{s})/d$ where d is the hydraulic diameter defined by $d = 2ab/(a+b)$ and velocities are related to the dimensionless velocities U, V, W by $\bar{U} = \nu U/d$, $\bar{V} = \nu V/d$, $\bar{W} = \nu W/d$ where ν is the kinematic viscosity of fluid. The pressure and time t are related to the dimensionless pressure P by $\bar{P} = \rho\nu^2 P/d^2$ and time T by $t = Td^2/\nu$, respectively. If we assume that the flow is fully developed and the pitch is so small that torsion of the channel can be neglected, the basic governing equations can be expressed as follows

The equation of motion:

$$\frac{\partial U}{\partial T} + U\frac{\partial U}{\partial X} + V\frac{\partial U}{\partial Y} - \frac{KW^2\cos\theta}{\lambda}$$
$$= -\frac{\partial P}{\partial X} + \frac{\partial^2 U}{\partial X^2} + \frac{\partial^2 U}{\partial Y^2} + \frac{K}{\lambda}D^*U - \frac{U^*K^2\cos\theta}{\lambda^2} \tag{9}$$

Nomenclature

a = width of channel on the north or south surface
A = area
b = width of channel on the east or west surface
$\mathbf{B}$ = binormal vector
d = hydraulic diameter, $2ab/(a+b)$
De = Dean number, $\mathrm{Re}\sqrt{K}$
f = friction factor, $2\tau_w/\bar{w}^2_{av}$
$\bar{f}$ = averaged axial shear stress, $\int(\partial w/\partial n)_w dA/A$
g^{ij} = metric tensor
i = index
j = index
k = index
$\bar{K}$ = curvature
K = dimensionless curvature, $\bar{K}d$

$\mathbf{N}$ = normal vector
$\bar{P}$ = pressure
p = dimensionless pressure, $d^2\bar{P}/\rho\nu^2$
$\mathbf{r}$ = position vector
Re = Reynolds number, $\bar{W}_{av}d/\nu = W_{av}$
t = time
T = dimensionless time
$\mathbf{T}$ = tangent vector
U, V, W = dimensionless velocity components in X, Y, and Z directions
$\bar{U}, \bar{V}, \bar{W}$ = velocity components, $(U, V, W)/(d/\nu)$
X, Y, Z = dimensionless coordinate
x, y, z = Cartesian coordinate
$\bar{x}, \bar{y}, \bar{s}$ = new coordinate, $(X, Y, Z)d$

ν = kinematic viscosity
θ = angle of inclination
ρ = density
$\bar{\tau}$ = torsion
τ_w = mean shear stress at wall
α, β = index
ψ = dimensionless stream function
ω = relaxation factor
$\Gamma^i_{\beta k}$ = Christoffel symbols

Subscript

c = value for curved ducts
s = value for straight ducts
w = value of wall
av = averaged value

Table 1 Numerical test for different grid systems in two cases; Case 1: $\partial P/\partial Z = -20000$, $K = 0.01$, $\theta = 30$ deg; case 2: $\partial P/\partial Z = -40000$, $K = 0.05$, $\theta = 30$ deg

	Grid system	De	fc/fs
case 1	28 x 28	57.95	1.2096
	20 x 20	58.00	1.2086
	10 x 20	58.61	1.1960
case 2	28 x 28	189.31	1.6559
	20 x 20	190.50	1.6455
	10 x 20	193.07	1.6237

$$\frac{\partial V}{\partial T} + U\frac{\partial V}{\partial X} + V\frac{\partial V}{\partial Y} + \frac{KW^2\sin\theta}{\lambda}$$
$$= -\frac{\partial P}{\partial Y} + \frac{\partial^2 V}{\partial X^2} + \frac{\partial^2 V}{\partial Y^2} + \frac{K}{\lambda}D^*V + \frac{U^*K^2\sin\theta}{\lambda^2} \quad (10)$$

$$\frac{\partial W}{\partial T} + U\frac{\partial W}{\partial X} + V\frac{\partial W}{\partial Y} + \frac{U^*KW}{\lambda}$$
$$= -\frac{1}{\lambda}\frac{\partial P}{\partial Z} + \frac{\partial^2 W}{\partial X^2} + \frac{\partial^2 W}{\partial Y^2} + \frac{K}{\lambda}D^*W - \frac{K^2W}{\lambda^2} \quad (11)$$

The equation of continuity:

$$\frac{\partial}{\partial X}(\lambda U) + \frac{\partial}{\partial Y}(\lambda V) = 0 \quad (12)$$

where

$$\lambda = 1 + K(X\cos\theta - Y\sin\theta),$$
$$U^* \equiv U\cos\theta - V\sin\theta$$
$$D^* \equiv \cos\theta\frac{\partial}{\partial X} - \sin\theta\frac{\partial}{\partial Y}$$

The boundary conditions on the velocity components are obtained from the no-slip and no-porous conditions at the duct walls. Therefore at $X = \pm 1/2$ and $Y = \pm 1/2$ we have

$$U = V = W = 0 \quad (13)$$

If the torsion of the duct, $\tau \neq 0$, additional terms will be contributed by the torsion parameter in equations (9)–(11). The three components of pressure gradient are all coupled in the three component equations. If $\Theta = 0°$ the equations (9)–(12) reduces to that of references [2–5].

It is not possible to obtain an analytical solution for these differential equations, which are nonlinear, coupled parabolic equations. In order to solve this problem of steady fully developed flow, a numerical method of steady-state approach can be used. Equations (9)–(12) with boundary condition (13) are integrated in time using a time step of forward difference.

Solution Procedure

For the asymmetrical flow field induced by an angle of inclination, one must consider the full domain for this problem. Since the boundary conditions do not depend on time, the unsteady-state problem (equations (9)–(12)) will converge to a steady-state solution. In our numerical solution, a central difference scheme based on the ADI (alternating direction implicit) method is implemented on a uniformly spaced grid system with 20×20 square cells. Such a grid system has been employed in past numerical works concerning curved duct flows by Austing [10], Partankar [15], Joseph [2], and Cheng [3]. The velocities at corners and the pressure at cell centers are indicated by subscripts i and j representing X and Y coordinates, whereas the superscript k represents the marching time step. A numerical test has been made to make sure that this grid system has a sufficient accuracy at $\theta = 30$ deg. As shown in Table 1, the relative errors for both the friction 0.7 percent.
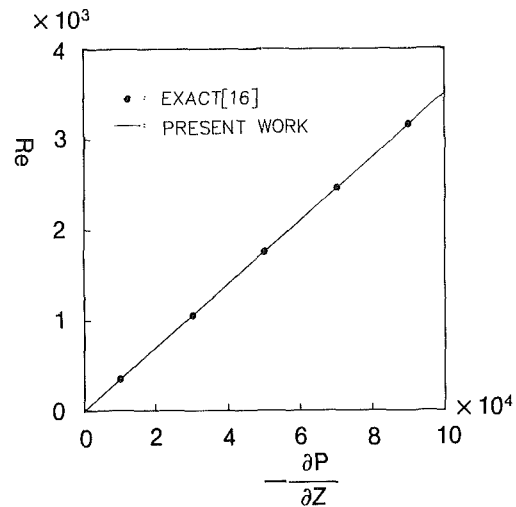
Fig. 2 Reynolds number versus pressure gradient for $K = 0$

By substituting X and Y momentum equations (9)–(10) into continuity equation (12) for each cell in finite difference form, one obtains the auxiliary pressure equations [2]. Therefore the pressure distribution can be solved simultaneously throughout the 20×20 equations. A general outline of the main steps of numerical procedure is as follows:

(1) The velocity distributions (U, V, and W) are guessed initially.

(2) From the initially guessed value of velocity distributions $U_{i,j}^k$ and $V_{i,j}^k$ an estimate of the cross-stream pressure, $P_{i,j}^{k+1}$ is obtained by employing point iteration to solve the auxiliary pressure equations.

(3) The transverse velocities $U_{i,j}^{k+1}$, $V_{i,j}^{k+1}$ and axial velocity $W_{i,j}^{k+1}$ are calculated with the ADI method aided by preliminary pressure $P_{i,j}^{k+1}$ and the prescribed pressure gradient $\partial P/\partial Z$.

(4) The known values $U_{i,j}^{k+1}$, $V_{i,j}^{k+1}$ and $W_{i,j}^{k+1}$ to $U_{i,j}^k$, $V_{i,j}^k$ and $W_{i,j}^k$ are updated.

(5) The steps (2) to (4) are repeated until the following convergence criterion is satisfied for all nodes

$$\text{abs}((E_{i,j}^{k+1} - E_{i,j}^k)/E_{i,j}^{k+1}) < 10^{-4}$$

where E stands for P, U, V, or W.

It is necessary to use an underrelaxation factor ω in solving the pressure equations in order to make the solution converge. A relaxation factor ω ranging from 1 to 0.7 is guessed for Dean numbers increasing from 13 up to 250.

Other authors who studied the problem of curved channel flow had the same difficulty of defining a convergence criterian since the solutions exhibit oscillations in the neighbourhood of the expected steady-state solution. So, their numerical criterion was similarly defined as

$$\text{Max}(E_{i,j}^{k+1} - E_{i,j}^k)/\text{Max}(E_{i,j}^{k+1}) < 10^{-3}.$$

The goal of the present work was to compare the solutions for various angles of inclination. It is necessary to use the criterion in step (5) to obtain a more accurate solution. The computing time required was about twenty minutes on a VAX 11/780 computer for every case investigated.
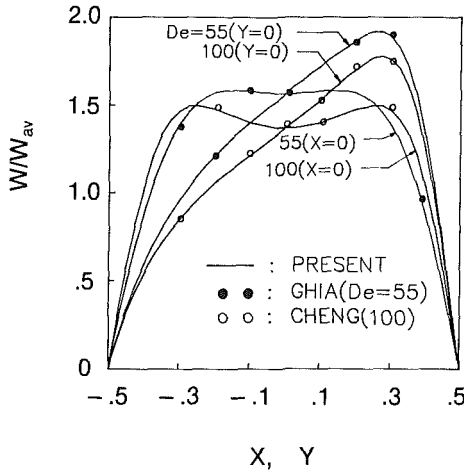
Results and Discussions

Among several theoretical and experimental papers [2–7] concerning curved rectangular channel flow, the effect of angle of inclination had never been considered. For the limiting case of straight rectangular channel flow as $K = 0$, Fig. 2 shows that the present results of Reynolds number as a func-

Table 2 Reynolds number and Dean number compared with the literature as $\theta = 0$ deg

| $\frac{\partial P}{\partial Z}$	K	Re	De	fc/fs
-4×10^3	0.01	139.4/[139]	13.94/[13.9]	1.01[1.01]
-9×10^3	0.01	295.7/[295]	29.57/[29.5]	1.07[1.07]
-1.9×10^4	0.01	554.2/[548]	55.42/[54.8]	1.21[1.22]
-4×10^4	0.01	1033.8/[1000]	103.3/[100.0]	1.37[1.41]
-1.1×10^5	0.01	2185.0/[2026]	218.5/[202.6]	1.78[1.91]
-2.5×10^4	0.25	466.9/[430]	233.4/[214.8]	1.89[2.04]

[] : Result of Cheng[3]

Fig. 3   Axial flow profile at $X=0$ and $Y=0$ for $\theta = 0$

Fig. 4   Influence of inclination angles θ on streamline contours with $\Delta\psi = 1.2$ for $-\partial P/\partial Z = 45000$ and $K = 0.05$

tion of pressure gradient are in agreement with the exact solution [16]. Other results of the special case $\Theta = 0$ deg are compared with Cheng's work [3] in Table 2. Due to the different condition of criterion for convergence, the comparison shows a slight discrepancy of at most 8 percent at a Dean number around 230. In addition to the above comparisons in Table 2 and Fig. 2, the axial velocity profiles at $X=0$ and $Y=0$ are shown to be in agreement with available references as shown in Fig. 3.

When the cross section of the square channel is with an inclination angle Θ greater than 0 deg, the geometry is no longer horizontally symmetric until the angle of inclination is equal to 45 deg. In Figs. 4 and 5, the stream function contours and the axial velocity distribution for various angles of inclination are plotted, respectively. The patterns for both streamfunction and axial velocity at $\Theta = 0$ and $\Theta = 45$ deg are symmetrical as is seen by the straight dividing streamline. The centrifugal force towards the outer wall induced from the axial component of momentum attains a maximum value near the outer wall of a channel. For channels with inclination angles $0 < \Theta < 45$ deg as shown in Fig. 4(b), (c), the secondary flow in the upper part of the channel makes a smaller turn to return along the boundary near the outer wall surface than the lower part of the channel. Thus, a vortex of greater strength is developed in the upper part of the channel. Similarly, the vortex in the lower part of the channel has a greater strength than that in the upper part of the channel as $45 < \Theta < 90$ deg. This can be seen in Figs. 4(e) and 4(f). In addition, the second pair of vortices occurs at the inclination angle 0 deg only. This is because the outer wall for other angles of inclination is no longer perpendicular to the plane of the channel centerline except at $\Theta = 0$ deg. In Fig. 5, the maxima of axial velocity driven by the centrifugal force and effected by the channel corner is located in the lower right as $0 < \Theta < 45$ deg and in the upper right as $45 < \Theta < 90$ deg.
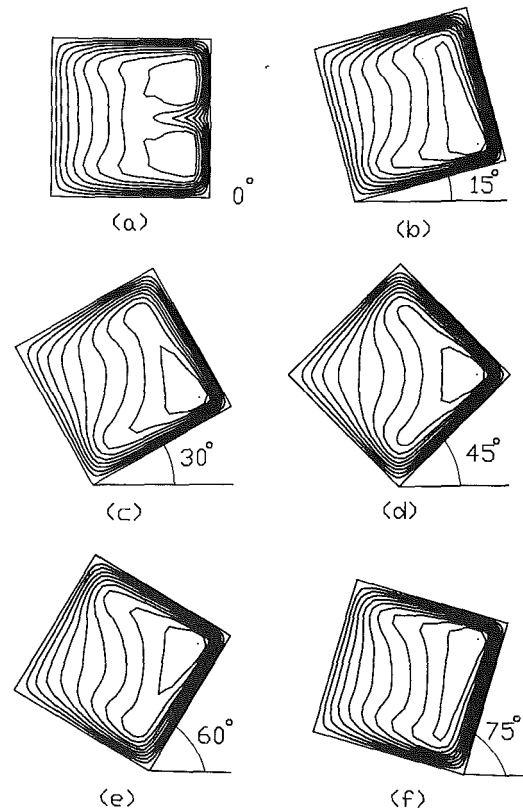
Fig. 5   Influence of inclination angles θ on axial-flow velocity distribution with $\Delta W = 168.7$ for $-\partial P/\partial Z = 45000$ and $K = 0.05$
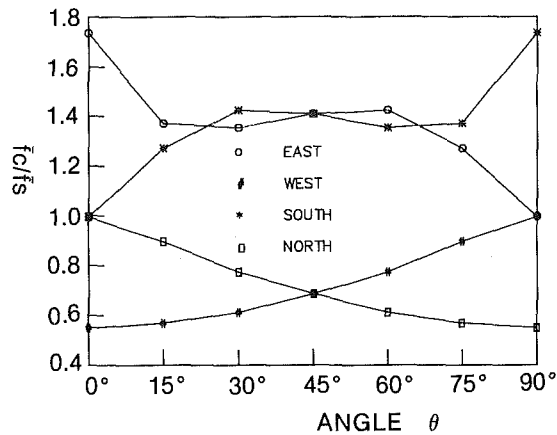
Fig. 6 Averaged axial shear stresses at various inclination angles on four oriented surfaces for $-\partial P/\partial Z = 45000$ and $K = 0.05$
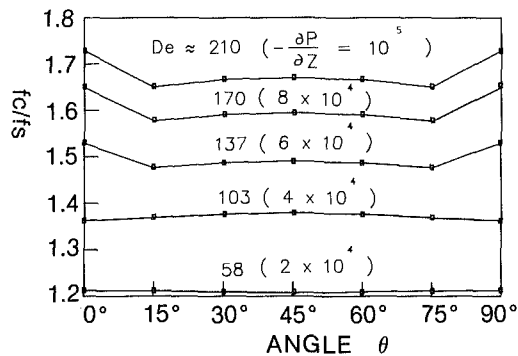

Fig. 7 Friction factor ratios at various inclination angles for $-\partial P/\partial Z = 10^5, 8 \times 10^4, 6 \times 10^4, 4 \times 10^4, 2 \times 10^4$, respectively, as $K = 0.01$

Fig. 8 Friction factor ratios as a function of pressure gradient for various inclination angles with $K = 0.05$

Fig. 9 Friction factor ratios as a function of pressure gradient for various inclination angles with $K = 0.01$

The associated average axial shear stresses on the four oriented surfaces denoted in Fig. 1 are plotted in Fig. 6 for various angles of inclination and for the same pressure gradient and channel curvature. However, the friction factor ratios calculated for the same nondimensional averaged axial velocity are the same for complementary angles of inclination as seen in Fig. 7. The friction factor ratio as a function of pressure gradient is shown in Fig. 8, at four inclination angles, $\Theta = 0$, 15, 30, and 45 deg, for the curvature $K = 0.05$. At $\Theta = 0$ deg, it is noted that an abrupt change in fc/fs occurs when the Dean number is about equal to 125, for which Dean's instability is believed to happen [7]. When the value of curvature decreases to $K = 0.01$, similar phenomena are obtained at $De \approx 125$ as shown in Fig. 9. The discontinuity in the curve $\Theta = 0$ deg of Figs. 8 and 9 is not a creation of the numerical scheme. It is the reflection of the physical phenomena when secondary flow with symmetric two-cell vortices switches to symmetric four-cell vortices as the parameter $\partial P/\partial Z$ increase across a critical value. Some authors [17, 18] dealing with the heating problems in horizontal straight pipes with symmetry also obtained a discontinuity owing to the same physical mechanism as ours. For $\Theta \neq 0$ deg, the symmetric condition can no longer apply and the discontinuity is not present in our numerical calculations. In other words, the dominating effect on the sudden increase of friction factor ratio is actually controlled by the Dean number. The friction factor ratio for $\Theta = 0$ deg has a lower value than those for other angles of inclination if $De < 125$, while for $De > 125$ the friction factor ratio for $\Theta = 0$ deg is larger than that for others angles.

Concluding Remarks

1. To obtain a lower friction factor ratio in curved square channel flows, one should choose an angle of inclination $\Theta = 0$ deg when $De < 125$, or $\Theta = 15$ or 75 deg when $De > 125$.
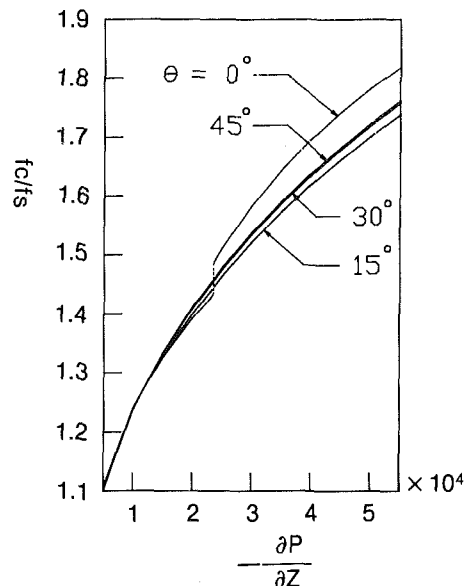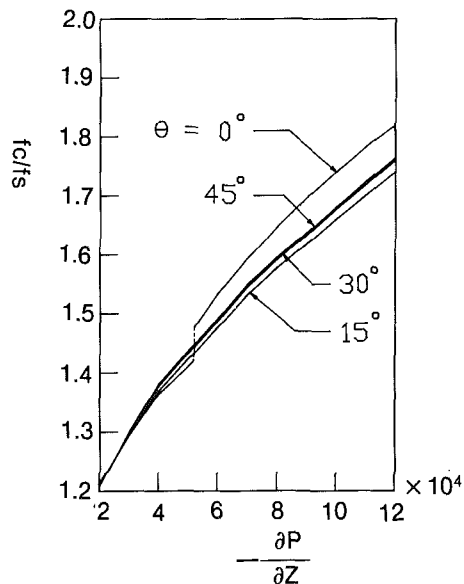
2. At the inclination angles $\Theta = 0$, and 45 deg, the stream function contours and axial velocity distributions are symmetrical with respect to the horizontal bisecting streamline.

3. The strength of the vortex at the lower part of the channel cross section is smaller when $0 < \Theta < 45$ deg and higher when $45 < \Theta < 90$ deg.

4. The maximum axial velocity is located in the right lower part of the channel cross-section if $0 < \Theta < 45$ deg, and in the right upper part if $45 < \Theta < 90$ deg.

5. An interesting extension of the present research will be to consider heat and mass transfer in curved rectangular channel flow in the presence of angles of inclination.

References

1 Berger, S. A., Talbot, L., and Yao, L. S., "Flow in Curved Pipes," *Ann. Rev. Fluid Mech.*, Vol. 15, 1983, pp. 461–512.

2 Joseph, B., Smith, E. P., and Adler, R. J., "Numerical Treatment of Laminar Flow in Helically Coiled Tubes of Square Cross-section," *AIChE J.*, Vol. 21, 1975, pp. 965–979.

3 Cheng, K. C., Lin, R. C., and Ou, J. W., "Fully Developed Flow in Curved Rectangular Channels," ASME JOURNAL OF FLUIDS ENGINEERING., Vol. 98, 1976, pp. 41-48.

4 Ghia, K. N., and Sokhey, J. S., "Laminar Incompressible Viscous Flow in Curved Ducts of Rectangular Cross-section," ASME JOURNAL OF FLUIDS ENGINEERING., Vol. 99, 1977, pp. 640-648.

5 Sokhey, J. S., "Analysis of Three-Dimensional Incompressible Viscous Flow in Curved Ducts," PhD thesis, University of Cincinnati, 1977.

6 Hille, P., and Vehrenkamp, R., "The Development and Structure of Primary and Secondary Flow in A Curved Square Duct," J. Fluid Mech., Vol. 151, 1985, pp. 219-241.

7 Ghia, K. N., Ghia, U., and Shin, C. T., "Study of Fully Developed Incompressible Flow in Curved Ducts, Using A Multi-Grid Technique," ASME JOURNAL OF FLUIDS ENGINEERING., Vol. 109, 1987, pp. 226-236.

8 Dean, W. R., "Note on The Motion of Fluid in A Curved Pipe," Philos. Mag., Vol. 20, 1927, pp. 208-223.

9 Dean, W. R., "The Streamline Motion of Fluid in A Curved Pipe," Philos. Mag., Vol. 30, 1928, pp. 673-693.

10 Austin, L. R., and Seader, J. D., "Fully Developed Viscous Flow in Coiled Circular Pipes," AIChE J., Vol. 19, 1973, pp. 85-94.

11 Ito, H., "Theory on Laminar Flows Through Curved Pipes of Elliptic and Rectangular Cross-Sections," Rep. Inst. High Speed Mech., Tohoku Univ., Sendai, Jpn., Vol. 1, 1951, pp. 1-16.

12 Masliyah, J. H., "On Laminar Flow in Curved Semicircular Ducts," J. Fluid Mech., Vol. 99, 1980, pp. 469-479.

13 Wang, C. Y., "On The Low-Reynolds Number Flow in A Helical Pipe," J. Fluid Mech., Vol. 108, 1981, pp. 185-194.

14 Kreyszig, E., Advanced Engineering Mathematics, Fourth Edition, Wiley, New York, 1979, pp. 379-382.

15 Patankar, S. V., Pratap, V. S., and Spalding, D. B., "Prediction of Laminar Flow and Heat Transfer in Helical Coiled Pipes," J. Fluid Mech., Vol. 62, 1974, pp. 539-551.

16 Yih, C. S., Fluid Mechanics, West River Press, Michigan, 1979, pp. 309-312.

17 Chou, F. C., and Hwang, G. J., "Combined Free and Forced Laminar Convection in Horizontal Rectangular Channels for High ReRa," The Canadian Journal of Chemical Engineering, Vol. 62, 1984, pp. 830-836.

18 Law, H. S., Masliyah, J. H., and Nadakumar, K., "Effect of Nonuniform Heating on Laminar Mixed Convection in Ducts," ASME Journal of Heat Transfer, Vol. 109, 1987, pp. 131-137.

Check Valve Behavior Under Transient Flow Conditions: A State-of-the-Art Review

A. R. D. Thorley
Thermo-Fluids Engineering Research Centre,
The City University,
London, United Kingdom

Recent advances in the understanding of check valve behavior are reviewed. It is evident that the basis now exists for providing reliable information on valve dynamics that is in a form that can be easily assimilated and used by pipeline design engineers. The use of nondimensional valve performance curves is discussed and recommended. Manufacturers are encouraged to provide these data. Design engineers are charged with the responsibility of using it and are provided with guidelines for so doing.

Introduction

Check valves are items of equipment that were originally developed and fitted to pipelines in order to prevent the lines draining backwards when pumps stopped – and sometimes also to prevent the downstream reservoirs from emptying. In addition, they prevented reverse rotation of pumps, thereby avoiding damage to seals and to the brush gear of the driving motors.

It was thought, initially, that the valves simply had to close fairly quickly and to seal effectively. The early designs, therefore, were based in general on the concept of a simple swinging disc (closure element). These were usually quite adequate to protect relatively low head systems but as pumping pressures increased, multi-pump systems evolved and surge protection devices such as air vessels became more common, so too did the phenomenon of "check valve slam."

In these simple swing check valves, in which the moving element has to travel through a significant distance, e.g., 60–90 deg, and in which its position is controlled almost entirely by the movement of the fluid, the mean velocity of the fluid is backward at the instant of closure. This reverse flow velocity is reduced immediately to zero giving rise to high pressures and the valve slam phenomenon. The name is derived from the fact that as the valve nears its seat, reducing the backward flow, a pressure rise builds up which accelerates the closure, so that at the last moment the valve disk does indeed "slam" onto its seat.

This problem has assumed increasing importance in recent years and led to various test programs, modifications to existing valves, and the development of new styles of valve. For several years some degree of confusion existed over the most appropriate remedies for the problem of valve slam and the criteria that should be applied when selecting the most suitable check valve for a particular application.

Through the efforts of a number of researchers [1–12] the behavior of check valves is now understood more clearly, enabling them to be selected with greater confidence in their performance.

Systems Most at Risk

Piping systems and check valves that are most at risk are those where pumps are delivering against relatively high pressure heads. In particular one can cite examples of multi-pump installations such as deep mine drainage, power station condensate and boiler feed pumps where major problems are known to have occurred.

For example, Fig. 1 shows a section of a cooling water system comprising four pumps in parallel and which has experienced major problems with check valve slam. Normally up to three pumps are in service with one as a standby. The pumps are rated at 50 m head when delivering 833 l/s at a speed of 980 rev/min and having a power requirement of 470 kW.

As a result of attempting to protect the pump with a carelessly selected swing check valve major problems of check valve slam, line vibration and failure occurred. Figure 2 illustrates pressure-time histories obtained from controlled tests following a pump trip when, in the upper trace, a swing check
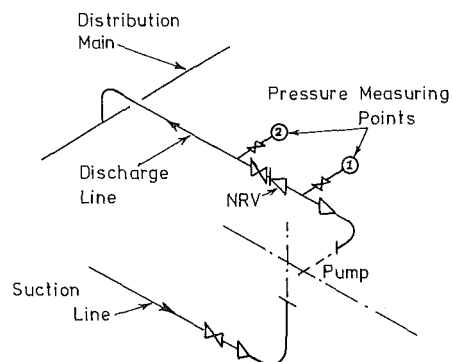

Fig. 1 Layout of one of four similar feed pumps arranged in parallel showing the location of the valves and pressure measuring points
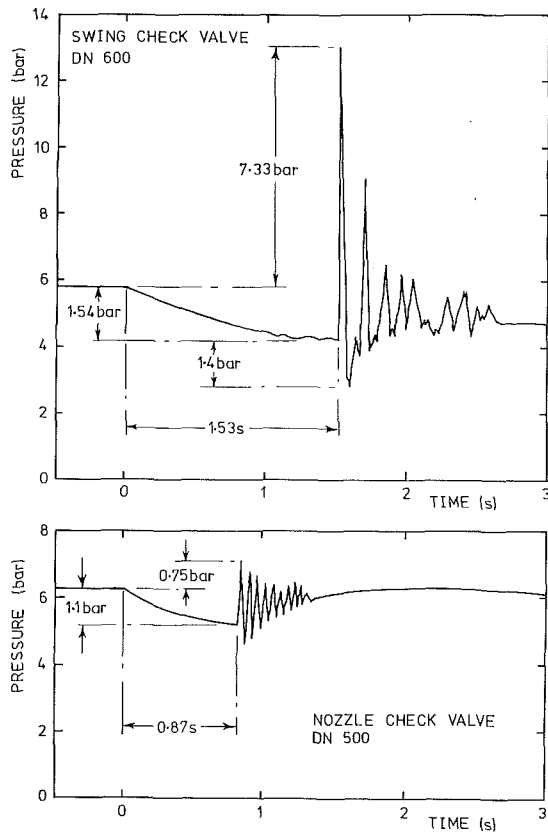
Copyright © 1989 by ASME

Fig. 2 Comparison of pressure-time histories immediately downstream of the check valve (point 2) in Fig 1. Three pumps were in service initially; this one was tripped out at zero time.

Fig. 3 Pressure-time records for a manual pump changeover when the pumps are fitted with counter-weighted swing check valves

Fig. 4 Figure 3, but with the pump fitted with nozzle type check valves

valve was fitted. For comparison purposes, the lower trace is for the same conditions but with a nozzle type check valve used instead.

The test conditions were that three pumps were running and one, for which the results are given, was tripped out. The only differences between the two sets of tests were (*a*) the nominal diameters of the swing and nozzle check valves were 600 mm and 500 mm respectively and (*b*) the pump impeller was reduced from 650 mm to 620 mm diameter. However, the initial steady conditions were of the same order for both tests and yet the results are markedly different.

Another example is illustrated with Figs. 3 and 4 which refer to a power station condensate extraction system. Several comparions have been made [13] but the figures shown concern a manual pump changeover. The sequence in both cases is:

Pump 'B' running – Start Pump 'A'
– Trip out Pump 'B'.

Figure 3 shows the pressure-time response when the pumps are protected by swing check valves; Fig. 4 is the corresponding response when nozzle type nonreturn valves were fitted instead.

These are two of several multi-pump examples [14] that could be quoted by way of illustration. However, even single pump installations can be at risk, particularly if they supply a pipeline protected by an air vessel. In such a case, when the power driving the pump is lost the air vessel acts as an energy source analogous to other pumps continuing to run in parallel. Liquid is forced out of the air vessel and into the system tending to maintain forward flow down the pipeline but also tending to flow back through the pump. If the check valve is slow in responding ideal conditions for hazardous check valve slam are created. Figure 5 is an example pressure-time history for a laboratory test on such a system.
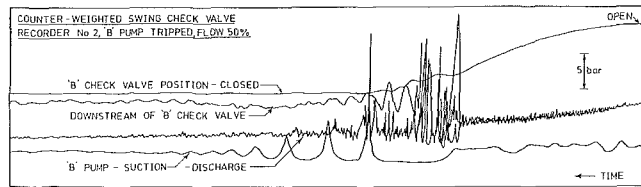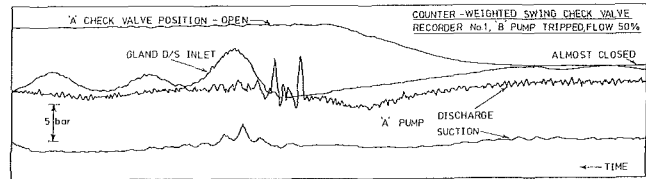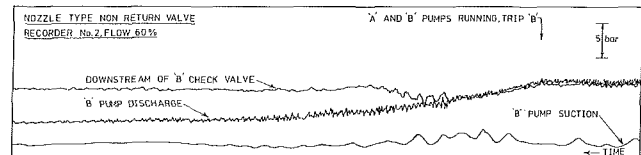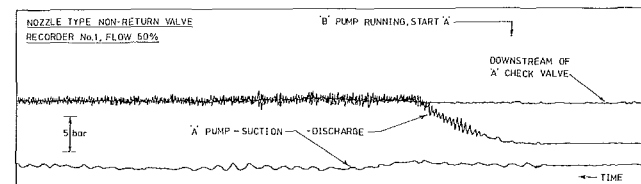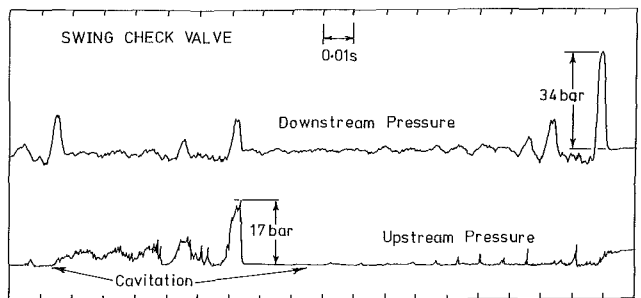
Fig. 5 An example of upstream and downstream pressure-time histories for tests on a swing check valve in a single line following a simulated pump trip. Note that "time" goes from right to left.

Since the final flow stoppage is virtually instantaneous, the pressure transient created on the downstream side of the valve is a "rapid" event in the context of fluid transients and the magnitude ΔH of the pressure head rise caused by the reduction in flow velocity from V_R to zero may be estimated from the well-known Joukowski equation, i.e.,

$$\Delta H = \frac{cV_R}{g} \tag{1}$$

where c is the speed of propagation of transient pressure waves in the pipeline (typically 1000–1200 m/s in steel pipelines) and g is acceleration due to gravity. In approximate terms:

$$\Delta H \simeq 100 \, V_R \quad \text{metres head.}$$

It is therefore imperative that the maximum reverse velocity V_R which occurs virtually at the instant of closure, should be reduced as near to zero as possible. This can only be achieved

by careful design and selection of check valves which must be matched to the system of which they are an integral part.

It should be noted also that the occurrence of high transient pressures is not restricted to the downstream side. On the upstream side of the closing valve, as the reverse velocity is reduced to zero, the falling pressure may easily drop to the vapour pressure of the liquid and a vaporous cavity produced. This cavity will normally collapse rapidly in response to pressure waves reflected from further upstream giving rise to large pressure pulses which may, in some circumstances, cause the check valve to reopen momentarily and then crash back onto its seat. The remedy is to select a valve that is capable of responding sufficiently quickly to the changing flow conditions so that pressure fluctuations due to the valve closure itself are within acceptable limits. This does not necessarily mean that closure must occur at the instant the flow velocity is zero, the pipeline may be capable of withstanding a rapid shut-off from a small forward or reverse velocity.

Equally it is misleading to define or specify valve responses in terms of a required closure time since it is not this in itself that is important, but the flow velocity at the instant of closure. This is dependent on the system being considered and although a particular time delay is acceptable for a given valve on one system it would usually be quite inappropriate for another.

Characterizing the Dynamic Behavior of Check Valves

In seeking to understand how check valves respond to rapidly changing flow conditions engineers have had two principal motives:

(i) To establish the desirable characteristics of check valves to provide a basis for improved design and selection, and

(ii) To develop suitable mathematical means of describing valve response for inclusion in computer codes used to predict fluid transient behavior of pipelines.

These objectives prompted two lines of research, a variety of experimental studies [1, 2, 4, 8, 11–14] in which several valve types were studied independently and under different circumstances, and theoretical studies [3, 5, 6, 10, 11, 12, 14, 15] which in the main referred to attempts at developing equations of motion for the valves, although two [12, 16] introduce the use of dimensional analysis and dynamic similarity to enable experimental data to be expressed in terms of useful equations.

Desirable Characteristics

The empirical studies previously referenced were undertaken on both prototype plant and test facilities in engineering laboratories. Despite the results having been produced from a variety of sources there were sufficient comparisons that some meaningful conclusions could be drawn [5, 14]. The principal ones were that a good response to changing flow conditions could be obtained if:

(i) The moving parts of the valve are of low inertia,
(ii) Their motion is assisted by a spring or springs, and
(iii) The distance/angle through which the moving elements have to travel is small.

The extent to which actual valves possess these features can be illustrated graphically in the form of Dynamic Performance Characteristics after the fashion first proposed by Provoost [4] – see Fig. 6.

The vertical axis is the maximum reverse velocity that occurs during valve closure, usually immediately before the moving elements are seated. The base line is the mean deceleration of the liquid column as the flow is brought to rest. In practice,
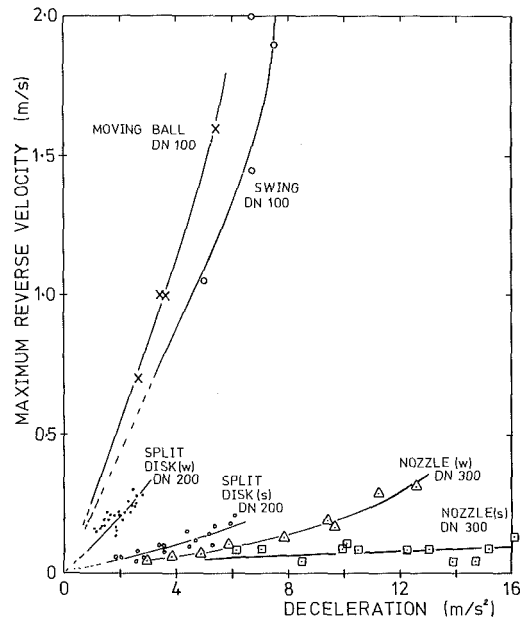

Fig. 6 Typical dynamic performance characteristic, after the style of Provoost [2, 3] which should be provided by valve manufacturers

this is the slope of the main part of the velocity-time trace, which seems to be fairly constant in many cases.

On such a performance chart, the ideal curve would be coincident with the horizontal axis. The swing check and ball valves which are the subject of the upper curves are clearly a poor match, whereas the nozzle valve with a strong spring is the best suited to the system.

To select a check valve for a particular system the procedure to be adopted is to determine the deceleration of the liquid column (dV/dt) under expected transient or fault conditions and then by reference to valve performance characteristics select a valve that has an acceptable dynamic response, i.e., not necessarily the best, but one that is adequate for the job. In some systems swing check valves may still be good enough, but in others a very high level of performance may be essential.

Before proceeding to a discussion of how these experimentally determined dynamic characteristics can be used in conjunction with computer codes, the purely theoretical developments which were evolving concurrently will be mentioned briefly, for completeness.

Theoretical Studies

When a valve, or any other component, is incorporated into a mathematical model of the unsteady flow through a piping system it is necessary to have equations relating the pressure change "ΔH" across it to the flow "Q" through it, i.e.,

$$\Delta H = f(Q) \tag{2}$$

The precise form of the equation depends on the nature of the component, and for valves can include experimentally determined loss coefficients and the state of opening or closure as preferred. For check valves this leads into a need for equations relating the forces and torques to the kinematic behavior of the moving elements. For example, for swing check valves, torques due to gravity, T_G, fluid pressure, T_P, friction T_f, buoyancy T_B, and springs T_S, are related to the angular acceleration $\ddot{\theta}$ by:

$$T_G + T_P + T_f + T_B + T_S = (I_D + I_F)\ddot{\theta} \tag{3}$$

The right-hand side of this equation contains the inertia I_D and I_F of the valve door and adjacent fluid, respectively.

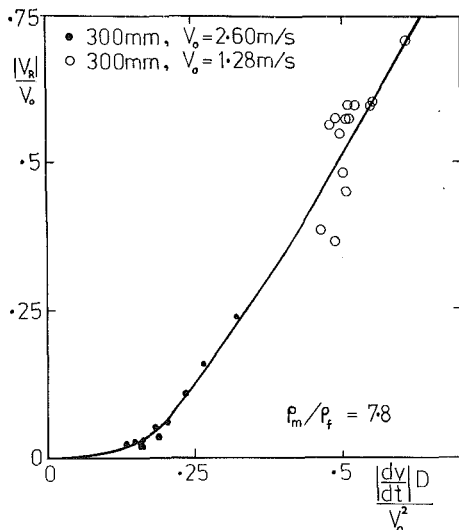When the valve elements move axially, as in nozzle and

Fig. 7 Dimensionless dynamic characteristic for a nonreturn valve

plunger type valves (3) the general form of the corresponding equation of motion is similar to equation (3). Forces replace torques and masses replace inertias.

The gravitational, buoyancy and externally applied torques, together with the inertia of the moving elements in the valve, are easily determined from valve dimensions and material properties. The remaining terms require some degree of speculation supported by carefully controlled experiments for the deduction of empirical coefficients. For example, it may be postulated that the friction torque, T_f, would be of the form:

$$T_f = K_1 + K_2 \theta^n \qquad (4)$$

in which K_1, K_2 are constants and n an arbitrary, and perhaps constant, power.

Similarly, hydrodynamic forces/torques will depend on the rapidly changing flow patterns around the valve, its position and the flowrate Q, e.g.

$$T_P = f(Q, \theta, \dot{\theta}, \ddot{\theta}) \qquad (5)$$

The precise form cannot be found analytically – a probable form might be supposed and empirical coefficients determined for particular examples.

The remaining inertia term, I_F, refers to the added mass effect of the fluid moving in close proximity to the valve door. It is somewhat speculative, but from experiments in air and water [17] it does appear that the added mass effect for a circular swinging gate valve could be estimated as being equivalent to a sphere of fluid having a diameter the same as the valve door and with their geometric centers coincident.

Due to the indeterminate nature of some of the components of equation (3), and the wide variety of valve types and sizes, recent developments in the form of non-dimensional groups [14, 12] especially when allied [12] to the Provoost style dynamic characteristics would appear to show most promise for inclusion in computer models of transient flow.

Scaling Laws and Dimensionless Characteristics

The benefits of model testing in thermo-fluids engineering are well-known and such techniques are frequently used – pumps, turbines, aerofoil sections etc., being common examples. In particular, model testing frequently helps keep development costs within acceptable limits as well as providing important insights into fluid flow phenomena.

An essential pre-requisite of model testing is that geometric similarity must exist between model and prototype. This helps ensure kinematic similarity, i.e., similarity of flow pattern,

which in turn leads to dynamic similarity or similarity of forces and torques.

The hope is then that data collected from experiments with models can be expressed in terms of suitable non-dimensional parameters which will apply to both the model and the prototype.

Combining and extending ideas proposed by Collier and Hoerner [16] and Koetzier et al. [12] parameters that are relevant to the dynamic behavior of many non-return valves are:

D characteristic diameter
dV/dt mean fluid deceleration
V_o flow velocity when the valve is just fully open (critical velocity)
V_R maximum reverse velocity just prior to closure
ρ_m density of the moving elements
ρ_f density of the fluid
F_o net spring and gravitational force on the moving element when just fully open
F_s net spring and gravitational force on the moving element when closed
μ fluid viscosity
Δp frictional pressure drop across the valve
x distance travelled by the moving element from its seat.

These eleven parameters, which between them contain the three fundamental properties of mass, length and time, can be arranged into eight independent groups using one of the several techniques that are available (18), e.g., Buckingham-Pi theorem or the Rayleigh method.

Taking ρ_f, D, and μ as the repeating variables the following groups can readily be developed:

$$\frac{D}{V_o^2} \cdot \frac{dV}{dt} \; ; \; \frac{V_R}{V_o} \; ; \; \frac{F_o}{\rho_f V_o^2 D^2} \; ; \; \frac{\Delta p}{\rho_f V_o^2} \; ; \; \rho_f \frac{V_o}{\mu} D;$$

$$\frac{\rho_m}{\rho_f} \; ; \; \frac{F_o}{F_s} \; ; \; \frac{x}{D}$$

This set really applies to valves in which the moving element translates in an axial direction. A similar set can, however, be derived for swing type valves and split disc types, in which case the forces would be replaced by torque, T_o/linear characteristic dimension. The third and last parameters would then be:

$$\frac{T_o}{\rho_f V_o^2 D} \text{ and } T_o/T_s$$

Complete matching of these groups between models and prototypes will be impossible, but some can be ignored as being of minor importance and the others categorized into two groups: (a) those of primary importance and (b) those of secondary importance which should be kept as nearly consistent as reasonably possible.

Of minor importance will be the non-dimensional critical force, $F_o/\rho_f V_o^2 D^2$, frictional pressure drops and viscous effects generally in terms of Reynolds numbers. Collier and Hoerner [16], for example, showed from a series of tests that at various opening positions of a split disk (dual plate) valve the ratio $\Delta p/\rho_f V_o^2$ was essentially constant.

It will be noted that the first two non-dimensional groups contain the principal terms of the dynamic characteristic shown in Fig. 6. This points to the idea that dimensionless characteristics can be expressed in equation form as:

$$\frac{V_R}{V_o} = \phi \left(\frac{D}{V_o^2} \cdot \frac{dV}{dt} \, , \, \frac{\rho_m}{\rho_f} \, , \, \frac{F_o}{F_s} \, , \, \frac{x}{D} \right) \qquad (6)$$

and also suggests ways to develop experimental programs to provide the maximum amount of useful information from the minimum number of tests. For example, Fig. 7 (taken from
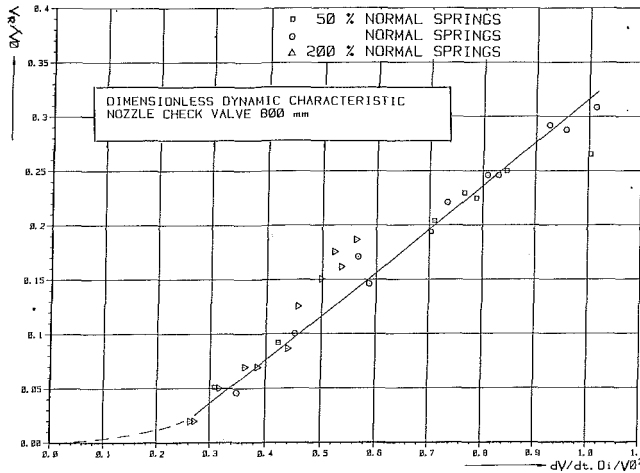
Fig. 8 Dimensionless dynamic characteristic for a 800 mm nominal bore nozzle type check valve for three spring strengths

Fig. 9 Indication of how nondimensional valve performance curves may be used for check valve selection. Valves T4 and T5 would be suitable.

Koetzier et al. [12] is a plot of V_R/V_o versus $D/V_o^2 \cdot dV/dt$, assuming all other three parameters in equation (6) are constant. Figure 8 is a similar diagram for a nozzle type of nonreturn valve. Three sets of data are shown, having been obtained from tests into the effect of spring strength on valve response. It is observed that the normal and weak springs give essentially the same response although there is a slight deviation with the strong springs. Given that mean fluid decelerations are used to obtain these data points the degree of scatter for preliminary results of this nature is not unreasonable and indicates that this approach has definite promise.

All of the results to which reference has been made relate to tests in water. From equation (6) one of the dimensionless parameters is ρ_m/ρ_f, the density ratios of the moving element and the fluid in the pipeline. No attempt has yet been made to assess how closely it is necessary to conform to this ratio when other fluids are being pumped. For example, if, say, oil of relative density 0.875 is being pumped, how important is it that the valve elements be manufactured from a material correspondingly lighter to obtain the same dynamic response? Future tests with different fluids and valve elements of different materials will provide an indication.

Representation of Check Valve Behavior in Computer Codes

The most common assumption in computer codes is to assume that the valves close at the instant the flow reaches zero at that location, even though it may be recognized that this is not quite true. Some attempts have been made to incorporate a delay using techniques such as swept volume during closure, e.g., based on reverse velocity multiplied by the area of the moving element, but it has been acknowledged (reference [11], for example) that these methods can also be quite inaccurate.

If, as a result of incorporating data from several valve sizes in the same homologous groups, it transpires that a single curve results, a much better and simple representation of check valve behavior will be possible. A strategy for achieving this is as follows:

(i) From a knowledge of the permissible maximum pressure in the pipeline and valve casing (due to acceptable stress and shock load levels) specify an acceptable pressure head change ΔH due to a sudden stoppage.

(ii) From equation (1), obtain the maximum permitted reverse velocity V_R, by solving:

$$V_R = g\Delta H/c \qquad (1)$$

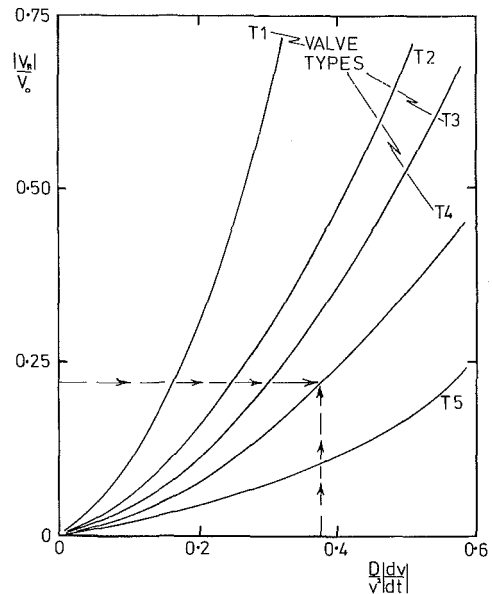(iii) Normalize V_R by dividing by V_o, the flow velocity

when the valve is just fully open – sometimes taken from experience or by design as 75 percent of the intended flow velocity. This will give an upper limit on charts such as Fig. 7.

(iv) In the computer code to be used for transient analysis, the boundary condition representing the check valve should arrange for the valve to close at the instant the flow velocity reaches the value of V_R.

(v) From the predicted velocity-time history at the valve up to this point the mean fluid deceleration is obtained. Normalizing this with V_o and D, and reading up on Fig. 9 to intersect with the corresponding V_R/V_o line enables a valve with a suitable dynamic response to be selected.

(vi) The pressure-time histories should also be scrutinized carefully to confirm that the maximum pressures experienced adjacent to the valve do indeed remain within acceptable limits.

In order to adopt the foregoing strategy it is essential that adequate dynamic response curves are available. It has been argued previously [9, 12] that just as pump and turbine manufacturers are expected to produce performance curves for their equipment, so too should manufacturers of check valves. It is even more true now than before.

Responsibilities and Liabilities

The pipeline design engineer responsible for specifying components for his systems has a duty to ensure that they are the most appropriate and cost-effective. In the context of check valves, as with other components, he can only do this if he is provided with adequate data. For example, he must have all the information necessary to follow through the procedures outlined in the previous section – which in turn means that:

(i) Valve manufacturers must accept the responsibility for providing authentic performance data on their products. Eventually, insurance companies may insist upon it.

(ii) The designers responsible for the overall system should ensure that fluid transient studies are carried out for the proposed system, encompassing all the possible scheduled and unscheduled operating scenarios that are likely to produce hazardous conditions – and the "worst case" adopted as the design criteria.

In recognition that many systems are not installed as designed or operated as intended it is also the responsibility of

the engineer in overall charge to review the situation at the commissioning stage. It is only then that certain assumptions such as wave propagation speeds, pump performance data, friction losses, etc., used in the fluid transient studies, can be confirmed.

Concluding Remarks

The last 6–10 years has witnessed notable advances in the understanding of check valve behavior. A basis has been established for graphically representing valve dynamic response from measurements taken under laboratory conditions. Nondimensional representation of the important terms maximizes the use to which such data can be put and provides useful guidelines for future valve testing.

The nondimensional performance curves also enable check valves to be represented by simple boundary condition routines in computer programs. The key feature is to establish the maximum acceptable reverse velocity through the valve and use this as the control parameter in the program. The mean deceleration of the fluid then provides the vital link to selecting the most appropriate check valve commensurate with meeting cost and performance criteria.

Acknowledgments

References

1 Provoost, G. A., "The Dynamic Behaviour of Non-Return Valves," Paper J1, *Procs. 3rd Int. Conf. on Pressure Surges*, BHRA, 1980, pp. 415–428.

2 Collier, S. L., and Hoerner, C. C., "A Facility and Approach to Performance Test of Check Valves," Procs. ASME Paper No. 82-Pet-16, Energy Sources Technology Conf., New Orleans, March 1982; ASME JOURNAL OF FLUIDS ENGINEERING, Vol. 105, Mar. 1983, pp. 620–67.

3 Kubie, J., "Performance and Design of Plug-Type Check Valves," *Procs. I.Mech.E.*, Vol. 176, 1982, pp. 47–56.

4 Provoost, G. A., "The Dynamic Characteristics of Non-Return Valves," Paper 14, *11th IAHR Symposium of the Section on Hydraulic Machinery, Equipment and Cavitation; Operating Problems of Pump Stations and Power Plants*, Amsterdam, Sept. 1982.

5 Thorley, A. R. D., "Dynamic Response of Check Valves," Paper F1, *Procs. 4th Int. Conf. on Pressure Surges*, BHRA, Bath, Sept. 1983, pp. 231–242.

6 Provoost, G. A., "A Critical Analysis to Determine the Dynamic Characteristics of Non-Return Valves," Paper F4, *Procs. 4th Int. Conf. on Pressure Surges*, BHRA, Bath, Sept. 1983, pp. 275–286.

7 Erdody, I., and Bokemeier, V., "The Closure Behaviour of Undamped Swing Check Valves," *Procs. 5th Int. Symposium on Water Column Separation*, IAHR, Obernach, 1981.

8 Pake, M. C., "Non-Return Valve Testing: Description of a Rig and Preliminary Results for a Double Disc Valve," *Procs. 6th Int. Symposium on Hydraulic Transients in Power Stations*, IAHR, Gloucester, 1983.

9 Thorley, A. R. D., "Can We Develop a Safe Check Valve?" Paper H2, *Procs. Int. Conf. on Developments in Valves and Actuators for Fluid Control*, BHRA, Oxford, Sept. 1985, pp. 293–304.

10 Ellis, J., and Mualla, W., "Selection of Check Valves," Paper H1, *Procs. 5th Int. Conf. on Pressure Surges*, BHRA, Hannover, Sept. 1986, pp. 213–222.

11 Perko, H. D., "Check Valve Dynamics in Pressure Transient Analysis," Paper H3, *Procs. 5th Int. Conf. on Pressure Surges*, BHRA, Hannover, 1986, pp. 229–236.

12 Koetzier, H., Kruisbrink, A. C. H., and Lavooij, C. S. W., "Dynamic Behaviour of Large Non-Return Valves," Paper H4, *Procs. 5th Int. Conf. on Pressure Surges*, BHRA, Hannover, 1986, pp. 237–244.

13 Fox, R. E., "Dungeness "B" Power Station Condensate System Surge Tests," APC Report No. 1, Mar. 1980 and Report No. 3, Apr. 1981.

14 Thorley, A. R. D., "A Comparative Review of Check Valve Performance," Confidential Research Report TF/1282/1, The City University, London, Dec. 1982.

15 Schneider, D., "Dynamisches Verhalten von Doppelruckschlag-Klappen," (Dynamic Behaviour of Dual Plate Wafer Check Valves) der Zeitschrift 3R-International, Vulkan-Verlag, 1985.

16 Collier, S. L., and Hoerner, C. C., "Development of Affinity Relations for Modelling Characteristics of Check Valves," ASME *Journal of Energy Resources Technology*, Vol. 103, Sept. 1981, pp. 196–200.

17 Thorley, A. R. D., and Oei, J. H., "Dynamic Behaviour of a Swing Check Valve," *Procs. 5th Int. Symposium on Water Column Separation*, IAHR, Obernach, Sept. 1981.

18 Massey, B. S., "Units, Dimensional Analysis and Physical Similarity," Van Nostrand Reinhold, London, 1971.

M. P. Sharma
Department of Petroleum Engineering,
University of Wyoming,
Laramie, Wy.

C. T. Crowe
Department of Mechanical Engineering,
Washington State University,
Pullman, Wash.

Application of Computer Modeling in the Design of a Multiphase Flow Metering System

Two numerical models (CONVAS and PSI-Cell) for analyzing steady nonequilibrium gas-particle flow through a venturi and an orifice plate are discussed. These models are validated by comparing the predictions with experimental data. Utilizing these models, parametric curves for venturis and orifice plates have been generated. Using these curves a methodology has been outlined for designing a two-phase mass flowmeter.

1 Introduction

The flow of gases with suspended particles is encountered in diverse industrially important energy and environment related applications. The applications range from pulverized coal combustion and gasification, air pollution control systems, pneumatic conveying of granular materials, and numerous chemical engineering processes to more exotic, advanced, and unconventional systems for nuclear, geothermal, and magneto-hydrodynamic power. These areas of application share a common need for improved measurement techniques, particularly flow metering. Unlike metering the flow of a single gaseous or liquid phase (for which accurate orifice and/or venturi coefficients are available), metering two-phase flows is more art than science. The complexity of multiphase flows has defied a systematic analytic design methodology.

Industrial methods for metering the flow of gas-particle suspensions currently in use are, by necessity, unsophisticated. For example, the flow rate of pulverized coal into a combustor is often metered by weighing the coal deposited on a moving belt. This system is not amenable to fine adjustments in the fuel flow rate to achieve the optimal combustion efficiency and economy. If a venturi or an orifice could be used on line with a certain level of reliability, a fuel-flow control system comparable to gas- or oil-fired burners could be realized. Similar situations arise in other industrial applications of gas-particle flows. Some attempts [1, 2] have been made to establish flow coefficients for gas-particle flow through orifices and venturis. Early studies [3] indicated that the presence of particles in a gas stream had no detectable effect on the pressure drop across an orifice; that is, the pressure drop across an orifice could be used to measure the gas flow rate even though particles were present in the gas stream. Further studies indicated that particles did affect the pressure drop across the venturi, the pressure drop being that corresponding to a homogenous gas-particle mixture. Thus the venturi measured the flow rate of the mixture. This observation was applied to the design of a flow-metering system con-

sisting of an orifice and a venturi in series which yield data sufficient to determine the flow rate of each phase. Even though the device was successful on the laboratory scale, it was found inoperative on an industrial scale [4]. A re-evaluation of this technique shows that failure in industrial applications is attributable to unavailability of adequate scaling laws or analytical models to assess scale effects. These studies have shown that the effect of particles on the pressure drop across a venturi or orifice depends on the loading (mass of particles/mass of gas) and Stokes number [5].

The Stokes number is defined as the ratio of kinetic relaxation time of the particle to the system transit time. If the Stokes number is large, insufficient time is available for the particle to maintain velocity equilibrium with the gas and, correspondingly, there is little effect of the particles on the pressure field. Such is the situation for the orifice. On the other hand, if the system transit time is large compared to the particle's relaxation time, the particles are better able to maintain velocity equilibrium with the gas, and there is a corresponding effect on the pressure field. Such are the conditions for the venturi. At very large scale, the Stokes number is small for both the orifice and venturi, so the combination is incapable of detecting the flow rate of the individual phases. The limits of applicability can only be established by experiment or valid numerical models.

Gas particle flow through a venturi can be analyzed assuming quasi-one-dimensional flow using the "conservative variable" approach [6]. The acronym for this model is CONVAS (Conservative Variable and Source). A more sophisticated model—the PSI-Cell (Particle Source in Cell) [7]—is necessary for two dimensional orifice flow. The purpose of this paper is to illustrate the application of CONVAS and PSI-Cell models in the design of a venturi-orifice type two-phase flow meter. The viability of these models has been established by comparing the predictions with the experimental data.

2 Basic Approach

The primary difficulty is modeling two-phase flows arises
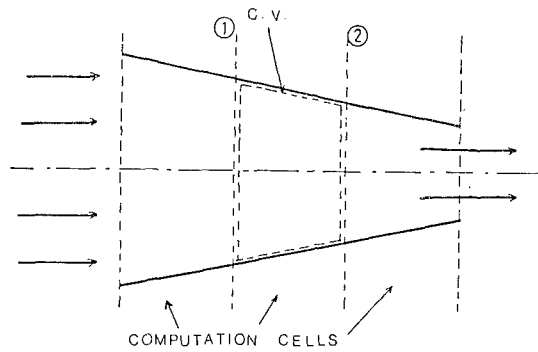
Fig. 1 Computational cells and control volume for CONVAS model

Fig. 2 Computational scheme for CONVAS model

from the synergistic interaction of mass, momentum and energy transfer between the phases. This is called coupling phenomena [6].

The basic approach is first to divide the flow field into a series of computational cells and to regard each cell as a control volume. The change in the momentum of the particles as they pass through a cell is regarded as a source (or sink) to the momentum of the gaseous phase; that is, if a particle is accelerated by the flow field there must be a corresponding decrement of the gas momentum in the same direction within the cell.

The particle trajectories are obtained by integrating the equations of motion for the particles in the gas flow field, utilizing an appropriate expression for the drag coefficient. The particle trajectories and velocity along trajectories is obtained using the Lagrangian approach, which is the most straightforward approach for the particulate phase. Recording the momentum of the particles upon crossing cell boundaries provides the particle momentum source terms for the gas-flow equations.

3 CONVAS Model

The quasi one-dimensional gas-particle flow field is divided into a number of computational cells and each cell is con-
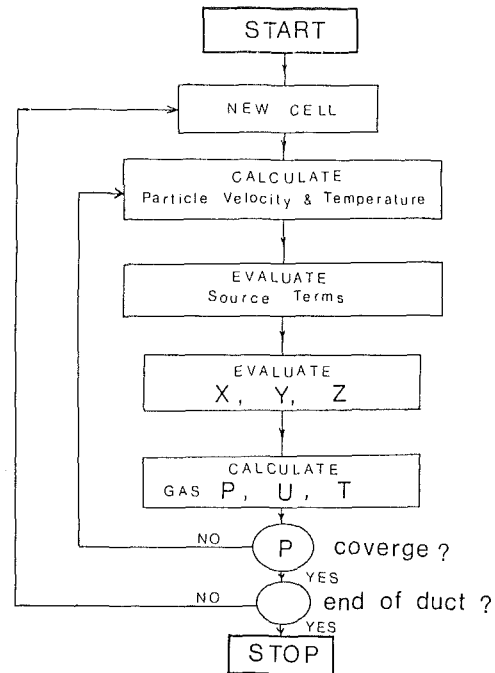
sidered a control volume, Fig. 1. The conservation equations for mass, momentum, and energy for a typical control volume can be written in terms of conservative variables X, Y, and A as:

$$X_2 = X_1 + \Delta \dot{m}_p \tag{1}$$

$$Y_2 = Y_1 + \Delta \dot{M}_P + \left(\frac{P_1 + P_2}{2}\right)(A_2 - A_1) - F_{wx} \tag{2}$$

$$Z_2 = Z_1 + \Delta \dot{E}_P + \dot{Q} \tag{3}$$

where the conservative variables are defined as:

$$X = \rho U A, \quad Y = PA + XU, \quad Z = (h + 1/2 \ U^2)\rho U A \tag{4}$$

Nomenclature

A = area
A_p = particle cross section area
a = coefficients in momentum equations
C_D = drag coefficient
C_{pg} = specific heat of gas at constant pressure
C_v = specific heat of gas at constant volume
C_{pp} = specific heat of particle material
C_0, C_1, C_2, C = turbulence model coefficients
D = diameter of duct
d, d_p = diameter of a particle
d_0 = orifice diameter
d_t = throat diameter of a venturi
E = energy
$\Delta \dot{E}_P$ = energy source due to particles

F = force
F_{SL} = starting location mass-friction
F_{di} = particle size mass fraction
f = drag factor
G = mass flux, rate of turbulent kinetic energy generation
h = specific enthalpy
I = axial cell location
J = transverse cell location
k = specific heat ratio, kinetic turbulent energy
L = length of the converging section of a venturi
M = momentum flux
ΔM_A = momentum source due to area change
$\Delta \dot{M}_P$ = momentum source due to particles
m_p = mass of a particle

$\Delta \dot{m}_p$ = mass source term
$\dot{m}_p$ = mass flow rate of particles
$\dot{m}_g$ = mass flow rate of gas
n = number of particles/time
P, p = pressure
$\Delta P_{mt}, \Delta P_{mo}$ = pressure drop for mixture flow in venturi (throat); in orifice
$\Delta P_{gt}, \Delta P_{go}$ = pressure drop for gas flow in venturi (throat); in orifice
$\dot{Q}$ = heat transfer rate
R = gas constant
Re = particle Reynolds number
S = source term
St = Stokes number
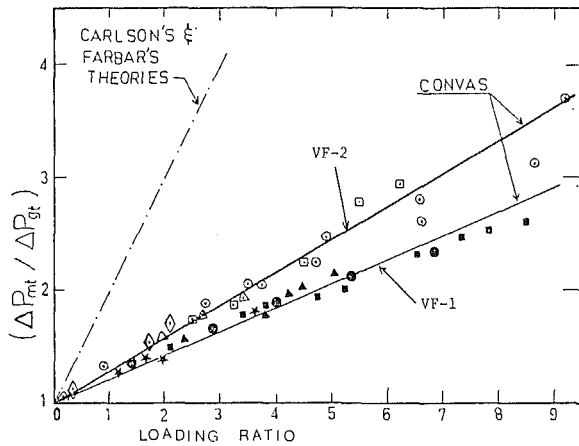St_o = Stokes number for orifice
St_v = Stokes number for venturi

Fig. 3 Comparison of CONVAS predictions with Farber's experimental data [1] for two venturis VF-1 and VF-2

$\Delta \dot{m}_p$, $\Delta \dot{M}_p$, and $\Delta \dot{E}_P$ are source terms due to particles. h, P, ρ, U are specific enthalpy, pressure, density, velocity of gas and A is cross-sectional area of the duct. F_{wx} and $\dot{Q}$ are shear force and heat transfer at the wall of the duct.

The source terms are evaluated by integrating the equations of motion and energy of a particle moving in a gas medium. The reader should refer to the reference (7) for details.

$$\Delta \dot{M}_p = z \, \dot{m}_g \, (V_1 - V_2) \qquad (5)$$

$$\Delta \dot{E}_p = \frac{1}{2} z \, \dot{m}_g \, (V_1^2 - V_2^2) + z \, \dot{m}_g C_{pp} \, (T_{p1} - T_{p2}) \qquad (6)$$

The solution procedure starts by guessing P_2 and then following calculational steps shown on the flow chart, Fig. 2.

To illustrate the applicability and reliability of CONVAS, the predictions of the nondimensional pressure differential through a venturi are compared with the experimental data of Farbar [2] (coal particles), and Sharma [5] (silica particles), Figs. 3 and 4. In these figures the results predicted by CONVAS-theory (the solid lines) are compared with the ex-
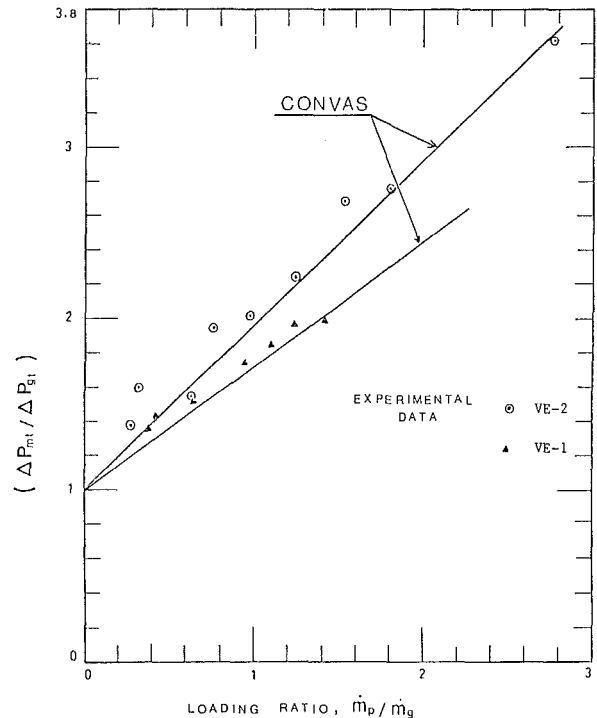

Fig. 4 Comparison of CONVAS predictions and Sharmas' experimental data for two venturi's VE-1 and VE-2 [5]

perimental data (dots) obtained by Farber [1] (in Fig. 3) and Sharma [5] (in Fig. 4). Two lines in Fig. 3 belong to two different designs of venturis, used by Farber. Similarly in Fig. 4, the two lines belong to the results of two different designs. Details of these designs are available in reference [5].

The excellent agreement establishes that CONVAS can be reliably used in the design and analysis of gas-particle flows through venturis.

_____ **Nomenclature (cont.)** _____

T = temperature of gas
T_p = particle temperature
t = time
T_g = relaxation time for gas flow field
U = x-direction velocity of the gas (one dimensional)
$\mathbf{u}$ = gas velocity vector
$\mathbf{u}_p$ = velocity vector for a particle
V = particle velocity (one dimensional)
X = mass conservative variable
x = first coordinate direction
Y = momentum conservative variable
y = second coordinate direction
Z = energy conservative variable
z = particle loading ratio

β = diameter ratio ($d/_0D$ for orifice, d_t/D for venturi
θ = angle of converging section of venturi
ϵ = turbulent energy dissipation
$\sigma_\kappa, \sigma_\epsilon$ = turbulent Prandtl numbers for κ and ϵ, respectively
ρ = density of gas
ρ_p = density of particle material
τ = dynamic characteristic time
τ_Q = thermal characteristic time
μ = viscosity, microns
ν = kinematic viscosity
κ = turbulent kinetic energy

Subscripts

1 = upstream conditions

2 = downstream conditions
I, J = index for grid nodes
N, S, E, W = north, south, east, west
o = orifice
g = gas
v = venturi
m = mixture of gas and particles

Superscripts

j = trajectories
x = axial direction
y = traverse direction

Acronyms

CONVAS = conservative variable and source model
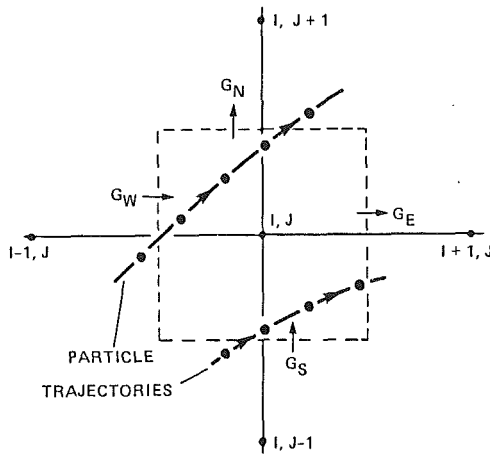PSI-Cell = particle-source-in-cell model
SM = signal Magnification

Fig. 5 Computational cell for PSI-cell model

4 PSI-Cell Model

The two-dimensional steady flow of gas-particle mixture through an orifice can be analyzed using the PSI-Cell Model [5]. After dividing the flow field into a number of rectangular cells, finite-difference equations for momentum of the gas phase are written for each cell, incorporating the contribution due to the condensed phase as a source term. The entire flow-field solution is obtained by solving the system of algebraic equations constituting the finite-difference equations for each cell.

Refer to the cell shown in Fig. 5 which encloses a typical node (I, J). The four faces of this cell are identified as points on a compass: north, south, east, and west. The continuity equation for steady flow of the gas-particle mixture through this cell (control volume) is:

$$G_E + G_N - G_W - G_S + \Delta \dot{m}_p = 0 \qquad (7)$$

where G_i is the mass flux rate of the gas through the "ith" face and $\Delta \dot{m}_p$ is the net mass efflux rate of the particles from the cell.

If the particles are not reacting (burning, evaporating, or condensing), then the mass source term is zero. Such is the situation for the application of this paper.

Having located the cells for the continuity equation as enclosing the nodal points, the cells for the momentum equation must be located between nodes. Referring to Fig. 5, one notes that the u-component of velocity in the continuity equation is not the velocity at the nodal point but halfway between nodes. Consequently, the control volume used to solve for u from the x-momentum equation is displaced from that used for the continuity equation. The momentum equation in the x-direction for steady flow requires that

$$-M_W^x + M_E^x - M_S^x + M_N^x + \Delta M_P^x = (P_{I-1,J} - P_{I,J})A_N + S_P^x \qquad (8)$$

where M_P^x is the momentum flux of the gas in the x-direction across the "ith" face, ΔM_P^x is the net efflux of x-momentum from the cell due to the droplets, $P_{I,J}$ is the pressure at node (I,J), and S_P^x arises from the variation in effective viscosity in the flow field [8]. The momentum flux consists of that due to convection and diffusion (viscosity). Body force terms have been neglected.

One notes that the net efflux of momentum due to the droplets can be regarded as the momentum source term to the gaseous phase. The net droplet momentum efflux from a cell due to trajectory "j" which traverses the cell is given by

$$\Delta \mathbf{M}_{P,j} = \dot{n}_j [(m\mathbf{V})_{\text{out}} - (m\mathbf{V})_{\text{in}}] \qquad (9)$$

where $\mathbf{V}$ is the droplet velocity. The net momentum efflux for all trajectories which pass through the cell is

$$\Delta \mathbf{M}_P = \sum_j \Delta \mathbf{M}_{P,j} \qquad (10)$$

The cell used for the y-momentum equation is located below and midway between the nodes (I,J) and $(I,J-1)$.

Two more equations are used in the numerical program to model the turbulence and to determine the effective viscosity. The turbulent field is described by the local intensity of turbulence and the dissipation rate, commonly referred to as the k-ϵ model.

In order to evaluate the source terms due to the presence of the particles, the particle equation of motion is integrated utilizing the velocity and pressure field of the gas. The original details are available in reference [7]. The rearranged form of the equation of motion of a particle is

$$d\mathbf{V}/dt = (18\mu f/\rho_p d^2)(\mathbf{U} - \mathbf{V}) \qquad (11)$$

where, $f = C_D \, \text{Re}/24 = 1 + 0.15 \, R_e^{.687}$ for $\text{Re} \le 1000$

$$\text{Re} = \frac{\rho |\mathbf{V} - \mathbf{V}| d}{\mu} = \text{particle Reynolds number}$$

It is to be noted that the Reynolds number used in equation (11) is particle Reynolds number (not pipe Reynolds number) and is defined in a special way. Particle drag coefficient correlation given above has been found valid up to particle Reynolds number value of 1000. The critical value of particle Reynolds number (at which laminar to turbulent transition would occur) is approximately 1.0.

Integrating equation (11) assuming the gas velocity is constant over the time of integration yields

$$\mathbf{V} = \mathbf{U} - (\mathbf{U} - \mathbf{V}_0)\exp(-\Delta t/\rho_P d^2/18\mu f) \qquad (12)$$

where V_0 is the initial particle velocity and Δt is the time interval. After determining the new droplet velocity after time Δt, the new droplet location is determined from

$$\mathbf{x}_p = \mathbf{x}_{p,o} + (\mathbf{V} + \mathbf{V}_o)\Delta t/2 \qquad (13)$$

where $\mathbf{x}_{p,o}$ is the droplet position at the beginning of the time increment.

Turbulence Model Equations. The turbulence closure problem has to be solved before attempting to solve the conservation of mass and momentum equations. A summary of the existing turbulent closure models has been compiled by Launder and Spalding [9]. A two equation model is used in this analysis to account for the turbulence and to determine the effective viscosity. The turbulence field is described by the local kinetic energy (intensity) of turbulence (κ) and the dissipation rate (ϵ). The two-equation model consists of the solutions to the transport equations for these two physical quantities κ and ϵ.

$$\frac{\partial}{\partial x}(\rho u \kappa) + \frac{\partial}{\partial y}(\rho v \kappa) - \frac{\partial}{\partial x}\left(\frac{\mu}{\sigma_\kappa}\frac{\partial \kappa}{\partial x}\right)$$
$$- \frac{\partial}{\partial y}\left(\frac{\mu}{\sigma_\kappa}\frac{\partial \kappa}{\partial y}\right) = G - C_0 \rho \epsilon \qquad (14)$$

$$\frac{\partial}{\partial x}(\rho u \epsilon) + \frac{\partial}{\partial y}(\rho v \epsilon) - \frac{\partial}{\partial x}\left(\frac{\mu}{\sigma_\epsilon}\frac{\partial \epsilon}{\partial x}\right)$$
$$- \frac{\partial}{\partial y}\left(\frac{\mu}{\sigma_\epsilon}\frac{\partial \epsilon}{\partial x}\right) = \frac{C_1 \epsilon G}{\kappa} - \frac{C_2 \rho \epsilon^2}{\kappa} \qquad (15)$$

$$G \equiv 2\mu\left[\left(\frac{\partial u}{\partial x}\right)^2 + \left(\frac{\partial v}{\partial y}\right)^2\right] + \mu\left[\frac{\partial u}{\partial y} + \frac{\partial v}{\partial x}\right]^2$$

where σ_κ and σ_ϵ is considered as the turbulent Prandtl numbers for κ and ϵ, and are treated as constants. C_0, C_1, and C_2 are other constants. G is rate of generation of κ and $\rho \epsilon$ is rate of
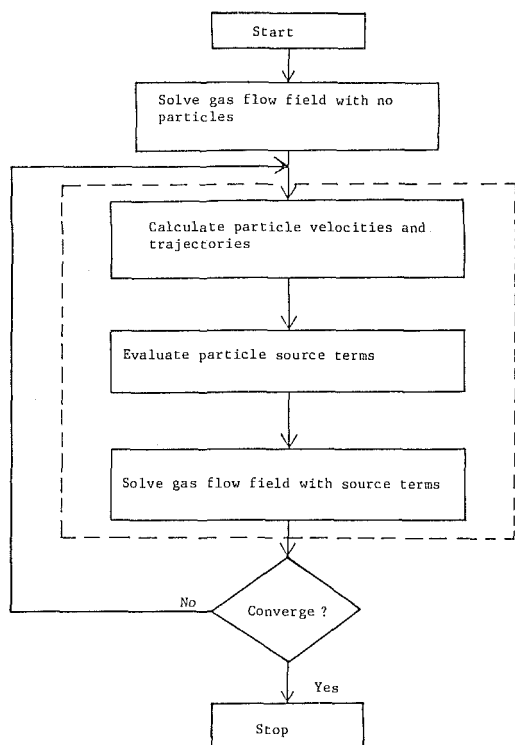
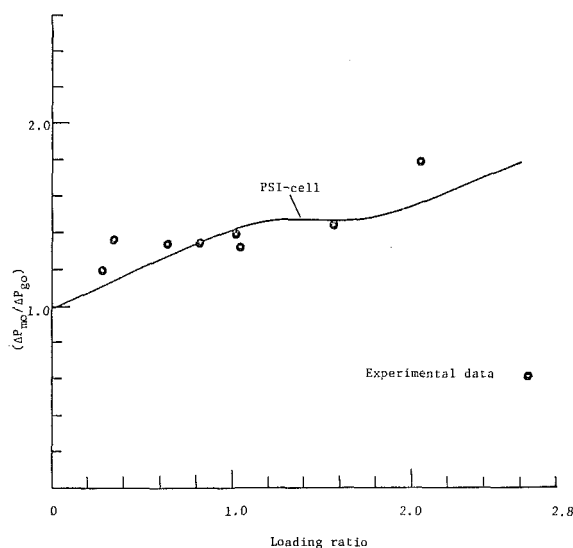**Fig. 6 Computational scheme for PSI-cell model**

Fig. 7 Comparison of PSI-cell predictions and experimental data for orifice flow [5]

dissipation. The finite-difference form of these equations is incorporated into the program to yield the kinetic energy of turbulence and the dissipation rate as related to the mean velocity field. Having evaluated the turbulence intensity and dissipation rate in a cell, the effective viscosity is determined using Prandtl-Kolmogorov formula:

$$\mu = \frac{C_\mu \rho \kappa^2}{\epsilon} \tag{16}$$

where C_μ is a constant.

The values of various global constants in this model are taken from [9].

No attempt is made to include the effect of particles on the turbulence field because little is known about the quantitative effect of particle size and concentration on the turbulence parameters.

It should be also noted that though the κ–ϵ model is a significant improvement over mixing length models, it still assumes that Reynolds stresses depend only on the local mean velocity gradients, and that turbulence adjusts itself instantly to local changes in the mean flow field. On the contrary, it is well established that "history" and "action-at-distance" are dominant in establishing local turbulence characteristics. Two-equation model, however, has been found satisfactory in many flows of interest [9].

The complete solution for the droplet-gas flow field is executed as shown in Fig. 6. The calculation is done by first solving the gas flow field assuming no droplets are present. Using this flow field, droplet trajectories are calculated, and the momentum source terms for each cell throughout the flow field are determined. The gas flow field is solved again incorporating these source terms. The new gas flow field is used to establish new droplet trajectories which constitutes the effect of the gas phase on the droplets. Calculating new source terms and incorporating them into the gas flow field constitutes the effect of the droplet cloud on the gas phase, thereby completing the "two-way" coupling. After several iterations the flow field equations are satisfied to within a predetermined value and the solution which accounts for the mutual interaction of the droplets and gas is obtained.

The comparison of the predicted and measured pressure drops across an orifice is shown in Fig. 7. The data are plotted as the ratio of pressure drop with particles to that for a clean gas versus the loading ratio (mass flow rate of particles/mass flow rate of gas). By definition, the pressure ratio is unity at a loading ratio of zero. The data were taken from [5]. One notes favorable agreement between the predicted and measured values, which lends support to the validity of the model. The validation of these models have been further established in other gas-particle flow applications and are reported in a recent review paper [10].

5 Design Curves

CONVAS and PSI-Cell models are used to generate design curves for designing a two-phase flowmeter consisting of a venturi and an orifice place. The primary design parameters are,

$$St_v = \frac{\rho_p d^2_p}{18 \cdot \mu \cdot f} \cdot \frac{U_{in}}{L} \cdot \frac{D-d_t}{2L} \quad \text{(for venturi)} \tag{17}$$

$$St_o = \frac{\rho_p d^2_p}{18 \cdot \mu \cdot f} \cdot \frac{U_{in}}{D} \quad \text{(for orifice)} \tag{18}$$

$$\beta = d_o/D \text{ (orifice)}; = \frac{d_t}{D} \quad \text{(venturi)} \tag{19}$$

$$Z = m_p/m_g \tag{20}$$

$$\theta = \frac{D-d_t}{2L} \tag{21}$$

where D is diameter of duct, d is diameter of orifice, d_t is venturi throat diameter, and L is length of converging section of venturi.

The design curves for orifice plate are shown in Fig. 8. It shows the variation of the threshold values of particle loading (z) with Stokes number (St_o) for different β values (d_o/D). The threshold value of loading is defined as the maximum value of z for which particles have "no effect" on the gas pressure field (for a given St_o and β). Each curve divides the z-St_o plane into two regions. Left of this curve is the region of "no effect" of particles on the gas pressure field. To measure the gas flow rate only, an orifice has to be designed such that the parameters lie in the "no effect" region of this plane.
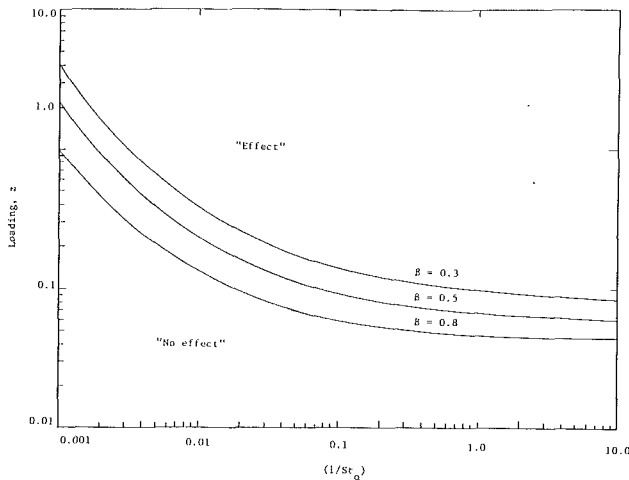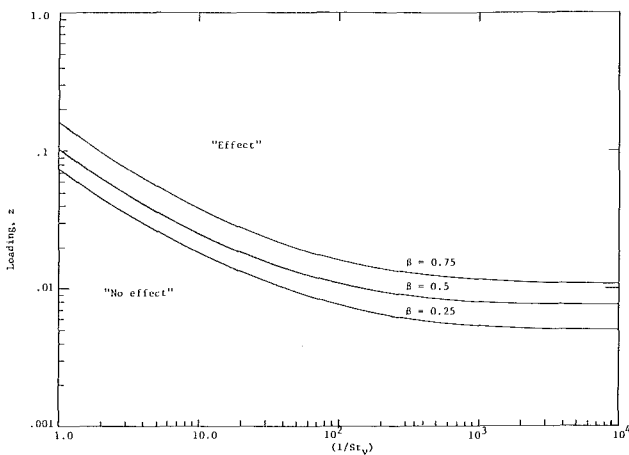
Fig. 8   Design curves for orifice plates

Fig. 9   Design curves for venturis

Fig. 10   Signal magnification curves

The design curves for venturis are shown in Figs. 9 and 10. Figure 9 shows the variation of the threshold values of particle loading (z) with the Stokes number (St_v) for different β values (d_t/D). Each curve divides the plane into regions of "no effect" and "effect" of particles on the venturi throat pressure. To be able to measure the particle flow rate, the venturi must be designed such that the parameters lie in the "effect" region of the curve.

Figure 10 is a plot of signal magnification ($SM = \Delta P_{mt}/ \Delta P_{gt}$) versus the particle loading for different values of venturi Stokes number (St_v). ΔP_{mt} and ΔP_{gt} are pressures at the venturi throat for mixture and gas flow, respectively. Using the SM curves, a venturi can be designed to produce a desired magnification (for accuracy of measurement) of particle effect on the throat pressure drop. The SM curves can also be used to calculate particle loading if gas flow rate is known and ΔP_{mt} is measured.

6   Design Methodology

Given the information on the range of fluid flow rates, fluid properties, particle material density and size distribution, range of particle loading and signal magnification requirements, following steps should be followed in designing a flowmeter:

1. Calculate St_o based on the smallest size of the particle in the flow.

2. Determine a value of β for the maximum value of particle loading using Fig. 8, such that there is no effect of the particles on the orifice pressure drop.
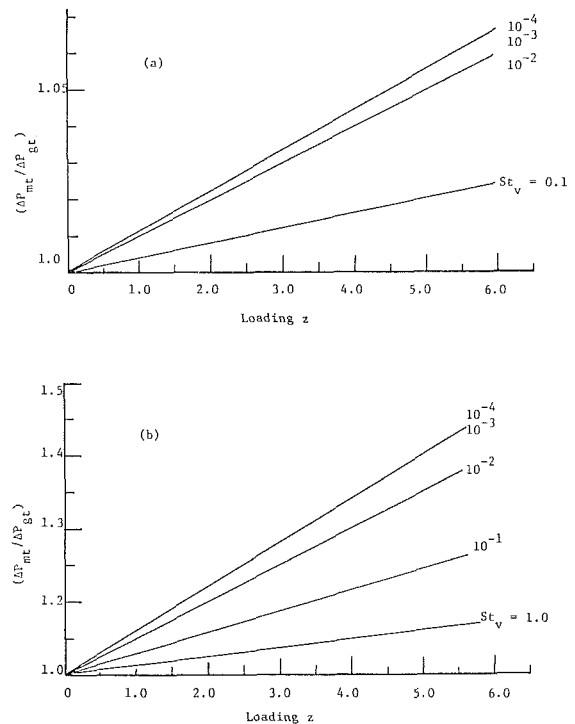
3. Calculate τ_p based on the largest size of the particle in the flow and then follow either one of the following steps:

(a) For the minimum value of particle loading, choose a combination of β and St_v from Fig. 9 such that the particles have an effect on the venturi throat pressure. From this value of St_v and calculated value of τ_p, determine an appropriate value of L (or θ) using equation (14).

(b) If a requirement on the signal magnification is to be met, Fig. 10 should be used. For the given value of minimum loading and signal magnification, choose a combination of β and St_v from Fig. 10. Using equation (14) and the value of ρ_p from Step 3, determine an appropriate value of L (or θ) for the venturi.

The two primary elements should be separated by a minimum distance of ten pipe diameters. Taps should be made according to standard design specifications [11].

Design curves in Figs. 8 to 10 have been generated for a Reynolds number (Re) range around 10,000. For Re vastly different than this value, new sets of design curves should be generated using the computer programs discussed in previous sections and available in [5].

The venturi can be installed upstream or downstream of the orifice. There is no theory to establish the preference of one choice over the other. For a compact flowmeter, the venturi should be placed on the upstream side so that a minimum flow disturbance is created before the orifice plate, and, therefore, the distance between the two elements could be kept to minimum. This arrangement has been favored in practice.

7   Conclusions

A philosophy and methodology of design for a gas-particle flowmeter using orifice plate and venturi elements has been presented. The methodology is based upon newly developed theoretical models and methods of calculating gas-particle flows. These theoretical models have been validated with experimental data for dilute gas-particle flows.

This paper has presented a conceptual design of a flow meter for multiphase flow environment. The questions related to performance and accuracy of such a flowmeter are matters

of actual experience in installation, operation and extensive experimentation. This is another phase of this problem. This study sets the theoretical basis for such investigations.

Acknowledgments

The authors acknowledge the invaluable assistance of Linda Brooks of the University of Wyoming in typing the manuscript. The valuable assistance of Mr. Haus Hauge and Mr. Trond Jensen, graduate students of Petroleum Engineering, University of Wyoming, in typing the complicated equations has left marks of their newly acquired expertise and is sincerely appreciated.

References

1 Farbar, L., "The Venturi as a Meter for Gas-Solids Mixtures," *Ind. Eng. Chem.*, Vol. 44, 1952, p. 2947.

2 Graczyk, C., "The Application of the Venturi Tube to the Measurement Rate of Coal Dust Flow Transported by Air," *Acta. Imeko*, Vol. 4, 1961, p. 251.

3 Carlson, H. M., Frazier, P. M., and Engdahl, R. B., "Meter for Flowing Mixtures of Air and Pulverized Coal," *Trans. ASME*, Vol. 70, 1948, p. 65.

4 Saltsman, R. D., "The BCR Gas-Solids Flow Meter," Inf. Cir. 8314, U.S. Bureau of Mines, 1966.

5 Sharma, M. P., "Numerical and Experimental Study of Gas-Particle Flows in Orifices and Venturis: Application to Flow Meter Design," Ph.D. thesis, Washington State University, 1977.

6 Sharma, M. P., and Crowe, C. T., "A Novel Physico-Computational Model for Quasi-One-Dimensional Gas-Particle Flows," ASME JOURNAL OF FLUIDS ENGINEERING, Vol. 100, Sept. 1978.

7 Crowe, C. T., Sharma, M. P., and Stock, D. E., "The Particle-Source-in-Cell (PSI-Cell) Model for Gas-Droplet Flows," ASME JOURNAL OF FLUIDS ENGINEERING, Vol. 99, June 1977.

8 Wormeck, J. J., "Computer Modeling of Turbulent Combustion in a Lonwell Jet-Stirred Reactor," Ph.D. thesis, Washington State University, 1976.

9 Launder, B. E., and Spalding, D. B., *Mathematical Models of Turbulence*, Academic Press, New York, 1972.

10 Crowe, C. T., "Review of Numerical Models for Dilute Gas-Particle Flows," ASME JOURNAL OF FLUIDS ENGINEERING, Vol. 104, Sept. 1982.

11 Bean, H. S., *Fluid Meters—Their Theory and Applications*, 6th ed. ASME, New York, 1971.

Drying of an Initially Saturated Fractured Volcanic Tuff

A. J. Russo

D. C. Reda

Sandia National Laboratories,
Albuquerque, NM 87185

The isothermal drying of an initially saturated welded tuffaceous rock was studied experimentally. Gamma-beam densitometry was used to measure the material's effective porosity distribution prior to the drying experiment. It was then used to measure liquid saturation distributions during a 1400 hour drying period. The core selected for study was taken from the Busted Butte outcrop at the Nevada Test Site, part of the Topopah Spring Member of Paintbrush tuff. This specimen contained several microfractures transversely oriented to the direction of the water or vapor migration. These fractures were found to be regions of rapid dryout or low saturation even though they were displaced from the surface over which dry nitrogen was flowing. An imbibition experiment was performed earlier on the same core. In the imbibition experiment the presence of most of these microfractures was detected by discontinuities in the measured saturation curves, which indicated a delay in liquid transport past the microfractures. The mechanism for this "inside out" drying is believed to be capillary action that removes water from the larger-pore fracture zone. Vapor pressure lowering in the fine pore region, which would result in transport by evaporation, diffusion and condensation, is thought not to be important at room temperatures. Modeling of this dryout experiment reproduced some of the overall features of the experiment but underpredicted the saturation near the drying surfaces.

Introduction

Theoretical and experimental investigations of the technical feasibility of nuclear waste isolation within proposed geologic repositories are being done [1]. The Nevada Nuclear Waste Storage Investigations (NNWSI) Project is addressing the feasibility of isolating heat-producing waste canisters at Yucca Mountain, Nevada, within tuffaceous rocks located above the water table. To accomplish this task, the physics of two-phase flows (of water and water vapor) through partially saturated tuff are being studied. In the near-field region flow may be driven by coupled thermal/hydrological processes and in the far-field, flow may be driven by purely hydrological processes (e.g., infiltration, fracture flows, or imbibition into the matrix material). Hydrological mechanisms would also dominate in the near-field region after the initial, high-heat-load period had passed. In the past a great deal of theoretical and experimental work in transport in porous media has been done. An excellent review article on the theoretical aspects of drying is reference [2]. More recent numerical work is included in reference [3]. Results of some recent field experiments in tuffaceous alluvium are reported in reference [4].

In this investigation, the isothermal drying of an initially saturated core of tuffaceous rock was studied experimentally. This study had three objectives: (1) to obtain measurements that would aid in understanding the physical mechanisms of drying in a fine-pore fractured medium; (2) to use these measurements to help characterize the geologic medium from

which the core was taken; and (3) to provide data that would be useful in the evaluation of numerical models.

Experimental Method

Figure 1 shows a schematic of the experimental apparatus. A cylindrical core sample (described in the next section) was dried and then brought to saturation by driving water into both ends of the evacuated core under pressure [5]. The core was mated to gold-plated copper end-plugs that had air passages machined for access to the end faces of the core; the entire column was then encased in a flexible, impermeable sleeve of polyvinylidene fluoride (Kynar) shrink tubing. Continuous metal bands were compression-fitted over the outer surface of the sleeve/end-plug at each end of the assembly. This compression seal was positioned over an inner o-ring-in-groove seal to provide complete isolation between the cylindrical surface of the core sample and the environment.

The core/end-plug assembly was positioned on the centerline of the test vessel, and the annular region surrounding it was filled with pressurized water at 5.5 MPa. This confining pressure was applied prior to saturating the core and was maintained throughout the imbibition and drying portions of the experiment. This pressure served to apply a net radial circumferential stress on the sample representative of the lithostatic loads at proposed repository depth, as well as to ensure that no flow bypass occurred between the outer surface of the rock and the inner surface of the confining sleeve. Miniature thermocouple beads were positioned every 2.75 cm along the outside of the sleeve to monitor the core axial
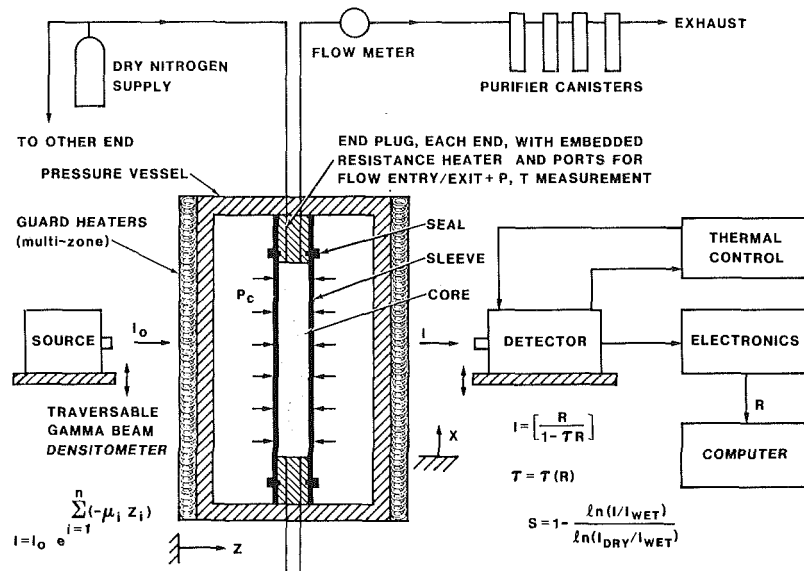
Fig. 1 Schematic of experiment

temperature distribution. The entire test vessel was surrounded by a multizone guard heater, coupled by feed-back loops to thermal controllers. For the present experiment these heaters were not used.

Pressurized dry nitrogen from a regulated gas cylinder was fed into each end-plug (at 0.07 MPa), past the end of the core in three 2.4-mm-wide circular grooves in the end-plug face and out of the same end-plug. This flow pattern exposed approximately 30 percent of the end face of the core to the flowing dry nitrogen. The nitrogen flowing out of each end-plug was fed into a serial bank of desiccant canisters (Matheson Type 452 replaceable gas purifiers) and then vented to the room atmosphere (only the lines to the upper plug are shown in Fig. 1 to avoid redundancy). Each of the desiccant canisters was removed and weighed periodically to determine the mass of water that had evaporated from the core since the previous measurement. The desiccant canisters were changed often enough so that the last canister in the series always registered a negligible weight gain, which ensured that virtually all the water leaving the core was captured. The pressure and flow rate of the drying gas at each end of the core was monitored and recorded. To begin the experiment the gas flow rate was set at 5 standard cm³/s. The initial weight loss measurements indicated a maximum evaporation rate of about 21 μg/s from each end of the core. Using the equation,

$$\dot{M}_{\text{vin}} = \rho q \qquad (1)$$

where $\dot{M}_{\text{vin}}$ is the mass flow rate of water vapor from each end of the core, ρ is the density of vapor in the end-plug region,

and q is the volume flow rate of the dry nitrogen, the density ρ can be calculated and the partial pressure of the vapor in the exiting gas (at room temperature $= 20°$C in this case) can be determined. For the conditions indicated, this pressure was found to be approximately 550 Pa. Since the vapor pressure of water of 20°C is 2339 Pa, this gas flow rate was adequate to maintain a strong drying condition at the ends of the core. As the test progressed, the evaporation rate diminished to less than 2 μg/s, and the flow rate was reduced to 1.25 cm³/s (after 39 days). This kept the exit vapor pressure to less than 200 Pa for most of the drying period. Figures 2 and 3 show the maximum vapor pressure at the end-plug exit for the top and bottom end-plugs, respectively. The fact that the vapor flow rates from the two core ends were slightly different indicates that there is some inhomogeneity in the core properties.

The dry gas flow was continued for 58 days and the canister weight changes were recorded every one or two days. At each weighing period gamma-beam densitometer scans were taken along the centerline of the test vessel (and core) and compared with the "wet and dry" measurements to determine the saturation levels at each axial location as a function of time. A description of the gamma-beam calculations is given in reference [5]; however, a synopsis of that theory will be given here for completeness.

Gamma-beam densitometry relies on the attenuation and scattering of known-energy photons as they pass through matter [6]. In the present case, a cesium-137 pellet (5 curies) emitted 0.662 MeV photons from a source vault. These photons exited the source vault, through a 6.35-mm collimator tube,

───────── **Nomenclature** ─────────

C = beam contrast ($I_{\text{dry}}/I_{\text{wet}}$)
D = core diameter
$|ds|$ = uncertainty in measured saturation
I = beam intensity
I_0 = initial beam intensity
L = core length
$\dot{M}$ = mass flow rate
q = gas volume flow rate
R = measured count rate

S = liquid saturation
T = temperature
t = time
x = axial coordinate
z = beam pathlength in material
μ = linear attenuation coefficient
ρ = vapor density
τ = electronic system time constant

ϕ = effective porosity

Subscripts

dry = at $S = 0$ state
H_2O = value for water
i = material i
wet = at $S = 1$ state
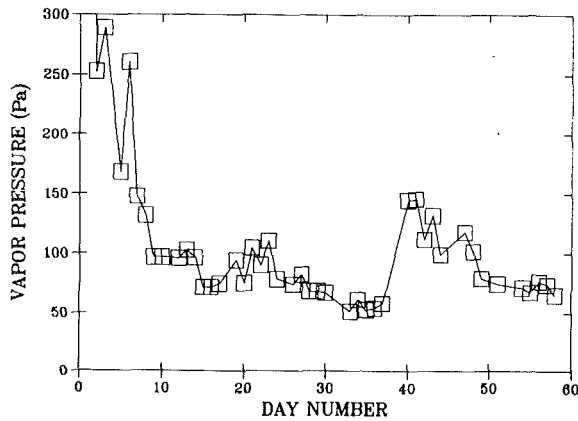vin = vapor flow at end-plugs

TOP BOUNDARY CONDITION

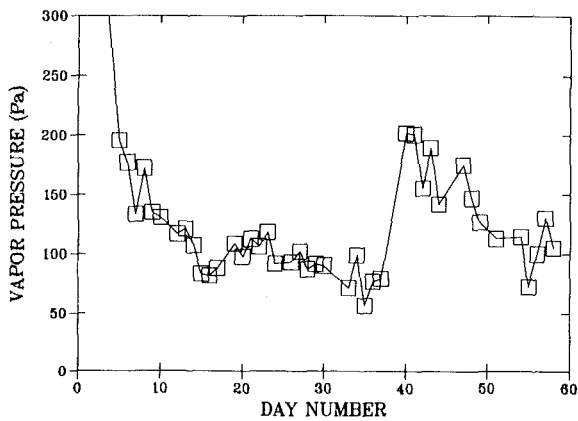Fig. 2 Maximum vapor pressure at the upper end of the core

BOTTOM BOUNDARY CONDITION

Fig. 3 Maximum vapor pressure at the lower end of the core

Fig. 4 Contrast method schematic for electronics calibration
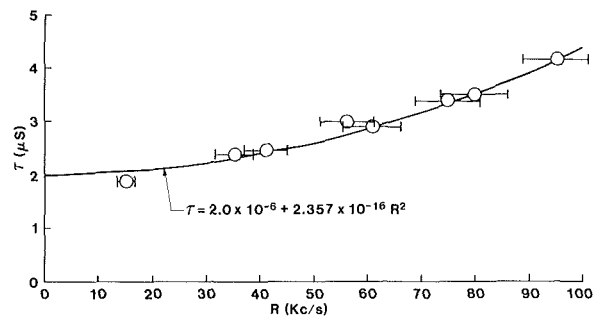
Fig. 5 System time-constant calibration curve

and passed through the pressure vessel and core sample. The reduction of the initial beam intensity, I_0, by scattering and absorption is described by equation (2).

$$I = I_0 \exp\left[-\sum_{i=1}^{n} \mu_i z_i\right] \qquad (2)$$

where I is the beam intensity of unattenuated photons exiting the test chamber and $\mu_i z_i$ is the product of the total linear attenuation coefficient, μ_i, and the path length, z_i, for material i (n is the total number of materials in the beam path).

After passing through the test fixture, gamma photons enter a detector vault through a collimator tube (also 6.35 mm) and strike a sodium iodide crystal to produce visible photons. These visible photons are detected by a photomultiplier tube, which, together with a build-in preamplifier, send a voltage pulse to counting electronics for each photon detected. The magnitude of this voltage pulse is proportional to the energy of the incoming gamma photon. A single-channel analyzer is then used to discriminate pulse height, yielding a count rate R (counts/second) proportional to the intensity of unattenuated photons, I. At high fluxes, some pulses "overlap" in time and are subsequently lost to the counting electronics. The conversion of the measurement R back to the intensity I is thus nonlinear, depending on the characteristic time constant τ of the detection system:

$$I = \frac{R}{1 - \tau R} \qquad (3)$$

where $\tau = \tau(R)$ is a time constant function that must be obtained by calibration of the system electronics. Figure 4 shows a schematic of the "contrast calibration method" used.

In that procedure, some "baseline" attenuation (by any material) produces an intensity I_1 and corresponding count rate R_1. The baseline intensity is then "contrasted" by the addition of a material of known thickness and composition to the beam path. In the present case, water ($\mu = 0.0853$/cm) was used for the material of known composition, and aluminum blocks of varying thickness were used as the baseline material. A count rate, R_2, corresponding to the contrasted intensity I_2 ($I_2 < I_1$) is then measured.

By systematically changing the thickness of the baseline material(s), and by repeating the above procedure, data over the entire count rate regime of interest can be obtained. From equations (2) and (3), the time constant (averaged between R_1 and R_2) at each point is

$$\tau = \frac{R_1 - R_2 e^{\mu z}}{R_1 R_2 (1 - e^{\mu z})} \qquad (4)$$

where μz refers to the contrast material (water) and all other quantities on the right-hand side are known.

A calibration curve for $\tau(R)$ can then be generated by curve-fitting the measured data. The curve used is shown in Fig. 5 where the horizontal bars define the R_2 to R_1 range measured in each contrast test. All measurements taken during the drying experiments were in the range 13 to 15 kc/s, and deadtime corrections were thus small.

In order to minimize signal drift effects, the crystal and photomultiplier tube (both housed in the detector vault) were held at a constant temperature (20°C) by use of a cooling-coil and thermal bath flow loop. A reference attenuation measurement was taken at the start of each data scan by positioning the beam to penetrate the metal end-plug rather than the core sample. Any variations in signal level due to gain or source strength drift would thus be observed and accounted for in data reduction. Unfortunately, the room temperature could

only be controlled to $20 \pm 3\,°C$ so that the small thermally-induced density changes in the system were not accounted for.

The procedure for using this instrumentation for measuring core porosity, ϕ, and liquid saturation, S, at each axial location can now be summarized. At each x/L location, the limiting dry and wet intensities were calculated from the measured count rate before and after imbibition, respectively. The contrast distribution, $C(x/L) = I_{dry}/I_{wet}$ was stored on a disk file for later use. This total change in signal (dry to wet) is due solely to the filling of the core's effective porosity with a path length of liquid water equal to the product ϕD, where D is the core diameter. The attenuations caused by all the other materials in the beam path cancel out of the ratio (I_{dry}/I_{wet}), yielding

$$\phi = \frac{\ln C}{\mu_{H_2O} D} \qquad (5)$$

where the attenuation coefficient for water and the core diameter are both known. It follows from equation (2), that for any intermediate saturation $0 < S < 1$,

$$S = 1 - \frac{\ln(I/I_{wet})}{\ln(I_{dry}/I_{wet})} \qquad (6)$$

Uncertainty in the measurement of S due to finite count times, denoted by $|ds|$, can be estimated from prior error analysis [7],

$$|ds| = [\sqrt{Rt}(1 - \tau R)\ln C]^{-1} \qquad (7)$$

In the present application $R = 13$ to 15 kc/s, t, the counting interval at one scan point $= 100$ s, $(1 - \tau R) = 0.97$, and $C = 1.05$ to 1.10, defining a maximum uncertainty $|ds| = 0.01$ to 0.02. Because of room temperature variations and other drifts, the overall uncertainty in the drying experiments was found to be of order $|ds| \approx 0.05$; therefore, the following procedure was used to correct the measurements. The total moisture content of the core was calculated from the measured gamma-beam saturation values and compared with the moisture content calculated from the weight loss measurements which were accurate to at least ± 1 percent, and the reference count rate from the end-plug measurement was adjusted to bring the two values into agreement. The corrected saturation values were therefore valid to within $\equiv 0.02$.

Core Characterization

A block of densely welded tuff was taken from the Busted Butte outcrop at the Nevada Test Site (the Topopah Spring member of Paintbrush tuff). A series of adjacent core samples was drilled from this block and separate cores were used to make permeability and porosity measurements to characterize the matrix material. The liquid permeability of the unfractured matrix material was measured to be 3 to 5×10^{-19} m² independent of the temperature in the range 25 to 90°C .[8] The gas permeability was measured as a function of average pore pressure by Reda [9]; results showed gas permeability to be linearly proportional to inverse pore pressure (the Klinkenberg effect), from a value of 5×10^{-19} m² at "infinite" pressure to 5×10^{-18} m² at atmospheric pressure. On the basis of these results, and assuming a tortuosity factor of 5, the average pore diameter of the matrix material was estimated to be 8×10^{-9} m.

A cylindrical core 5.08 cm in diameter and 24.77 cm long was precision ground from the original rock specimen for use in the imbibition [5] and drying experiments. Visual inspection of this core showed it to contain a transverse microfracture near one end and a 10 cm long "altered zone" near the mid-core region, where the densely welded matrix material changed from its basic brown/tan/pink coloration to a predominantly grayish coloration.

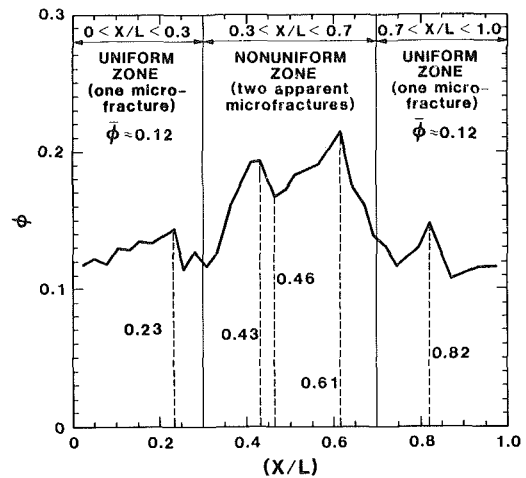Attenuation measurements were made at uniform spacings

Fig. 6 Core porosity profile from gamma-beam measurements

of one beam diameter along the entire length of the core, defining a spatial resolution of $\Delta x/L = 0.0256$. A direct comparison of the dry and wet scans allowed the effective porosity distribution, $\phi(x/L)$, to be determined from equation (5). Results are shown in Fig. 6.

Consistent with the results of the visual inspection, the core was found to have several distinctive zones and features. Two regions, each of length $|\Delta x/L| = 0.3$, originating at opposite ends of the core, were found to be of essentially the same average porosity ($\phi = 0.12$), the only apparent difference being the existence of a single transverse microfracture in the region, $0.7 < x/L < 1.0$ crossing the core centerline at $x/L = 0.82$. Since the gamma-beam diameter is much larger than any single microfracture such microfractures result in a spread out peak in intensity when they are encountered [10].

These observations indicate that (1) a beam defined porosity peak indicates the presence of a transverse microfracture plane (or a very thin layer of altered material) and (2) the beam crossed these features in an essentially edge-on orientation as it was traversed along the core centerline.

The altered zone in the central region of the core was found to have a higher effective porosity ($\phi \approx 0.18$) with two distinctive peaks, one at $x/L = 0.43$ and one at $x/L = 0.61$. These did not correspond to any visually observed fractures at the core surface; however, they did result in discontinuities in the progress of the wetting front during the imbibition experiment. The smaller peak, shown in Fig. 6, at $x/L = 0.23$ did not correspond to any visible discontinuity, nor did it have any influence on the imbibition front; however, it did affect the saturation curve during drying in a similar way to the other apparent microfractures. Further observations of these apparent fracture regions are planned during posttest sectioning of the core.

Experimental Results

A total of 45 saturation distribution scans and captured-vapor weight measurements were made over a 58-day drying period. The data aquisition time per core scan was ≈ 1 hour, with attenuation measurements being recorded at an axial spacing of one beam diameter ($\Delta x/L = 0.0256$). All data were assigned the time at the start of a scan; hence, the temporal resolution was to the nearest hour. Weight loss measurements were made on a Mettler type AE166 electronic balance to a precision of 1 mg.

The results of the captured-vapor weight loss measurements are shown in Fig. 7. From the measured porosity data of the core and its known dimensions, the amount of water contained in the fully saturated core was estimated to be 75.4 g. A
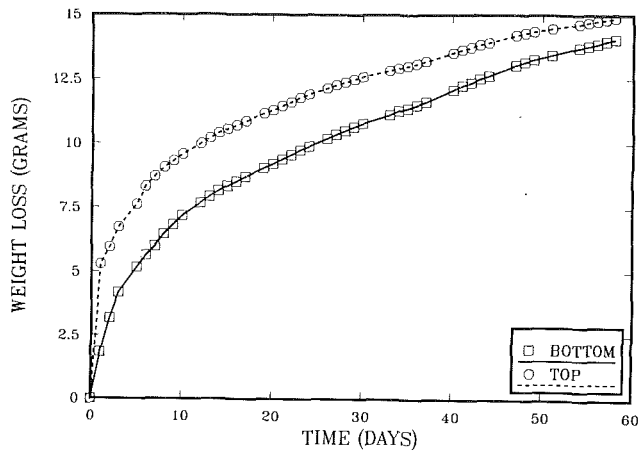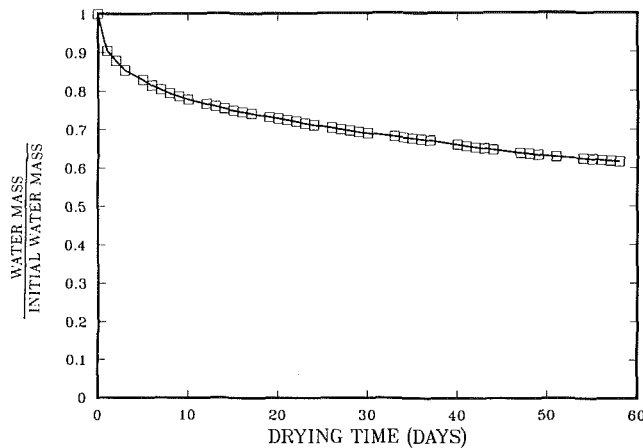
Fig. 7 Rate of water removal from each end of the core

Fig. 8 Average core saturation from weight loss measurements

Fig. 9 Core saturation profile from gamma-beam measurements after 2 days

Fig. 10 Core saturation profile from gamma-beam measurements after 29 days

large fraction of this water (≈ 10 percent) was removed on the first day, with the bulk of it (7 percent) coming from the top end of the core. This end was found to be of *lower* permeability during imbibition. The reason for the difference in evaporation from the two core ends is not known, but the fact that a fracture zone was close to the top of the core may have influenced this asymmetry. After the first day, the weight loss rate slowed considerably, with evaporation from the bottom end of the core often slightly greater than that from the top. To avoid having to replace the dry nitrogen gas bottles too often, the gas flow rate was reduced from 5 cm³/s on the first day to 4.2 cm³/s on days 2 through 10, to 3.3 cm³/s on days 11 through 17, to 2.5 cm³/s on days 18 through 33, and 1.25 cm³/s thereafter as the evaporation rate slowed. These changes in gas flow rate appeared to have no significant effect on the evaporation rate from either end of the core. The total average saturation of the core as a function of time is shown in Figure 8. This curve was used as a reference to correct for temperature-induced variations in the gamma-beam saturation data.

Figures 9 through 11 show the corrected saturation data along the axis of the core after the 2nd, 29th, and 58th days of drying. The vertical lines in these figures indicate the locations where microfractures are believed to exist. From Fig. 9 it can be seen that almost immediately the saturation in the vicinity of the porosity peaks (microfractures) was reduced [1]. As

---

[1]The absolute value of S in the fracture cannot be measured because the gamma beam diameter is much larger than the fracture width so that only some space-averaged quantity can be reported.
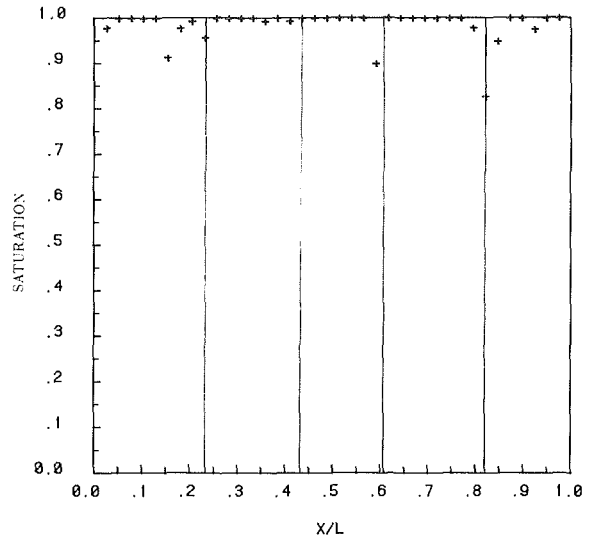
time progressed (Figs. 10–11) a lower saturation was always maintained in the same regions although the general saturation level was declining. Surprisingly the core seemed to be drying from the inside out since the lowest saturation levels occur near the center of the core. Since the porosity of the core was the highest in that region, it would be expected that the pore size might also be larger there and that capillary forces would tend to draw water into the end regions. An alternate possibility is that the very small pore sizes cause a reduction of vapor pressure in some regions and transport from the large to small pores occurs by evaporation, vapor diffusion, and condensation. *At room temperatures, however, the vapor pressures (and vapor pressure gradients) are low, and diffusion rates are very slow, so this is not considered likely.* A numerical model was used to simulate the experiment [11]. The numerical model accounted for vapor diffusion and the results of the model indicated that vapor diffusion was very small. The calculated saturation profiles of the model agreed fairly well with the experimental observations except near the core ends, where the observed values remained higher than numerical predictions.

The fact that water can be transported from the interior of the core to the surface across microfractures raises some in-
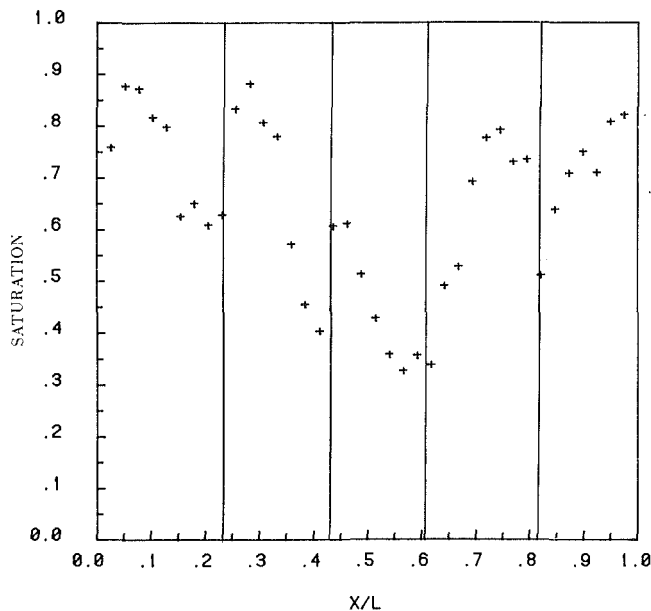
Fig. 11 Core saturation profile from gamma-beam measurements after 58 days

teresting questions about waste isolation calculations. For example, how fast will a tracer particle in the high porosity region take to migrate to the surface during drying? Future experiments will attempt to answer such questions.

Conclusions

During the isothermal drying process in small-pore tuffaceous rocks, the presence of microfractures and high porosity regions significantly affect the saturation distribution within the rock. These high-porosity regions appear to dry first even though they are internal to the core volume. This result was observed as the core dries from 100 to 40 percent in the high porosity regions. Transport of water through the rock appears to be dominated by capillary flow of the liquid.

The rate of water vapor mass loss from the core was almost independent of the gas flow rate of the drying gas for this experiment which kept the maximum pressure of the vapor at the surface below 10 percent of the equilibrium vapor pressure at the core temperature.

As a consequence of matrix material nonuniformities and the presence of the microfractures, detailed characterization and modeling of transport through tuffaceous rocks on a submeter scale will be very difficult. Calculation of solute transport will be hampered by lack of information on the micromechanics of porous flow.

References

1 Roseboom, Jr., E. H., "Disposal of High-Level Nuclear Waste Above the Water Table in Arid Regions," U.S. Geological Survey Circular, 1983, p. 903.

2 Whitaker, S., "Simultaneous Heat, Mass, and Momentum Transfer in Porous Media: A Theory of Drying," Advances in Heat Transfer, ed J. P. Hartnett and T. F. Irvine, Jr., Academic Press, London, 1977, p. 119.

3 Hadley, G. R., "Numerical Modeling of the Drying of Porous Materials," Sandia National Labs Report, SAND-83-2332C, CONF-840750-1, July 1984.

4 Williams, R. E., McGrath, D. A., Boland, J. R., and Post, R. S., "Monitoring of Heat and Moisture Migration from Radioactive Waste Disposed in Augered Shaft," Waste Management '87: Waste Isolation in the U.S., Technical Programs and Public Information, Univ. of Arizona Nuc. Eng. Dept., Tucson, 1987, p. 381.

5 Reda, D. C., "Influence of Transverse Microfractures on the Imbibition of Water into Initially Dry Tuffaceous Rock," Flow and Transport Through Unsaturated Fractured Rock, Amer. Geophysical Union Monograph 42, 1987, pp. 83–90.

6 Hewitt, G. F., Measurement of Two Phase Flow Parameters, Academic Press, London, 1978.

7 Reda, D. C., Hadley, G. R., and Turner, J. R., "Application of the Gamma-Beam Attenuation Technique to the Measurement of Liquid Saturation for Two-Phase Flows in Porous Media," Proceedings of 27th International Instrumentation Symposium, ISA, Indianapolis, IN, 1981.

8 Reda, D. C., "Liquid Permeability Measurements on Densely Welded Tuff Over the Temperature Range 25° to 90°C," SAND85-2482, Sandia National Laboratories, 1985.

9 Reda, D. C., "Slip-Flow Experiments in Welded Tuff: The Knudsen Diffusion Problem," Chapter 36, Coupled Processes Associated with Nuclear Waste Repositories, Academic Press, NY, 1987, p. 485–493.

10 Reda, D. C., and Russo, A. J., "Experimental Studies of Oil Withdrawal from Salt Cavities via Fresh-Water Injection," SAND83-0347, Sandia National Laboratories, 1984.

11 Bixler, N. E., Eaton, R. E., and Russo, A. J., "Drying Analysis of a Multiphase, Porous-Flow Experiment in Fractured Volcanic Tuff," in Fundamentals of Heat Transfer in Drying, Joint ASME/JSME Meeting, Honolulu, Hawaii, March 22–27, 1987.

APPENDIX A

The data presented in this paper are compiled in the NNWSI Data Records Management System, File Number 51/LO7.A-12/04/85. No hydrologic property values were measured in the experiment described, and the data presented are not currently considered as information necessary to be entered into the NNWSI Science and Engineering Properties Data Base (SEPDP). If, at a future date, the data presented here are used in the validation of a computer code whose predictions may be used in repository licencing arguments, the data will be entered into the SEPDP.

L. d'Agostino
NATO-CNR
Research Fellow.

T. Pham
Undergraduate Student.

S. Green
Postdoctoral Fellow.

California Institute of Technology,
Pasadena, California 91125

Comparison of a Cavitation Susceptibility Meter and Holography for Nuclei Detection in Liquids

This work compares the results obtained from a Cavitation Susceptibility Meter (CSM) and from direct holographic observations for the detection of cavitation nuclei in tap water samples. The CSM uses a cavitating venturi tube to measure the concentration of active cavitation nuclei as a function of the pressure at the venturi throat, while the holographic system measures the nuclei concentration size distribution. Microbubbles are used as the dominant type of cavitation nuclei. The data from the two nuclei detection methods are then compared and interpreted in view of the expected dynamic behavior of microbubbles in the CSM venturi throat. Both results show that the concentration of active cavitation nuclei initially increases exponentially with the applied tension, reaches a maximum and remains nearly constant thereafter when few additional nuclei are left to cavitate. In its current configuration the CSM tends to underestimate the concentration of active cavitation nuclei and to overestimate the value of the nuclei critical pressure as a consequence of sensitivity limitations and interference effects between the cavities.

1 Introduction

Early studies have shown (Knapp et al., 1970) that the maximum tensile strength that liquids can sustain is considerably reduced by the presence of weak spots, generically called "nuclei." Although their nature has not yet been fully understood, the presence of nuclei is important in many flows of technical interest, where they are responsible for initiating or variously modifying the occurrence of cavitation. In this respect the concentration of nuclei which become unstable at a given level of tension is a fundamental parameter in the attempt to predict the onset of cavitation, to model its development and to deduce scaling laws capable of extending the results obtained from model tests to full scale operation. Therefore, significant efforts have been made in developing methods to detect nuclei inside liquids (Billet 1986a, 1985). The nuclei detection techniques most frequenctly used in cavitation studies include photography, holography, acoustical, and optical scattering, Coulter Counters and acoustical attenuation. For the purpose of cavitation research a common disadvantage of all the above methods is that only the size-concentration distribution of the nuclei is measured. The value of the critical tension that makes each nucleus unstable, as required for cavitation studies, must therefore be deduced indirectly from size measurements, which is possible only in the case of microbubbles. Solid particles, when detected and recognized, may or may not be included in the measurement of nuclei concentration, but no information is

provided about their critical tension, although only some of the solid particles are known to be active cavitation nuclei.

To overcome these difficulties Oldenziel (1982a, 1982b, 1982c) recently proposed a new instrument, the Cavitation Susceptibility Meter (CSM), where the internal flow of a liquid through a glass venturi is used to induce cavitation at the throat and bubbles are detected optically. The CSM developed at Neyrtec (Le Goff and Lecoffre, 1983, Shen et al., 1984) is based on the same principle, but utilizes a stainless steel venturi, where cavitation bubbles are counted by monitoring the noise generated by their collapses in the diffuser downstream of the throat section (Lecoffre and Bonnin, 1979). In both these applications the flow in the venturi is turbulent due to the relatively high velocity in the inlet line to the test section and the unperturbed throat pressure is obtained from the measurement of the flow rate and of the upstream pressure using energy and continuity considerations. At high cavitation nuclei concentrations the growth of a nucleus can perturb the pressure in the surrounding liquid and prevent neighboring nuclei from cavitating. This error is reduced by decreasing the size of the cavitation region and the concentration of unstable nuclei is computed by dividing the observed number of cavitation events by the volume of the liquid sample.

The operation of CSM's is limited by the occurrence of mutual interference between cavitation nuclei and the resulting saturation (choking) of the flow, which modify the pressure in the throat section of the venturi with respect to its steady state noncavitating value. Other problems frequently encountered are the occurrence of flow separation in the diffuser and of sheet cavitation in the throat section of the

---

venturi tube. Yet, when compared to other nuclei detection techniques, CSM's have several advantages: they provide a direct measurement of both the nuclei critical tension and concentration, thus eliminating the problem of the uncertain behavior of particles as cavitation nuclei; there is no limitation on the size of the smallest detectable nuclei and the analysis of the data requires a comparatively short time.

In this work we report the application of both a CSM with optical cavitation monitoring and direct holographic observations to the measurement of cavitation nuclei in water samples. Microbubbles are used as the dominant kind of cavitation nuclei in order to facilitate the correlation of their mechanical properties with their concentration size distribution measured by the holographic method. The data from the two cavitation nuclei detection techniques are then compared and interpreted in view of the expected dynamical behavior of microbubbles in the throat of the CSM venturi tube.

2 Experimental Apparatus and Procedure

The CSM used in this investigation has been recently developed at Caltech and is based on the use of a transparent venturi tube where the detection of cavitation and the measurement of the local flow velocity are carried out optically. The main considerations leading to the present design and the implementation of the whole system have been described in detail elsewhere (d'Agostino and Acosta, 1983; d'Agostino, 1987; d'Agostino and Acosta, 1987), therefore only a review of the relevant aspects is given here. The connections of the various parts comprising the CSM are illustrated in Fig. 1. The water sample passes through the throat section of the blown glass venturi tube (VT) and is finally collected in the exhaust tank (ET). The pressure in the exhaust tank can be adjusted in order to regulate the flow and vary the pressure at the venturi throat where cavitation occurs (see Fig. 2). Contrary to previous CSM applications, in the present case the flow possesses a laminar potential core in all operational conditions. The throat velocity is measured by a Laser Doppler Velocimeter (LDV) and the upstream pressure by an absolute pressure transducer (UPT). The throat pressure is then calculated from the upstream pressure and the local flow
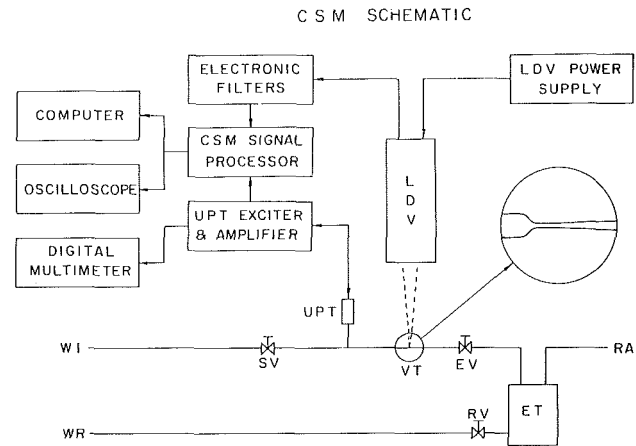

C S M SCHEMATIC

Fig. 1 Schematic of the various components of the CSM experimental apparatus: water inlet (WI), sampling valve (SV), upstream pressure transducer (UPT), venturi tube (VT), exhaust valve (EV), exhaust tank (ET), regulated air pressure line (RA), return valve (RV), water return (WR), laser Doppler velocimeter (LDV)

velocity using Bernoulli's equation for ideal, incompressible, steady, fully wetted flow. Several runs in rapid sequence and at different flow conditions are needed to measure the active nuclei concentration as a function of the throat pressure.

The main characteristics of the venturi tube are: throat diameter $D_t \simeq 1$ mm, throat section length $L_t \simeq 5$ mm, geometric contraction and expansion ratios $C_c \simeq 1/100$, and $C_e \simeq 1.44$, respectively, and minimum throat pressure of about -35 kPa corresponding to atmospheric inlet pressure and a throat velocity of about 14.8 m/s. The LDV signal, filtered by the adjustable band-pass electronic filters in order to isolate the Doppler frequency, is also used to detect the occurrence of cavitation at the throat of the venturi tube. The analysis of the signals from the LDV and the upstream pressure transducer is carried out by a specially designed electronic Signal Processor for real time generation and temporary storage of the data. At the conclusion of each run the

Nomenclature

A = CSM venturi cross-sectional area

A_t = CSM venturi throat cross-sectional area

c = unstable nuclei concentration

C_c = CSM venturi geometric contraction ratio

C_e = CSM venturi geometric expansion ratio

D_t = CSM venturi throat diameter

L_f = bubble detection length

L_t = CSM venturi throat length

N = holographic bubble count

p = pressure

p_b = bubble external pressure

p_e = CSM venturi exit pressure

p_g = bubble internal gas pressure

p_i = CSM venturi inlet pressure

p_o = bubble equilibrium external pressure

p_t = CSM venturi throat pressure

p_v = liquid vapor pressure

q = CSM venturi volume flow rate

q_b = CSM venturi volume flow rate at the bubble location

q_e = CSM venturi exit volume flow rate

q_i = CSM venturi inlet volume flow rate

R_o = bubble equilibrium radius

R = bubble radius

R_f = bubble detection radius

R_o = bubble equilibrium radius

S = bubble surface tension

t = time

T = liquid temperature

u = velocity

u_b = bubble velocity

u_t = CSM throat velocity

x = CSM venturi axial coordinate

x_b = bubble axial coordinate

x_e = CSM exit section axial coordinate

x_i = CSM throat inlet section axial coordinate

α = dissolved air content

γ = bubble gas specific heat ratio

ρ = liquid density

σ_{u_t} = throat velocity data standard deviation

Subscripts

b = bubble

e = CSM venturi tube exit

i = CSM venturi tube inlet

o = reference equilibrium conditions

t = venturi tube throat

v = vapor

Acronyms

CSM = Cavitation Susceptibility Meter

ET = Exhaust Tank

EV = Exhaust Valve

LDV = Laser Doppler Velocimeter

RA = Regulated Air

RV = Return Valve

SV = Sampling Valve

UPT = Upstream Pressure Transducer

VT = Venturi Tube
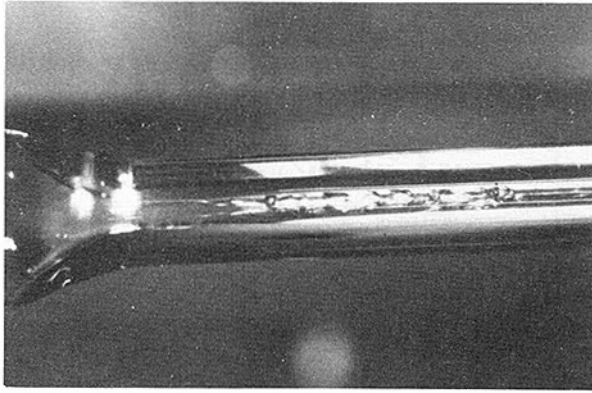
WI = Water Inlet

WR = Water Return

Fig. 2 Traveling bubble cavitation of a tap water sample initially at atmospheric pressure in the CSM venturi tube. The flow is from left to right. The throat pressure is about—15 kPa and the throat velocity about 14.8 m/s.
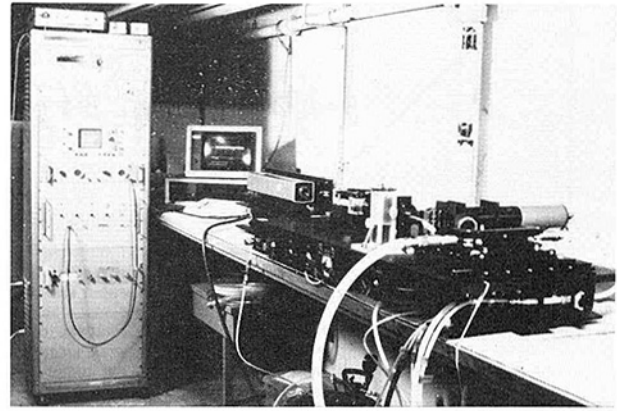

Fig. 3 General view of the CSM experimental apparatus. In the foreground on the right: the I-beams supporting the laser and the baseplate where most of the optical and fluidic components are mounted. In the background: the electronic instrumentation rack (left) and the data acquisition computer (center).

collected data are transferred to the microcomputer for final acquisition, storage on magnetic disk and reduction. The LDV signal is normally monitored by an oscilloscope and the signal of the upstream pressure transducer by a digital multimeter. A general view of the experimental apparatus is shown in Fig. 3.

The typical optical properties of the LDV scatterers naturally present in the CSM flow cannot be anticipated with any degree of accuracy, since they depend on the characteristics of the suspended matter in the sampled water and no artificial seeding can be used without greatly interfering with the water quality measurement. However, cavities will clearly be present in the venturi throat section as long as measurements with the CSM can be made. Since the pressure gradient in the venturi throat is ideally zero, so is the slip velocity of the two phases and the cavities themselves can therefore be safely used as velocity tracers. The possibility of recording the velocity of cavities also provides some useful indirect information on their origin. In fact, the typical cavity size is much larger than the boundary layer thickness at the CSM throat and therefore the cavities generated by free stream nuclei travel at the potential core speed, while those just released from nearby surface nuclei are significantly slower. A dual beam back-scattering LDV measures the CSM throat velocity. The back-scattering configuration combines the advantages of greater simplicity with superior optical efficiency when operating in the scattering regime expected from cavities whose average size clearly much exceeds the wave length of the illuminating laser beams. The LDV focal volume is located about 3 mm from the beginning of the venturi throat section, which experience showed to give best results. It extends far across the venturi walls in the direction of the optical axis and also covers the whole throat in the vertical direction. Therefore the LDV signal can effectively monitor the occurrence of cavitation, but at the same time spurious velocity readings in the boundary layer may occur. This effect is taken into account in the reduction of the data and corrected when necessary.

A frequency counter is used to measure the LDV Doppler frequency in order to preserve the information on the individual Doppler bursts and use the LDV signal for measuring flow velocity and monitoring the occurrence of cavitation at the same time. The custom-made CSM Signal Processor responds to the band-pass filtered LDV signal from the photomultiplier and to the amplified output of the upstream transducer. The photomultiplier generates a burst when an inhomogeneity such as a cavity or a suspended particle scatters light during its motion through the LDV focal volume. After band-pass filtering, this burst ideally consists of a Doppler carrier frequency modulated by a Gaussian-shaped envelope. The Doppler frequency is proportional to the velocity of the scatterer. The amplitude of the burst's envelope is primarily

related to the size of the scatterer, although it also depends in a complex way on its shape, optical properties and on the location of its trajectory through the LDV focal volume. The CSM Signal Processor compares the LDV signal to adjustable electronic threshold levels in order to reject residual noise. It uses the intensity of the LDV bursts to monitor the occurrence of cavitation and the Doppler modulated frequency to measure the flow velocity. The instantaneous upstream pressure of the water is provided by the output of the pressure transducer.

The settings of the electronic thresholds are of crucial importance for the operation of the CSM since they determine the number of cavitation events recognized and counted in given flow conditions. In principle the choice of these thresholds is linked to the definition of a general criterion for discriminating in dynamic conditions unstable cavitating nuclei from stable ones and to the existence of a firm relation linking the size of the scatterers to their LDV signature. The second apsect of the problem can be partially resolved by calibrating the LDV signal from cavities of known sizes. However, the definition of a criterion for the discrimination of the unstable cavities is essentially equivalent to the precise definition of the cavitation inception conditions. This is still an open problem in cavitation research, common to all currently devised techniques of cavitation nuclei detection, including holographic observation. Until these two problems are satisfactorily solved the selection of the electronic thresholds of the CSM remains, at least to some extent, arbitrary. In the present case it has been carried out empirically, trying to optimize the operation of the electronics and to ensure the applicability of the same thresholds to the full range of the expected operational conditions. Finally, the average size of the cavities corresponding to the electronic thresholds has been estimated by comparing the mean arrival rate of cavitation events recorded by the CSM Signal Processor with simultaneous high speed pictures of the cavitating flow in the CSM throat (see Fig. 2).

The CSM system has been calibrated using a mercury barometer for the upstream absolute pressure transducer and a rotating disk in air as a source of a controlled velocity field for the LDV. The analysis of the optical system using the theory of paraxial Gaussian light beams shows that the Doppler frequency is not affected by the curvature of the venturi optical interfaces in the cross sectional plane and that its relation to the velocity is the same in air as in the CSM flow as long as the walls of the venturi tube are parallel. The CSM in-

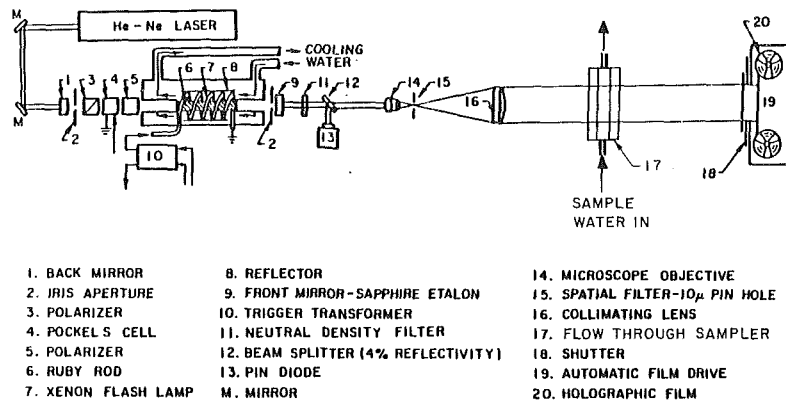| 1. BACK MIRROR | 8. REFLECTOR | 14. MICROSCOPE OBJECTIVE |
2. IRIS APERTURE	9. FRONT MIRROR-SAPPHIRE ETALON	15. SPATIAL FILTER-10μ PIN HOLE
3. POLARIZER	10. TRIGGER TRANSFORMER	16. COLLIMATING LENS
4. POCKELS CELL	11. NEUTRAL DENSITY FILTER	17. FLOW THROUGH SAMPLER
5. POLARIZER	12. BEAM SPLITTER (4% REFLECTIVITY)	18. SHUTTER
6. RUBY ROD	13. PIN DIODE	19. AUTOMATIC FILM DRIVE
7. XENON FLASH LAMP	M. MIRROR	20. HOLOGRAPHIC FILM

Fig. 4 Schematic of the holographic experimental apparatus

strumentation error was always negligible with respect to the intrinsic dispersion of the data due to the physical nature of the measured quantities. Typically the standard deviation in the determination of the average throat pressure is a few hundred Pascals and the relative error in the measurement of the unstable nuclei concentration is a few percent. These errors are relatively small, but they strictly refer to the measurement process alone. In a broader sense the indeterminacy of the water quality also includes repeatability errors and the effects of the above uncertainties in the relationship between the LDV signal intensity and the size of the cavitating bubbles and in the discrimination of unstable nuclei from the stable ones. The inclusion of all error sources involved makes the measurements of the liquid quality with CSM's (and with other alternative methods) considerably more uncertain than it would first appear from the above considerations.

Holograms of the sampled water were taken using the experimental arrangement illustrated in Fig. 4 in an optical test cell located on the CSM water inlet line, about two meters upstream of the venturi. The cell (see Fig. 5) guides the water between two optically flat windows and its design is intended to minimize the perturbation of the flow from and to the connecting lines. The transit time of the water from the cell to the venturi is typically of the order of 15 seconds. The temperature of the sampled water is measured with a thermometer and its air content with a manometric van Slyke meter immediately after each series of CSM runs. The holocamera itself has been described in detail previously (O'Hern, Green and Morss, 1986; O'Hern, Katz and Acosta, 1985). A pulsed ruby laser produces a coherent collimated beam. Some of the light is diffracted by particles and bubbles in the sample volume, while the remainder passes through undiffracted. Interference between the diffracted and undiffracted light is recorded on film as a hologram. After film processing the hologram is reconstructed by passing collimated He-Ne laser light through the film. The difference in wave length of the ruby and He-Ne laser light causes distances normal to the holographic plane to be compressed on reconstruction, but does not affect the in-plane image. The real image produced by the reconstruction process is highly magnified and displayed on a video monitor. The resolution of the holographic system is limited to 5 μm. The dimensions in the holographic plane of objects in the sample volume are measured directly from the video image with an estimated maximum error of about 5 μm. Bubbles are distinguished from particles by their sphericity and brightness.

3 Experimental Results and Discussion

The results reported in this section have been obtained by testing tap water with a large concentration of suspended
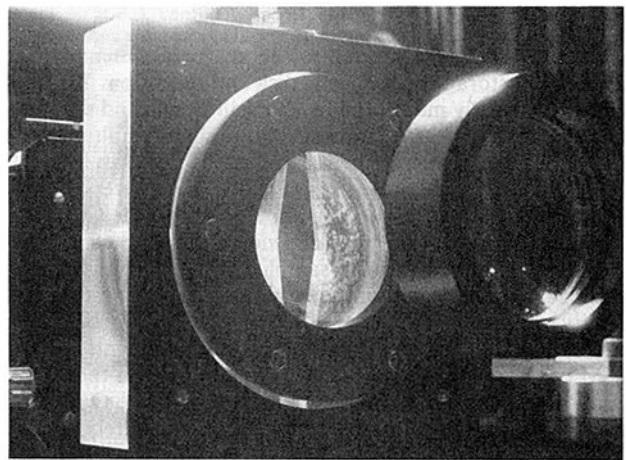

Fig. 5 Optical test cell mounted in the holographic apparatus on the CSM inlet water line. The water flows between the two optical windows from the bottom to the top of the cell. Holograms are recorded by shining short pulses of collimated coherent light through the water stream.

microbubbles, typically about three orders of magnitude larger than measured in ocean waters. The CSM and holographic data refer to water samples from the same source independently recorded at different times. However, our extensive experience with the application of the above two nuclei detection techniques to the same water source indicates that the present CSM and holographic data can still be usefully compared before the results of ongoing simultaneous measurements become available.

An example of the application of holographic observation to the measurement of the nuclei size distribution in a tap water sample is shown in Fig. 6 and the corresponding concentration of nuclei with equilibrium radius greater than or equal to R_o is plotted in Fig. 7. When many nuclei are present in the holographic volume the quality of in-line holograms is degraded due to the consequent optical distortion of the reference and subject beams and the useful resolution of the system is reduced to bubbles with radii not smaller than about 20 μm.

In order to compare the CSM and holographic data we now consider the response of an isolated bubble in the CSM venturi throat. The solution of this problem is expressed in terms of the unperturbed throat pressure p_t necessary for the bubble to grow from its initial equilibrium radius R_o and far field pressure p_o to a final detectable radius R_f over a distance L_f that identifies the location of the LDV focal point from the beginning of the venturi throat section. A number of
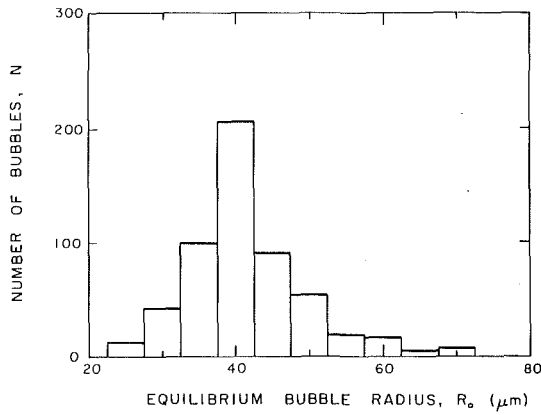
Fig. 6 Nuclei size distribution measured by holographic observation in a tap water sample with temperature $T = 20°C$, pressure $p_o = 88.8$ kPa and air content $\alpha = 18.8$ ppm
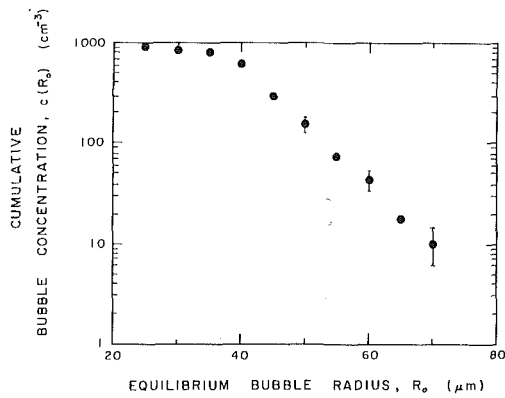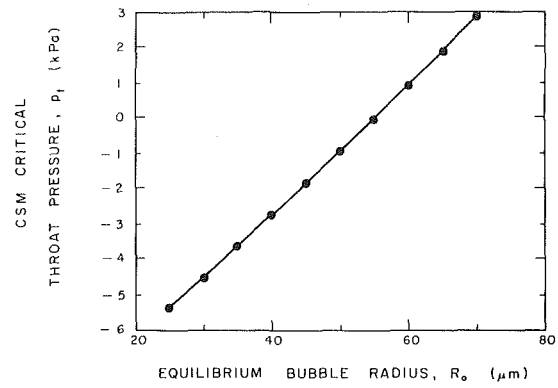

Fig. 8 Critical pressure required for a bubble initially at rest with equilibrium radius R_O in a liquid of pressure $p_O = 88.8$ kPa to grow to a final radius $R_f = 250$ μm while convected in a semi-infinite cylindrical duct of diameter $D_t = 1$ mm over a distance $L_f = 3$ mm from the inlet section

Fig. 7 Cumulative concentration of bubbles with radius not smaller than R_o in the tap water sample of Fig. 6. The sample characteristic are: temperature $T = 20°C$, pressure $p_o = 88.8$ kPa, air content $\alpha = 18.8$ ppm and volume 0.616 cm^3.

$$-I_i \frac{dq_i}{dt} + \frac{p_i - p_b}{\rho} - \frac{q_b^2}{2A_b^2} = 0 \tag{4}$$

$$-I_e \frac{dq_e}{dt} + \frac{p_b - p_e}{\rho} + \frac{q_b^2}{2A_b^2} - \frac{q_e^2}{A_e^2} = 0 \tag{5}$$

where $A_b = A(x_b)$, p_i and p_e are constant and:

$$I_i \simeq \int_{x_i}^{x_b} \frac{dx}{A(x)}; \ I_e \simeq \int_{x_b}^{x_e} \frac{dx}{A(x)} \tag{6}$$

Equations (2) through (5) are then transformed by introducing perturbation quantities (such as $p_b = p_t + p_b'$, $u_b = u_t + u_b'$, etc.) with respect to the steady state solution and linearized for small changes in the volume fluxes. Finally, if $I_i \simeq x_b / A_b = u_t t / A_t \ll I_i + I_e$, which is essentially equivalent to considering the dynamics of a bubble entering a semi-infinite pipe of constant cross sectional area A_t, the perturbation and Rayleigh-Plesset equations can be reduced to the following second order differential equation for the bubble radius $R(t)$:

$$\frac{2\pi\rho u_t}{A_t} \left[2tR^2 \frac{d^2R}{dt^2} + 4tR \left(\frac{dR}{dt} \right)^2 + R^2 \frac{dR}{dt} \right] +$$

$$+ \rho R \frac{d^2R}{d^2t} + \frac{3}{2}\rho \left(\frac{dR}{dt} \right)^2 - p_g \left(\frac{R_o}{R} \right)^3 + \frac{2S}{R} + p_t = 0 \tag{7}$$

where p_t and u_t are the steady state pressure and velocity at the throat. Note that the solution of the above equation depends on A_t, the throat cross-sectional area.

The throat pressure p_t computed by numerically integrating the above equation for $p_o = 88.8$ kPa, $R_f = 250$ μm, $L_f = 3$ mm and $D_t = 1$ mm is shown in Fig. 8 as a function of the initial bubble radius R_o. The choice of the final radius R_f (carried out as mentioned in Section 2) is somewhat uncertain because the LDV signal amplitude depends on several uncontrollable factors besides the cavity size, while the other parametric data are more safely representative of the conditions in the venturi throat. The throat pressure determined in this way is then used to express the holographic data of Fig. 7 in a form directly comparable with CSM data, namely in terms of the concentration of active cavitation nuclei as a function of the applied pressure. The results are shown in Fig. 9 together with the CSM measurements in a similar tap water sample. Both data sets are repeatable within a factor of two. The relative r.m.s. error in estimating the nuclei concentration from the number of counts N in each data group approaches $1/\sqrt{N}$ when $N > 10$. The number of counts is about 900 for CSM data and is shown in Fig. 6 for holographic data. Thus the estimation error is rather small in both cases when compared to the repeatability of the measurement. Both detection methods indicate that the

hypotheses are made in order to construct a simplified set of equations which nevertheless models the interactions between the bubble and the liquid. First the flow is assumed to be one-dimensional, ideal, incompressible and the relative motion of the bubble with respect to the surrounding liquid is neglected. The bubble, moving along the centerline of the duct with instantaneous position $x_b(t)$ and velocity $u_b(t)$, remains spherical and its radius $R(t)$ is determined by the Rayleigh-Plesset equation (Plesset and Prosperetti, 1977; Knapp, Daily, and Hammit, 1970):

$$p_b = p_g \left(\frac{R_o}{R} \right)^\gamma - \frac{2S}{R} - \rho \left[R \frac{d^2R}{dt^2} + \frac{3}{2} \left(\frac{dR}{dt} \right)^2 \right] \tag{1}$$

where ρ is the liquid density, S is the surface tension, γ is the ratio of the specific heats of the gas in the bubble and diffusive effects are neglected, i.e., p_g is constant. Here p_b is the external pressure driving the bubble volume changes and it is assumed to be equal to the pressure of the liquid in the proximity of the bubble. Then, from the continuity and unsteady Bernoulli's equations for the inlet flow upstream of the bubble (subscript i) and the exit flow downstream of the bubble (subscript e):

$$q_i - q_b + 2\pi R^2 \frac{dR}{dt} = 0 \tag{2}$$

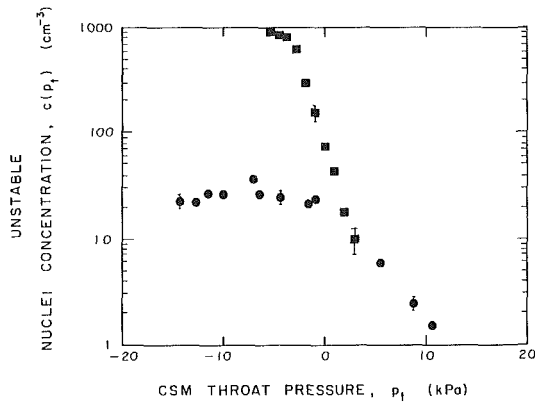$$q_e - q_b + 2\pi R^2 \frac{dR}{dt} = 0 \tag{3}$$

Fig. 9 Unstable nuclei concentration $n(p_t)$ measured by holographic observation (squares) and by the CSM (circles) as a function of the venturi throat pressure p_t. The holographic data refer to the tap water sample of Fig. 6 and the CSM data to a similar sample with temperature $T = 21°C$, pressure $p_o = 95.9$ kPa and air content $\alpha = 20.8$ ppm.
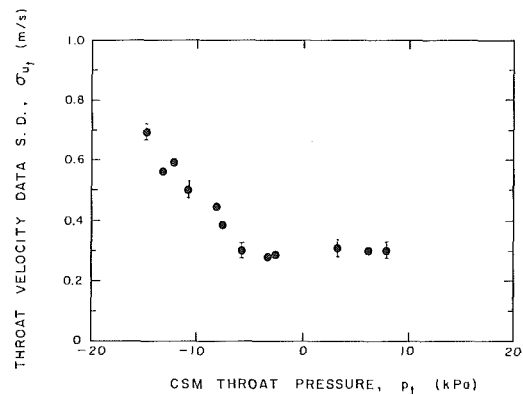

Fig. 10 Standard deviation of the throat data σ_{u_t} measured by the CSM as a function of the throat pressure p_t in the tap water sample of Fig. 9 with pressure $p_o = 95.9$ kPa, temperature $T = 21°C$ and air content $\alpha = 20.8$ ppm

concentration of cavitation nuclei initially increases exponentially with the applied tension, as also reported by other investigators (Oldenziel, 1982; Shen and Gowing, 1984; Shen et al., 1986). When the throat pressure is further reduced below about -2 kPa the concentration of cavitation nuclei reaches a maximum and remains nearly constant thereafter. Photographic records and the statistical analysis of time delays between cavitation events clearly indicate that short range (order D_t) pressure perturbations are insignificant (d'Agostino, 1987; d'Agostino and Acosta, 1987) and therefore that the cavitating nuclei concentration only depends on the average pressure in the CSM throat. Nuclei interference only affects the concentration of cavitating nuclei indirectly through the modifiction of the average pressure field, for example by limiting the minimum attainable pressure above the fully wetted flow value (choking). The CSM data of Fig. 10 also show that the levelling of the cavitating nuclei concentration is accompanied by the increase of the throat velocity data standard deviation from a previously constant value. These results indicate that the observed behavior of the cavitating nuclei concentration reflects the actual lack of cavitation nuclei that become active when the throat pressure is lowered below a certain value and that a further decrease of the throat pressure simply produces a more violent growth and collapse of the available population of active nuclei, thus making the cavitating flow more unsteady and increasing the dispersion of the throat velocity data.

The comparison of the results in Fig. 9 also shows that the concentration of unstable nuclei varies significantly both in magnitude and distribution in the two cases. In particular, the holographic data indicate a maximum concentration of unstable nuclei more than one order of magnitude larger than measured by the CSM. This is not surprising since holographic observation ideally accounts for all nuclei present in a given size range, while the finite sensitivity of the CSM in the detection of cavitation events can clearly allow a rather large number of nuclei to go undetected depending on the settings of the relevant thresholds. On the other hand, the wider range of the CSM data as a function of the throat pressure is likely to be due at least in part to the assumption of fully wetted flow in the computation of the throat pressure. This assumption is justified when only occasional cavitation events take place in the CSM throat, but clearly looses validity at the high cavitation rates of the CSM data in Figs. 9 and 10 (up to 500 events per second). When a large number of cavities is continuously present in the cavitation region of the venturi tube the collective effects of the bubble volume changes produce a global,

permanent, quasi-steady increase of the pressure throughout the venturi test section (choked flow conditions). The neglect of this effect leads therefore to underestimating the value of the throat pressure and explains the larger range of the CSM data with respect to the holographic results. Comparison of the mean distance between cavitation events measured by the CSM Signal Processor with the length of the cavitation region in the venturi is an effective indicator of saturation (choking) in the CSM venturi.

Conclusions

The two nuclei detection methods examined in this note are based on quite different physical principles. Holographic observation performs a static measurement of the concentration size distribution of potential cavitation nuclei. The CSM, on the other hand, carries out a direct test of nuclei cavitation in controlled dynamic conditions, where the concentration of active cavitation nuclei depends on the pressure at the CSM venturi throat. Therefore the results obtained from the two methods are not immediately comparable and must be correlated by taking into account the dynamic behavior of cavitation nuclei in the CSM venturi throat. Both detection methods clearly show that the concentration of active cavitation nuclei increases at first about exponentially with the applied tension, reaches a maximum and remains nearly constant thereafter when few additional nuclei are left to cavitate. The concentration of unstable nuclei measured with the two methods is significantly different in magnitude and distribution as a function of the throat pressure. The simplifying assumptions introduced to correlate the holographic and CSM results do not model the effects of fluid mechanical interference among the cavities. These effects become important in the CSM flow at high cavitation rates and, together with the inherent sensitivity limitations of the CSM, are the most likely causes of the observed discrepancies in the results of the two cavitation nuclei detection methods considered herein.

Acknowledgments

References

Billet, M., 1986a, "The Importance and Measurement of Cavitation Nuclei," *Advancements in Aerodynamics*, Fluid Mechanics and Hydraulics, Minneapolis, Minnesota, pp. 967-989.

Billet, M., 1986b, Personal communication.

Billet, M., 1985, "Cavitation Nuclei Measurement—A Review," ASME *Cavitation and Multiphase Flow Forum*, Albuquerque, New Mexico, pp. 31-38.

Chahine, G. L., and Shen, Y. T., 1986, "Bubble Dynamics and Cavitation Inception in Cavitation Susceptibility Meters," ASME JOURNAL OF FLUIDS ENGINEERING, Vol. 108, pp. 444-452.

d'Agostino, L., 1987, "Experimental and Theoretical Study on Cavitation Inception and Bubbly Flow Dynamics," Ph.D. thesis, California Institute of Technology, Calif.

d'Agostino, L., and Acosta, A. J., 1983, "On the Design of Cavitation Susceptibility Meters," 1983, American Towing Tank Conference, Hoboken, NJ.

d'Agostino, L., and Acosta, A. J., 1987, "A Cavitation Susceptibility Meter with Optical Cavitation Monitoring," 18th International Towing Tank Conference, Kobe, Japan.

Godefroy, H. W. H. E., Jansen, R. H. J., Keller, A. P., and van Renesse, R. L., 1981, "Comparison of Measuring and Control Methods of the Water Quality with Respect to Cavitation Behaviour," Delft Hydraulics Laboratory Publication.

Katz, J., O'Hern, T. J., and Acosta, A. J., 1984, "An Underwater Holographic Camera System for Detection of Microparticulates," ASME *Cavitation and Multiphase Flow Forum*, New Orleans, Louisiana, pp. 22-25.

Knapp, R. T., Daily, J. W., and Hammitt, F. G., 1970, *Cavitation*, McGraw-Hill.

Lecoffre, Y., and Bonnin, J., 1979, "Cavitation Tests and Nucleation Control," *International Symposium on Cavitation Inception*, New York, New York, pp. 141-145.

LeGoff, J. P., and Lecoffre, Y., 1983, "Nuclei and Cavitation," *14th Symposium on Naval Hydrodynamics*, National Academy Press, pp. 215-242.

Oldenziel, D. M., 1982a, "A New Instrument in Cavitation Research: the Cavitation Susceptibility Meter," ASME JOURNAL OF FLUIDS ENGINEERING, Vol. 104, pp. 136-142.

Oldenziel, D. M., Jansen, R. H. J., Keller, A. P., Lecoffre, Y., and van Renesse, R. L., 1982b, "Comparison of Instruments for Detection of Particles and Bubbles in Water During Cavitation Studies," *Proceedings of Symposium on Operating Problems of Pump Stations and Power Plants*, IAHR, Amsterdam.

Oldenziel, D. M., 1982c, "Utility of Available Instruments during Cavitation Tests," *Proceedings of Symposium on Operating Problems of Pump Stations and Power Plants*, IAHR, Amsterdam.

Oldenziel, D. M., 1979, "New Instruments in Cavitation Research," *International Symposium on Cavitation Inception*, New York, New York, pp. 111-124.

O'Hern, T. J., Green, S. I., and Morss, E. P., 1986, "Measurements of Oceanic Nuclei Distributions," ASME *Cavitation and Multiphase Flow Forum*, Atlanta, Georgia, pp. 23-26.

Shen, Y. T., and Gowing, S., 1985, "Scale Effects on Bubble Growth and Cavitation Inception in Cavitation Susceptibility Meters," ASME *Cavitation and Multiphase Flow Forum*, Albuquerque, NM, pp. 14-16.

Shen, Y. T., Gowing, S., and Pierce, R., 1984, "Cavitation Susceptibility Meters by a Venturi," *ASME International Symposium on Cavitation Inception*, pp. 9-18.

Shen, Y. T., Gowing, S., and Eckstein, B., 1986, "Cavitation Susceptibility Measurements of Ocean, Lake and Laboratory Waters," David W. Taylor Naval Ship Research and Development Center, Report DTNSRDC-86/D19.

Unsteady Structure Measurement of Cloud Cavitation on a Foil Section Using Conditional Sampling Technique

A. Kubota
Graduate Student.

H. Kato
Professor.

H. Yamaguchi
Associate Professor.

M. Maeda
Research Associate.

Department of Naval Architecture,
Faculty of Engineering,
University of Tokyo,
Tokyo 113 Japan

The structure of flow around unsteady cloud cavitation on a stationary two-dimensional hydrofoil was investigated experimentally using a conditional sampling technique. The unsteady flow velocity around the cloud cavitation was measured by a Laser Doppler Anemometry (LDA) and matched with the unsteady cavitation appearance photographed by a high-speed camera. This matching procedure was performed using data from pressure fluctuation measurements on the foil surface. The velocities were divided into two components using a digital filter, i.e., large-scale (low-frequency) and small-scale (high frequency) ones. The large-scale component corresponds with the large-scale unsteady cloud cavitation motion. In this manner, the unsteady structure of the cloud cavitation was successfully measured. The experimental result showed that the cloud cavitation observed at the present experiment had a vorticity extremum at its center and a cluster containing many small cavitation bubbles. The convection velocity of the cavitation cloud was much lower than the uniform velocity. The small-scale velocity fluctuation was not distributed uniformly in the cavitation cloud, but was concentrated near its boundary.

1 Introduction

Cavitation on a stationary foil section oscillates cyclically within a certain range of cavitation numbers, even if the far field flow condition is steady. This unsteady cavitation sheds a cavitation cloud in each cycle (Kermeen, 1956). It is well known that cloud cavitation results in the generation of severe noise, vibration, and erosion (Knapp, 1955). Therefore it is very important to understand the mechanism.

This unsteady cavitation on a stationary foil section has been investigated by many researchers (Wade and Acosta, 1966; Izumida et al., 1980). For example, Alexander (1974) observed it in detail and found Strouhal numbers in the range of 0.1 to 0.16. Nishiyama et al. (1983) reported the relationshiop between cavity length and fluid forces such as lift and drag. However, no study of the detailed flow structure at unsteady cavitation has yet been done.

This paper describes experiments concerning the structure of flow around an unsteady cavitation cloud on a stationary two-dimensional hydrofoil using a conditional sampling technique (Davies, 1976; Kiya and Sasaki, 1985a). An important feature of this study is the use of foil-surface pressure fluctuations as a conditional signal to extract the large-scale structure of the cloud cavitation.

The pressure was measured by pressure pickups mounted flush on the foil surface and high-speed film was shot at the same time as shown in Fig. 1(a). The conditional-sampled shape of the cavitation cloud was determined using the low frequency component of the pressure fluctuation as conditional sampling signal. The flow field velocity and foil-surface pressure were measured simultaneously using the setup shown in Fig. 1(b). Because of the limitations of the experimental apparatus, only one component of velocity at one point could be measured at a time. The unsteady structure of the cavitation cloud was obtained from these results using the pressure fluctuation as a parameter. This measurement method is based on the existence of strong correlation between the foil-surface pressure fluctuations, the shape of the cavitation cloud and the velocity fluctuations around it.

2 Experimental Setup and Method

All the experiments in this paper were carried out in the Foil Test Section of the Cavitation Tunnel at the Department of Naval Architecture, University of Tokyo. The working section is of rectangular form, 600 mm high by 150 mm wide. The velocity range of test section is 2 to 19.5 m/s and the turbulence level of mean flow is about 0.2 percent. A foil section named an E.N. foil was tested whose characteristics were investigated at the authors' laboratory (Yamaguchi and Kato, 1983). It is a symmetrical hydrofoil with an elliptic nose and smoothened to straight line form at the after end. Both the
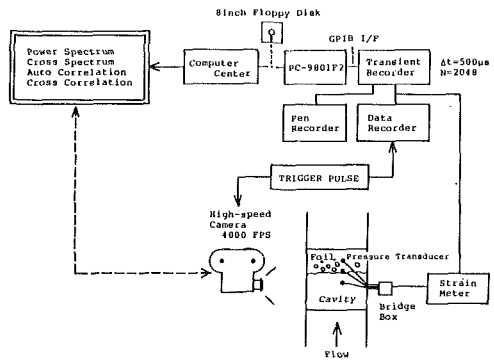
(a) Measurement of foil surface pressure fluctuations and cavitation appearance
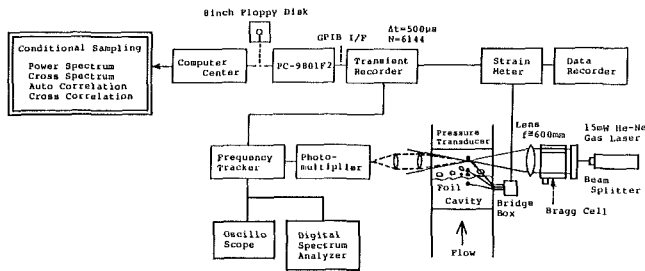
(b) Measurement of foil surface pressure and velocity fluctuations
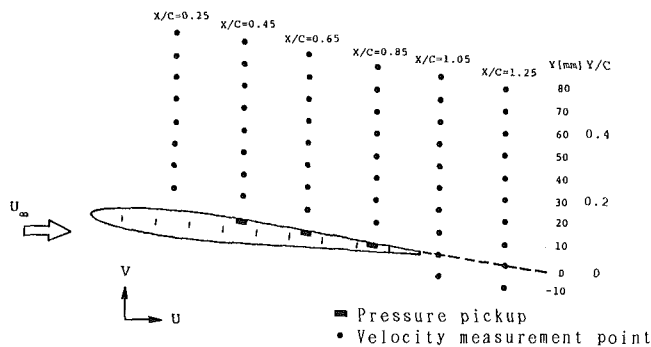
Fig. 1 Schematic diagram of the measuring systems

Fig. 2 Measurement points for pressure and velocity

Fig. 3 Photographs of unsteady behavior of cloud cavitation (side view; backward lighting; $\sigma = 1.2$; $\alpha = 6.2$ deg)

chord length and the span width are 150 mm and the thickness ratio is 8 percent.

Pressure pickups measuring the foil-surface pressure fluctuations were mounted at three points, $X/C = 0.45, 0.65, 0.85$ from the leading edge. They were 6 mm in diameter, of strain gauge type, 2 kgf/cm² in capacity and frequency characteristics being flat to 20 kHz.

The velocity fluctuation was measured by a Laser Doppler Anemometry (15 mW, He-Ne gas laser, forward scattered) at the points shown in Fig. 2. The spanwise position of measurement was $Z/C = 0.6$ which was the same as that of the pressure pickups on the foil surface.

These pressure and velocity waveforms were recorded by a transient recorder with a sampling time of 500 μs. The number of samples were 2048 and 6144, respectively. The film speed of the 16 mm high-speed camera was about 4000 FPS. For each experiment, a trigger pulse was used to mark the starting point

---

Nomenclature

C = chord length of the hydrofoil

C_p = pressure coefficient ($= (P - P_\infty)/(0.5\rho U_\infty^2)$)

f = shed frequency of cavitation cloud

l_e = time-averaged end position of attached cavity

P = local pressure

P_∞ = pressure in uniform flow

Re = Reynolds number based on uniform flow velocity and chord length of the hydrofoil

U = time-averaged flow velocity in longitudinal direction

U_∞ = uniform flow velocity

U_c = convection velocity of cavitation cloud

u = flow velocity in longitudinal direction

V = time-averaged flow velocity in normal direction

v = flow velocity in normal direction

w = flow velocity in spanwise direction

α = attack angle

ρ = mass density of water

σ = cavitation number ($= (P_\infty - \text{(vapor pressure)})/(0.5\rho U_\infty^2)$)

τ = time lag from conditional sampling signal

ϕ = phase

ω = vorticity
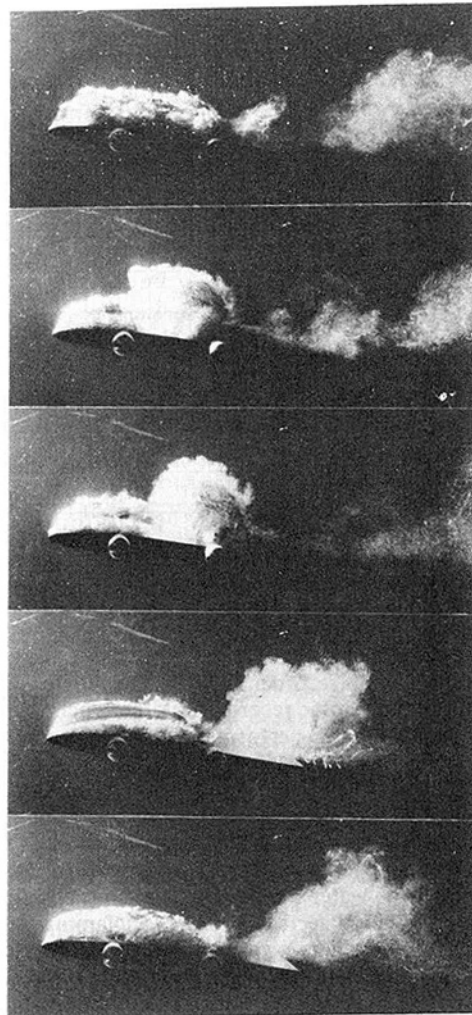
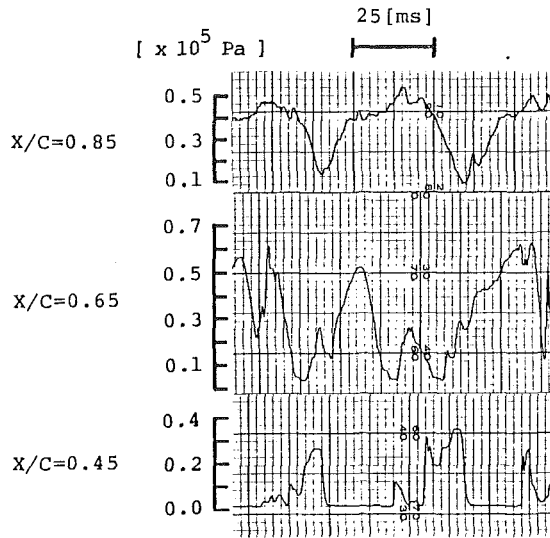$\langle \ \rangle$ = conditionally averaged value

Fig. 4 Examples of raw waveform of the foil surface pressure signal ($\sigma = 1.2$; $\alpha = 6.2$ deg; Uncertainty in pressure $= \pm 1.5 \times 10^3$ Pa)

[RAW]   [FILTERED]

Fig. 5 Waveform, power spectrum and auto-correlation of raw and low-pass filtered pressure fluctuations ($\sigma = 1.2$; $\alpha = 6.2$ deg; $X/C = 0.65$; Uncertainty in pressure $= \pm 0.05$)

Fig. 6 An example of power spectrum of longitudinal velocity fluctuation ($\sigma = 1.2$; $X/C = 0.65$; $Y/C = 0.267$)

of both the transient recorder data file and the film. Thus, the digital and photographic records could be synchronized later.

The experiments were performed at an attack angle α of 6.2 deg and cavitation number σ of 1.0, 1.2, and 1.4. However, this paper discusses only the results at $\sigma = 1.2$. At this condition, cavitation clouds were shed most cyclically. Since the uniform flow velocity U_∞ at the test condition was set at 8.0 m/s, the Reynolds number Re changed from 1.2 to 1.4×10^6 depending on the water temperature. In noncavitating condition, the present foil section had a short laminar separation bubble at the leading edge and no turbulent separation (Yamaguchi and Kato, 1983). The air content in the water was kept at 10–15 percent of the saturated condition at 1 atm.

The time-averaged attached cavity end position l_e/C was 0.41 at $\sigma = 1.2$ (Yamaguchi and Kato, 1983). Figure 3 shows photographs of the cavitation cycle. Though they were not taken successively in one cycle, they are arranged in a series to illustrate the cavitation cycle.

3 Experimental Results and Discussion

3.1 Foil Surface Pressure Fluctuations. Figure 4 shows waveforms of foil surface pressure. At the location $X/C = 0.45$, when the pressure pickup was covered with sheet cavitation, it indicated a constant value which agreed with vapor pressure.

The left side of Fig. 5 shows the waveform, its power spectrum and the auto-correlation coefficient of the pressure fluctuation at $X/C = 0.65$. The pressure is nondimensionalized by the dynamic pressure $1/2\rho U_\infty^2$. As shown in this figure, one clear peak exists in the power spectrum and it corresponds to the cloud cavitation shedding frequency.

The authors consider that the low frequency component of the pressure fluctuation is caused by the large-scale cyclic development and convection of the cavitation cloud, and the high frequency component is related to impact presure due to bubble collapse and turbulence due to small-scale vortices. For this reason, low-pass filtering of the pressure fluctuation can extract the component due to large-scale cloud cavitation unsteadiness. From spectral analysis of the raw data, the authors set the cut-off frequency at 40 Hz, approximately 1.5 times the spectrum peak frequency. This spectrum peak frequency was observed to be constant throughout the series of experiment at this condition.

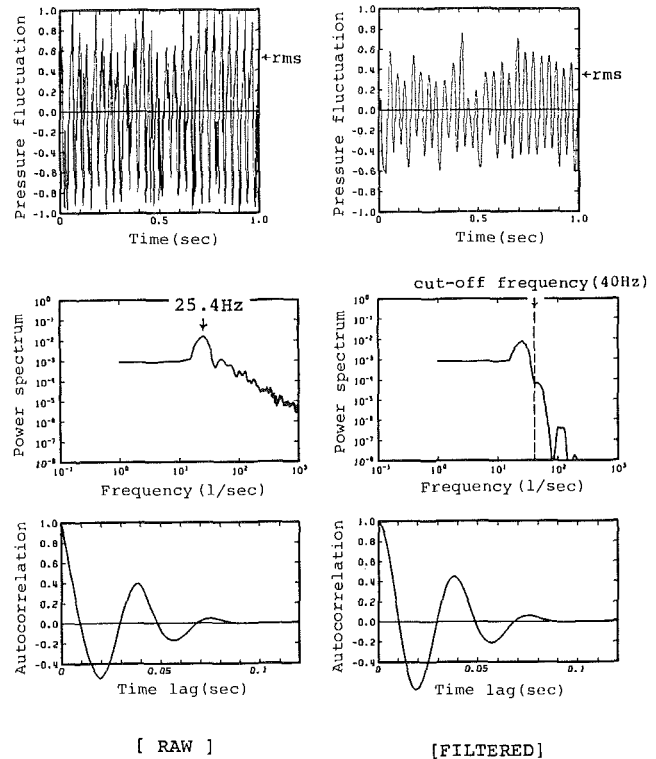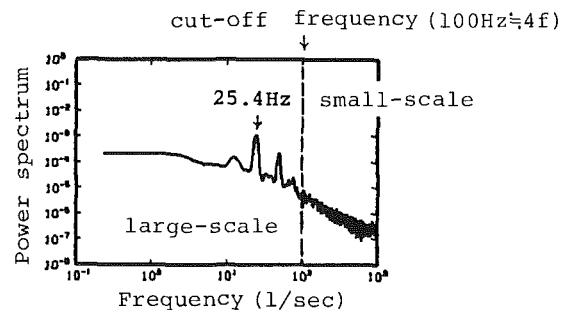The right side of Fig. 5 shows the filtered waveform of the

pressure fluctuation and its power spectrum and auto-correlation coefficient. The power spectrum shows that, after filtering, only the low-frequency pressure fluctuation energy remains.

3.2 Decomposition of the Components of Unsteady Velocities. The velocities u and v were decomposed into three parts (Kiya and Matsumura, 1985b);

$$
\begin{aligned}
u &= \langle u \rangle + \bar{u} + u' \\
v &= \langle v \rangle + \bar{v} + v'
\end{aligned} \tag{1}
$$

$$\underbrace{\phantom{\langle u \rangle + \bar{u}}}_{\substack{\text{large-scale} \\ \text{component}}} \quad \underbrace{}_{\substack{\text{small-scale} \\ \text{component}}}$$

where $\langle\ \rangle$ means the conditionally averaged fundamental component of the large-scale cavitation structure, $\sim$ means the large-scale sample deviations from $\langle\ \rangle$ and $'$ means the incoherent small-scale fluctuation. The large-scale sample deviations $\bar{u}$, $\bar{v}$ may be associated with the change of the
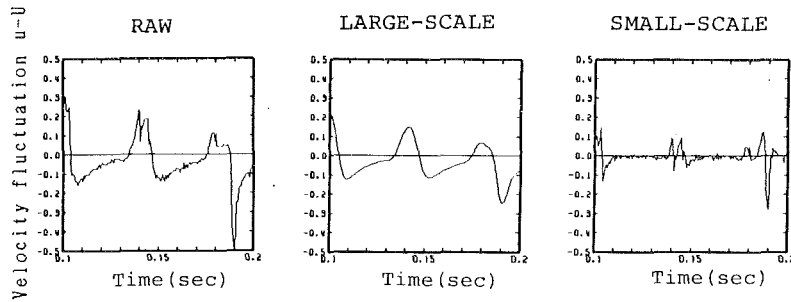
Fig. 7 Waveform of velocity and large- and small-scale components of longitudinal velocity fluctuation ($\sigma = 1.2$; $X/C = 0.65$; $Y/C = 0.267$; Uncertainty in velocity $= \pm 0.01$)
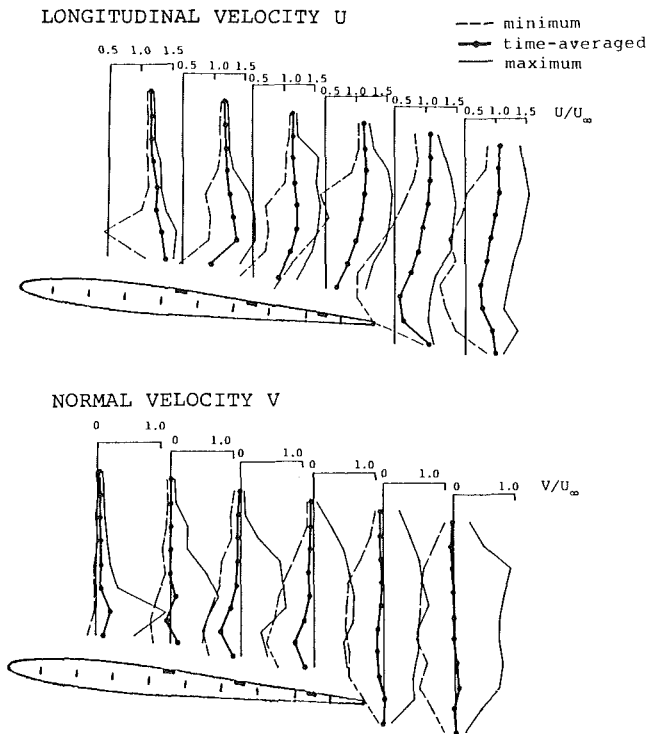

Fig. 8 Distribution of time-averaged, maximum and minimum velocities ($\sigma = 1.2$)

scale, intensity and position of the large-scale structure between the individual cycles.

The small-scale fluctuation may be associated with the local characteristics of the large-scale structure. It is extracted by high-pass filtering, because a large-scale fluctuation can exist only in a lower frequency range than a small-scale one.

Figure 6 shows an example of a velocity fluctuation power spectrum. The velocity is nondimensionalized by the uniform flow velocity. It shows the highest peak at the frequency of cloud shedding, i.e., 25.4 Hz. This is the same frequency as that of the pressure fluctuation, seen in Fig. 5. There is only one large peak due to harmonics, situated at 50 Hz. Therefore the authors have set the cut-off frequency to extract the small-scale fluctuation component at 100 Hz which is 4 times the cloud-shedding frequency. Figure 7 shows an example of the measured velocity fluctuation waveform, and how it is decomposed into large- and small-scale components.

3.3 Data Analysis Procedure Using Conditional Sampling Technique. The data analysis was conducted in the following way:

First, the pressure signal at $X/C = 0.65$ was chosen as the conditional signal. The signal was low-pass filtered at the frequency of 40 Hz, then each three successive digitized data were compared to find a peak which is used as the conditional point of phase $\phi = 0$. In this analysis, only significant peaks were selected using a threshold level of the peak height which was taken equal to the rms value of the pressure fluctuation.

Phase ϕ was defined as

$$\phi = 2\pi(t - t_i)f_0$$

where f_0 = spectrum peak frequency
t_i = time of ith peak in pressure fluctuation

As a result, the number of peaks chosen by the above procedure was 76.2 percent of all peaks.

Secondly, $\langle u \rangle$ and $\langle v \rangle$ were obtained by averaging the data at the same phase in the range of -0.05 s $\leq \tau \leq 0.05$ s where $\tau = 0$ corresponds the time of the conditional signal peak ($t = t_i$). Because the tracker output was held when the valid signal from the photomultiplier was not obtained, the sample of the same value as that of the previous sample was excluded from the analysis. This process reduced the number of the samples around each peak from 60 to 30–50. When the number of valid data became less than 20, that set was omitted from the analysis judging that the number of the samples was not enough.

The vorticity of the large-scale structure $\langle \omega \rangle$ was obtained from $\langle u \rangle$ and $\langle v \rangle$ using equation (3).

$$\langle \omega \rangle = \frac{\partial}{\partial x}\langle v \rangle - \frac{\partial}{\partial y}\langle u \rangle$$

$$\doteq -\frac{1}{\langle u \rangle}\frac{\partial}{\partial t}\langle v \rangle - \frac{\partial}{\partial y}\langle u \rangle \tag{3}$$

Finally, $\tilde{u}$ and u', $\tilde{v}$ and v' were decomposed by a high-pass filter. Each component of fluctuating energy, as shown below, was obtained.

Overall : $\langle (u - \langle u \rangle)^2 \rangle$, $\quad\quad \langle (v - \langle v \rangle)^2 \rangle$

Large-scale : $\langle \tilde{u}^2 \rangle$, $\quad\quad\quad\quad \langle \tilde{v}^2 \rangle$

Small-scale : $\langle u'^2 \rangle$, $\quad\quad\quad\quad\quad \langle v'^2 \rangle$

3.4 Large-Scale and Small-Scale Structure of Cloud Cavitation. Figure 8 shows the distribution of time-averaged, maximum, and minimum velocities. The distribution of time-averaged longitudinal velocity U shows the formation of a boundary layer near the foil surface and the wake behind it. As to time-averaged normal velocity V, large negative values were measured at $X/C = 0.65$, 0.85, and $Y/C = 0.133$. At $X/C = 0.25$ where the cavitation clouds were formed, the maximum normal velocity was very large and of the same order as the uniform flow velocity U_∞. Conversely, minimum longitudinal velocity was very small ($\langle 0.5U_\infty \rangle$) there.

Figure 9 shows the distribution of the rms velocity fluctuation intensities. In the region where cloud cavitation was formed, the fluctuations of v were much stronger than those of u. In the wake region, both components of the fluctuation inten-
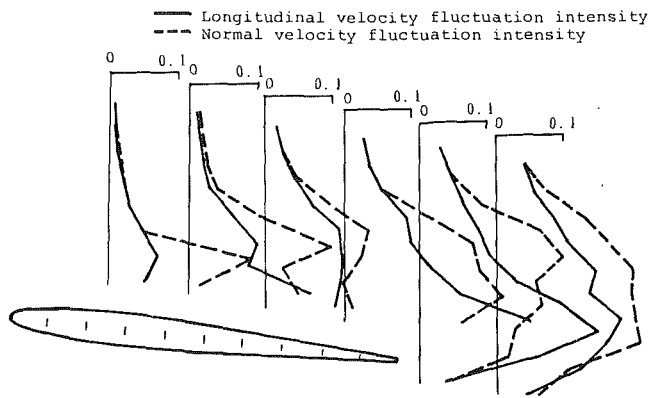
Fig. 9 Distribution of the rms velocity fluctuations $\sqrt{(u-U)^2}$, $\sqrt{(v-V)^2}$ ($\sigma = 1.2$; Uncertainty in the rms velocity $= \pm 0.02$)
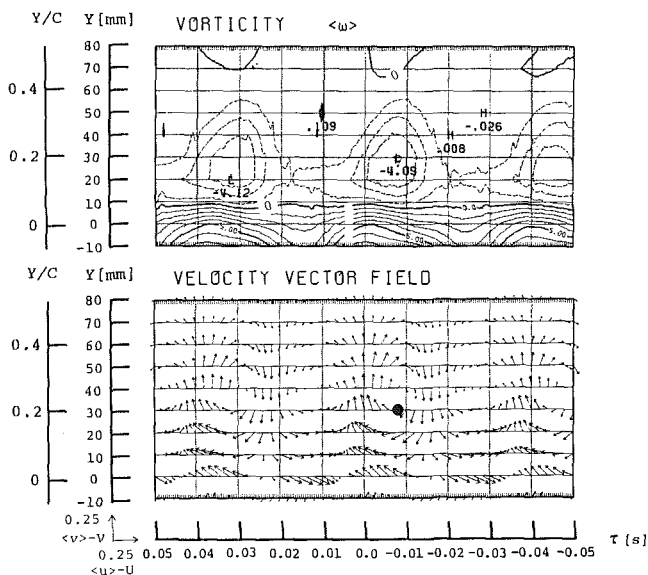

Fig. 10 Time-space (τ, Y) distributions of vorticity (contour interval = 1.0) and velocity fluctuation vector field; solid circle shows the center of the vortex ($\sigma = 1.2$; $X/C = 1.05$)

Fig. 11 Time-space (τ, Y) distributions of overall, large- and small-scale longitudinal fluctuation velocity energy (contour interval = 0.01, 0.005, 0.0025, respectively); the solid circle shows the center of the vortex; H and L mean the higher and lower extreme points ($\sigma = 1.2$; $X/C = 1.05$)

sity were very high and the high value zone of v extended wider than that of u.

An example of the unconditionally averaged velocity fluctuations ($\langle u \rangle - U$, $\langle v \rangle - V$) is shown in Fig. 10. Figure 10 is shown in the time-space domain (τ, Y). The abscissa is time difference from the conditional signal when the right-hand side corresponds to the downstream, and the ordinate is the vertical distance from the foil surface (see Fig. 2). Figure 10 also shows the contour lines of vorticity (positive in counterclockwise). A large clockwise rotating flow is observed from these figures. Since the contour lines of vorticity show a extremum (solid circle) near the center of the rotating flow, this can be interpreted as a real vortex with vorticity. Figure 11 shows the time-space distributions of the overall, large- and small-scale longitudinal fluctuating velocity energy. Those three figures give a rough idea of how the energy is distributed in the cavitation cloud. Overall the large-scale fluctuating velocity energies are high around the center of the cavitation cloud (solid circle) and also behind the trailing edge of the foil. The small-scale incoherent velocity fluctuation $\langle u'^2 \rangle$ is not distributed uniformly in the cavitation cloud, but concentrated near its boundary. This may be caused by the collapse of bubbles there.

Figure 12 shows the space distribution of the conditionally averaged velocity fluctuation vector ($\langle u \rangle - U$, $\langle v \rangle - V$), the

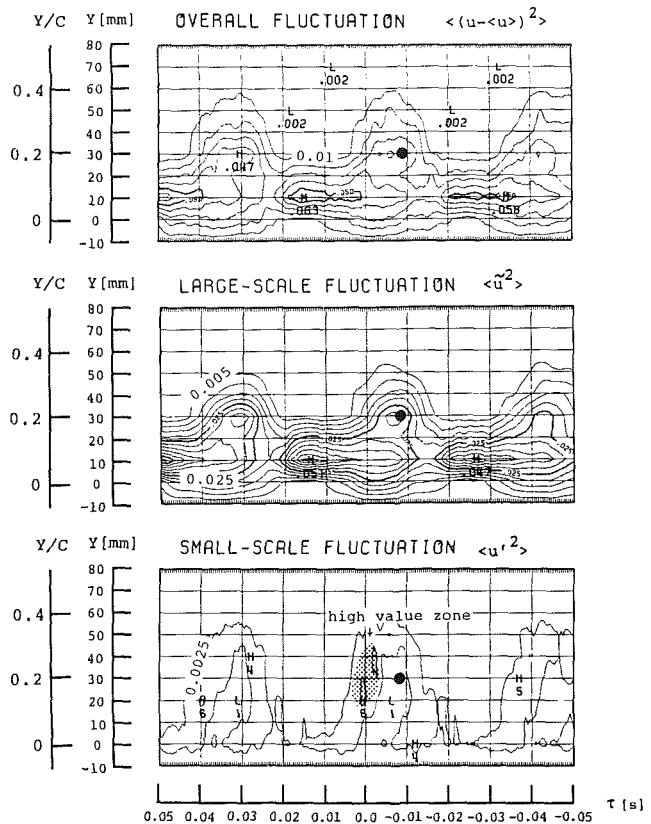foil surface pressure and the shape of cavitation region at phase intervals of $1/4\pi (\approx 0.005$ s). The cavitation shape was determined by making sketches from the high-speed films, where attention was paid to the position of the cloud and the trailing edge of the attached cavity. One cycle of cloud cavitation is shown in Fig. 12. From these figures, we can see that the large clockwise rotating flow follows the generation of the cloud cavitation resulting in a low pressure on the foil surface. The cavitation clouds observed at the present experiment have a concentrated vorticity region at their center and contain clusters of many small cavitation bubbles.

Another interesting finding is that a strong upward flow was observed at the front part of the cavitation cloud when it formed. It is seen in Fig. 12 for $\phi = 1/2\pi$. The velocity vectors shown are conditionally averaged ones of about 50 cycles. Therefore the actual peaks are much higher than conditionally averaged peaks. The record of raw v values at $X/C = 0.25$ and $Y/C = 0.13$ is shown in Fig. 13. The upward flow velocity sometimes becomes the same order of magnitude as the uniform flow velocity. Thus, it can be concluded that cloud cavitation is caused by ascending low-speed fluid including many small cavity bubbles near the foil surface.

Since there is a strong correlation between the large-scale cavitation cloud structure and the low frequency component of the foil-surface pressure fluctuation, we can calculate the convection velocity of the cavitation cloud U_c using the cross-correlation between two pressure fluctuations measured at different points simultaneously. The result is shown in Fig. 14. In this figure, the cloud velocity observed from high-speed film and the time-averaged velocity at the center of the cloud measured by LDA are also shown. These three velocities agree with each other and they are much lower than the uniform
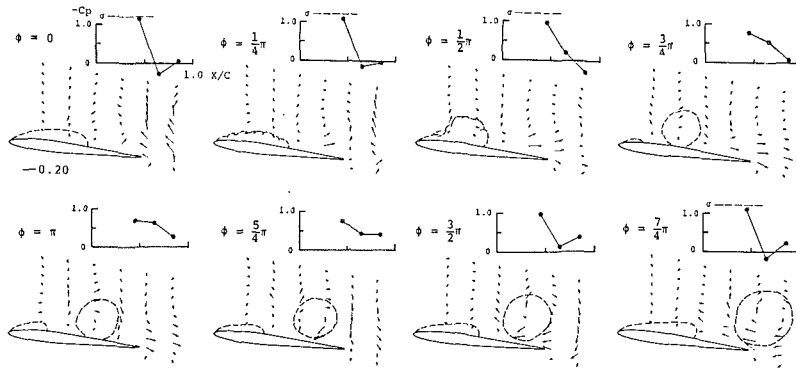
Fig. 12 Conditionally averaged vectors of the velocity fluctuations ($\langle u \rangle - U$, $\langle v \rangle - V$), the foil-surface pressure distributions and the shapes of the cavitation regions ($\sigma = 1.2$; $\alpha = 6.2$ deg)
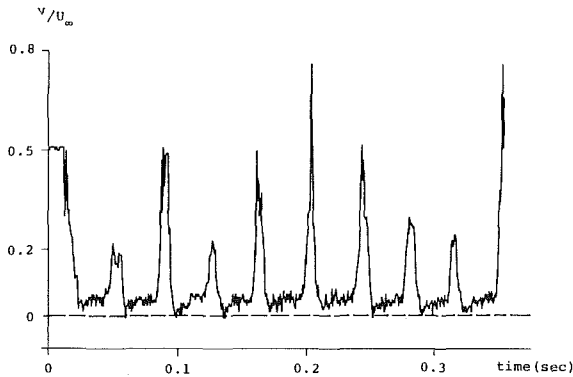

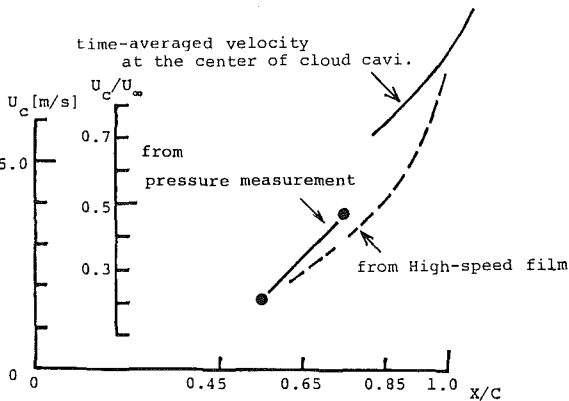Fig. 13 Waveform of normal velocity v ($\sigma = 1.2$; $X/C = 0.25$; $Y/C = 0.133$)

Fig. 14 The convection velocity of the cavitation cloud ($\sigma = 1.2$)

a "croissant" vortex

Fig. 15 The three-dimensional structure of cavitation cloud ($\sigma = 1.2$; $X/C = 0.65$)
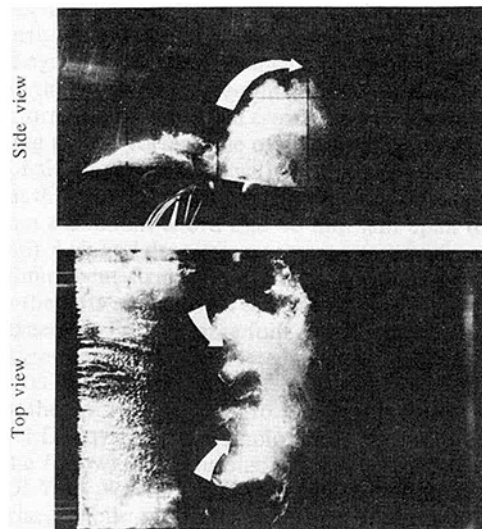
Fig. 16 Simultaneous photographs of large-scale structure of cloud cavitation ($\sigma = 1.2$; $\alpha = 6.2$ deg)

flow velocity. The velocity increased as the cavity flowed downstream.

3.5 Three-Dimensional Structure of Cavitation Cloud. Measurements were also performed in the spanwise section of $X/C = 0.65$ in order to clarify the three-dimensional structure of cavitation cloud. For this measurement, the minimum value of the foil-surface pressure fluctuation was adopted as the conditional signal. This means that the center of the cavitation cloud is located right over the pressure pickup at $\tau = 0$. The spanwise averaged velocity $\langle w \rangle$ was calculated using the continuity equation with the assumption that $\langle w \rangle$ was symmetrical about the mid-span ($Z/C = 0.5$) position in the spanwise direction and that the density change term was negligible.

The resulting three-dimensional velocity vectors are shown in Fig. 15 (a). The three-dimensional cavitation cloud structure is a stretched vortex whose configuration looks like a
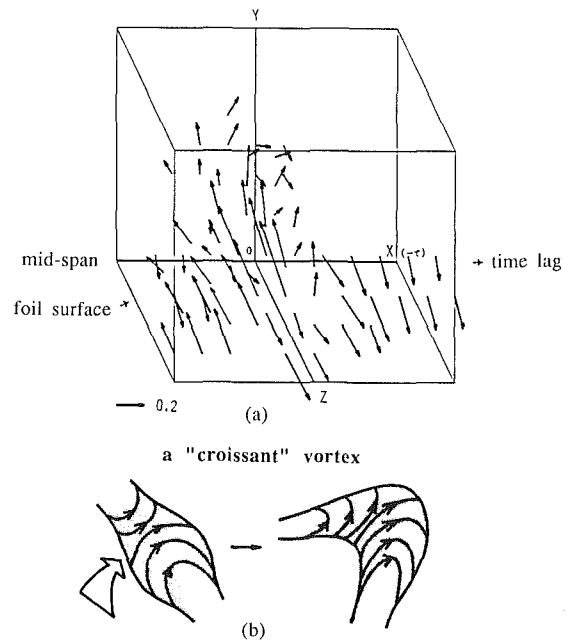
"croissant" as shown in Fig. 15 (b). Figure 16 shows a "croissant" cavity seen on the foil surface in a flow field with cloud cavitation. Such "croissant" vortex cavities were also ob-

served at the rear end of stable sheet cavitation though the size was much smaller than that in Fig. 16.

4 Conclusions

In this paper, large- and small-scale flow structures around unsteady cloud cavitation on a stationary two-dimensional hydrofoil were investigated experimentally using a conditional sampling technique. The large-scale flow structure is connected to the coherent component of the development of cavitation and its convection, and the small-scale structure is the incoherent component associated with the large-scale structure.

The following results were obtained:

(1) The unsteady structure of cloud cavitation was successfully measured by Laser Doppler Anemometry using a conditional sampling technique. In this procedure, the foil-surface pressure fluctuation was adopted as the conditional signal.

(2) The cloud cavitation observed at the present experiment has a concentrated vorticity region at the center of the cloud and it contains many small cavitation bubbles. The three-dimensional cavitation cloud structure is a stretched vortex whose configuration looks like a croissant.

(3) The convection velocity of the cavitation cloud is much lower than the uniform flow velocity. The velocity increases as the cavity flows downstream.

(4) When the cavitation cloud was formed, strong upward flow was observed at the front of it. Therefore it is concluded that cloud cavitation is formed by ascending low-speed fluid near the foil surface.

(5) The small-scale incoherent velocity fluctuations are not distributed uniformly in the cavitation cloud, but are concentrated near its boundary. They may be caused by the collapse of bubbles there.

References

Alexander, A. J., 1974, "Hydrofoil Oscillations Induced by Cavitation," *Conference on Cavitation*, Edinburgh, IMechE, pp. 3-5.

Davies, M. E., 1976, "A Comparison of the Wake Structure of a Stationary and Oscillating Bluff Body, Using a Conditional Averaging Technique," *Journal of Fluid Mechanics*, Vol. 75, Part 2, pp. 209-231.

Izumida, Y., Tamiya, S., Kato, H., and Maeda, M., 1980, "The Relationship Between Characteristics of Partial Cavitation and Flow Separation," *10th IAHR Symposium*, Tokyo, pp. 169-181.

Kermeen, R. W., 1956, "Water Tunnel test of NACA 4412 and Walchner Profile 7 Hydrofoil in Non-Cavitating Flows," Hydrodynamic Laboratory, California Institute of Technology, Pasadena, Calif., Report No. 47-5.

Kiya, M., and Sasaki, K., 1985a, "Structure of Large-Scale Vortices and Unsteady Reverse Flow in the Reattaching Zone of a Turbulent Separation Bubble," *Journal of Fluid Mechanics*, Vol. 154, pp. 463-491.

Kiya, M., and Matumura, M., 1985b, "Turbulence Structure in Intermediate Wake of Circular Cylinder," *Bulletin of JSME*, Vol. 28, No. 245, pp. 2617-2624.

Knapp, R. T., 1955, "Recent Investigation of the Mechanics of Cavitation and Cavitation Damage," *Trans.* ASME, Vol. 77, pp. 1045-1954.

Nishiyama, T., Yoshioka, S., and Akama, M., 1983, "Time Series Analysis of Hydrofoil Cavitation (1st Report)," *Transactions of the JSME (Series B)*, Vol. 49, No. 448, p. 2655-2661 (in Japanese). *Bulletin of JSME*, Vol. 27, No. 230, pp. 1798 (abstract).

Wade, R. B., and Acosta, A. J., 1966, "Experimental Observation of the Flow Past a Plano-Convex Hydrofoil," ASME JOURNAL OF FLUID ENGINEERING, Vol. 88, No. 1, pp. 273-283.

Yamaguchi, H., and Kato, H., 1983, "On Application of Nonlinear Cavity Flow Theory to Thick Foil Sections," *Conference on Cavitation*, Edinburgh, IMechE, pp. 167-174.

Tip Vortex Cavitation Inhibition by Drag-Reducing Polymer Solutions

D. H. Fruman

S. S. Aflalo[1]

Groupe Phénomènes d'Interface,
Ecole Nationale Supérieure de
Techniques Avancées,
91120 Palaiseau, France

This paper presents previous and recent results obtained by the authors concerning the modification of the tip vortex cavitation of a finite span hydrofoil by drag-reducing polymer solutions. Experiments were conducted with homogeneous solutions and with semidilute solutions ejected at the tip of the wing. Measurements of the onset cavitation number for tip vortex cavitation, hydrodynamic forces on the hydrofoil and tangential velocities in the tip vortex have been conducted. The results show that tip vortex cavitation is inhibited in all cases but for different reasons. In homogeneous polymer solutions the lift of the hydrofoil, and hence the circulation, is considerably reduced leading to a less intense vortex as shown by tangential velocity measurements. With semidilute polymer solution ejections there is no noticeable change of the hydrodynamic forces but a significant modification of the tangential velocities in the core region. The mechanism for tip vortex cavitation inhibition is thus completely different in these two situations.

Introduction

Methods to delay and inhibit tip vortex cavitation have been investigated (Platzer and Souders, 1979 and 1981). More recently, Inge and Bark (1983) have implied, from noise measurements, that tip vortex cavitation inception is delayed in a 10 ppm homogeneous POLYOX WSR 301 solution, while Fruman et al. (1985) and Aflalo (1987) have shown that tip vortex cavitation inhibition is obtained by ejecting semidilute solutions of the same polymer and of SEPARAN AP 30 from the tip of an elliptical hydrofoil. In Inge's case the cavitation inhibition was theoretically ascribed (Inge, 1983) to the normal stresses developed by the polymer solution, while in the case of polymer solution ejection LDA measurements showed a modification of the tangential velocity component large enough to justify a pressure increase in the vortex core and thus a retardation of the cavitation. These measurements also demonstrated that the intensity of the tip vortex was not modified by the ejection. However, no systematic force measurements were conducted in order to find if either the polymer ejection or the homogeneous polymer solutions caused a change of the lift capable of explaining the cavitation inception delay. This paper presents the results of these measurements and concludes that the cavitation inhibition, in the case of polymer ejection, is due solely to the modification of the tangential velocity profiles in the core region, while, in the case of homogeneous polymer solutions, is due to the reduction of the lift, and thus the reduction of the intensity of the vortex.

Experimental

Tests were performed in the ENSTA Cavitation Tunnel fit-

ted with a rectangular test section 80 mm wide and 150 mm high. The cavitation number was defined in the usual way,

$$\sigma = \frac{p_\infty - p_v}{\frac{1}{2}\rho U_\infty^2}$$

where p_∞ and U_∞ are the pressure and the velocity of the unperturbed flow and p_v is the vapor pressure of the water at the temperature of the tests. Tip vortex cavitation desinence, henceforth defined by σ_d, was determined visually but it was checked against noise measurements with good results (Aflalo 1987). In this work two three-dimensional hydrofoils of elliptical planform and symmetrical cross section were employed for generating the tip vortex: one of 40 mm maximum chord and 60 mm half span provided with a 1 mm diameter injection orifice at the tip of the wing (called the large foil) and the other of 30 mm maximum chord and 40 mm half span (called the small foil). Lift and drag measurements were performed using a two-component strain gauge balance which was calibrated prior to the tests and showed a linear response in the range of forces expected. For the large foil, axial and tangential velocity measurements were conducted using a single component backscatter DISA LDA system at a downstream distance of 20 cm from the tip. For the small foil a two component backscatter TSI LDA system was employed. Tests were conducted under the following conditions: (*a*) without and with a 1000 ppm POLYOX WSR 301 polymer solution ejection at the tip of the large foil, and (*b*) with pure water and with an homogeneous solution of the same polymer with a concentration of about 10 ppm circulating in the tunnel fitted with the small foil.

To perform the latest tests, a master solution of about 1500 ppm was fabricated 24 hours prior to the tunnel tests and its drag-reducing properties were checked by flowing, at a con-
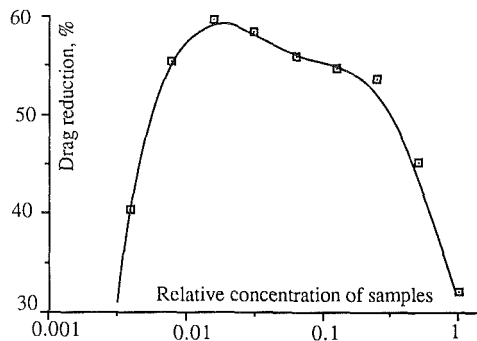

Fig. 1 Drag reduction as a function of the relative concentration of samples prepared with the 1500 pp POLYOX WSR 301 master polymer solution
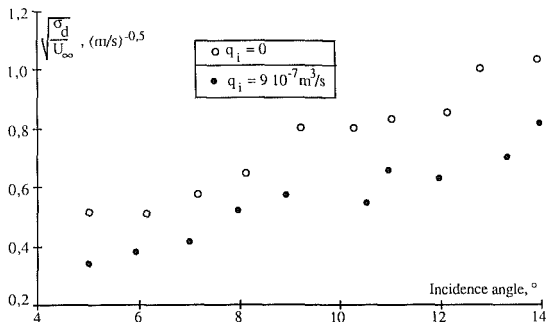

Fig. 2 Desinent cavitation number versus incidence angle for water and semidilute polymer ejection

a) Incidence angle, 10°

b) Incidence angle, 5°

Fig. 3 Tangential velocities versus distance to vortex axis as function of the ejection rate

stant flow rate, diluted fractions of a sample of the master solution through a 1 mm diameter capillary tube.

As shown in Fig. 1, a maximum drag reduction of 60 percent was achieved for a dilution of about 1/125th, a dilution close to the one is expected to be reached once the master solution is mixed with the water content of the cavitation tunnel. This was performed by injecting the master solution slowly into the tunnel through one of the pressure ports while the water was circulated at a velocity of about 5 m/s. Samples of the circulating solution were drawn and tested for their drag-reducing properties so as to check for any possible mechanical degradation during the two full days which lasted the force measurements and the tip vortex cavitation tests. No significant changes were detected. In order to check the repeatability of the results, tests were performed with homogeneous solutions prepared at different times following the same procedure.

Results

Foil Tip Polymer Solution Ejection.

Figure 2 shows the square root of the desinent cavitation number divided by the free stream velocity as a function of the incidence angle for pure water and for the ejection of a 1000 ppm POLYOX WSR 310 solution at an ejection flow rate of 0.9 cm^3/s. This presentation of results, suggested by Bovis (1980), has been shown to provide a good correlation of data for elliptical planform hydrofoils. As shown in the figure, the polymer ejection gives rise to a significant reduction of the desinent cavitation number. The ejection velocity is only of the order of 1 m/s, well below the free stream velocity in the cavitation tunnel. Tests were also conducted by ejecting either pure water or a water-glycerine solution having a viscosity of 6.5 mPa.s, about three times the viscosity of the polymer solution, and a specific mass of 1.15 g/cm^3. For ejection flow rates comparable to and even much larger than those employed during the ejection of the polymer solution, no
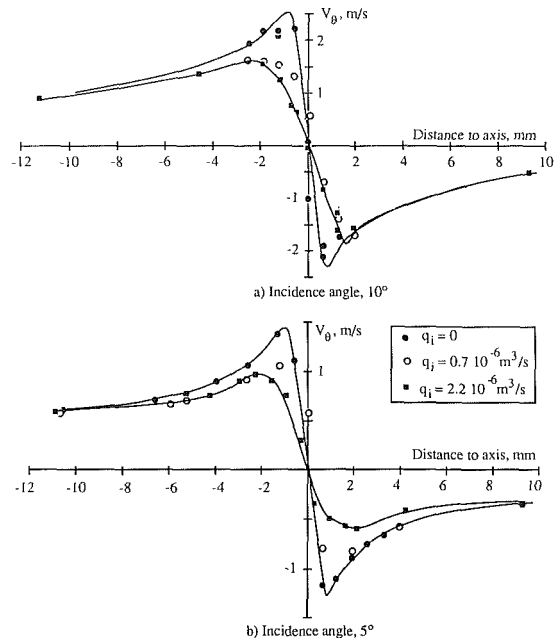
significant modification of the desinent cavitation number was detected. It should be pointed out that, owing to the fact that its specific mass was larger than that of water, the water-glycerine solution was subjected to a strong centrifugal separation effect that drove it out of the vortex core. For well developed cavities the ejection of the polymer solution led to complete disappearance of it, while no changes were observed with water and water-glycerine solutions ejection at equal flow rates. The inhibition effects seem thus to be associated to the peculiar properties of the polymer solution and not to the ejection process itself.

In order to determine the causes of such a remarkable effect, both measurements of the forces on the hydrofoil and of the velocity field of the tip vortex were conducted with and without polymer ejection. Lift and drag force measurements did not indicate any significant change during the polymer solution ejections at flow rates responsible for a decrease of the critical cavitation number of up to 60 percent (Aflalo, 1987). However, the vertical (nearly tangential) velocities in the vortex showed a striking modification as shown in Fig. 3.

For increasing ejection flow rates the maximum tangential velocity decreases and the vortex core radius increases while the velocities outside the core remain unchanged. Also, there is no marked differences between the modified velocity profiles for 0.7 and 2.2 cm^3/s ejection rates. This indicates that a saturation effect is reached for ejection rates of the order of 1 cm^3/s. The vortex intensities were estimated by fitting a potential vortex velocity distribution to the tangential velocity components outside the core, corrected to take into account the wall effects. They compare favorably with the circulation computed from the lift measurements. Thus, it seems clear that the polymer ejection causes a modification of the roll up process without effecting the hydrodynamics of the lifting body.

Homogeneous Polymer Solution

General Observations. During the mixing of the concentrated solution with the water circulating in the tunnel at constant rotary speed of the pump, the following measurements were performed: total flow rate, reference pressure in the test section and local tangential and axial velocity components for a radial position corresponding to the maximum tangential velocity in pure-water flow. Figure 4, showing these different
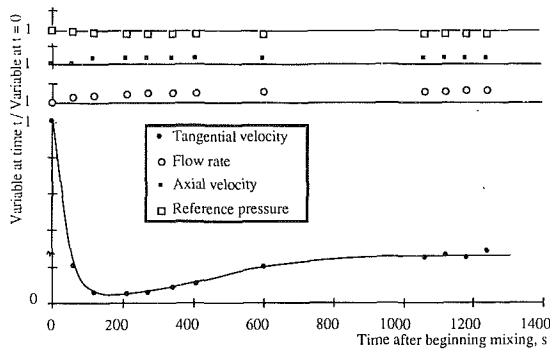
Fig. 4 Evolution of the flow rate, the reference pressure, and the axial and tangential velocity components as a function of the time elapsed after beginning the mixing of the master solution in the cavitation tunnel

measurements in nondimensional form (ratio of the measurement made at time t to the one made at time zero), indicates that the flow rate and the axial velocity slightly increase while the reference pressure slightly decreases during the build-up of the polymer concentration in the cavitation tunnel. The tangential velocity component shows the occurrence of a dramatic drop at the very beginning of the mixing followed by a small increase later on. In absolute terms the initial drop corresponds to a change of the tangential velocity component from 2,07 to 0,1 m/s. Even if it is too early to reach any conclusion from these measurements, it is clear that the modification of the tangential velocity component at the measuring station can not, in any way, be related to the other flow changes.

It is interesting to note that, since the flow rate increases and the reference pressure decreases, the cavitation number decreases during the mixing process. Therefore, if tip vortex cavitation was present at the beginning of the mixing process it should increase during the build-up of the polymer concentration. An additional experience was thus conducted by making the flow conditions in the tunnel such that a well developed tip vortex cavitation occurred on the hydrofoil. Then, a new mixing process was started during which pictures of the cavity were taken. Figure 5 shows the modification of the cavitation number with time and three pictures, taken with a shutter speed of 1/2000 s, before starting the mixing, a few minutes after starting and at the end of the process. It can be easily recognized that the polymer concentration build-up leads to a reduction of the intensity of the cavitation, as exemplified by the reduction of the diameter of the vapor core and the shortening of the cavity length, in spite of a 15 percent reduction of the cavitation number. Also, a close inspection of the pictures shows that the length of the sheet cavitation on the upper surface of the foil increases during the mixing process. This is a rather unexpected finding which is currently under investigation and will be discussed in a following paper.

From the above general observations it appears that several significant changes of the flow characteristics and of the cavitation appearance occur during the build-up of the polymer concentration in the cavitation tunnel. The most striking effects are: (i) the dramatic reduction of the tangential velocity at the measuring station (ii) the decrease of the cavitation number as a result of the increase of the flow rate and of the reduction of the reference pressure, and (iii) the modification of the geometric characteristics of the gaseous core. Other global and local measurements confirming these general observations are presented next.

Critical Cavitation Numbers. The visual detection of cavitation inception is prone to errors due to the perception of the operators as well as to the difficulty of precisely defining either inception or desinence. This is more so because
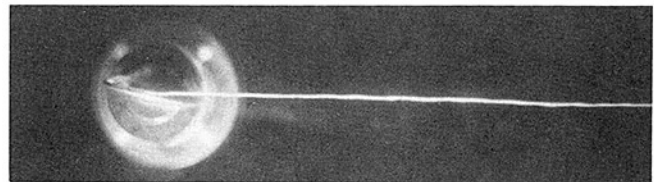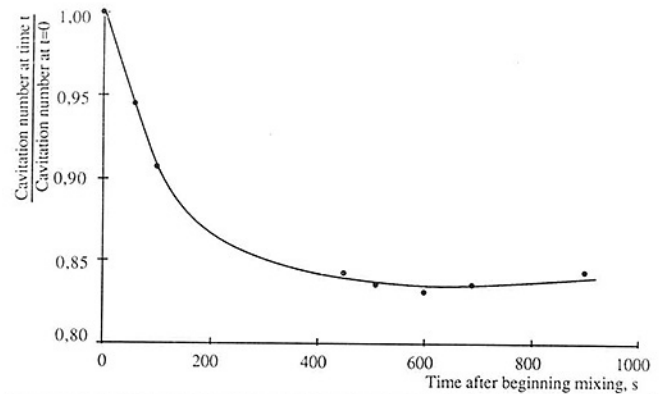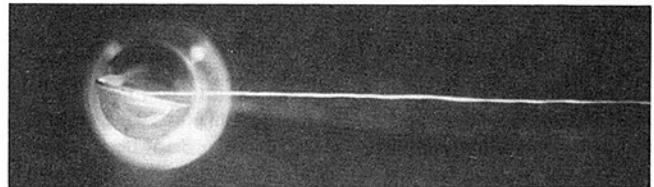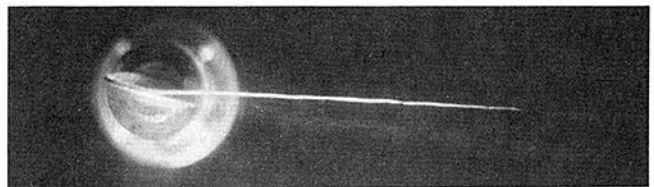
Fig. 5 Evolution of the cavitation number as a function of the time elapsed after beginning the mixing and cavity shape at three different times
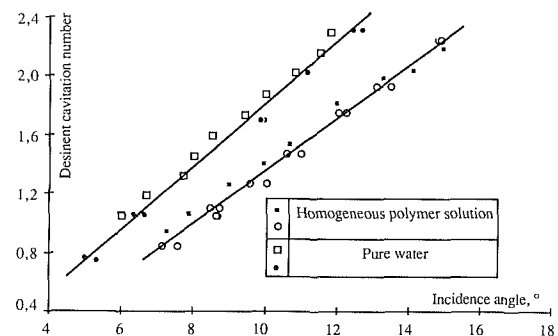
Fig. 6 Desinent cavitation number as a function of the incidence angle for pure water and the homogeneous polymer solution

desinence does not occur in the same way in water and homogeneous polymer solutions. In the first case, the cavity detach from the tip but bubbles can still be seen downstream; in the second case full detachment of the cavity coincides with the complete disappearance of bubble growth. In order to resolve some ambiguity of previous results (Fruman, 1988) experiments have been duplicated with two homogeneous solutions prepared at different times following the same procedure. Figure 6 shows the desinent cavitation number as a function of the incidence angle for the pure water and the

Fig. 7 Lift coefficient versus incidence angle in pure water and in the homogeneous polymer solution.

Fig 9 Tangential velocities versus distance to vortex axis for pure water and the homogeneous polymer solution for two incidence angle

Fig. 8 Drag coefficient versus incidence angle in pure water and in the homogeneous polymer solution

	U_∞,m/s	α,°
□	5	5
■	5,5	5
●	5	10
○	5,5	10

Fig. 10 Computed pressure difference for semidilute polymer ejection relative to water versus the nondimensional ejection rate

homogeneous polymer solution in the case of the small foil and for free stream velocities of 8 and 8.4 m/s.

It is clear that the desinent cavitation number is significantly diminished when a homogeneous polymer solution flows in the cavitation tunnel. This result, in agreement with the general observations discussed earlier, h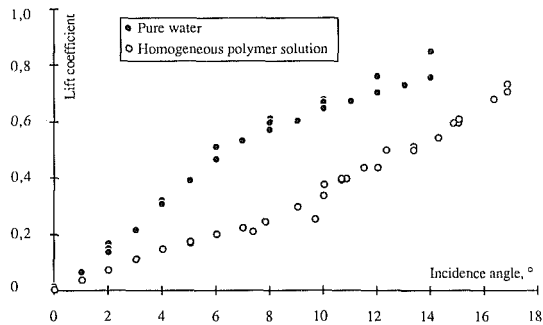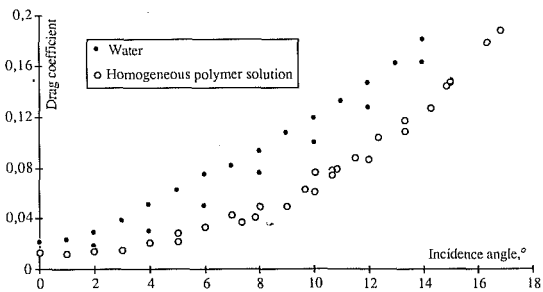as to be critically reconsidered in the light of what is already known about the effect of homogeneous polymer solutions on the hydrodynamic forces on hydrofoils and, in particular the associated lift reduction effect (Wu, 1969 and Sarpkaya, 1974). This effect is analyzed next.

Lift and Drag Forces. Figure 7 shows that the lift coefficient is significantly reduced in the homogeneous polymer solution as compared to pure water. While the water data indicates the classical linear behavior followed by the down-bending associated with the occurrence of flow separation, the polymer solution data shows an initial nearly linear growth for incidence angles below about 10 deg followed by a steeper nearly linear growth for larger angles. For incidence angles large enough, say 15 deg or more, the lift coefficients for water and polymer solution are very close to each other due to the predominant effect of flow separation.

This dramatic change of the lift should have a counterpart on the drag forces since such a strong modification of the circulation must cause a significant modification of the induced drag. The drag coefficient for pure water and the homogeneous polymer solution is shown in Fig. 8. At a zero incidence angle the drag coefficient is only slightly reduced in the homogeneous polymer solution, showing thus that the contribution of friction reduction is very small and within the experimental accuracy. For increasing incidence angles the drag coefficients in the homogeneous polymer solution become significantly smaller than those in pure water, indicating that the induced and pressure drag contributions are dampened by the peculiar properties of the polymer solution. Since the lift-to-drag ratio are very close together regardless of the circulating fluid, it can be said that the drag reduction is directly related to the lift reduction and very mildly affected by the friction reduction.
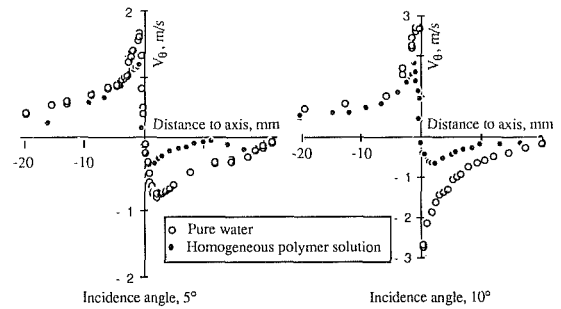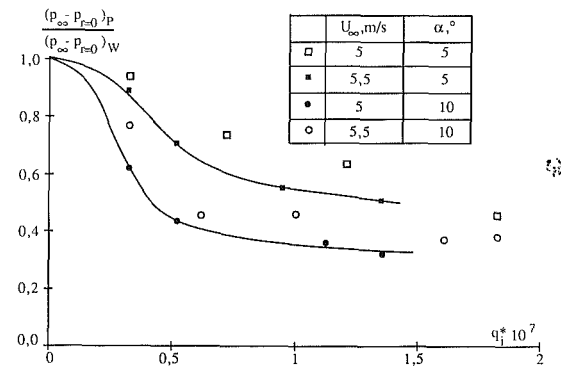
Tangential and Axial Velocity Modifications. Measurements were performed at equal mean velocities in the cavitation tunnel for two incidence angles, 10 and 5 deg, the day the solution was prepared. The axial velocities did not show any peculiar behavior which could be ascribed to the presence of the polymers, whereas the tangential velocities displayed marked differences as shown in Fig. 9. The maximum tangential velocity was reduced by a large amount while the dimension of the vortex core did not seem to be significantly affected; outside the core the velocities were reduced, in particular in the wake region, demonstrating a reduction of the circulation over the wing. Compared to the measurements presented in the General observations section, where the position of the measuring volume was kept fixed during the concentration build-up, it is clear that both the tangential velocities and the position of the vortex center were modified. Since the velocity gradient in the vortex core is extremely large, even a very small change of its position leads to a very large change of the local velocity.

Analysis and Discussion

In the general case of a non-Newtonian fluid the radial pressure gradient for a linear vortex is given by,

$$\frac{d(p-\tau_{rr})}{dr} = \rho \frac{V_\theta^2}{r} + \frac{(\tau_{\theta\theta}-\tau_{rr})}{r}$$

where τ_{rr} and $\tau_{\theta\theta}$ are the extra stresses in the radial and azimuthal direction, respectively. Since the stress term is *a priori* unknown let us evaluate the eventual contribution of the velocity term to the modification of the pressure at the vortex axis by,

$$p_\infty - p_{r=0} = \rho \int_0^\infty \frac{V_\theta^2}{r} \, dr$$

Figure 10 shows the values of $p_\infty - p_{r=0}$ for the ejection of the polymer solution (subscript P) divided by those of pure

water flow without ejection (subscript W) as a function of a nondimensional ejection flow rate,

$$q^*_i = \frac{q_i c}{U_\infty b c_m}$$

where q_i is the ejection flow rate, c is the concentration, b is the half span of the wing, and c_m is its maximum chord.

For the same value of p_∞ the pressure in the center of the vortex will be much larger for polymer solution ejection than for water at the same test conditions. In order to reach cavitation onset the reference pressure has to be decreased leading to a reduction of the critical cavitation number. Thus, tip vortex cavitation inhibition is, in the case of a polymer solution injection at the extremity of the wing, strongly associated with the modification of the tangential velocity profile in the vortex core region (Fruman et al., 1985, Aflalo, 1987). The contribution of the normal stresses $(\tau_{\theta\theta} - \tau_{rr})$ to the force balance in the radial direction, if any, is probably very small. The justification of the observed phenomenon is certainly of a different nature.

Large swelling effects of polymer solutions jets of the same polymer at comparable concentrations have been reported in the literature for ejections from capillary tubes into a stagnant fluid (Fruman et al., 1984) and for ejections from two dimensional slits in a cocurrent stream of water circulating at a velocity much larger than the ejection velocity (Fruman and Galivel, 1980). These effects result from the non-Newtonian (viscoelastic) properties of the polymer solutions and are scaled by the deformation rate (ratio of the ejection velocity to the diameter of the capillary or to the thickness of the slit). It can thus be especulated that the polymer solution ejected at the tip of the wing swells when exiting the capillary tube and modifies the roll-up process by creating a displacement effect. This is supported by the fact that the ejection of water and water plus glycerin did not introduce any significant change of the cavitation characteristics of the tip vortex.

Based on the tangential velocity profiles, an analogous computation of the pressure change has been conducted in the case of the homogeneous polymer solution flow. As it can be suspected by inspecting Fig. 9, the pressure on the axis of the tip vortex will be, at an equal reference pressure, substantially increased. The ratio (polymer-to-water) of the pressure differences (wall-to-core) for 5 and 10 deg are, respectively, of 0.7 and 0.4, comparable to those obtained in the case of a semidilute polymer solution ejection. In order to get a better understanding of the dominant phenomenon responsible for the cavitation inhibition in homogeneous polymer solutions, the desinent cavitation numbers have been plotted in Fig. 11 versus the lift coefficients computed by fitting the data of Fig. 7.

Surprisingly enough, the data show that at an equal lift coefficient the desinent cavitation number is larger for homogeneous polymer solutions than for pure water. At this stage of this research, it can be especulated that this unexpected behavior is mainly due to the difference in the visual appreciation of the conditions for desinence. As previously mentioned, in the case of water, detachment of the cavity from the tip of the wing occurs earlier than complete disappearance of the bubbles within the vortex core downstream, whereas, in the case of the polymer solution, detachment coincides with full disappearance of bubbles in the vortex core. Thus, the increase of the desinent cavitation number observed in Fig. 11 may be only apparent. This specific problem deserves more research which is currently underway.

In any event, the simultaneous modification, due to even very small amounts of the drag-reducing polymer, of both the lift coefficients of the hydrofoil and the tangential velocities of the vortex can justify the cavitation inhibition observed in the homogeneous polymer solutions.
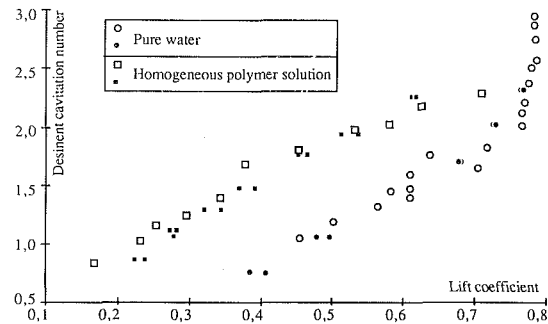

Fig. 11 Desinent cavitation number versus lift coefficient in pure water and the homogeneous polymer solution

Conclusions

For semidilute polymer solutions (1000 ppm) ejected from the tip of an elliptical hydrofoil, measurements of the desinent cavitation numbers, force coefficients and vortex tangential velocities lead to the following conclusions:

(i) at an equal incidence angle the desinent cavitation number with polymer solution ejection is smaller than without ejection,

(ii) lift coefficients are not affected by the ejection process,

(iii) the maximum tangential velocity decreases, the size of the viscous core increases and the intensity of the vortex remains constant during polymer solution ejection,

(iv) the increase of the pressure on the axis of the vortex, computed from the tangential velocity distributions, justifies the decrease of the critical cavitation number.

Similar types of measurements performed in homogeneous polymer solutions at low concentrations (≈ 10 ppm) have shown that:

1) at an equal incidence angle the desinent cavitation number in the homogeneous polymer solution is smaller than in pure water,

2) at an equal incidence angle the lift coefficient in the homogeneous polymer solution is also smaller than in water,

3) the tangential velocities of the vortex, and hence the intensity of the vortex, are decreased in homogeneous polymer solutions,

4) for equal lift coefficients, the desinent cavitation number increases in homogeneous polymer solutions,

5) the above apparent enhancement of the cavitation occurrence seems to be related to the visual appreciation of transition between a vapor core and a noncavitating flow.

These results clearly show that the mechanism for cavitation inhibition with dilute polymer ejection from the tip of a wing and in homogeneous polymer solutions is completely different. In the first case it is due to a local modification (limited to the core region) of the tangential velocities of the vortex without changing the lift (and hence the circulation) of the foil. In the second case, it is due to the modification of the lift (and hence the circulation) of the foil and the associated change of the tangential velocities.

Experimental Uncertainty

Cavitation Number. The reference pressure was measured with an accuracy of 10^3 Pa (1 percent of full scale) and the reference velocity (flow rate) with an accuracy of 0.1 m/s. The instrumental accuracy of the cavitation numbers is 0.05. The critical values of the cavitation number were determined by visual inspection and are affected by a significant experimental inaccuracy. Only data for which repeated tests were performed and unambiguous results were obtained are reported in the paper.

Incidence Angles. The incidence angles were measured with an accuracy of 1/10 of a degree. With the force balance mounted, the zero incidence angle was determined by getting the zero lift position of the foil. Without the force balance, cavitation desinence tests were performed for positive and negative angles and the results were symmetrized to obtain the zero incidence angle.

Force Measurements. The accuracy of the force measurements was estimated to 0.5 N. The instrumental accuracy of the force coefficients is evaluated to 0.01.

Velocity Measurements. The absolute accuracy of the laser anemometry system is of the order of few cm/s. The major inaccuracy is associated with the measurements of the tangential velocities in the core region where they are particularly sensible to the vertical position of the measuring volume with respect to the vortex axis. Care was taken to have a vertical distance between the horizontal plane defined by the crossing beams and the vortex axis of less than 0.25 mm.

Acknowledgments

References

Aflalo, S., 1987, "Inhibition de la cavitation de tourbillon marginal," Thesis, University Paris VI.

Bovis, A., 1980, "Etude asymptotique du phenoméne de cavitation-cavités non sphénriques," Thesis Université Paris VI.

Fruman, D. H., and Galivel, P., 1980, "Anomalous Effects Associated with Drag-Reducing Polymer Ejection Into Pure-Water Turbulent Boundary Layers," *Viscous Flow Drag Reduction*, G. R. Hough, ed., Progress in Astronautics and Aeronautics, Vol. 72.

Fruman, D. H., Perrot, P., and Bouguechal, J., 1984, "On the Swelling of Submerged Jets of Dilute and Semi-Dilute Polymer Solutions," *Chem. Eng. Commun.*, Vol. 27, pp. 101–118.

Fruman, D. H., Bismuth, D., and Aflalo, S., 1985, "Effect of Polymer Solutions on Tip Vortex Cavitation," *The Influence of Polymer Additives on Velocity and Temperature Fields*, B. Gampert, ed., Springer-Verlag Berlin-Heidelberg.

Fruman, D. H., 1988, "Tip Vortex Cavitation in Polymer Solutions," *1988 Cavitation and Multiphase Flow Forum*, ASME FED No. 64.

Inge, C., 1983, "Effect of Polymer Additives on Tip Vortex Cavitation," Tech. Rep. TRITA-MEK 83-05, Roy. Inst. of Tech. Stockholm.

Inge, C., and Bark, G., 1983, "Tip Vortex Cavitation in Water and in Dilute Polymer Solution," Tech. Rep. TRITA-MEK 83-12 Roy. Inst. of Tech., Stockholm.

Platzer, G. P., and Souders, W. G., 1979. "Tip Vortex Cavitation Delay With Application to Marine Lifting Surfaces. A Literature Review," DWT Naval Ship R & D Center Report 79/051, Bethesda, MD.

Sarpkaya, T., 1974, "On the Performance of Hydrofoils in Dilute Polyox Solutions," *International Conference on Drag Reduction*, Cambridge, England.

Souders, W. G., and Platzer, G. P., 1981, "Tip Vortex Characteristics and Delay on a Three Dimensional Hydrofoil," DWT Naval Ship R & D Center Report 81/007, Bethesda, Md.

Wu, J., 1969, "Lift Reduction in Additive Solutions," *Journal of Hydronautics*, Vol. 3, No. 4, pp. 198–200.

Visualizing the Connectivity of Vortex Systems for Pitching Wings

P. Freymuth[1]

The global visualization of vortex systems of pitching wings is explored. The topological law that vortex strands need to be connected aids in comprehending the visualized vortex systems and in assessing the quality of visualization. Viscous and viscous-turbulent diffusion facilitate the reconnection of vortex strands.

Introduction

The strands of finite vortex systems need to be closed. This topological law by Helmholtz readily applies to viscous flow around bodies with negligible rotation of their surfaces (in case of surface rotation vortex strands can terminate at the surface). While the vortex strands need to be closed (or terminated at a rotating body surface) viscous and viscous-turbulent diffusion alow reconnection of strands.

A piercing question concerning the visualization of vortex systems is how well it documents the connectivity of the strands. Two-dimensional laser-sheet cuts of dye tracers in water [1, 2] and of smoke tracers in air [3] in flow over delta wings document considerable crossectional detail of the vortices but do not address connectivity. Cuts achieved by smoke rake [4] or smoke wire [5] in air are hard to interpret because of the curvature such cuts assume in three-dimensional flow. The injection of dye through strategically placed holes in the body surface allows the visualization of limited vortex core sections in particular in steady water flow [6, 7], but do not show an entire vortex system.

A method which focuses on the connectivity of finite vortex systems is the homogeneous application of liquid titanium tetrachloride to vorticity producing body surfaces in air flow. White fumes then emanate where vorticity is produced, thus tagging the developing vortex strands and visualizing their connectivity. The method has been well established in accelerated starting flow around various half wings and wings [8–11] and is readily available for the investigation of vortex systems in other unsteady flow configurations.

The focus of the current paper is a visual investigation of the vortex systems which develop behind finite wings when they pitch to high angles of attack. The importance of pitching wings for application to highly maneuverable aircraft has

recently been pointed out by Gad-el-Hak and Ho [1]. Our visualizations revealed that reconnection processes are especially common in these configurations. Our visualizations therefore gravitate toward the elucidation of reconnection processes of the vortex strands. A version of this paper had been presented at the First National Fluid Dynamics Congress [12].

Experimental Setup

Rectangular and triangular flat wings were mounted in a horizontal wind tunnel which has been previously described [11]. The wing was fastened at its pressure side to a beam construction ending in a handle bar on top of the tunnel. This allowed manual pitching of the wing with the pitch axis located at the quarter chord. Illumination was from the top of the tunnel. Movies were taken through a side wall of the tunnel at a rate of 64 frames/s. $TiCl_4$ was introduced along the wing perimeter by means of a brass pipette prior to pitching of the wing. Wind tunnel speed during flow visualization was always kept constant at 61 cm/s.

The parameter space for pitching wings exposed to steady flow is very large and includes the Reynolds number, dimensionless pitch rate, pitch history and wing shape. Only a few diverse examples are shown to capture the essence of the vortex connection and reconnection processes, without exhausting the subject.

Experimental Results

A powerful starting vortex develops when pitching a rectangular wing rapidly (during a time of 0.5 s) from 0 to a 60 deg angle of attack. This is conveyed by the two 35 mm photographs shown in Fig. 1. In this paper flow is always from left to right. The chord length is 15cm, the vertical span is 30 cm. View is at the suction side of the wing. Figure 1(a) depicts an earlier stage in the development than Fig. 1(b). The large vortex loop to the right of the airfoil was formed from vorticity of the pressure side boundary layer and separated from the trailing edge and from the wing tips during pitchup. The loop connects to the front corners of the wing. Simultaneously, because of the high angle of attack, vorticity also separates from the suction side boundary layer and forms a leading edge dynamic stall vortex which also connects to the front corners (Fig. 1(a)), thus completing a closed vortex system in accordance with Helmholtz's law. Subsequently in Fig. 1(b) the anchoring of the combined leading and trailing edge vortex system to the front corners gets somewhat lost, presumably because of viscous and turbulent annihilation of the nearly counterrotating leading and trailing edge tip vortices. Reconnection then occurs further downstream. Unfortunately, turbulence blurs some of the detail. In addition to the main vortex loop numerous lesser starting vortices join the vortex system. These vortices feed into the tip vortices in the
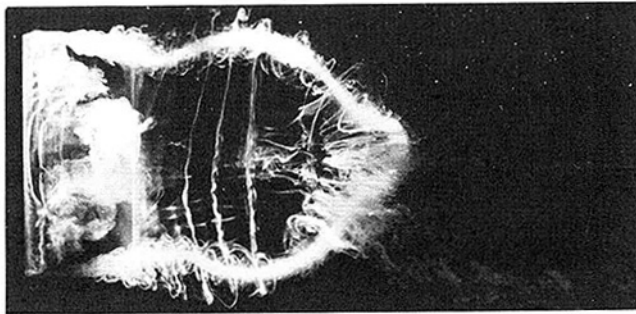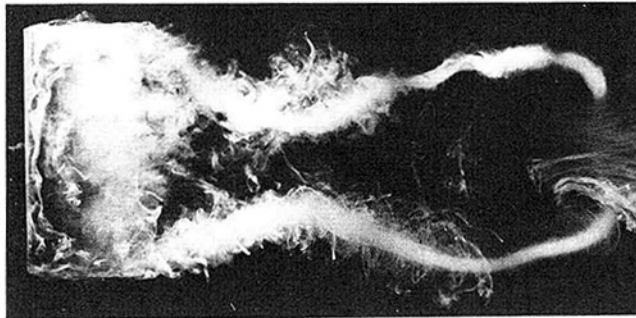
Fig. 1 Global or top view of vortex patterns for a rectangular wing after rapid pitch from 0 to 60 deg within 0.5 s. $c = 15$ cm, aspect ratio $ar = 2$, $U_0 = 61$ cm/s. $R = U_0 \, c/\nu = 5100$. (a) Time after start of pitch $t = 1$ s; (b) $t = 2$ s.
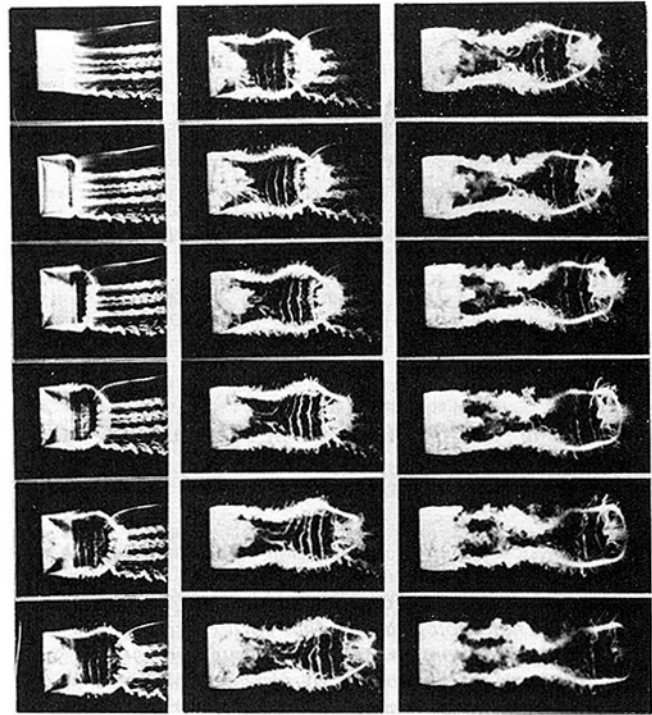

Fig. 2 Sequence for the rectangular wing in pitch from 0 to 30 deg in 0.5 s. $c = 15$ cm $ar = 2$, $U_0 = 61$ cm/s, $R = 5100$, time between consecutive frames $\Delta t = 1/8$ s.

form of multihelical cones but the individual vortex strands are not fully resolved.

It should be mentioned that inadvertently some smoke is introduced in regions where no vorticity exists and which contributes to the "optical noise" of the photographs. For instance, some smoke "mills around" the vortex core of the trailing edge vortex loop, particularly in the far downstream region.

Figure 2 shows an entire sequence of movie frames for the rectangular wing in pitch from 0 to 30 deg. Consecutive frames are a time $\Delta t = 1/8$ s apart from each other. Frames are ordered into columns from top to bottom and then across columns from left to right. Pitchup is completed in frame 5, column 1. The development of the leading and trailing edge vortex loops, and the narrowing of the trailing edge loop are clearly visible.

Figure 3 shows a square wing with 15cm side length in pitch from 0 to 30 deg. The narrowing of the trailing edge vortex loops proceeds to the point where a vortex ring forms. The remaining part of the loop reconnects to the left of the ring although details of this process are blurred by turbulence.

Figure 4 shows the rectangular wing in a quick pitch up-down maneuvers from 0 to 30 to 0 deg. In this case a vortex ring forms by reconnection of the two counterrotating trailing edge starting vortices which form during the pitch up and down phases. The remaining parts of the trailing edge vortex loops which in column 1 connect to the leading edge corners annihilate each other diffusively in column 2, leaving an independent vortex ring. Also the leading edge dynamic stall vortex loop seems to form a ring but it becomes so turbulent that it has the appearance of a puff.

Vortex ring formation by narrowing of a vortex loop similarly as in Fig. 3 was also found behind an equilateral triangular wing in pitch from 0 to 60 deg and is shown in Fig. 5. A side of the triangle heads into the wind and a corner points downstream.

If the corner of the triangle heads into the wind then the pitching process did not create a vortex ring but a series of in-
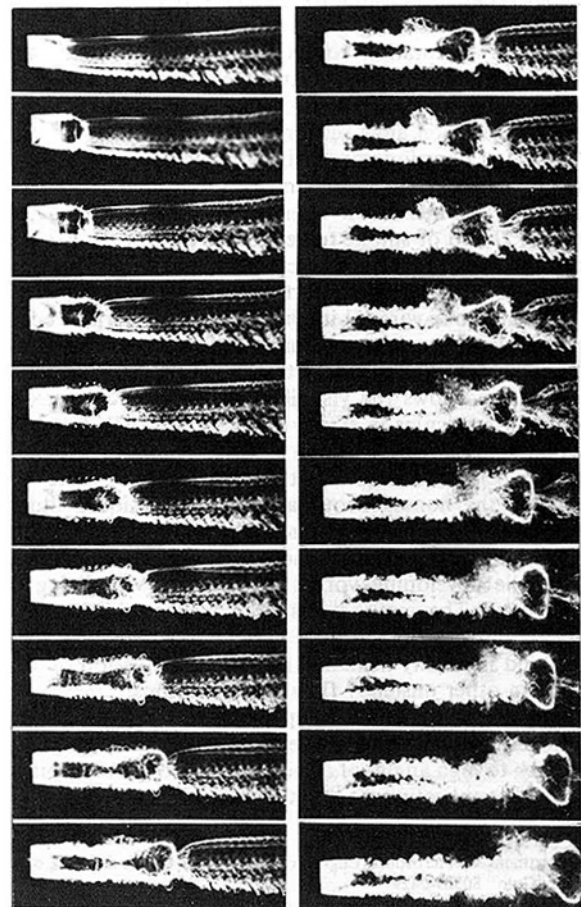

Fig. 3 Square wing in rapid pitch from 0 to 30 deg in 0.5 s. $c = 15$ cm, $U_0 = 61$ cm/s, $R = 5100$, $\Delta t = 1/8$ s.
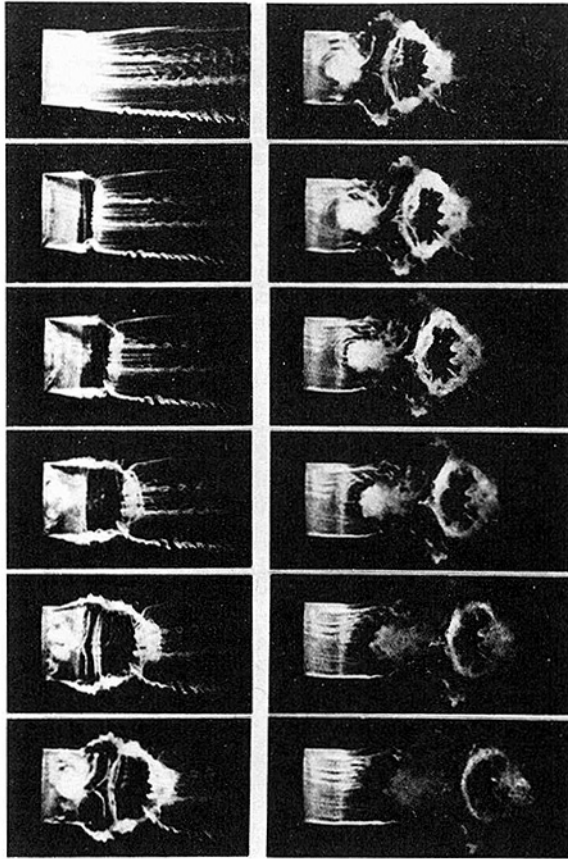
Fig. 4 Rectangular wing, pitch up-down maneuver from 0 to 30 to 0 deg within 0.5 s. $c = 15$ cm, $ar = 2$, $U_0 = 61$ cm/s, $R = 5100$, $\Delta t = 1/8$ s.

tertwined trailing edge vortex loops as is shown in Fig. 6. These loops initially connect to the leading edge conical tip vortices but connectivity gets lost in column 2 because of strong turbulence.

Figure 7 displays vortex patterns for the square wing in periodic pitch between 0 and 30 deg. The connectivity of the vortex strands gets very intriguing and is not fully resolved, mainly because of turbulence. The patterns may loosely be interpreted as irregularly shaped and connected vortex rings.

Conclusions

The connectivity of vortex patterns separating from finite wings in pitch has been visualized with moderate success. Current limitations have been outlined. Our methods of visualization appear to be widely applicable.

Acknowledgment

References

1 Gad-el-Hak, M., and Ho, C. M., "Unsteady Vortical Flow Around Three-Dimensional Lifting Surfaces," *AIAA J.*, Vol. 24, 1986, pp. 713–721.

2 Gad-el-Hak, M., Blackwelder, R. F., "Control of the Discrete Vortices from a Delta Wing," *AIAA J.*, Vol. 25, 1987, pp. 1042–1049.

3 Payne, F. M., Ng. T. T., and Nelson, R. C., "Visualization and Flow Survey of Leading Edge Vortex Structure on Delta Wing Planforms," Paper AIAA-86-0330, 1986.

4 Head, M. R., "Flow visualization in Cambridge University engineering department," *Flow Visualization*, Vol. 11, 1982, pp. 399–403.

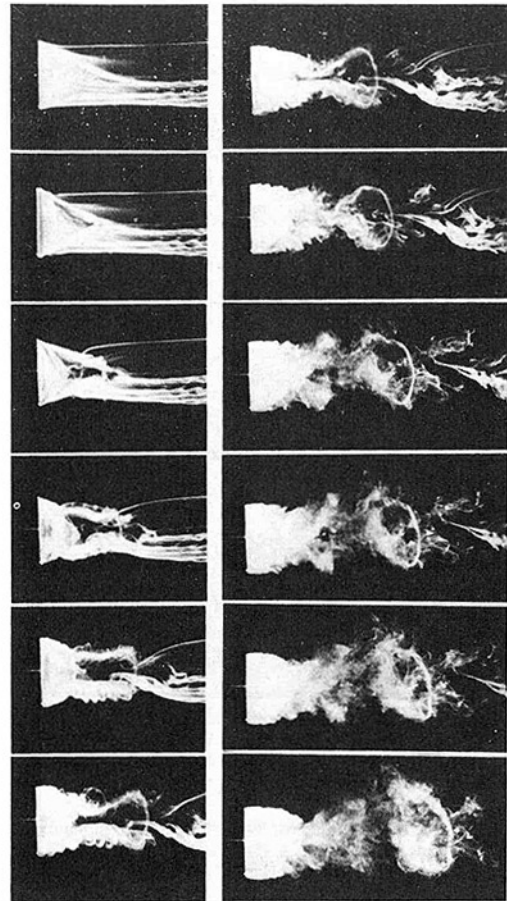Fig. 5 Equilateral triangle with one side heading into the wind. Side length $l = 5$ cm, $U_0 = 61$ cm/s, $Re = U_o l/\nu = 5100$. Pitch is from 0 to 60 deg within 0.5 s, $\Delta t = 1/8$ s. Note in frame 1 pitching had already started to 2 deg.
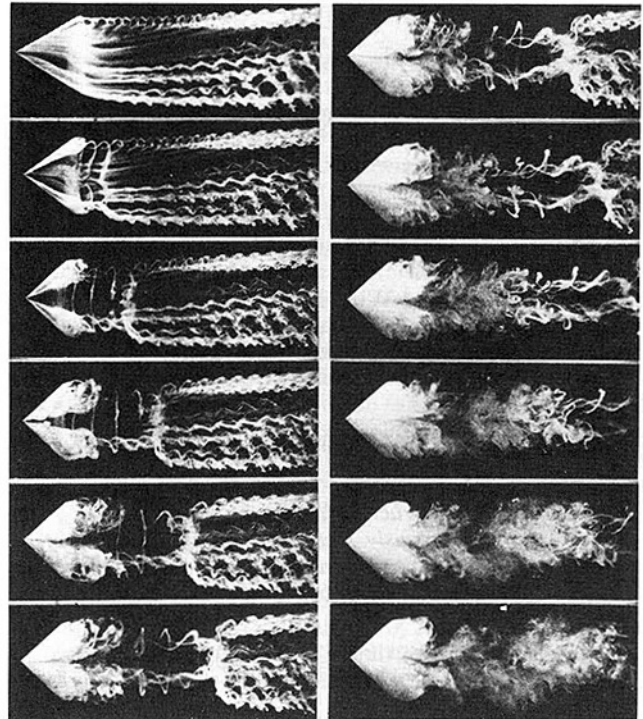

Fig. 6 Equilateral triangle with a corner heading into the wind. $l = 15$ cm, $U_0 = 61$ cm/s, $Re = 5100$. Pitch is from 0 to 60 deg within 0.5 s, $\Delta t = 1/8$ s.

Fig. 7 Square wing in periodic pitch from 0 to 30 deg, $f = 2$Hz. $c = 15$ cm, $U_0 = 61$ cm/s, $R = 5100$, $\Delta t = 1/32$ s. Remarks: $\alpha = 30$ deg in frame 3, column 1; $\alpha = 0$ deg in frame 5, column 2; the last 2 frames of column 3 are part of the next cycle.

5 Adler, J. N., and Luttges, M. W., "Three-Dimensionality in Unsteady Flow About a Wing," Paper AIAA 85-0132, 1985.

6 Werle', H., "Visualization Hydrodynamique D'E'coulements Instationaries," *ONERA Note Technique*, No. 180, 1971.

7 Werle', H., "Separation Structures on Cylindrical Wings," *Recherche Aerospatiale*, Vol. 53-74, 1986-3.

8 Freymuth, P., Finaish, F., and Bank, W., "The Wing Tip Vortex System in a Starting Flow," *Zeitschrift fuer Flugwiss. u. Weltraumforsch.*, (*ZFW*), Vol. 10, 1986, pp. 116–118.

9 Freymuth, P., Finaish, F., and Bank, W., "Visualization of Wing Tip Vortices in Accelerating and Steady Flow," *AIAA J. Aircraft*, Vol. 23, 1986, pp. 730–733. See also Paper AIAA-86-1096, 1986.

10 Freymuth, P., "Parametric Exploration of Unsteady Wing Tip Vortices," *Flow Visualization IV*, 1987, pp. 419–424.

11 Freymuth, P., "Further Visualization of Combined Wing Tip and Starting Vortex Systems," *AIAA J.*, Vol. 25, 1987, pp. 1153–1159.

12 Freymuth, P., "Visualization of the Connectivity of Vortex Systems for Pitching Wings," Paper AIAA-88-3549-CP, 1988.

A Multi-Sensor Hot-Wire Probe to Measure Vorticity and Velocity in Turbulent Flows

P. Vukoslavčević,[1,2] J.-L. Balint,[2] and J. M. Wallace[2]

The design and construction of a miniature hot-wire probe capable of simultaneously measuring all components of the velocity and vorticity vectors in turbulent flows are presented. A brief description of the probe resolution and calibration as

[1] On leave from the Veljko Vlahovic University, Titograd, Yugoslavia.

[2] Department of Mechanical Engineering, The University of Maryland, College Park, MD 20742

well as the procedure to solve the cooling equations are given. Preliminary testing in the irrotational region of the flow shows that the spurious vorticity obtained from the probe due to system measurement error does not exceed 8 percent of the RMS vorticity fluctuation levels measured over the region $y^+ = 15 - 45$ in a turbulent boundary layer.

Nomenclature

A, B = King's law coefficients
C_{ijk}, C_i = probe geometry coefficient, and geometric array center, respectively
E_{ij} = hot-wire sensor Wheatstone bridge voltage
H = boundary layer shape factor $= \delta^*/\theta$
h = distance between sensors supporting prongs
K_{ijk} = calibration coefficients
l = hot-wire sensor length
n = King's law exponent
Re_x = Reynolds number based on the distance from the leading edge $= U_\infty x/\nu$
Re_θ = Reynolds number based on the momentum thickness $= U_\infty \theta/\nu$
U_∞ = wind tunnel free stream velocity
U, V, W = streamwise, normal and spanwise components of the instantaneous velocity vector, respectively
u_τ = friction velocity $= (\tau_w/\rho)^{1/2}$
x, y, z = streamwise, normal and spanwise directions, respectively
α = angle between the prongs direction and the wire normal
δ = boundary layer thickness
δ^* = boundary layer displacement thickness
η = Kolmogorov microscale
ν = fluid kinematic viscosity
ρ = fluid density
θ = boundary layer momentum thickness
Ω = ohms
τ_w = wall shear stress
ω_i = fluctuating component of vorticity
$\overline{(\ )}$ = time averaged quantity
$(\ )'$ = RMS value of fluctuating quantity

Subscripts

e = effective angle or velocity
i = array number or vector component index
j = wire number
k = calibration coefficient index

Superscript

$+$ = normalization with wall variables u_τ and ν

Introduction

The fundamental role that vorticity plays in turbulent flow dynamics has been emphasized in many theoretical and experimental investigations over the past fifteen years. Extensive efforts have been made to develop instruments capable of measuring this defining property of turbulence. In a recent paper, Wallace (1986) has reviewed the techniques available to date. Optical methods, laser-doppler velocimetry and hot-wire anemometry have achieved some success in attempts to determine vorticity field characteristics. The present note briefly describes the design, construction, calibration and operation of a nine-sensor hot-wire probe which measures both the velocity and vorticity vectors of turbulent flows. The performance of the probe in a turbulent boundary layer will also be mentioned.

Fig. 7 Square wing in periodic pitch from 0 to 30 deg, $f=2$Hz. $c=15$ cm, $U_0=61$ cm/s, $R=5100$, $\Delta t=1/32$ s. Remarks: $\alpha=30$ deg in frame 3, column 1; $\alpha=0$ deg in frame 5, column 2; the last 2 frames of column 3 are part of the next cycle.

5 Adler, J. N., and Luttges, M. W., "Three-Dimensionality in Unsteady Flow About a Wing," Paper AIAA 85-0132, 1985.

6 Werle', H., "Visualization Hydrodynamique D'E'coulements Instationaries," *ONERA Note Technique*, No. 180, 1971.

7 Werle', H., "Separation Structures on Cylindrical Wings," *Recherche Aerospatiale*, Vol. 53-74, 1986-3.

8 Freymuth, P., Finaish, F., and Bank, W., "The Wing Tip Vortex System in a Starting Flow," *Zeitschrift fuer Flugwiss. u. Weltraumforsch., (ZFW)*, Vol. 10, 1986, pp. 116-118.

9 Freymuth, P., Finaish, F., and Bank, W., "Visualization of Wing Tip Vortices in Accelerating and Steady Flow," *AIAA J. Aircraft*, Vol. 23, 1986, pp. 730-733. See also Paper AIAA-86-1096, 1986.

10 Freymuth, P., "Parametric Exploration of Unsteady Wing Tip Vortices," *Flow Visualization IV*, 1987, pp. 419-424.

11 Freymuth, P., "Further Visualization of Combined Wing Tip and Starting Vortex Systems," *AIAA J.*, Vol. 25, 1987, pp. 1153-1159.

12 Freymuth, P., "Visualization of the Connectivity of Vortex Systems for Pitching Wings," Paper AIAA-88-3549-CP, 1988.

A Multi-Sensor Hot-Wire Probe to Measure Vorticity and Velocity in Turbulent Flows

P. Vukoslavčević,[1,2] **J.-L. Balint,**[2] **and J. M. Wallace**[2]

The design and construction of a miniature hot-wire probe capable of simultaneously measuring all components of the velocity and vorticity vectors in turbulent flows are presented. A brief description of the probe resolution and calibration as

[1] On leave from the Veljko Vlahovic University, Titograd, Yugoslavia.

[2] Department of Mechanical Engineering, The University of Maryland, College Park, MD 20742

well as the procedure to solve the cooling equations are given. Preliminary testing in the irrotational region of the flow shows that the spurious vorticity obtained from the probe due to system measurement error does not exceed 8 percent of the RMS vorticity fluctuation levels measured over the region $y^+ = 15-45$ in a turbulent boundary layer.

Nomenclature

A, B	=	King's law coefficients
C_{ijk}, C_i	=	probe geometry coefficient, and geometric array center, respectively
E_{ij}	=	hot-wire sensor Wheatstone bridge voltage
H	=	boundary layer shape factor = δ^*/θ
h	=	distance between sensors supporting prongs
K_{ijk}	=	calibration coefficients
l	=	hot-wire sensor length
n	=	King's law exponent
Re_x	=	Reynolds number based on the distance from the leading edge = $U_\infty x/\nu$
Re_θ	=	Reynolds number based on the momentum thickness = $U_\infty \theta/\nu$
U_∞	=	wind tunnel free stream velocity
U, V, W	=	streamwise, normal and spanwise components of the instantaneous velocity vector, respectively
u_τ	=	friction velocity = $(\tau_w/\rho)^{1/2}$
x, y, z	=	streamwise, normal and spanwise directions, respectively
α	=	angle between the prongs direction and the wire normal
δ	=	boundary layer thickness
δ^*	=	boundary layer displacement thickness
η	=	Kolmogorov microscale
ν	=	fluid kinematic viscosity
ρ	=	fluid density
θ	=	boundary layer momentum thickness
Ω	=	ohms
τ_w	=	wall shear stress
ω_i	=	fluctuating component of vorticity
$\overline{(\ )}$	=	time averaged quantity
$(\ )'$	=	RMS value of fluctuating quantity

Subscripts

e	=	effective angle or velocity
i	=	array number or vector component index
j	=	wire number
k	=	calibration coefficient index

Superscript

$+$	=	normalization with wall variables u_τ and ν

Introduction

The fundamental role that vorticity plays in turbulent flow dynamics has been emphasized in many theoretical and experimental investigations over the past fifteen years. Extensive efforts have been made to develop instruments capable of measuring this defining property of turbulence. In a recent paper, Wallace (1986) has reviewed the techniques available to date. Optical methods, laser-doppler velocimetry and hot-wire anemometry have achieved some success in attempts to determine vorticity field characteristics. The present note briefly describes the design, construction, calibration and operation of a nine-sensor hot-wire probe which measures both the velocity and vorticity vectors of turbulent flows. The performance of the probe in a turbulent boundary layer will also be mentioned.
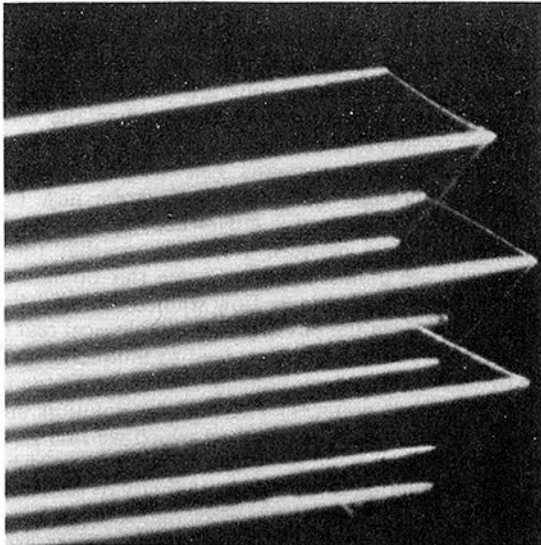
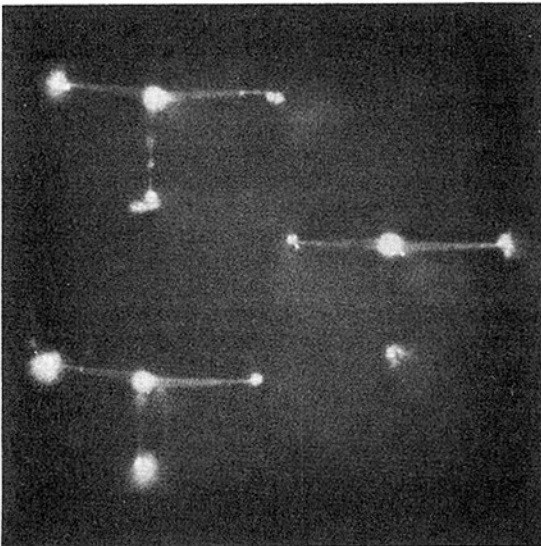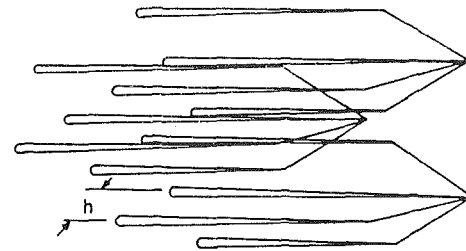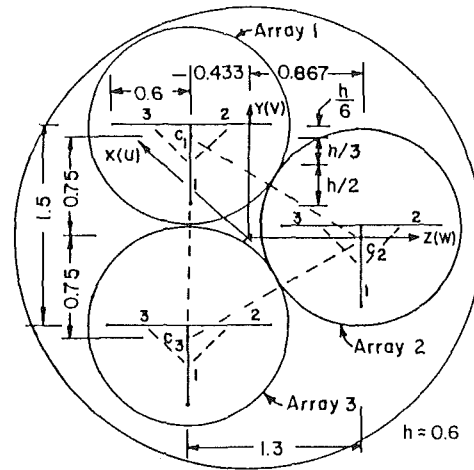Fig. 1(a) Side view photograph of the nine-sensor probe

Fig. 1(c) Schematic of the nine-sensor probe (side view)

All Dimensions in mm.

Fig. 1(d) Schematic of the nine-sensor probe (end view)

Fig. 1(b) End view photograph of the nine-sensor probe

Design and Construction of the Probe

The probe consists of three arrays of three hot-wire sensors oriented at 45 deg to the mean flow as seen in the side and end view photographs of Figs. 1(a) and 1(b) and in the schematic of the prongs and hot-wire arrangement of Figs. 1(c) and 1(d). The diameter of the probe sensing area is 2.5 mm with a distance between the array centers of 1.3–1.5 mm, and a distance between the supporting prongs of 0.6 mm. The diameter of the tungsten hot-wire sensors is 2.5 μm, and their length l is about 0.85 mm, giving a length to diameter ratio of 340.

In order to measure all three velocity components at each array location accurately, the arrays should have sensing areas smaller than the Kolmogorov microscale η. For the boundary layer in which this probe has been used ($R_\theta \approx 1250$–3000) and with the probe positioned at a distance $y^+ \approx 14$ from the wall, each array sensing diameter is about 1 to 3 Kolmogorov scales [Tennekes and Lumley (1972)]. The probe should also be able to adequately resolve the vorticity field in this flow. Several investigations by flow visualization and hot-wire anemometry have shown that the core diameters of vortices observed in the wall region are about 30 viscous lengths [Wallace (1982)]. The

probe sensing area diameter is about 7 to 20 viscous lengths in this Reynolds number range, which is adequate to resolve these wall layer vortices. Furthermore, the resolution of a Kovasznay-type vorticity meter has been investigated by Wyngaard (1969) who concludes that a reasonable value for η/l should not be smaller than 0.3 if one wants to resolve the vorticity field adequately. The nine-sensor probe nearly satisfies this criterion in the wall region of the boundary layer at $R_\theta \approx 2100$.

The nine-sensor probe design and construction was initiated by Wassman and Wallace (1979) and greatly improved over the past few years by Vukoslavčević, Balint, and Wallace [Balint et al. (1984), Balint (1986)]. The method of probe fabrication is a tedious task because of its small size, complex design, and fragility. The main problem is to fit twelve supporting prongs in the smallest feasible space and still satisfy the resolution criteria described above. Also, arrangement of the prongs with very small distances between them raised two difficult problems: first to avoid electrical shorts between the prongs or between the prongs and the probe body, and second to maintain them in place so that they keep the desired array geometry. Several technical solutions and various prong materials have been tried. The latest version of the probe uses nickel plated tungsten wires of about 255 μm as supporting prongs which are tapered to about 75 μm at their tips.

Probe Operation

Each wire is operated separately, except for the common ground connection of each array, by constant temperature anemometer bridge circuits. Two difficulties arose when this was first attempted. First it was discovered that resistances of the common ground prong of each array greater than about 0.3Ω caused a feedback instability in the circuits when they were operated simultaneously. Additionally, electrical crosstalk between the circuits resulted from this common

resistance. The stability problem has been overcome by nickel plating the tungsten wire prongs to reduce their resistance to about 0.1Ω or less which also substantially reduces the cross-talk. The problem of self and mutual inductance was also investigated and was found to be negligible for our range of frequencies. If the effect of the common ground resistance is not considered, the overheat resistance ratio is conventionally defined. When the common ground resistance is taken into account, however, the overheat ratio depends on the number of sensors operated, and an expression for the actual ratio has been derived. When operated at an overheat ratio of about 1.2, there is no detectable thermal interference between the arrays over the operating speed range. In addition, a correction is applied to each sensor voltage in order to account for ambient temperature variation during the experiment. For small temperature ranges ($2°C$ to $3°C$), it is found that a linear voltage correction is satisfactory.

Equations (1) are the nonlinear algebraic forms taken by the three expressions for the squares of the effective cooling velocities acting at the centers of the vertical sensors of each array in terms of the three velocity components at the centroid of the arrays, expanded in a Taylor series to first order. The array number is indicated by the subscript i and the sensor number by the subscript j ($j=1$ for a vertical wire).

$$U_{e_{ij}}^2 = \left[K_{ij1}\left(U_0 + C_{ij1}\frac{\partial U}{\partial z} + C_{ij2}\frac{\partial U}{\partial y}\right)\right.$$
$$\left. + K_{ij2}\left(V_0 + C_{ij3}\frac{\partial V}{\partial z} + C_{ij4}\frac{\partial V}{\partial y}\right)\right]^2$$
$$+ \left[K_{ij3}\left(W_0 + C_{ij5}\frac{\partial W}{\partial z} + C_{ij6}\frac{\partial W}{\partial y}\right)\right]^2 \quad (1)$$

Similarly, the cooling equations for horizontal wires ($j=2,3$) are obtained by permuting V and W in equations (1). The $K_{ijk}s$ are calibration coefficients and the $C_{ijk}s$ are constant coefficients for a given array geometry which are positive or negative fractions of h (see Fig. 1 (d)). U_0, V_0, and W_0 are the unknown velocity components at the centroid of the probe, $\partial U/\partial y$, $\partial U/\partial z$, $\partial V/\partial y$, $\partial V/\partial z$, $\partial W/\partial y$, and $\partial W/\partial z$ are the velocity gradients in the plane normal to the axis of the probe, and h is the average of the projected sensor lengths on this plane. The effective cooling velocities, U_{eij}, are related to the measured bridge voltages through calibration relations of the King's law form:

$$E_{ij}^2 = A_{ij} + B_{ij}U_{eij}^n \quad (2)$$

where the $E_{ij}s$ are the measured voltages, the $A_{ij}s$ and $B_{ij}s$ are additional calibration coefficients and the ns are calibration exponents which are normally taken as 0.5 but can be ex-

shown that when a second real root occurs, it will be outside the domain of physical flow possibilities (the range of possible ratios $K_v = V/U$ and $K_W = W/U$) if the geometry and operating conditions of the probe are near optimum conditions. These optimum conditions occur when the effective angles of the sensors to the mean flow are 45 deg and when the coefficients K_{ij3} of equations (1), which account for aerodynamic blockage, are unity. The probe now in use, shown in Fig. 1, has effective angles between $44° - 46°$ and blockage coefficients between 1.16-1.26 so that the nonphysical roots are almost always outside this domain of K_v and K_W for the boundary layer flow studied to date, allowing us to choose between the physical and nonphysical real roots. The equations can therefore be solved to uniquely determine the set of three velocity components at each array for nearly all digitized sets of voltages. The iterative solution method used is the Newton-Raphson method which we find typically to converge in three iterations. The velocity components at each array, accounting for the nonuniformity of the flow over the probe to first order, as well as the velocity gradients $\partial U/\partial y$, $\partial U/\partial z$, $\partial V/\partial y$, $\partial V/\partial z$, $\partial W/\partial y$, and $\partial W/\partial z$ are thus determined. The streamwise gradients $\partial U/\partial x$, $\partial V/\partial x$, and $\partial W/\partial x$ are then determined as indicated above.

Calibration and Testing of the Probe

The probe is placed in the irrotational core of the wind tunnel and the calibration is carried out in two steps. First, the probe is aligned with the flow axis, and the free stream velocity U_∞ is varied over a speed range corresponding to the experimental conditions to be investigated (rpm calibration). U_∞ is then set to the typical value encountered in the flow region of interest and the probe is successively pitched and yawed in the ± 20 deg range, by increments of 5 deg. Each hot-wire sensor voltage response E_{ij} is related to the effective cooling velocity U_{eij} by King's law, as expressed in equation (2), and the velocity gradients over the probe are equal to zero. During the rpm calibration, the effective velocity U_{eij} can be expressed as $U_{eij} = U_\infty \cos\alpha_{eij}$ where α_{eij} is the effective angle of sensor ij. A least square fit of E^2_{ij} versus U^n_∞ determines the values of quantities A_{ij} and B_{ij} $(\cos\alpha_{eij})^n$. Additional information about the $B_{ij}s$ and $K_{ijk}s$ is obtained from the pitch/yaw calibration.

Probe Performance in a Turbulent Boundary Layer

Measurements have been taken in a nominally zero pressure gradient turbulent boundary layer within the buffer layer, the logarithmic region and the velocity defect region. The characteristics of this boundary layer investigated are summarized in the following table:

U_∞(m/s)	δ(m)	θ(m)	Re_θ	δ^*(m)	H	Re_x	$u_\tau/U\infty$
2.39	0.1397	0.0136	2100	0.0175	1.28	1.3×10^6	0.042

perimentally determined. A solution of this set of nine equations [equations (1)] yields these nine unknowns. One of the three streamwise gradients, $\partial U/\partial x$, can be obtained directly from the continuity equation and the other two, $\partial V/\partial x$ and $\partial W/\partial x$, must be obtained using Taylor's hypothesis, $\partial/\partial x = -(1/\bar{U})(\partial/\partial t)$, in the flow region where it is found to be a good approximation. The adequacy of this approximation is assessed directly with the probe since the value of $\partial U/\partial x$ from continuity can be compared to $(-1/\bar{U})(\partial U/\partial t)$.

The iterative solution procedure involves combining the equations to eliminate U_i and W_i yielding a second order function of the form $f(V_i)=0$ when the equations are redefined in terms of the velocity components at the centroids of each array. Imaginary roots are ignored, but there still remains the problem of choosing between the two possible real roots of $f(V_i)$. A thorough study of the nature of the equation has

The mean steamwise velocity profile measurements shown in Fig. 2 exhibit the logarithmic and wake region characteristics very well. The average deviations from the law of the wall are 1.4 percent in the logarithmic region and 2.5 percent in the wake region. Moreover, the statistics of all three components of the velocity vector have been determined and compared to wall region boundary layer data as well as channel flow data previously reported in the literature. The rms, Reynolds stress and skewness and flatness distributions of the velocity fluctuations can be found in Balint et al. (1987); they indicate that the velocity field measurements obtained by the nine-sensor probe are very satisfactory. Another indication of the probe performance are the *directly* measured mean velocity gradients normalized with wall variables v and u_τ presented in Figs. 3 and 4. Because of flow symmetry, all of them but $\partial\bar{U}/\partial y$ should be equal to zero. Instead, rather constant
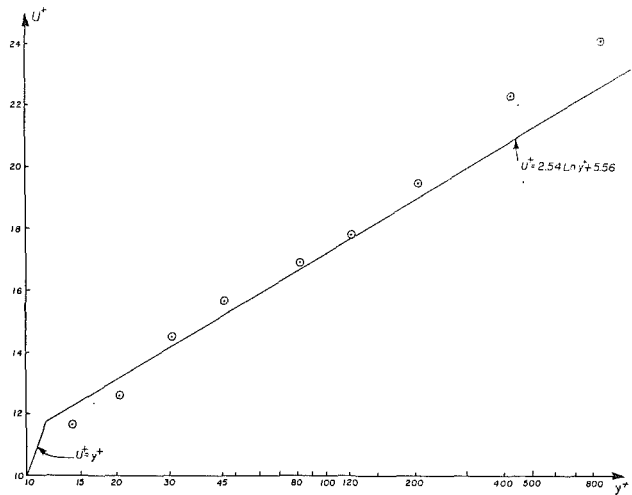
Fig. 2 Mean streamwise velocity normalized by the friction velocity u_τ and the kinematic viscosity ν

Fig. 3 Normal gradient of mean streamwise velocity, normalized by wall variables ν and u_τ $(\partial/\partial x_i)^+ = (\partial/\partial x_i)(\nu/u_\tau^2)$

Fig. 4 Mean velocity gradients (same normalization as in Fig. 3)

residual values are observed throughout the boundary layer and they provide information on the accuracy of this type of measurements. It should be pointed out that the streamwise gradients $\partial U/\partial y$ are very difficult to measure directly (by differencing instantaneous velocities over a few Kolmogorov lengths) because they decrease very rapidly for measurement locations beyond the viscous sublayer ($y^+ \approx 5$). Nevertheless, the agreement between the measured values and a fit of velocity data given by Spalding (1961) is quite good.

The rms, skewness and flatness distributions of all three vorticity fluctuation components, $\omega_i{}'$, are given in Balint et al. (1987). They are compared there to the streamwise component measurements of Kastrinakis and Eckelmann (1983) and the large-eddy simulation calculations of all three components by Moin and Kim (1982). Our data agree reasonably well with the 1983 experimental measurements, but only show the same trends as the 1982 simulations, being over twice the magnitude throughout the range $20 \leq y^+ \leq 400$. The vorticity skewness factors are almost zero for the streamwise and normal directions, as expected from flow symmetry. However, the spanwise skewness factor of vorticity retains a negative value throughout the extent of the boundary layer which may be related to spanwise vortex stretching activity.

Error Estimates

The free stream velocity in the tunnel was measured with a Pitot tube connected to an electronic manometer. The pressure was determined with an accuracy of 10^{-4} Torr (10^{-4} mm Hg) thus giving an accuracy of 1 percent on U_∞ in the 0.8–2.8 m/s speed range. The accuracy on the velocity and vorticity fluctuation measurements were estimated by applying the Newton-Raphson algorithm to the rpm and pitch/yaw calibration data. During the rpm calibration the average error of the streamwise component U in the 0.8–2.8 m/s speed range was 2.2 percent; the residual V and W components measured by the probe in the same speed range averaged an absolute value of 0.025 m/s. For the pitch/yaw calibration (which was conducted at 1.38 m/s only) the average errors of components U, V, W were 1.5, 8.4, and 4 percent, respectively, in the ±15 deg range. For the ±10 deg angle of attack range, the relative errors on V and W are within 4 percent of the induced values. The average spurious vorticity components measured in the irrotational potential core during calibration were 6.3 s^{-1}, 4.8 s^{-1}, 7.3 s^{-1}, respectively. These values correspond to 7.2, 6.1, 7.6 percent of the rms vorticity fluctuations ω'_1, ω'_2, ω'_3 measured over the $y^+ = 15$–45 region of the turbulent boundary layer.
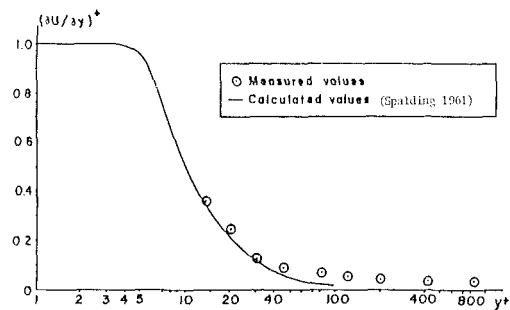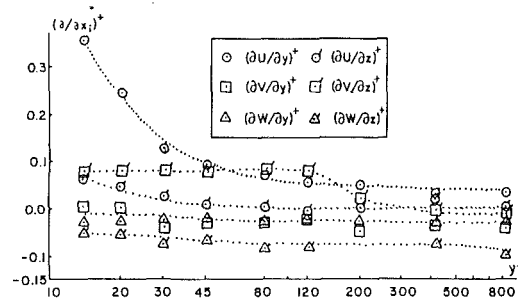
The use of Taylor's hypothesis to obtain streamwise gradients from the signal time derivative has been a common practice. Its application for isotropic turbulence is considered valid, but its use for turbulent shear flows has been questioned. The "classical" formulation of Taylor's hypothesis assumes "frozen" turbulence being convected with the local mean velocity $\bar{U}$ past the probe. However, in turbulent shear flows, where the fluctuations in the streamwise direction can be large, it seems more reasonable to choose a convection velocity accounting for the local fluctuations u; thus a short time averaged convection velocity U_c is preferred. It is of interest to compare the streamwise gradient values $\partial U/\partial x$ obtained by the Taylor's hypothesis and these values obtained from the continuity equation. The correlation coefficient between these quantities is a good indicator of their phase agreement. Such analysis takes, of course, the continuity equation value as the "true" reference value and Taylor's hypothesis value as the "tested" value. Unfortunately, both quantities are measured experimentally and therefore have uncertainties. The measured correlation coefficient, however, has the remarkably constant value of about 0.36 in the region $30 \leq y^+ \leq 120$ of the boundary layer. A better way to confirm that the use of Taylor's hypothesis gives an adequate estimation of $\partial U/\partial x$ is perhaps to compare it to $\partial U/\partial x$ obtained independently by a nonintrusive streamwise gradient probe or from direct numerical simulations. In any case, the measurements described above indicate that the rms magnitude of gradients $\partial/\partial x$ are much smaller than the gradients $\partial/\partial y$ or $\partial/\partial z$, suggesting that the contributions of the former to the vorticity components is significantly less important than the contributions of the gradients in the y or z directions.

Conclusions

This preliminary note reports a unique nine-sensor hot-wire probe capable of measuring all three components of velocity and all velocity gradients in bounded turbulent shear flows. The probe provides enough information to obtain vorticity and strainrate information. The satisfactory results obtained for the velocity field statistics and the directly measured mean

velocity gradients are good indicators of the proper operation of the probe and its adequacy to measure vorticity. Further investigation is being carried out in order to improve the technical imperfections of the probe and the accuracy of the measurements. Although the probe has been used so far in a turbulent boundary layer, it can be utilized in most standard, low-speed air flow facilities such as jets, wakes and mixing layers.

Acknowledgment

References

Balint, J.-L., Vukoslavčević, P., and Wallace, J. M., 1984, "Some Statistical Properties of the Vorticity Field of a Turbulent Boundary Layer," *Bulletin of the American Physical Society*, Vol. 29, p. 1535.

Balint, J.-L., 1986, "Contribution à l' étude de la structure tourbillionnaire d' une couche limite turbulente au moyen d'une sonde à neuf fils chauds mesurant le rotationnel," Thèse de Docteur d'Etat ès Sciences, Université de Lyon, France.

Balint, J.-L., Vukoslavčević, P., and Wallace, J. M., 1987, "A Study of the Vortical Structure of the Turbulent Boundary Layer," *Advances in Turbulence*, ed. G. Comte-Bellot and J. Mathieu, Springer-Verlag, p. 456.

Kastrinakis, E. G., and Eckelmann, H., 1983, "Measurement of Streamwise Vorticity in a Turbulent Channel Flow," *Journal of Fluid Mechanics*, Vol. 137, p. 165.

Moin, P., and Kim J., 1982, "Numerical Investigation of Turbulent Channel Flow," *Journal of Fluid Mechanics*, Vol. 118, p. 341.

Spalding, D. B., 1961, "A Single Formula for the Law of the Wall," *Journal of Applied Mechanics*, Vol. 28, p. 455.

Tennekes, H., and Lumley, J. L., 1972, *A First Course in Turbulence*, MIT Press, p. 159.

Wallace, J. M., 1982, "On the Structure of Bounded Turbulent Shear Flow: A Personal View," *Developments in Theoretical and Applied Mechanics*, Univ. of Alabama at Huntsville, Vol. 11, p. 509.

Wallace, J. M., 1986, "The Measurement of Vorticity in Turbulent Flows," *Experiments in Fluids*, Vol. 4, p. 61.

Wassmann, W. W., and Wallace, J. M., 1979, "Measurement of Vorticity in Turbulent Shear Flow," *Bulletin of the American Physical Society*, Vol. 24, p. 1401.

Wyngaard, J. C., 1969, "Spatial Resolution of the Vorticity Meter and Other Hot-Wire Arrays," *Journal of Scientific Instruments*, Vol. 2, p. 983.

A Useful Approximation to the Error Function: Applications to Mass, Momentum, and Energy Transport in Shear Layers

P. R. Greene[1]

Specific mass, momentum, and energy flux transport integrals are given by the sequence $I_1 = \int erfc(x)dx$, $I_2 = \int erfc^2(x)dx$, and $I_3 = \int erfc^3(x)dx$ for the error function velocity distribution typical of some laminar and turbulent shear layers. In this report, the Gaussian function $A \exp(-b(x-x_0)^2)$ is used to approximate the error function within 0.21 percent, allowing a direct approximate closed-form evaluation of these transport flux integrals. Mass, momentum, and energy flux are accurate to within 0.22, 0.15, and 0.11 percent, respectively, over the entire shear layer. To achieve this same degree of accuracy with a Taylor series requires in excess of 10 terms. Each of the sequence of approximate functions can be inverted to yield the inverse function, i.e., $erfc^{-1}(x)$, etc., also in closed-form. The results presented here are also applicable to the error

function as it appears in heat transfer and probability and statistics type problems. A coefficient table is included to allow evaluation of the error function and its various integrals.

Introduction

The error function is a defined function; defined, within a constant, as the integral of the Gaussian distribution. It arises as the solution to a wide variety of problems in fluid mechanics, heat transfer, statistical mechanics, laminar and turbulent shear layers, probability and statistics, etc. It would be nice, therefore, to have a closed-form result for this integral, but unfortunately, this seems impossible. This problem is well recognized, and there exist a large number of approximations to the error function (reference [12]), some of which are closed-form, and others are series-like, with various leading terms.

For our application, i.e., mass, momentum, and energy flux is shear layers, we propose here another approximation, considerably more tractable than the others, although somewhat less accurate. The error function is piecewise approximated[2] as a displaced Gaussian, and this results in considerable mathematical simplifications when integrating various powers of the error function itself. The surprise is that, although the basic approximation is only good to slide rule accuracy, the accuracy improves when the approximate error function is raised to various powers and integrated. Another interesting result is that all of the various powers and integrals of the powers of the approximate error function are also Gaussian, and thus easily differentiable. This may prove useful, from a control-volume approach, in the differential equations governing the time and space development of laminar and turbulent shear layers.

Results

The sequence of functions $erfc(x)$, $\int erfc(x) \, dx$, $\int erfc^2(x)$ dx, and $\int erfc^3(x) \, dx$ correspond to the velocity, mass flux, momentum flux, and kinetic energy flux in a shear layer with an error function velocity profile [1, 3, 4, 6]. One can evaluate the error function and its first 4 derivatives from tables (Selby, 1971).[3] Also tabulated are the complementary error function $erfc(x)$ and its first 4 integrals (Abramowitz and Stegun, 1965). Tables of this type are accurate to 4 or more significant figures. However, for many applications, an approximate answer is more useful. Integrals of powers of the complementary error function, i.e., $\int erfc^n(x) \, dx$ are not tabulated.

Since it is relatively easy to differentiate, one way of estimating the error function is to use a Taylor series. Also, since the function $e^{x^2} erf(x)$ can be differentiated, we can arrive at a Taylor-like series with leading factor e^{-x^2} (Abramowitz and Stegun, 1965). This converges much more rapidly than the standard Taylor series. However, for the purposes of integration of powers of the approximate error function, these series present a problem. From the hint provided by the e^{-x^2} leading term, it seems reasonable to approximate $erfc(x)$ with the function $A \exp(-b(x-x_0)^2)$, i.e., a displaced Gaussian. This is a 3-parameter closed-form function, with A, the amplitude, b, the width factor, and x_0, the

[1] B. G. K. T. Consulting, Ltd., Huntington, NY 11743.

[2] Piecewise, in the sense that one displaced Gaussian is used for the positive x-axis, and a symmetric one is used for the negative x-axis.

[3] We use here the notation $Erf(x)$ to denote the "mathematical" error function, as per Selby (1971), and the notation $erf(x)$ to denote the "engineering" error function, as per Schlichting (1968). These are related by a simple transformation.

velocity gradients are good indicators of the proper operation of the probe and its adequacy to measure vorticity. Further investigation is being carried out in order to improve the technical imperfections of the probe and the accuracy of the measurements. Although the probe has been used so far in a turbulent boundary layer, it can be utilized in most standard, low-speed air flow facilities such as jets, wakes and mixing layers.

Acknowledgment

References

Balint, J.-L., Vukoslavčević, P., and Wallace, J. M., 1984, "Some Statistical Properties of the Vorticity Field of a Turbulent Boundary Layer," *Bulletin of the American Physical Society*, Vol. 29, p. 1535.

Balint, J.-L., 1986, "Contribution à l' étude de la structure tourbillionnaire d' une couche limite turbulente au moyen d'une sonde à neuf fils chauds mesurant le rotationnel," Thèse de Docteur d'Etat ès Sciences, Université de Lyon, France.

Balint, J.-L., Vukoslavčević, P., and Wallace, J. M., 1987, "A Study of the Vortical Structure of the Turbulent Boundary Layer," *Advances in Turbulence*, ed. G. Comte-Bellot and J. Mathieu, Springer-Verlag, p. 456.

Kastrinakis, E. G., and Eckelmann, H., 1983, "Measurement of Streamwise Vorticity in a Turbulent Channel Flow," *Journal of Fluid Mechanics*, Vol. 137, p. 165.

Moin, P., and Kim J., 1982, "Numerical Investigation of Turbulent Channel Flow," *Journal of Fluid Mechanics*, Vol. 118, p. 341.

Spalding, D. B., 1961, "A Single Formula for the Law of the Wall," *Journal of Applied Mechanics*, Vol. 28, p. 455.

Tennekes, H., and Lumley, J. L., 1972, *A First Course in Turbulence*, MIT Press, p. 159.

Wallace, J. M., 1982, "On the Structure of Bounded Turbulent Shear Flow: A Personal View," *Developments in Theoretical and Applied Mechanics*, Univ. of Alabama at Huntsville, Vol. 11, p. 509.

Wallace, J. M., 1986, "The Measurement of Vorticity in Turbulent Flows," *Experiments in Fluids*, Vol. 4, p. 61.

Wassmann, W. W., and Wallace, J. M., 1979, "Measurement of Vorticity in Turbulent Shear Flow," *Bulletin of the American Physical Society*, Vol. 24, p. 1401.

Wyngaard, J. C., 1969, "Spatial Resolution of the Vorticity Meter and Other Hot-Wire Arrays," *Journal of Scientific Instruments*, Vol. 2, p. 983.

A Useful Approximation to the Error Function: Applications to Mass, Momentum, and Energy Transport in Shear Layers

P. R. Greene[1]

Specific mass, momentum, and energy flux transport integrals are given by the sequence $I_1 = \int erfc(x)dx$, $I_2 = \int erfc^2(x)dx$, and $I_3 = \int erfc^3(x)dx$ for the error function velocity distribution typical of some laminar and turbulent shear layers. In this report, the Gaussian function $A \exp(-b(x-x_0)^2)$ is used to approximate the error function within 0.21 percent, allowing a direct approximate closed-form evaluation of these transport flux integrals. Mass, momentum, and energy flux are accurate to within 0.22, 0.15, and 0.11 percent, respectively, over the entire shear layer. To achieve this same degree of accuracy with a Taylor series requires in excess of 10 terms. Each of the sequence of approximate functions can be inverted to yield the inverse function, i.e., $erfc^{-1}(x)$, etc., also in closed-form. The results presented here are also applicable to the error

function as it appears in heat transfer and probability and statistics type problems. A coefficient table is included to allow evaluation of the error function and its various integrals.

Introduction

The error function is a defined function; defined, within a constant, as the integral of the Gaussian distribution. It arises as the solution to a wide variety of problems in fluid mechanics, heat transfer, statistical mechanics, laminar and turbulent shear layers, probability and statistics, etc. It would be nice, therefore, to have a closed-form result for this integral, but unfortunately, this seems impossible. This problem is well recognized, and there exist a large number of approximations to the error function (reference [12]), some of which are closed-form, and others are series-like, with various leading terms.

For our application, i.e., mass, momentum, and energy flux is shear layers, we propose here another approximation, considerably more tractable than the others, although somewhat less accurate. The error function is piecewise approximated[2] as a displaced Gaussian, and this results in considerable mathematical simplifications when integrating various powers of the error function itself. The surprise is that, although the basic approximation is only good to slide rule accuracy, the accuracy improves when the approximate error function is raised to various powers and integrated. Another interesting result is that all of the various powers and integrals of the powers of the approximate error function are also Gaussian, and thus easily differentiable. This may prove useful, from a control-volume approach, in the differential equations governing the time and space development of laminar and turbulent shear layers.

Results

The sequence of functions $erfc(x)$, $\int erfc(x) \, dx$, $\int erfc^2(x) \, dx$, and $\int erfc^3(x) \, dx$ correspond to the velocity, mass flux, momentum flux, and kinetic energy flux in a shear layer with an error function velocity profile [1, 3, 4, 6]. One can evaluate the error function and its first 4 derivatives from tables (Selby, 1971).[3] Also tabulated are the complementary error function $erfc(x)$ and its first 4 integrals (Abramowitz and Stegun, 1965). Tables of this type are accurate to 4 or more significant figures. However, for many applications, an approximate answer is more useful. Integrals of powers of the complementary error function, i.e., $\int erfc^n(x) \, dx$ are not tabulated.

Since it is relatively easy to differentiate, one way of estimating the error function is to use a Taylor series. Also, since the function $e^{x^2} erf(x)$ can be differentiated, we can arrive at a Taylor-like series with leading factor e^{-x^2} (Abramowitz and Stegun, 1965). This converges much more rapidly than the standard Taylor series. However, for the purposes of integration of powers of the approximate error function, these series present a problem. From the hint provided by the e^{-x^2} leading term, it seems reasonable to approximate $erfc(x)$ with the function $A \exp(-b(x-x_0)^2)$, i.e., a displaced Gaussian. This is a 3-parameter closed-form function, with A, the amplitude, b, the width factor, and x_0, the

---

[1] B. G. K. T. Consulting, Ltd., Huntington, NY 11743.

[2] Piecewise, in the sense that one displaced Gaussian is used for the positive x-axis, and a symmetric one is used for the negative x-axis.

[3] We use here the notation $Erf(x)$ to denote the "mathematical" error function, as per Selby (1971), and the notation $erf(x)$ to denote the "engineering" error function, as per Schlichting (1968). These are related by a simple transformation.

Table 1 Coefficients for the Gaussian approximation to the error function and its integrals

Standard "engineering" definition of the error function: $(\operatorname{erfc}(x)=1-\operatorname{erf}(x)=I_0(x))$	$I(x)=\operatorname{erf}(x)=\dfrac{2}{\pi^{1/2}}\displaystyle\int_0^x e^{-t^2}\,dt$
Definition of the shear layer transport integrals: $(n>0)$	$I_n(x)=\displaystyle\int_x^\infty \operatorname{erfc}^n(t)\,dt$
The 3-parameter "Displaced Gaussian" approximation to the $\operatorname{erfc}(x)$ and the transport integrals: (n = 0,1, 2, 3)	$I_n(x)=A_n\exp(-b_n(x+x_n)^2)$

$n=$	Applications:	A_n Gaussian Amplitude	b_n Gaussian Width	x_n Gaussian Centerline	x_c Critical Match Point	Max. abs. error
0	Heat transfer, velocity distr., etc.	1.5577	0.7182	0.7856	0.955	0.42%
1	Mass flux	1.9276	0.6392	1.3864	0.9	0.22%
2	Momentum flux	2.0096	1.2680	1.1932	0.6	0.15%
3	Energy flux	2.6117	1.8560	1.1372	0.3	0.11%

Note: This approximation is only valid for $x>0$. For the case $n=0$, we can easily extend the approximation to $x<0$ by symmetry considerations. The critical match point x_c is adjustable, as per the equations in the Appendix, depending on the type of error estimator we wish to minimize.

centerline, being adjustable. The constants A, b, and x_0 are specified by matching the function and its first derivative at $x=0$, and by matching the function at a critical match point $x=x_c$. In Table 1, as explained in the Appendix, the match point $x_c=0.955$ is selected to minimize the absolute error between the approximate and the exact $\operatorname{erfc}(x)$, (equation 11).

It is not immediately obvious, but our approximation $A\,e^{-b(x-x_0)^2}$ can be raised to any power and integrated, yielding another error function. We can then reapproximate this new error function with another translated Gaussian of the form $A_1\,e^{-b_1(x-x_1)^2}$. Since two sequential approximations have been made, errors will accumulate. Nevertheless, the mass, momentum, and energy flux integrals are accurate to within 2 percent using this technique of sequential approximations. This degree of accuracy is quite acceptable, because experimentally, for some applications, it is difficult to demonstrate conservation of momentum within 5 percent (Greene and Hill, 1975).

This calculation suggests that it is reasonable to directly approximate the transport integrals with a displaced Gaussian, and this has been done in Table 1 with much greater accuracy than using the sequential approximations. As before, the function and its first derivative are matched at $x=0$, and the function itself is matched at $x=x_c$ (see the Appendix for general equations). This technique improves the accuracy by a factor of 10 to 20 for the transport integrals, yielding a maximum absolute error of 0.22 percent for mass flux, 0.15 percent for momentum flux, and 0.11 percent for energy flux, i.e., slide rule accuracy or better. Thus we can say "the integral of the Gaussian is approximately Gaussian" and "the integrals of integral powers of the error function are approximately Gaussian."

Discussion

A priori, just as is the case with guessing the solution to differential equations, we would have no reason to suspect that the Gaussian can so closely approximate the sequence of 4 functions—$\operatorname{erfc}(x)$, $I_1(x)$, $I_2(x)$, and $I_3(x)$. This technique is really only justified because the errors incurred are acceptable for most applications.

For flows with a Gaussian velocity profile (references [1, 5, 8, and 9]), the mass, momentum, and energy flux integrands are also Gaussian, because $\phi^p(x_1, b_1)=\phi(x_1, b_2)$. So, for $n=1$, the results in Table 1 apply to all three of the transport flux integrals. So, we can estimate the mass, momentum, and energy flux for Gaussian jets, wakes, and shear layers within
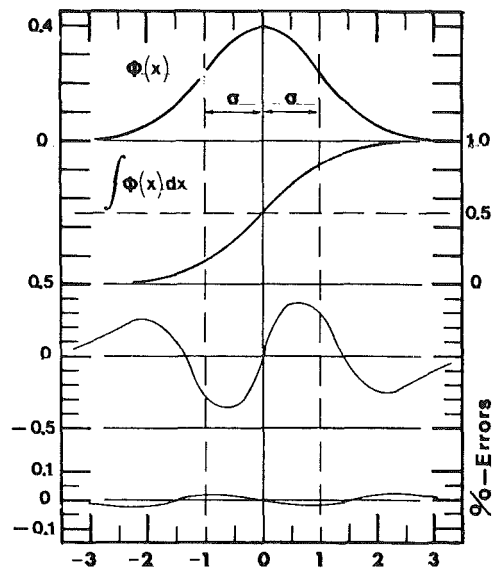

Fig. 1 Standard normal distribution with zero mean and standard deviation S. D. = 1 is graphed together with its integral function Erf(x). The third panel shows the absolute error between the three parameter approximation used in the text and the exact Erf(x). Note that the error fluctuations are limited to ± 0.4 percent over the entire range of the function. Normalizing instead of the full range of the Erf(x), i.e., 1.0, then the error fluctuations are limited to ± 0.2 percent, which is almost slide rule accuracy. The fourth panel represens a four parameter approximation to the Erf(x), not discussed here, where the exponent can vary. Under these conditions, the error fluctuations are limited to ± 0.025 percent, almost an order of magnitude more accurate than the three parameter approximate. For display purposes, we use here the standard "mathematical" definition Erf(x), whereas Table 1 uses the standard "engineering" definition erf(x).

0.42 percent relative to the centerline value, or within 0.21 percent over the entire flow.

For the more general case, integrating powers of the $\operatorname{erfc}(x)$, the net flux of mass, momentum, or energy in a layer from $x=a$ to $x=b$ is given by:

$$\phi_a^b=\int_a^b=\int_a^\infty-\int_b^\infty=I_n(a)-I_n(b)$$

$$(n=1, 2, 3)$$

An exact numerical evaluation of this expression requires an integration at each step, first to evaluate $\operatorname{erfc}(x)$, followed by

the integration over the layer. The work required is equivalent to evaluating a double integral. Thus, the closed-form approximate results in Table 1 can represent a saving of effort by 2 orders of magnitude (for $N = 10$, a typical minimum number of integration steps). This is at the expense of a loss of accuracy on the order of 0.15 percent for momentum, well within experimental limits.

Lastly, this approximation has the advantage that it can be inverted to yield the inverse function in closed form:

$$x(E) = x_0 + \sqrt{(1/b) \ln (A/E)}$$

where E represents any of $\mathrm{erfc}(x)$, $\int \mathrm{erfc}''(x) \, dx$.

These approximations may be useful for momentum integral theoretical techniques in shear layers with an assumed Gaussian or error function velocity profile.

Acknowledgments

APPENDIX I
Equations for the Coefficients

The coefficients b_n, x_n, and A_n for Table 1 are derived as follows. The function and slope at $x = 0$ are given by:

$$I_n(x = 0) = A_n e^{-b_n x_n^2} = K \tag{1}$$

$$dI_n/dx \Big|_{x=0} = K(-2 b_n x_n) = -S \tag{2}$$

At $x = x_c$, the function is:

$$I_n(x = x_c) = A_n e^{-b_n(x_c + x_n)^2} = C \tag{3}$$

Equation (2) can be solved for the product $b_n x_n$:

$$(b_n x_n) = (S/2K) \tag{4}$$

Multiplying out the quadratic term in equation (3) and substituting from equation (1) yields:

$$\ln(K/c) = b_n x_c (x_c + 2x_n) \tag{5}$$

From equation (4):

$$2x_n = (S/b_n K) \tag{6}$$

$$\ln(K/C) = b_n x_c^2 + (x_c S/K) \tag{7}$$

Thus, from equations (7), (4), and (1), we solve for the coefficients:

$$b_n = \frac{1}{x_c^2} [\ln(K/C) - (x_c S/K)] \tag{8}$$

$$x_n = (S/2b_n K) \tag{9}$$

$$A_n = K \exp(b_n x_n^2) \tag{10}$$

Equations (8), (9), and (10) must be solved sequentially, first substituting b_n from (8) in (9), and then b_n and x_n from (8) and (9) in (10).

For the solution presented in equations (8), (9), and (10), the value of x_c is determined by minimizing an error estimator e_i over the interval in question. Possible error estimators include:

$$e_1 = \Sigma |I - I_{\mathrm{exact}}| / I_{\mathrm{max}} \tag{11}$$

$$e_2 = \Sigma |I - I_{\mathrm{exact}}| / I_{\mathrm{exact}} \tag{12}$$

$$e_3 = \Sigma (I - I_{\mathrm{exact}})^2 / I_{\mathrm{max}} \tag{13}$$

$$e_4 = \Sigma (I - I_{\mathrm{exact}})^2 / I_{\mathrm{exact}} \tag{14}$$

The defined quantities e_1 and e_3 represent absolute error estimators, because they are relative to I_{max} over the interval,

whereas e_2 and e_4 are relative error estimators. e_1 and e_2 are linear absolute value error estimators; e_3 and e_4 are quadratic.

References

1 Abramovich, G. N., *The Theory of Turbulent Jets*, M.I.T. Press, Cambridge, Mass., 1963.

2 Abramowitz, M., and Stegun, I. A., *Handbook of Mathematical Functions*, Dover Publications, Inc., New York, 1965.

3 Batchelor, G. K., *An Introduction to Fluid Dynamics*, Cambridge Univ. Press, Cambridge, England, 1970.

4 Bird, R. B., Stewart, W. E., and Lightfoot, E. N., *Transport Phenomenon*, John Wiley & Sons, New York, 1960.

5 Bremhorst, K., "Unsteady Subsonic Turbulent Jets," *Recent Developments in Theoretical and Experimental Fluid Mechanics, Compressible and Incompressible Flows*, eds. Müller, U., Roesner, K. G., and Schmidt, B., Springer-Verlag, New York, 1979.

6 Greene, P. R., and Hill, W. G., Jr., "An Analytical Investigation of Experimental Problems Associated with Conservation of Momentum in a Jet Plume," Research Note #RN-363, Grumman Aerospace Corp., Bethpage, New York, 1975, 18 pp. Available on request from authors.

7 Guttman, I., and Wilks, S. S., *Introductory Engineering Statistics*, Wiley, New York, 1965.

8 Hill, W. G., Jr., and Greene, P. R., "Increased Turbulent Jet Mixing Rates Obtained by Self-Excited Acoustic Oscillations," ASME JOURNAL OF FLUIDS ENGINEERING, Vol. 99, No. 3, 1978, pp. 520–528.

9 Ramaprian, B. R., and Chandrasekhara, M. S., "Laser Doppler Anemometry Measurements in Plane Turbulent Jets," ASME JOURNAL OF FLUIDS ENGINEERING, Vol. 107, 1985, pp. 264–271.

10 Schlichting, H., *Boundary-Layer Theory*, McGraw-Hill, New York, 1968.

11 Selby, S. M., C. R. C. *Standard Mathematical Tables*, 19th Ed., Chemical Rubber Co., Cleveland, Ohio, 1971.

12 Vedder, J. D., "Simple Approximations for the Error Function and its Inverse," *Am. J. of Phys.*, Vol. 55, No. 8, 1987, pp. 762–763.

The Correction of X-Probe Results for Transverse Contamination

P. D. Clausen[1] and D. H. Wood[1]

This Note discusses the interpretation of X-probe measurements obtained in the presence of significant velocities transverse to the plane of the wires. To measure the three mean velocity components, the probe was used in two planes which gave a redundant estimate of the component along the probe axis. A correction of the measured mean velocities for transverse contamination is described and justified. It was found that the corrections reduced the mean component along the probe's axis by up to 20 percent, while the components orthogonal to that axis were hardly altered.

Nomenclature

A, B = King's law calibration constants, equation (1)
E = total instantaneous anemometer voltage, equation (1)
h^2 = transverse cooling or pitch factor, equation (2)
U = mean velocity along probe axis
U_c = cooling velocity, equations (2) and (3)
U_n = V or W, mean velocity normal to probe axis in plane of the wires
U_0 = normalizing velocity
U_t = V or W, transverse mean velocity
u = fluctuating velocity in direction of U
u_n, u_t = fluctuating velocities in direction of U_n and U_t

[1]Lecturer and Senior Lecturer, respectively, Department of Mechanical Engineering, University of Newcastle, N.S.W. 2308 Australia.

the integration over the layer. The work required is equivalent to evaluating a double integral. Thus, the closed-form approximate results in Table 1 can represent a saving of effort by 2 orders of magnitude (for $N = 10$, a typical minimum number of integration steps). This is at the expense of a loss of accuracy on the order of 0.15 percent for momentum, well within experimental limits.

Lastly, this approximation has the advantage that it can be inverted to yield the inverse function in closed form:

$$x(E) = x_0 + \sqrt{(1/b) \ln(A/E)}$$

where E represents any of $\text{erfc}(x)$, $\int \text{erfc}''(x)\, dx$.

These approximations may be useful for momentum integral theoretical techniques in shear layers with an assumed Gaussian or error function velocity profile.

Acknowledgments

APPENDIX I
Equations for the Coefficients

The coefficients b_n, x_n, and A_n for Table 1 are derived as follows. The function and slope at $x = 0$ are given by:

$$I_n(x=0) = A_n e^{-b_n x_n^2} = K \tag{1}$$

$$dI_n/dx \bigg|_{x=0} = K(-2 b_n x_n) = -S \tag{2}$$

At $x = x_c$, the function is:

$$I_n(x=x_c) = A_n e^{-b_n(x_c + x_n)^2} = C \tag{3}$$

Equation (2) can be solved for the product $b_n x_n$:

$$(b_n x_n) = (S/2K) \tag{4}$$

Multiplying out the quadratic term in equation (3) and substituting from equation (1) yields:

$$\ln(K/c) = b_n x_c (x_c + 2x_n) \tag{5}$$

From equation (4):

$$2x_n = (S/b_n K) \tag{6}$$

$$\ln(K/C) = b_n x_c^2 + (x_c S/K) \tag{7}$$

Thus, from equations (7), (4), and (1), we solve for the coefficients:

$$b_n = \frac{1}{x_c^2} [\ln(K/C) - (x_c S/K)] \tag{8}$$

$$x_n = (S/2b_n K) \tag{9}$$

$$A_n = K \exp(b_n x_n^2) \tag{10}$$

Equations (8), (9), and (10) must be solved sequentially, first substituting b_n from (8) in (9), and then b_n and x_n from (8) and (9) in (10).

For the solution presented in equations (8), (9), and (10), the value of x_c is determined by minimizing an error estimator e_i over the interval in question. Possible error estimators include:

$$e_1 = \Sigma |I - I_{\text{exact}}| / I_{\text{max}} \tag{11}$$

$$e_2 = \Sigma |I - I_{\text{exact}}| / I_{\text{exact}} \tag{12}$$

$$e_3 = \Sigma (I - I_{\text{exact}})^2 / I_{\text{max}} \tag{13}$$

$$e_4 = \Sigma (I - I_{\text{exact}})^2 / I_{\text{exact}} \tag{14}$$

The defined quantities e_1 and e_3 represent absolute error estimators, because they are relative to I_{max} over the interval,

whereas e_2 and e_4 are relative error estimators. e_1 and e_2 are linear absolute value error estimators; e_3 and e_4 are quadratic.

References

1 Abramovich, G. N., *The Theory of Turbulent Jets*, M.I.T. Press, Cambridge, Mass., 1963.

2 Abramowitz, M., and Stegun, I. A., *Handbook of Mathematical Functions*, Dover Publications, Inc., New York, 1965.

3 Batchelor, G. K., *An Introduction to Fluid Dynamics*, Cambridge Univ. Press, Cambridge, England, 1970.

4 Bird, R. B., Stewart, W. E., and Lightfoot, E. N., *Transport Phenomenon*, John Wiley & Sons, New York, 1960.

5 Bremhorst, K., "Unsteady Subsonic Turbulent Jets," *Recent Developments in Theoretical and Experimental Fluid Mechanics, Compressible and Incompressible Flows*, eds. Müller, U., Roesner, K. G., and Schmidt, B., Springer-Verlag, New York, 1979.

6 Greene, P. R., and Hill, W. G., Jr., "An Analytical Investigation of Experimental Problems Associated with Conservation of Momentum in a Jet Plume," Research Note #RN-363, Grumman Aerospace Corp., Bethpage, New York, 1975, 18 pp. Available on request from authors.

7 Guttman, I., and Wilks, S. S., *Introductory Engineering Statistics*, Wiley, New York, 1965.

8 Hill, W. G., Jr., and Greene, P. R., "Increased Turbulent Jet Mixing Rates Obtained by Self-Excited Acoustic Oscillations," ASME JOURNAL OF FLUIDS ENGINEERING, Vol. 99, No. 3, 1978, pp. 520–528.

9 Ramaprian, B. R., and Chandrasekhara, M. S., "Laser Doppler Anemometry Measurements in Plane Turbulent Jets," ASME JOURNAL OF FLUIDS ENGINEERING, Vol. 107, 1985, pp. 264–271.

10 Schlichting, H., *Boundary-Layer Theory*, McGraw-Hill, New York, 1968.

11 Selby, S. M., C. R. C. *Standard Mathematical Tables*, 19th Ed., Chemical Rubber Co., Cleveland, Ohio, 1971.

12 Vedder, J. D., "Simple Approximations for the Error Function and its Inverse," *Am. J. of Phys.*, Vol. 55, No. 8, 1987, pp. 762–763.

The Correction of X-Probe Results for Transverse Contamination

P. D. Clausen[1] and D. H. Wood[1]

This Note discusses the interpretation of X-probe measurements obtained in the presence of significant velocities transverse to the plane of the wires. To measure the three mean velocity components, the probe was used in two planes which gave a redundant estimate of the component along the probe axis. A correction of the measured mean velocities for transverse contamination is described and justified. It was found that the corrections reduced the mean component along the probe's axis by up to 20 percent, while the components orthogonal to that axis were hardly altered.

Nomenclature

A, B = King's law calibration constants, equation (1)
E = total instantaneous anemometer voltage, equation (1)
h^2 = transverse cooling or pitch factor, equation (2)
U = mean velocity along probe axis
U_c = cooling velocity, equations (2) and (3)
U_n = V or W, mean velocity normal to probe axis in plane of the wires
U_0 = normalizing velocity
U_t = V or W, transverse mean velocity
u = fluctuating velocity in direction of U
u_n, u_t = fluctuating velocities in direction of U_n and U_t

---

[1]Lecturer and Senior Lecturer, respectively, Department of Mechanical Engineering, University of Newcastle, N.S.W. 2308 Australia.

V, v = mean and fluctuating radial velocities
W, w = mean and fluctuating velocities in the direction orthogonal to U and V
$\Delta\psi$ = yaw angle, equation (3)
δ = pitch angle, equation (3)
θ_* = phase angle between blade and measurement position
ψ = effective wire yaw angle, equation (2)

Subscripts

c = cooling velocity, equation (2)
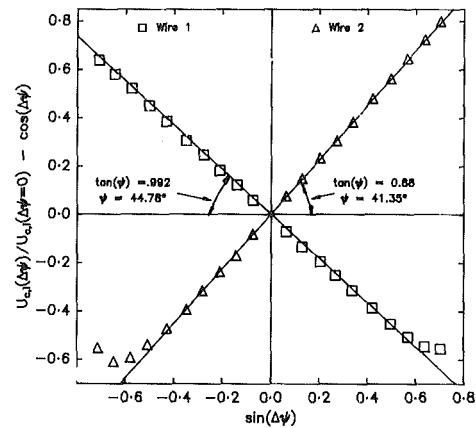i = 1, 2, wire number

Overbars denote ensemble averaging

Fig. 1 Extended yaw calibration of the X-probe. Uncertainty in sin $(\Delta\psi) = \pm 0.03$ at 20:1 odds. Uncertainty in ordinate $= \pm 0.04$ at 20:1 odds.

Introduction

This Note discusses the correction of mean velocity results from an X-probe for the effects of transverse mean velocities. These velocities, which lie in the plane normal to the plane of the wires, must be considered whenever it is *not* possible to align the probe axis with the direction of the mean velocity vector. We will not discuss the corresponding effects of fluctuating transverse velocities, which were analyzed by Muller [1] and Legg et al. [2]. The yaw (in the plane of the wires) and pitch (in the transverse plane) response are determined for a commercially available X-probe. We then describe a procedure to account for the effects of transverse velocities on mean velocity measurements from two orthogonal planes, the minimum number necessary to resolve all three mean velocities with an X-probe. The corrections were made after the initial data reduction that ignored the transverse component; of course, instantaneous corrections are impossible for any probe with less than three wires.

There are several important differences between the effects of transverse velocities on an X-probe and the more commonly used single wire probe. For example, the pitch response of one wire in an X-probe may be complicated by the presence of the other. However, an X-probe consisting of closely matched wires should accurately measure U_n even if transverse contamination is ignored. If so, then a comparison of the estimates for the mean and fluctuating axial velocity from the different measurement planes should immediately indicate the significance or otherwise of the transverse velocities.

Description of the Experiment and Measurement Techniques

The experiment which lead to this Note is described by Clausen et al. [3] and Clausen and Wood [4]. Measurements were made using a DISA 55P51 X-probe with 5 μm tungsten wires with 20 μm copper plated stubs that connected the 1.2 mm active length to the prongs. The probe was used to find the mean velocity and turbulence in the wake of a two-bladed shrouded wind turbine using phase-locked averaging, Gostelow [5]. The anemometer voltage was sampled 28 times during each revolution of the turbine for specified values of θ_*. The probe was always closely aligned with the conventional mean flow direction, to minimize the effects of the transverse velocities. The remaining effects which are discussed here arose because the phase-locked average mean velocities could be strong functions of θ_*.

The modified King's law was assumed to hold for each wire, so that

$$E_i^2 = A_i + B_i U_{c,i}^{0.45} \tag{1}$$

where the cooling or effective velocity $U_{c,i}$ was assumed to be just the velocity component normal to the wire, commonly referred to as the cosine cooling "law." That is

$$U_{c,i}^2 = [(U+u) + (U_n+u_n)\tan\psi_i]^2 + h_i^2(U_t+u_t)^2/\cos^2\psi_i \tag{2}$$
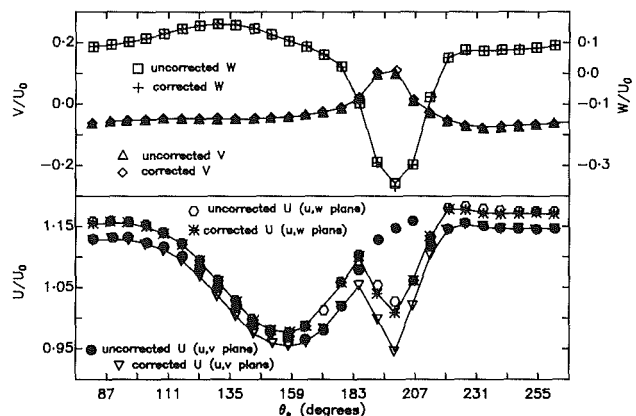
Fig. 2 Phase-locked averaged measurements in the wake of a wind turbine. Solid line is U from u,w-plane; X, U, from u, v-plane; $\triangle$, V; $\square$, W. All mean velocities are normalized by U_0. Uncertainty in normalized mean velocities $= \pm 0.02$ at 20:1 odds. $\diamond$, $\overline{u^2}$ from u,w-plane; *, $\overline{u^2}$ from u,v-plane; Ξ, $\overline{v^2}$; Z, $\overline{w^2}$; $\div$, $\overline{uw}$. All turbulence quantities are normalized by U_0^2. Uncertainty in normalized turbulence quantities $= \pm 0.05$ at 20:1 odds.

where $\cos\psi_i$ has been absorbed into B_i. The probe was calibrated in the core of a plane jet with the velocity parallel to the probe's axis and then yawed by $\Delta\psi$. It is easy to show, Bradshaw [6], that equation (2) then reduces to

$$U_{c,i}(\Delta\psi)/U_{c,i}(\Delta\psi=0) - \cos\Delta\psi = \sin\Delta\psi\tan\psi_i. \tag{3}$$

which allows the determination of ψ_i; this angle is not necessarily the geometric angle. Normally the calibration was done for only one $U_{c,i}(\Delta\psi=0)$ and over the range -25 deg $\leq \Delta\psi \leq +25$ deg. The extended range of ± 45 deg in Fig. 1 is a severe test of the adequacy of the cosine law. The results show that the law is valid, and longitudinal cooling can be ignored, whenever the instantaneous yaw angle is less than about ± 30 deg to the probe's axis. This is consistent with Jorgensen's [7] demonstration that longitudinal cooling effects are reduced by having stubs between the active wire and the prongs. The neglect of longitudinal cooling considerably simplifies the data analysis. We estimate the accuracy of the mean velocities in the absence of transverse contamination to be ± 2 percent of U_0. The error is within the height of the symbols used to plot them in Figs. 2, and 4. Similary the Reynolds stresses are accurate to within ± 5 percent, but this has no real significance for the corrections described below.

Initially, the transverse velocities were ignored in the data analysis, that is, h_i^2 was set to zero in equation (2) because the
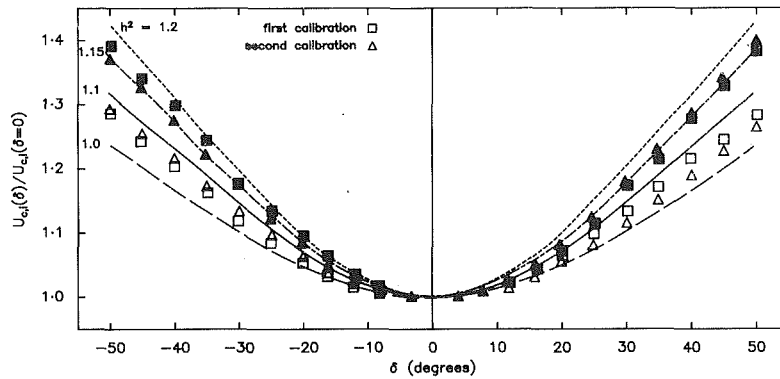
Fig. 3 Pitch calibration of X-probe. Open symbols denote wire 1, and closed symbols wire 2. Uncertainty in $\delta = \pm 0.5$ deg, in ordinate ± 0.02 at 20:1 odds. Some nearly co-incident points near $\delta = 0$ deg have been omitted for clarity. The lines show equation (4) for the values of h_i^2 indicated.
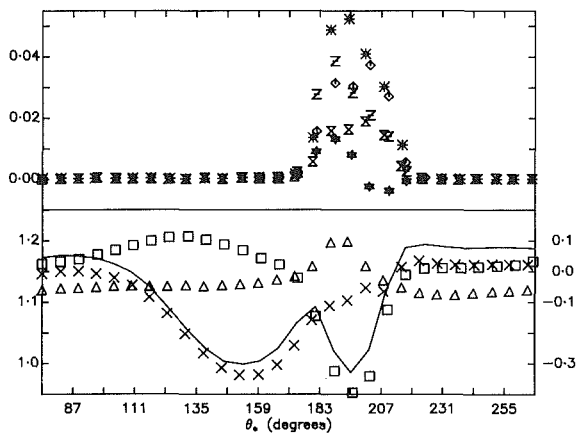

Fig. 4 Corrected mean velocities from Fig. 2. Solid lines connect the corrected results only. Uncertainties as in Fig. 2.

inclusion of the extra unknowns, U_t and u_t, would seriously complicate the data reduction. Profiles from the two measurement planes are shown in Fig. 2. (An explanation for the origin for θ_* in the figures is not necessary here.) The turbulence level in the wake (located approximately between 180 and 220 deg) is not high, as U_0 is comparable to the conventional average of U. However, W changes rapidly across the wake, and even changes sign and so produces a significant transverse velocity when the probe is in the u, v-plane. Thus the poor agreement between the two estimates of U and $\overline{u^2}$ in the wake is due largely to transverse contamination. Since the variation of V is much less than that of W, the u, w-plane results should be more accurate. We note that in many other profiles, good agreement between the measurements of $\overline{u^2}$ was always reflected in the agreement of U.

Transverse Velocity Corrections

If, during calibration, the probe is pitched at angle δ with $\Delta\psi = 0$, but with the other conditions the same as in the yaw calibration, equation (2) reduces to

$$U_{c,i}(\delta)/U_{c,i}(\delta = 0) = [\cos^2\delta + h_i^2 \sin^2\delta]^{1/2} \qquad (4)$$

from which h_i^2 can be determined. Two separate tests were performed at 17 ms^{-1}. The results in Fig. 3 show that $h_1^2 = 1.1$ and $h_2^2 = 1.05$ for the probe used to obtain the results in Fig 2. To the accuracy of determination, the pitch factors did not depend on δ. The symmetry of the pitch response is remarkable, especially at large magnitudes of δ, where we expected at least some aerodynamic interference. The pitch response is as sim-

ple as that of a single wire probe, and considerably simpler than that of the three-wire probe used by Andreopoulos [12].

To avoid using a binomial expansion of $\bar{U}_{c,i}$, the mean velocities were corrected using the four values of $\overline{U_{c,i}^2}$. The turbulence terms in $\overline{U_{c,i}^2}$ were assumed to be those measured with h_i^2 set to zero, and shown in Fig. 2. Strictly, this assumption is justified only when the turbulence level is low. The corrections were done iteratively starting with the estimate for V obtained with $h_i^2 = 0$, since, generally, V is the smallest mean velocity. This estimate was used in equation (2) with the appropriate h_i^2 to obtain U and W. Then W was used to find U from the other plane and recalculate V and so on. The iteration was terminated, typically after two iterations, when the maximum normalized difference between successive values of V was less than one percent for all twenty eight points.

Discussion

The corrected mean velocities from Fig. 2 are shown in Fig. 4. The maximum change to U in the u, v-plane is 20 percent, corresponding to mean yaw and pitch angles of 22 deg; the former is approaching the limit of validity for the cosine law. The change to U from the u,w-plane is much smaller. The remaining consistent difference in U between the two planes is attributed to slight changes in turbine operating conditions in the hour that elapsed between the measurements in the two planes. The corrections to V and W are always less than one percent of the final value even though there was a 16 percent difference in the wires' pitch response, as measured by the difference in $h^2/\cos^2\psi$. The pitch response of the X-probe used here is no more complex than that of a single wire probe. Thus the former is clearly preferable because it reduces significantly the time required for an experiment. The other obvious alternative, some sort of three-wire probe, would require more sophisticated data analysis, e.g., Andreopoulos [8] and Lakshminarayana [9]. Furthermore, the included angle of the cone of validity of the calibration of a three-wire probe is approximately 50 deg (see reference [9] for a summary of relevant results). Therefore, such a probe, like the X-probe used here, could not accurately measure the turbulence for cases such as Fig. 2 without adjusting the alignment.

Conclusions

The particular X-probe described here displayed extremely simple yaw and pitch response over a large range of angles. The effective cosine cooling law was adequate over ± 30 deg from the probe axis. Somewhat surprisingly, the pitch response was remarkably symmetric over ± 50 deg, showing that there was little aerodynamic interference of one wire by the other. The transverse or pitch factors h_i^2 were independent

of pitch angle. These results show that the response of an X-probe is no more complex than that of a single wire probe.

As expected, the comparison of the redundant estimates of U and $\overline{u^2}$ from the two measurement planes quickly indicated the importance or otherwise of the transverse velocities. The correction for these effects hardly altered V and W even when U was reduced by 20 percent and the pitch response of the wires differed by 16 percent. These results show that an X-probe, apart from having a smaller measuring volume than a three-wire probe, offers the distinct advantage of easily demonstrating when transverse contamination is important.

Acknowledgments

References

1 Müller, U. R., "On the Accuracy of Turbulence Measurements With Inclined Hot Wires," *J. Fluid Mech.*, Vol. 119, 1982, pp. 155–172.

2 Legg, B. L., Coppin, P. A., and Raupach, M. R., "A Three-Hot-Wire Anemometer for Measuring Two Velocity Components in High Intensity Boundary Layers," *J. Phys. E.*, Vol. 17, 1984, pp. 970–976.

3 Clausen, P. D., Piddington, D. M., and Wood, D. H., "An Experimental Investigation of Blade Element Theory for Wind Turbine. Part 1: Mean Flow Results," *J. Wind Engg. & Ind. Aero.*, Vol. 25, 1987, pp. 189–206.

4 Clausen, P. D., and Wood, D. H., "An Experimental Investigation of Blade Element Theory for Wind Turbine. Part 2: Phase-locked averaged Results," *J. Wind Engg. & Ind. Aero.*, Vol. 31, 1988, pp. 305–322.

5 Gostelow, J. P., "A New Approach to the Experimental Study of Turbomachinery Flow Phenomena," *ASME J. Engineering for Power*, Vol. 99, 1977, pp. 97–103.

6 Bradshaw, P., *An Introduction to Turbulence and its Measurement*, Pergammon, 1971.

7 Jorgensen, F. E., "Directional Sensitivity of Wire and Fiber-Film Probes," *DISA Information*, Vol. 11, 1971, pp. 31–37.

8 Andreopoulos, J., "Improvements in the Performance of Triple Hot-Wire Probes," *Rev. Sci. Instrum.*, Vol. 54, 1983, pp. 733–740.

9 Lakshminarayana, B., "Three Sensor Hot Wire/Film Technique for Three Dimensional Mean and Turbulence Flow Field Measurement," *TSI Quart.*, Vol. 8, 1982, pp. 3–13.

The Drag Coefficient of a Sphere in a Square Channel

L. C. Chow,[1] J. E. Leland,[2] J. E. Beam,[2] and E. T. Mahefkey[2]

Nomenclature

A_p = projected area
B = flow cross-sectional area
C_D = drag coefficient
d = diameter of sphere
d_t = diameter of circular tube
F_D = drag force on sphere
g = gravitational acceleration
K = surface roughness of sphere
m = mass of sphere
Re = Reynolds number, ud/ν
u = average fluid velocity upstream
V = volume of sphere
W = width of flow channel
ρ = fluid density
ν = fluid kinematic viscosity

[1] Department of Mechanical Engineering, University of Kentucky, Lexington, Ky, 40506.
[2] Air Force Aero Propulsion Laboratory, Wright-Patterson Air Force Base, Ohio 45433.

Introduction

The drag coefficient of a sphere in unconfined flow is given in most fluid mechanics texts, for example, Massey (1979). The drag coefficient, C_D, is determined by measuring the force exerted on the sphere by the fluid when the relative velocity between the sphere and the oncoming fluid, u, is known. C_D is defined by

$$F_D = C_D A_p \rho \, u^2/2 \qquad (1)$$

Fluid flow over a sphere located inside a tapered tube has been studied because of applications to flowmeter design (Blevins, 1984). The drag coefficient of a sphere inside a circular tube under the blockage conditions $0.5 < d/d_t < 0.92$ has also been determined for the regime of Reynolds numbers ($\text{Re} > 10^4$) where C_D is constant (Achenbach, 1974). At $A_p/B = 0.839$ ($d/d_t = 0.916$), the drag coefficient was measured to be about 39. Awbi and Tan (1981) have also measured the drag coefficient of a sphere in a square channel in the Reynolds number range where C_D is approximately constant. For the same blockage ratio (A_p/B), their results were lower than those of Achenbach (1974). The discrepancies were attributed to the development of the boundary layer in Achenbach's tests.

The purpose of this Note is to present the drag coefficient of a sphere in a square channel at low Reynolds numbers ($\text{Re} < 1800$). For smooth spheres, the drag coefficient depends on Re and the ratio d/W. This information is lacking in the literature.

Experimentation

To determine the drag coefficient, solid spheres were suspended in water flowing vertically upward in a square channel. In order to obtain C_D over a range of Re, nine types of spheres with three different diameters (small, medium and large) were used (see Table 1). The spheres were made of nylon, lexan, delrin, black glass, red sapphire, ceramic, stainless steel 316, stainless steel 440C, or tungsten carbide. According to the manufacturer, these are smooth spheres with a surface roughness of less than 4×10^{-6} cm. The masses of the spheres were measured to within 5×10^{-4} g with an analytical balance.

Five flow channels (with length of about 30 cm) were used. Each flow channel was made by covering a square groove machined into an aluminum piece with optically smooth glass. The widths of the channels are listed in Table 1. These widths were chosen so that two different d/W ratios can be obtained with the small, medium and large spheres. The d/W ratios are 0.886 ± 0.008 and 0.954 ± 0.008.

Demineralized, deionized water at about 20°C was supplied from a constant-head reservoir to the flow channel. The water flow rate was controlled by adjusting a needle valve connected between the reservoir and the flow channel so that the sphere was steadily suspended near the top of the vertical channel. For all the tests performed (see Table 1), the water flow inside the channel was laminar and the velocity profile just upstream of the sphere was essentially fully developed.

After the sphere was suspended by adjusting the flow rate, the water velocity, u, was determined by measuring the amount of water collected in a calibrated cylinder over a given amount of time. By repeating each test a minimum of five times, it was determined that u was accurate to within 7 percent for the worst case. The uncertainty in u was mostly due to

Table 1 Experimental conditions

Test	Sphere Size	d(cm, ±0.0013)	W(cm, ±0.0025)
1	small	0.3150	0.3302
2	medium	0.4724	0.4953
3	large	0.6325	0.6604
4	small	0.3150	0.3556
5	medium	0.4724	0.5334

of pitch angle. These results show that the response of an X-probe is no more complex than that of a single wire probe.

As expected, the comparison of the redundant estimates of U and $\overline{u^2}$ from the two measurement planes quickly indicated the importance or otherwise of the transverse velocities. The correction for these effects hardly altered V and W even when U was reduced by 20 percent and the pitch response of the wires differed by 16 percent. These results show that an X-probe, apart from having a smaller measuring volume than a three-wire probe, offers the distinct advantage of easily demonstrating when transverse contamination is important.

Acknowledgments

References

1 Müller, U. R., "On the Accuracy of Turbulence Measurements With Inclined Hot Wires," *J. Fluid Mech.*, Vol. 119, 1982, pp. 155–172.

2 Legg, B. L., Coppin, P. A., and Raupach, M. R., "A Three-Hot-Wire Anemometer for Measuring Two Velocity Components in High Intensity Boundary Layers," *J. Phys. E.*, Vol. 17, 1984, pp. 970–976.

3 Clausen, P. D., Piddington, D. M., and Wood, D. H., "An Experimental Investigation of Blade Element Theory for Wind Turbine. Part 1: Mean Flow Results," *J. Wind Engg. & Ind. Aero.*, Vol. 25, 1987, pp. 189–206.

4 Clausen, P. D., and Wood, D. H., "An Experimental Investigation of Blade Element Theory for Wind Turbine. Part 2: Phase-locked averaged Results," *J. Wind Engg. & Ind. Aero.*, Vol. 31, 1988, pp. 305–322.

5 Gostelow, J. P., "A New Approach to the Experimental Study of Turbomachinery Flow Phenomena," *ASME J. Engineering for Power*, Vol. 99, 1977, pp. 97–103.

6 Bradshaw, P., *An Introduction to Turbulence and its Measurement*, Pergammon, 1971.

7 Jorgensen, F. E., "Directional Sensitivity of Wire and Fiber-Film Probes," *DISA Information*, Vol. 11, 1971, pp. 31–37.

8 Andreopoulos, J., "Improvements in the Performance of Triple Hot-Wire Probes," *Rev. Sci. Instrum.*, Vol. 54, 1983, pp. 733–740.

9 Lakshminarayana, B., "Three Sensor Hot Wire/Film Technique for Three Dimensional Mean and Turbulence Flow Field Measurement," *TSI Quart.*, Vol. 8, 1982, pp. 3–13.

The Drag Coefficient of a Sphere in a Square Channel

L. C. Chow,[1] J. E. Leland,[2] J. E. Beam,[2] and E. T. Mahefkey[2]

Nomenclature

A_p = projected area
B = flow cross-sectional area
C_D = drag coefficient
d = diameter of sphere
d_t = diameter of circular tube
F_D = drag force on sphere
g = gravitational acceleration
K = surface roughness of sphere
m = mass of sphere
Re = Reynolds number, ud/ν
u = average fluid velocity upstream
V = volume of sphere
W = width of flow channel
ρ = fluid density
ν = fluid kinematic viscosity

[1] Department of Mechanical Engineering, University of Kentucky, Lexington, Ky. 40506.
[2] Air Force Aero Propulsion Laboratory, Wright-Patterson Air Force Base, Ohio 45433.

Introduction

The drag coefficient of a sphere in unconfined flow is given in most fluid mechanics texts, for example, Massey (1979). The drag coefficient, C_D, is determined by measuring the force exerted on the sphere by the fluid when the relative velocity between the sphere and the oncoming fluid, u, is known. C_D is defined by

$$F_D = C_D A_p \rho \, u^2/2 \qquad (1)$$

Fluid flow over a sphere located inside a tapered tube has been studied because of applications to flowmeter design (Blevins, 1984). The drag coefficient of a sphere inside a circular tube under the blockage conditions $0.5 < d/d_t < 0.92$ has also been determined for the regime of Reynolds numbers (Re $> 10^4$) where C_D is constant (Achenbach, 1974). At $A_p/B = 0.839$ ($d/d_t = 0.916$), the drag coefficient was measured to be about 39. Awbi and Tan (1981) have also measured the drag coefficient of a sphere in a square channel in the Reynolds number range where C_D is approximately constant. For the same blockage ratio (A_p/B), their results were lower than those of Achenbach (1974). The discrepancies were attributed to the development of the boundary layer in Achenbach's tests.

The purpose of this Note is to present the drag coefficient of a sphere in a square channel at low Reynolds numbers (Re < 1800). For smooth spheres, the drag coefficient depends on Re and the ratio d/W. This information is lacking in the literature.

Experimentation

To determine the drag coefficient, solid spheres were suspended in water flowing vertically upward in a square channel. In order to obtain C_D over a range of Re, nine types of spheres with three different diameters (small, medium and large) were used (see Table 1). The spheres were made of nylon, lexan, delrin, black glass, red sapphire, ceramic, stainless steel 316, stainless steel 440C, or tungsten carbide. According to the manufacturer, these are smooth spheres with a surface roughness of less than 4×10^{-6} cm. The masses of the spheres were measured to within 5×10^{-4} g with an analytical balance.

Five flow channels (with length of about 30 cm) were used. Each flow channel was made by covering a square groove machined into an aluminum piece with optically smooth glass. The widths of the channels are listed in Table 1. These widths were chosen so that two different d/W ratios can be obtained with the small, medium and large spheres. The d/W ratios are 0.886 ± 0.008 and 0.954 ± 0.008.

Demineralized, deionized water at about 20°C was supplied from a constant-head reservoir to the flow channel. The water flow rate was controlled by adjusting a needle valve connected between the reservoir and the flow channel so that the sphere was steadily suspended near the top of the vertical channel. For all the tests performed (see Table 1), the water flow inside the channel was laminar and the velocity profile just upstream of the sphere was essentially fully developed.

After the sphere was suspended by adjusting the flow rate, the water velocity, u, was determined by measuring the amount of water collected in a calibrated cylinder over a given amount of time. By repeating each test a minimum of five times, it was determined that u was accurate to within 7 percent for the worst case. The uncertainty in u was mostly due to

Table 1 Experimental conditions

Test	Sphere Size	d(cm, ± 0.0013)	W(cm, ± 0.0025)
1	small	0.3150	0.3302
2	medium	0.4724	0.4953
3	large	0.6325	0.6604
4	small	0.3150	0.3556
5	medium	0.4724	0.5334

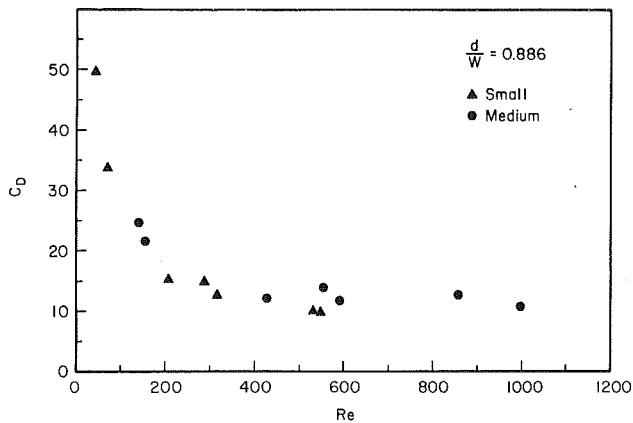Fig. 1 Drag coefficient versus Reynolds number at d/W = 0.954

Fig. 2 Drag coefficient versus Reynolds number at d/W = 0.886

a small degree of unsteadiness in the experiment due to vortex shedding.

Results

The drag coefficient is determined by the following equation,

$$C_D A_p \rho \; u^2/2 = (m - \rho \; V)g \qquad (2)$$

The results for $d/W = 0.954$ and 0.886 are shown in Figs. 1 and 2, respectively. The C_D values are accurate to within 16 percent. The major contributing factor to the uncertainty is the velocity measurement. By comparing Figs. 1 and 2, it can be observed that C_D is a strong function of d/W. At $d/W = 0.886$, the data obtained using the medium-size spheres are somewhat higher than those obtained using the small-size spheres (see Fig. 2). It is suspected that the tests with the medium-size spheres had a slightly larger d/W. Even with very careful machining, the uncertainty in the d/W ratio is 0.008.

The present results cannot be compared with those of Awbi and Tan (1981) because their area blockage ratio, A_p/B, is equal to 0.3 or less. However, Achenbach (1974) provided a correlation to determine C_D for a sphere in a circular tube at high Re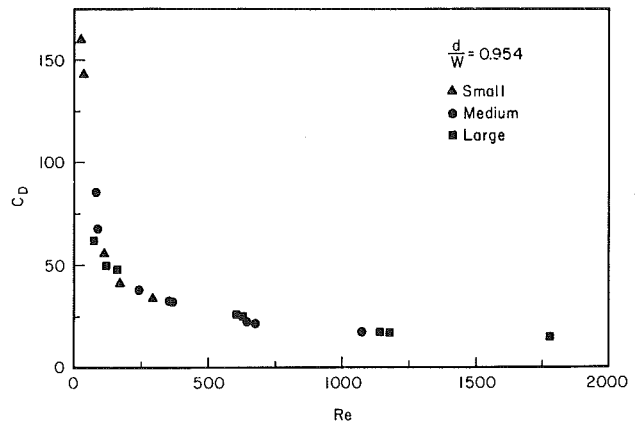 (Re $> 10^4$) where C_D is independent of Re. The present results are consistent with the results of Achenbach if the same area blockage ratio, A_p/B, is used in the comparison. For example, at $A_p/B = 0.715$, $(d/W = 0.954)$, the Achenbach's correlation yields a value of 10.5 for C_D in a circular tube whereas, the present experiment shows that C_D in a square channel is 14.8 at Re = 1780.

Conclusions

The present experiment has provided results for the drag coefficient of a sphere in a square channel at low Reynolds numbers. The drag coefficient depends significantly on both Re and the area blockage ratio. The present results complement previous work on drag coefficient measurements in the high Re regime where the drag coefficient is independent of Re.

References

Achenbach, E., 1974, "The Effects of Surface Roughness and Tunnel Blockage on the Flow Past Spheres," *J. Fluid Mech.*, Vol. 65, Part 1, pp. 113–125.

Awbi, H. B., and Tan, S. H., 1981, "Effect of Wind-Tunnel Walls on the Drag of a Sphere," *J. Fluids Engin.*, Vol. 103, pp. 461–465.

Blevins, R. D., 1984, *Applied Fluid Dynamics Handbook*, Van Nostrand Reinhold, New York.

Massey, B. S., 1979, *Mechanics of Fluids*, 4th ed., Van Nostrand Reinhold, New York.